Atom Probe Tomography Research on Catalytic Alloys and Nanoparticles



Qifeng Yang
Linacre College
University of Oxford

A thesis submitted for the degree of

Doctor of Philosophy

Hilary Term, 2018

To my Family.

Abstract

Atom Probe Tomography Research on Catalytic Alloys and Nanoparticles
Qifeng YANG
Linacre College, Oxford
A thesis submitted for the degree of Doctor of Philosophy
Hilary Term, 2018

Catalyst is a key component in the chemical industry, with more than 90% of total chemical products reliant on their use. However, the working mechanisms are in many cases still not fully understood. For heterogeneous catalysts, in which the reactions normally occur on solid phase materials, a better understanding of the catalytic surfaces, and how they evolve under reactive environments is recognised as the next step forward in the field.

This work presents a study utilising atom probe tomography (APT), combined with an in-situ reaction cell, to understand the initial oxidation processes of catalytic NiFe and NiCo model alloy systems. In order to improve reliability of results, a protocol was developed to clean the sample surfaces by field ion evaporation, eliminate sample surface contamination before in-situ oxidation was then performed.

APT was successfully applied to these alloys to characterise oxide development as a function of exposure time and temperature. APT also demonstrated surface enrichment induced by oxide formation remained after reduction of the alloy. The successful application of APT on the model alloys led to the next goal which was to associate the data to real catalytic particles. To achieve this, work was extended into the field of nanoparticle catalysts.

Nanoparticles with similar compositions to the model alloys were fabricated by chemical synthesis and were examined initially by transmission electron microscopy (TEM). The main goal of this phase was to investigate the surface segregation behaviour of the particles, identifying common behaviours with the model alloys. However, the presence of residual complex chemical environments around the particles following synthesis made APT analysis difficult. Therefore, an alternative method of particle fabrication was explored to better control the resulting materials for easier application of atom probe for nanoparticle analyses.

Metallic nanoparticles of Ag, AuCu, AuNi, and AuNiMo were made by an inert gas condensation method, deposited on suitable support materials and were subsequently analysed by APT, facilitated by an improved sample preparation method. Surface segregation on individual nanoparticles was detected. Together with other complementary surface-probing techniques, a complete understanding of these particles from micrometre down to the level of individual particles was achieved. The potential for APT is highlighted to play a key role in this approach to realise a complete understanding of the chemical order, microstructure in multimetallic nanoparticles designed for catalysis.

Preface

The work presented in this doctoral thesis has been carried out at the Department of Materials, University of Oxford from October 2013 to January 2018, under the supervision of Dr Paul Bagot, Dr Tomas Martin, Dr Eric Marceau and Prof. Michael Moody. All of the research carried out for this thesis is original, and where the work of others has been included it has been clearly referenced and acknowledged. No part of this thesis has been submitted for a degree at this, or any other university. Some of the work has been published in peer reviewed journals and presented at conferences and seminars as detailed below:

Journal Articles:

Q. Yang, D.E. Joyce, S. Saranu, G.M. Hughes, A. Varambhia, M.P. Moody and P.A.J. Bagot. *A combined approach for deposition and characterization of atomically engineered catalyst nanoparticles*. Catalysis, Structure & Reactivity, vol 1(3) 2015 125-131. doi: 10.1179/2055075815Y.0000000006

Q. Yang, V. Broadley, M Danaie, N. Young, D.E. Joyce, A.-F. Lamic-Humblot, A.-S. Mamede, Eric Marceau, T.L. Martin, M.P. Moody, P.A.J Bagot. *Synthesis and combined TEM/Atom Probe Tomography Characterisation of Au-based multimetallic Nanoparticles for Catalytic Applications.* In preparation.

Dichao Shi, **Qifeng Yang**, Christi Peterson, Anne-Félicie Lamic-Humblot, Jean-Sébastien Girardon, Anne CONSTANT, Lorenzo Stievano, Moulay Sougrati, Valerie Briois, Paul Bagot, Robert Wojcieszak, Sébastien Paul. *Bimetallic Fe-Ni/SiO2 catalysts for furfural hydrogenation: identification of the interplay between Fe and Ni during deposition-precipitation and thermal treatments*. Submitted to Catalysis Today.

Conferences:

Q. Yang, T. L. Martin, E. Marceau, M.P. Moody and P. A. J. Bagot. "Atom Probe Studies of Surface Segregation in Iron-Nickel Alloys under Oxidation/Reduction Environments" APT&M, Stuttgart, 2014. Poster Presentation.

Q. Yang, T. L. Martin, E. Marceau, M.P. Moody and P. A.J. Bagot. "Surface Segregation in Iron-Nickel alloys under Low Temperature Oxidation/Reduction Environments" UK Catalysis Conference, Loughborough, 2015. Oral Presentation.

Q. Yang, T. L. Martin, E. Marceau, D. Joyce, M.P. Moody and P. A. J. Bagot. "High Resolution Characterisation of Novel Catalytic Nanoparticles" EuroMat, Warsaw, 2015. Oral Presentation.

Q. Yang, V. Broadley, N. Young, T. L. Martin, M.P. Moody and P. A.J. Bagot. "Recent Progress in High Resolution Characterisation Approaches for Catalytic Nanoparticles" UK Catalysis Conference, Loughborough, 2016. Oral Presentation.

Q. Yang, V. Broadley, M. Danaie, D. Joyce, E. Marceau, N. Young, T. L. Martin, M.P. Moody and P. A.J. Bagot. "Au-based bimetallic and trimetallic catalytic nanoparticles as studied by Atom Probe Tomography and other complimentary techniques" APT&M, South Korea, 2016. Oral Presentation.

Q. Yang, T. L. Martin, E. Marceau, M.P. Moody and P. A. J. Bagot. "Atom Probe Tomography research on the surface composition of catalytic material" UK Catalysis Conference, Loughborough, 2017. Poster Presentation.

Acknowledgements

This work was made possible by a generous financial support from my family and enormous support from my wife. I hope my pursuit of this work is justified on their merits. I am especially appreciative of the guidance I received from my father in law, and I hope I have done a good work meeting his expectation.

The work presented in this thesis was made possible through the support of many people. First, I would like to thank my supervisors Dr. Paul A.J. Bagot, Dr Tomas L. Martin, Dr Eric Marceau, and Prof. Michael P. Moody for their outstanding support, guidance and high interest through the project. Paul has been very patient on teaching me how to become a researcher and Michael is always there for the additional care. Tom has been a good teacher both in science and life and I am so proud to have his confidence on me all the time. My external supervisor Dr Eric Marceau also provided priceless knowledge on catalysts. His kindness and unique sense of humour always inspire me when he comes to the town. My colleagues also provide me a great joy for staying in the group and in Oxford. I am so thankful to Dr James Douglas, who is always helpful on my English and always provides "wired" knowledge for great fun. Also, Dr Daniel Haley's great knowledge on the atom probe enables me to find the answer when struggling in the data analysis. Not to mention Dr Andrew London, his intelligence always inspires me to think and try new things.

Apart from academic work, I have a great time in Linacre College. I am so proud to work with so many smart people in various occasions. Especially, I want to thank Dr Nick Brown, the Principal of the college, his support and kindness is the greatest thing I have ever experienced.

At last, I want to thank my loving wife Liye again. You are the one who always stands by me and offers help. I could not finish this thesis without you.

Acronyms

AFM Atomic Force Microscopy

APT Atom Probe Tomography

BF Bright Field

DPU Deposition-Precipitation Reaction with Urea

EDX Energy Dispersive X-ray

FEM Field Emission Microscopy

FIB Focused Ion Beam

FIM Field Ion Microscopy

HAADF High Angle Anular Dark Field

HRTEM High Resolution Transmission Electron Microscopy

ICF Image Compression Factor

IGC Inert Gas Condensation

IVAS Imago Visualisation and Analysis Software

IWI Incipient Wetness Impregnation

LEAP Local Electrode Atom Probe

MCP Micro-plate Plate

MD Mild drying

Meso-Q Mantis Quadrupole Mass Filter

NPs Nanoparticles

PGM Platinum group metal

ROI Region of interest

TEM Transmission Electron Microscopy

UHV Ultra High Vacuum

XRD X-ray Diffraction

Contents

1 Introduction **1**

2 Literature Review **5**
2.1 Catalysis Fundamentals 6
2.1.1 Background of Catalysis 6
2.1.2 Metal based heterogeneous catalysts 11
2.1.2.1 Types of reactions and mechanisms 11
2.1.3 Durability, poisoning and regeneration 12
2.1.4 Multimetallic catalysts 14
2.2 Metallic systems explored in the thesis 15
2.2.1 Non-noble metal systems Ni, Fe, Co 16
2.2.1.1 Catalytic behaviour 16
2.2.1.2 Oxidation behaviour of Fe, Ni, Co, FeNi and NiCo 19
2.2.2 Noble metal Au-based alloys 34
2.2.2.1 Catalytic behaviour 34
2.2.2.2 Au based particles 36
2.3 TEM, FIM and APT study of catalysts 39
2.3.1 TEM Research on nanoparticles 39
2.3.2 Field Ion Microscopy and Field Emission Microscopy 41
2.3.3 Atom probe research on catalytic alloys and nanoparticles 46
2.4 Summary 61

3 Materials and Experimental methods **63**
3.1 Materials and Sample Preparation 64
3.1.1 Alloy wires 64
3.1.2 Preparation of nanoparticles by chemical synthesis 68
3.1.3 Preparation of nanoparticles by physical deposition 71
3.2 Field Ion Microscopy 77
3.3 Atom Probe Tomography 79
3.3.1 Basic principles 79
3.3.2 Data reconstruction protocol 86
3.3.3 Mass labelling protocol 89
3.4 Transmission Electron Microscopy 94
3.5 LEIS and XPS 98
3.6 AFM 101

3.7 XRD . . . 101

4 APT Characterisation of Oxidised Bimetallic Alloys 103
4.1 As-received alloys . . . 104
4.1.1 Crystallography . . . 104
4.1.2 Chemical compositions and contaminations . . . 108
4.1.3 Compositional measurements along zone axes and cleaned surfaces 108
4.2 Oxidation of alloys . . . 111
4.2.1 Oxidation of Ni10Fe90 alloy . . . 111
4.2.2 Oxidation of Ni48Fe52 alloy . . . 121
4.2.3 Oxidation of Ni90Fe10 alloy . . . 126
4.2.4 Oxidation of Ni50Co50 alloy . . . 138
4.3 Reduction of alloys . . . 141
4.3.1 30min 773K H_2 reduction on Ni10Fe90 . . . 141
4.3.2 30min 773K H_2 reduction on Ni48Fe52 . . . 141
4.4 Discussion and summary . . . 145
4.4.1 Oxide composition . . . 145
4.4.2 Ni enrichment . . . 149
4.4.3 Oxidation Kinetics . . . 149
4.4.4 Future work on alloy experiments . . . 152

5 Initial attempt: a TEM inspection of multimetallic nanoparticles fabricated by chemical method 155
5.1 Inspection of Ni50Fe50 particles reduced at 700°C . . . 156
5.2 Investigation of effect of reduction temperature on Ni50Fe50 particles . . . 162
5.3 Comparison of Ni50Fe50 and Ni50Co50 particles reduced at 700°C . . . 165
5.4 Discussion . . . 168

6 Inspection of nanoparticles fabricated by physical method: IGC 171
6.1 Characterisation of Ag monometallic nanoparticles . . . 172
6.1.1 Mass filter (MesoQ) . . . 172
6.1.2 SEM . . . 173
6.1.3 APT . . . 176
6.2 Characterisation of AuCu and AuCuMo nanoparticles . . . 181
6.2.1 MesoQ (mass filter) . . . 181
6.2.2 TEM . . . 183
6.2.3 EDX . . . 191
6.2.4 APT . . . 195
6.2.4.1 AuCuMo . . . 202
6.2.4.2 AuCu . . . 207
6.3 Characterisation of AuNi and AuNiMo nanoparticles . . . 209
6.3.1 MesoQ (mass filter) . . . 209
6.3.2 AFM . . . 211
6.3.3 TEM . . . 214
6.3.4 XPS . . . 216
6.3.5 LEIS . . . 218

6.3.6 APT 222
6.4 Discussion 227
6.4.1 Assessment of the IGC method for particle production 227
6.4.2 APT sample preparation 228
6.4.3 Technique capability and sample analysis protocol 231

7 Summary **233**

8 Conclusions **237**

9 Bibliography **239**

A Appendix-peak labelling **267**
A.1 Fe52Ni48 267
A.2 Ni90Fe10 273
A.3 Ni50Co50 277

B Appendix-experiment table **281**

Chapter 1

Introduction

Motivation

Catalysis is an important topic for chemistry since more than 90% industrial chemical reactions involve catalysts. In the field of heterogeneous catalysis, the surface composition of a catalyst determines its properties such as catalyst activity, poisoning, regeneration, all of which contribute significantly to the overall running cost of any process requiring catalysts. In addition, detailed composition information is essential for the development of future generation catalysts with improved performance. Therefore, the objective of this thesis is to understand the surface and bulk characteristics of catalytic alloys and multimetallic nanoparticles, especially chemical composition, via atomic resolution analytic techniques. In this thesis, atom probe tomography (APT) and high resolution transmission electron microscopy (HRTEM) are the two main tools for such characterisation, especially APT which is able to access atomic-scale levels of chemical information and evidence of element segregation near the sample surfaces. Sample preparation method for APT analysis is one of the main areas of pursuit in this thesis, as it is a major challenge to overcome for regular APT application to catalysts characterisation. Furthermore, there are two distinct classes of metals: noble and non-noble. Non-noble metals were investigated to evaluate the possibility of replacing noble metals in various chemical reactions, with particular emphasis on under-

standing surface segregation behaviour during reactions. Noble metals were only used here to explore new catalyst preparation routes including subsequent APT sample preparation methods. Overall, this thesis contains three high-level aims:

1. Understand the surface changes of model alloys under various gaseous environments, aiming to mimic catalyst behaviour during their cycle of use (non-noble metals)

2. Evaluate chemical and structural characteristics of nanoparticles synthesised by chemical methods (non-noble metals)

3. Development of a robust sample preparation method for as-deposited nanoparticle analysis by atom probe tomography (noble metals)

For the sake of simplicity, these three aims will be hereafter simplified to *model alloy* work, *nanoparticle by synthesis* work and *nanoparticle by condensation* work in the remaining of this thesis.

Scope of the project

With reference to the aims outlined above, the scope of this thesis can be categorised by the a) materials and b) techniques involved to examine such catalysts.

For low cost (non-noble) catalytic materials, Fe, Ni and Co alloys were used to mimic the surface behaviours of equivalent industrial catalysts intended for biomass transformations. Field Ion Microscopy (FIM) and APT were heavily involved to probe the surface composition change of those alloys under oxidising environments. To compare the APT results to actual nanoparticles, FeNi and NiCo nanoparticles made by chemical syntheses were analysed by TEM. The composition stability of these produced particles after exposing to air was investigated to compare with behaviours observed in model alloys. After all, direct observation of supported nanoparticles by atom probe has hardly been done. Therefore, an alternative route was investigated. As a start, Ag based nanoparticles were made via an inert gas condensation (IGC) method along with Au based AuCu, AuNi, AuCuMo and

AuNiMo nanoparticles which have been identified as exceptional catalysts for CO oxidation [1, 2]. Using these analyses, an analysis route was established for APT sample preparation of nanoparticles to check nano-scale composition segregation.

A number of complementary advanced surface analysis techniques were involved in this thesis, including FIM (including work with an in-situ oxidation cell), APT, HRTEM, AFM, XPS, LEIS, and so forth. The FIM together with the in-situ oxidation cell were most used for model alloy work. FIM was used to clean and image the material surface before conducting in-situ oxidation and APT was used to investigate resulting oxidised samples. HRTEM was mostly involved in the *nanoparticle by synthesis* work. APT, HRTEM, AFM, XPS, and LEIS were involved in the *nanoparticle by condensation* work. APT results of those nanoparticles were analysed together with information obtained from other techniques, confirming the effectiveness of the new sample preparation method.

Overall, this thesis was carried out in a collaboration among the Oxford Atom Probe group, the Catalysis research groups in Université de Lille, UPMC and Mantis Deposition Ltd. in Thame, Oxford, UK. Dr. Eric Marceau from Université de Lille led this collaboration from the French side. Dr Carmen Ciotonea from Université de Lille carried out nanoparticles syntheses and Dr Anne-Sophie Mamede conducted LEIS analyses. Dr Anne-Félicie Lamic-Humblot from UPMC conducted AFM analyses. Most of the HRTEM work was conducted in Oxford with Dr Mohsen Danaie from electron Physical Science Imaging Centre (ePSIC) in Harwell. Dr Vicky Broadley from Mantis deposition helped producing particles from IGC method.

Chapter 2

Literature Review

In this chapter, current literature on catalysis fundamentals, surface behaviour of non-noble and noble metal systems, along with advanced characterisation of nanoparticles used for catalysis are presented.

The Catalysis Fundamentals section summarises background information on the catalytic activity, selectivity, and poisoning of catalysts, together with recent trends in catalyst development. Surface behaviours of metallic catalysts are introduced, with emphasis on *Fe*, *Ni*, *Co*, *Au*, *Mo* and their alloys, which form the focus of the investigations in this thesis. Finally, a comprehensive literature review of current APT research on catalytic materials is presented, complemented by TEM research on related systems.

2.1 Catalysis Fundamentals

2.1.1 Background of Catalysis

The importance of catalysis Catalysts are used extensively in modern industry, playing vital roles in numerous fields such as food production, oil refining, and pharmaceutical production. Many major improvements in these areas since the industrial revolution would not have been possible without the development of catalysts [3]. Perhaps, the greatest success achieved by catalysts is their critical support in addressing issues arising due to the world's growing population. The total global population was restricted by food production for a long period lasting until the end of the nineteenth century [4]. Improvements in food production can be heavily linked to the development of man-made fertilisers, the production of which requires the catalytic production of NH_3. Nitrogen, as well as oxygen and carbon, are basic nutrients for plant growth. However, unlike oxygen and carbon, which can be obtained from the soil easily, free nitrogen is naturally unavailable due to the strong binding energy of the triple bonds in molecular nitrogen gas. In contrast, ammonia is a chemical that can release ionic nitrogen to plants efficiently, making it a highly suitable fertiliser for plant growth. Ammonia is not a naturally abundant chemical, however in the early 1900s this situation began to change. Scientists began to produce ammonia on an industrial scale using the Haber-Bosch process [5]. At this stage, food production boomed and the benefit of this process was astonishing: around one third of today's world population is living on food production underpinned by this method [6]. At the core of this process are iron-based catalysts that facilitate the key chemical reaction joining hydrogen and nitrogen. These catalysts were designed using a trial-and-error method, and more than 2500 materials were explored by Mittasch and co-workers to discover the proper *Fe* based catalyst, which is still in use today [7]. The process itself is conducted at 150-250 bar and 300-500 °C, and it is one of the largest energy-consuming processes in the industrialised world [5, 8]. Thus, a low temperature and low-pressure ammonia synthesis process is highly desirable from an economic perspective. It is believed that ruthenium based catalysts could be the basis for

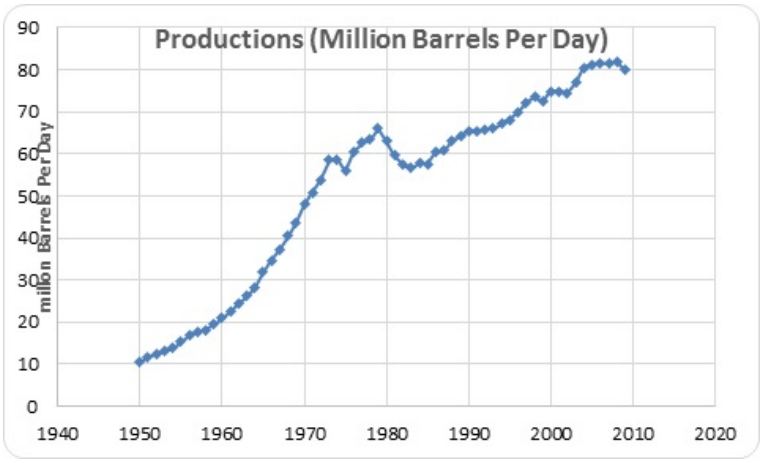

Figure 2.1.1 – Crude oil production from 1950-2009. It shows a significant increase of oil production from 1950. (Source: BP and Worldwatch)[12]

such a low temperature, low pressure ammonia synthesis process [8]. However, Ru deposits are scarce and consequently its price is high .

The oil industry is another field underpinned by substantial catalyst applications. After World War II, demand for oil from the aviation and automotive industries continually soared to cater for increased need for domestic and international mobility. As a result, oil consumption increased dramatically. Figure 2.1.1 shows oil production from 1950 up to 2010, during which an eight-fold increase in production has been documented. To cope with such demand, heavy oil has to be fractioned to produce fuel such as gasoline, diesel etc. For this purpose, man-made zeolite catalysts have been used to conduct heavy oil fractioning in a catalytic cracking reaction since 1964 [9]. Initially, zeolites doped with rare earth metals were used for moving-bed cracking of heavy oil. Subsequently ZSM-5 type zeolite became the main catalyst for the refinery process since it had high shape-selectivity in terms of product molecules [10, 11].

In recent years, catalyst development has been increasingly focused on environment protection as well as lowering the price of catalysts without detrimental impacts on their performance. Following this trend, a catalogue of catalysts has been invented to help protect the environment, such as hydrodechlorination of trichloroethylene to hydrocarbons using bimetallic $FeNi$ nanoparticles [13]. This reaction is used to purify water. More recent re-

search has been focused on producing energy from more environmental friendly resources, such as biomass to help reduce carbon dioxide emission [14–17].

Working mechanism of catalysis A catalyst is defined as "a substance that increases the rate at which a chemical system approaches equilibrium, without being consumed in the process."-F.W. Ostwald. It is key to understand that chemical reaction equilibrium can be achieved eventually with the absence of catalysts because it is controlled by the equilibrium constant K, which is defined by the Gibbs free energy of the process (equation 2.1.1). Hence K is determined by the enthalpy and entropy changes during the reaction.

$$\Delta G = \Delta H - T\Delta S \tag{2.1.1}$$

Molecules possess a certain amount of energy, either kinetic or potential energy, before any reaction happens. Reactions can only happen when they collide into each other with right angle and energy greater than the minimum energy barrier, the amount of which is called the activation energy, E_a, which is the energy difference between the reactants and activated complex as shown in Figure 2.1.2. In transition state theory, the activation energy is also called $\Delta G^{\ddagger}$. Given ΔG^0 is the change in Gibbs energy when reaction happens at standard state (1 bar, 298K), then the Gibbs free energy at given temperature T, is:

$$\Delta G = \Delta G^0 + RT\, ln\, K \tag{2.1.2}$$

where ΔG is the change in Gibbs free energy of the reaction, ΔG^0 is the standard Gibbs free energy and $K$is the equilibrium constant. When the reaction is at equilibrium, ΔG = 0, the equation 2.1.2 becomes:

$$0 = \Delta G^0 + RT\, ln\, K \tag{2.1.3}$$

and $\Delta G^0 = -RT\, ln\, K$. In transition state theory, the function can be written as:

$$\Delta G^{\ddagger} = -RT\, ln K^{\ddagger} \tag{2.1.4}$$

$$\Delta G^{\ddagger} = \Delta H^{\ddagger} - T\Delta S^{\ddagger} \tag{2.1.5}$$

where $\Delta G^{\ddagger}$ is the Gibbs energy of activation, $\Delta H^{\ddagger}$ is the enthalpy of activation and $\Delta S^{\ddagger}$ is the entropy of activation. Combining the function 2.1.4 and 2.1.5, the equilibrium constant can be written as:

$$ln K^{\ddagger} = -\frac{\Delta H^{\ddagger}}{RT} + \frac{\Delta S^{\ddagger}}{R} \tag{2.1.6}$$

with the molecular consideration, the frequency of vibration is given as:

$$v = \frac{k_B T}{\hbar} \tag{2.1.7}$$

where k_B is the Boltzmann's constant, T is the absolute temperature, and $\hbar$ is the reduced Planck's constant. The reaction rate constant can be written as:

$$k = \frac{k_B T}{\hbar} e^{\frac{-\Delta H^{\ddagger}}{RT}} e^{\frac{\Delta S^{\ddagger}}{R}} \tag{2.1.8}$$

Compared to a homogeneous gas phase reaction, the value of $\Delta S^{\ddagger}$ for a heterogeneous catalysed reaction is substantially lower since the reaction area is confined to the catalyst's surface. Therefore, heterogeneous catalysts act by reducing the activation energy E_a to increase the reaction rate constant k. Fundamentally, in order to be effective, it is believed that lowering the activation energy of a chemical reaction is the key mechanism for a functional catalyst. To reduce this energy barrier, a new chemical route must be established. In the case of heterogeneous catalysts this is achieved via the chemisorption of reagents onto a catalyst surface. The process of adsorbing new intermediates has a low activation energy. Figure 2.1.2 is a schematic diagram of the energy barrier changes with heterogeneous catalysts.

In most reactions, multiple sets of thermodynamic parameters exist, which can be exploited

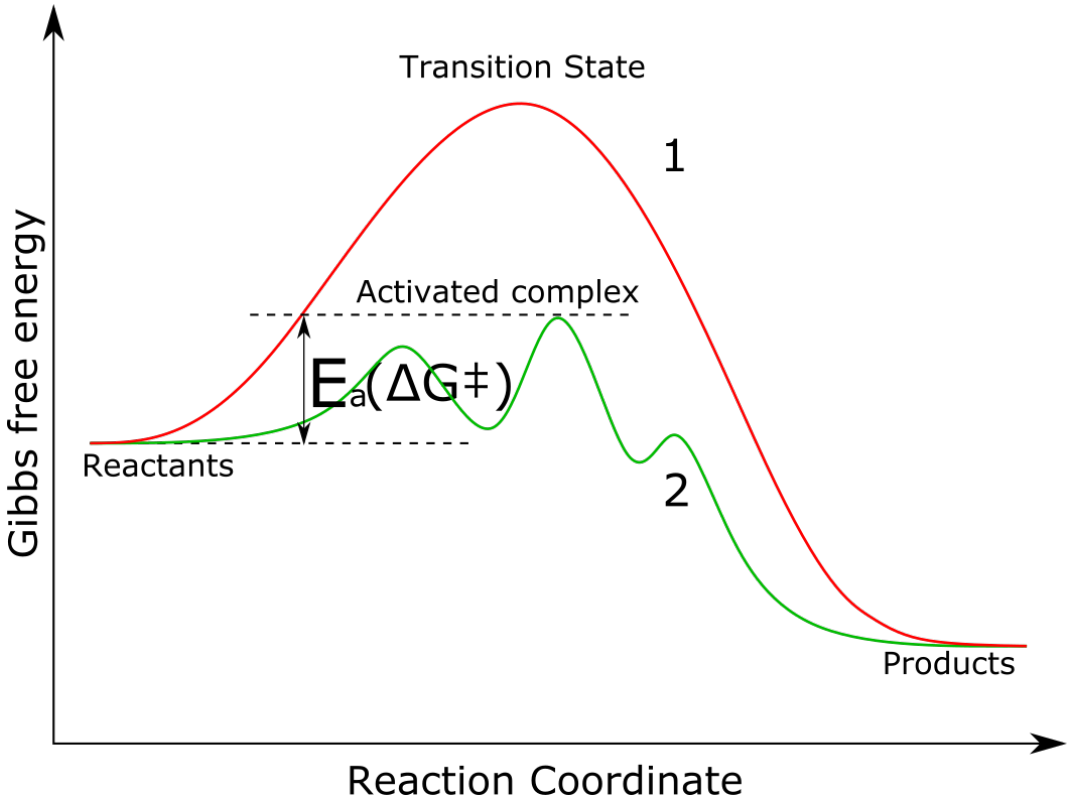

Figure 2.1.2 – Potential energy barrier for reaction without catalyst (line 1) and with catalyst (line 2)

by particular catalysts to select a preferred reaction route. Usually, the application of a catalyst is designed to maximise the generation of one specific product among the several that might be possible. Catalytic selectivity (S) is a way to measure the catalyst performance in terms of yielding the desired product. For a *product A,* this is shown in equation 2.1.9.

$$S = r_A / \sum^{all\ components} r_A + r_B + \cdots \tag{2.1.9}$$

where S is the selectivity, r_X is the production rate of component X.

Different forms of catalysts Catalysts are broadly categorised into two categories: homogeneous and heterogeneous. Homogeneous catalysts are present in the same phases as the reagents, whilst heterogeneous catalysts are not. A textbook example of homogeneous catalysis is the $Fe(II)$ or $Fe(III)$ catalysed reaction between iodide and peroxodisulphate

ions.

$$2I^{-}(aq) + S_2O_8^{2-}(aq) \rightarrow I_2(aq) + 2SO_4^{2-}(aq)$$

Another example of homogeneous catalysis in the gas phase is the catalysed breakdown of ozone by chlorofluorocarbons (CFCs). Chlorine radicals freed from CFCs break ozone into oxygen and the free radical species $ClO^{\bullet}$. This newly-formed radical then combines with oxygen radicals, which would otherwise form ozone, creating molecular oxygen and regenerating chlorine radicals:

$$(1)Cl^{\bullet} + O_3 \rightarrow ClO^{\bullet} + O_2 \ (2)ClO^{\bullet} + O \rightarrow Cl^{\bullet} + O_2$$

Heterogeneous catalysts are more widely utilised in industry. They are used in various forms designed to suit specific applications. In Figure 2.1.3, catalysts in the form of monoliths, pellets, and sheets are shown, which are designed for gas-solid reactions and liquid-solid reactions. A three-way converter is included in Figure 2.1.3a. Automotive exhausts pass through the narrow channels decorated with precious metal catalyst particles, reducing toxic NO_x into nitrogen, oxidising carbon monoxide into carbon dioxide, and oxidising unburnt fuel to CO_2. In this thesis, attention will be placed on heterogeneous catalysts and their respective model alloys. In these heterogeneous catalyst systems, chemical reactions occur at the interface between catalysts and the gas phase reagents, on the surface of these active catalysts. In such systems, the global kinetics of the process therefore depends on both the in-situ reaction rate at these catalyst surfaces and also the rate of reagents reaching and exiting from these sites, on which ongoing research is focused. However, it is only the surface of active catalysts that lies within the scope of this thesis.

2.1.2 Metal based heterogeneous catalysts

2.1.2.1 Types of reactions and mechanisms

Metal based catalysts are used in several important commercial reactions. Some of these reactions together with their catalysts are listed in Table 2.1.1, including nitrification, oxidation and/or reduction of respective reagents performed over metal catalysts. The active

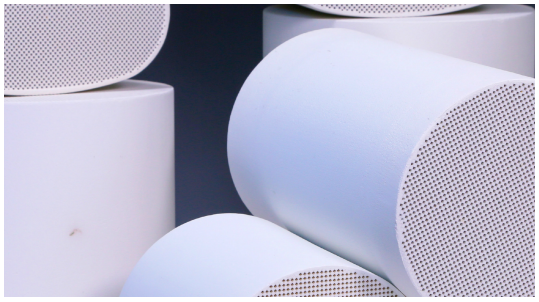

(a) Three way converter of automotive exhaust



(b) Methanol synthesis catalyst



(c) Precious metal catalysts used in fix bed reactors

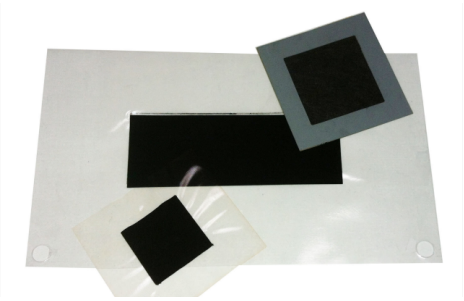

(d) Fuel cell membrane catalyst

Figure 2.1.3 – Heterogeneous catalysts in various forms (creative common licence)

sites of catalysts act as chemisorption sites for either N_2, O_2, and H_2, which then react with other compounds. For example, during the partial oxidation of methanol, Ag does not form stable oxide species on its surface even at high temperatures in an oxidising environment [18]. On the other hand, the formation of iron nitride on the iron based catalyst is still subject to debate for the Haber-Bosch process 100 years after its first introduction to industrial applications [19–21]. Therefore, the importance to understand the surface active sites is clear not only for new developed catalysts but also to better understand and improve those that for a long time have been deployed in service.

2.1.3 Durability, poisoning and regeneration

The selection criteria for industrial catalysts are not entirely aimed around high performance. Catalyst durability, poisoning resistance and regeneration ability are also of great importance. In fact, in some cases these characteristics override the importance of catalytic performance in terms of keeping overall running costs minimised. For example, the

Process	Reaction Formula	Catalyst	Application
Haber-Bosch	$3H_2(g)+N_2(g) \rightarrow 2NH_3(g)$	Fe based or Ru based [22]	Fertiliser
Water-gas shift	$H_2O(g)+CO(g) \rightarrow H_2(g)+CO_2(g)$	Fe based and Cu based [23]	Hydrogen production
Fischer-Tropsch	$nCO(g)+(2n+1)H_2(g) \rightarrow C_nH_{2n+2}(g)+nH_2O$	Co based and Fe based [24]	Fuel
Methanol oxidation	$CH_3OH+\frac{1}{2}O_2 \rightarrow CH_2O+H_2O$	Ag based and Mo based [18]	Fine chemicals

Table 2.1.1 – Several important reactions utilising commercial metal based catalysts

sintering effect of small particles is a well-known phenomenon. In particular this effect reduces the number of active sites, which then reduces overall reactivity [25]. Dispersion of small particles onto various substrates is one common method of reducing the sintering effect and boosting the catalytic reactivity [26, 27]. Another factor to prevent particle sintering is to select elements with high Tammann temperature [28]. In some reactions, the working temperature can reach as high as 600-700°C, above the Tammann temperature of most transition metals. Platinum group metals (PGM) are therefore selected as candidates for catalysts in such applications [29]. Furthermore, a synergy effect between support materials and particles is another way to boost catalyst reactivity and durability [19]. The combination of the catalyst particle and various substrates can give dramatically different results in terms of catalytic reactivity. For example, Ru nanoparticles supported on TiO_2 are three times more effective in comparison to Ru on carbon for the hydrogenation of lactic acid [30]. It is believed that TiO_2 as a support helps to adsorb and activate the acid while Ru activates H_2 molecules. Another pressing issue is poisoning of the catalyst surface. In most organic chemistry reactions, carbon and coke deposition on the catalytic surface can reduce catalyst reactivity by three routes: 1) contaminating the metal surface, 2) blockage of the catalysts pores, and 3) physical disintegration of the catalyst support [31]. In other reactions, hydrogen sulfide or other sulfur-containing components from the chemical reaction feedstock can drastically reduce catalyst activity by forming sulfides with active

catalyst sites [32]. Alloying of active metals has been identified as one method to improve anti-carbon or anti-coke deposition abilities [33, 34]. The last, but not the least, selection criterion is the regeneration and recycling of deactivated catalysts. This is because catalysts use a significant amount of PGM metals, which are not only expensive but also limited in total reserves. For example, to save costs Pd catalysts used for hydrogenation are regenerated by heating in steam at 350°C [35]. PGM metals used in three-way converters can be recycled up to 95% given good scrape collection of used ones [36]. In addition, it has been argued that only fuel cells that have been designed with recycling capabilities can enable a viable hydrogen economy [37].

2.1.4 Multimetallic catalysts

To improve catalyst performance, multimetallic catalysts have been investigated intensively [38]. It has been believed that an "electronic factor" affects the catalytic performance of these multimetallic systems [39]. Interests in alloy catalysts lie mostly among modification of original selectivity towards chemical products which are difficult to obtain [40, 41]. For example, adding a Pd layer of few atomic thickness on a Ag core catalyst the conversion of formic acid into hydrogen and carbon dioxide (no trace of carbon monoxide) with extremely high efficiency [42]. Surface geometry can be a significant controlling factor in alloy catalysts to determine selectivity, and the surface composition cannot be assumed to be identical to that of the bulk [38, 40]. For example, Sachtler et al. has reported surface segregation of *Cu* in *NiCu* bimetallic clusters during reaction. The addition of Cu dramatically reduces the ability of hydrogen to chemisorb on the surface, even in a alloy with as little as 5 at% Cu [43]. Sinfelt et al. concluded that an alloying component with lower heat of sublimation is more likely segregate to the surface. However, surface segregation may change depending on the gaseous environment. Williams et al. reported *Ni* segregated to the surface of *NiAu* particles under an oxygen environment [44]. It is important to note here that the stability of these particles is important in terms of their actual performance during industrial application. To further understand changes during reactions, a fundamental

knowledge is needed, particularly concerning the surface/active sites changing under reactive environments. Therefore, in this thesis, two fundamental questions are investigated:

1. What combination of characterisation techniques are adequate to investigate multimetallic systems in term of local chemistry?

2. What changes are experienced by multimetallic systems when they are exposed to different reactive environments?

2.2 Metallic systems explored in the thesis

Research on bimetallic catalytic systems has attracted much attention [38, 45], as by creating nano-sized alloy particles, it is possible to induce both a geometrical ensemble effect and an electronic ligand effect [46, 47]. These two effects give novel properties which monometallic catalysts do not possess and can significantly enhance the catalyst's performances. Multimetallic (more than two elements) nanoparticles are also of interest, but their higher order of complexity makes their controlled synthesis and characterisation even more challenging [48].

There are two fundamental questions that arise in multimetallic systems: (a) what is the distribution of the alloying elements? and (b) which species is the predominant surface element, and is this the most effective in catalytic reactions? Substantial research shows significant surface segregation of one of alloying components over others, such as surface segregation of Ag to Ag-Cu bimetallics, Cu to the surface of Au-Cu bimetallics and so forth [49–52]. Various mechanisms/reasons drive surface segregation, for example, different catalyst production methods, catalyst pre-treatments, reaction conditions, and air exposure [53–55]. In particular, reaction conditions can alter the surface chemistry drastically. Therefore a detailed understanding of surface changes is important for the further catalyst improvements. In the rest of this chapter, non-noble metal and noble metal systems are discussed, mostly around Ni, Fe, Co, Au and their alloys.

2.2.1 Non-noble metal systems Ni, Fe, Co

2.2.1.1 Catalytic behaviour

Fe, Ni and Co in the form of monometallic catalysts have been used for a number of important commercial reactions [56–58]. Their catalytic applications are well recognised, but the driving forces to obtain further improvements in performance remain strong. Alloying of these elements is currently being investigated towards this goal. The $NiFe$ bimetallic system is cheap and reserve-sustainable, making it attractive for catalyst development. One major reaction that can be catalysed is the hydrogenation reaction. $NiCo$ is used in reforming reaction.

Mössbauer spectroscopy, a technique highly sensitive to the oxidation state change of iron, is especially useful for the analysis of Fe containing catalysts [59]. Amelse et al. reported Fe carbide formation of a Fe/SiO_2 catalyst after a Fischer-Tropsch reaction of 90 min by Mössbauer spectroscopy [60]. Fe had undergone complete carburisation after 90 min at 255°C. Ishihara et al. found that by alloying Fe and Ni, the new bimetallic catalyst had a high conversation rate (up to 36 mol.%) for CO hydrogenation [61]. The oxidation and reduction properties of Fe, Ni and $Fe-Ni$ catalysts supported on silica were investigated by Unmuth et al. [62]. In this work it was found that the reducibility differs for different catalysts. At 425°C, H_2, 1 atm and 12 h, Ni oxide completely reduced to a metallic state, whereas in the case of iron oxide about 70% was transferred back to a metallic state. Additionally, they found the reduction of iron oxide underwent the Fe_2O_3 to Fe_3O_4 transformation before being fully reduced to the metallic state. The effect of adding Ni to Fe was believed to accelerate the completion of reduction process (as shown in Figure 2.2.1). A similar result has been achieved by Brown et al. [63]. In this study, they performed reduction studies on catalysts of iron, nickel and bimetallic iron nickel. They found that even an addition of 5wt% nickel into iron increased the reducibility of the formed oxides.

Steam reforming is another important reaction that utilises $FeNi$ catalysts. This reaction generally converts hydrocarbon containing chemicals into carbon monoxide and hydrogen.

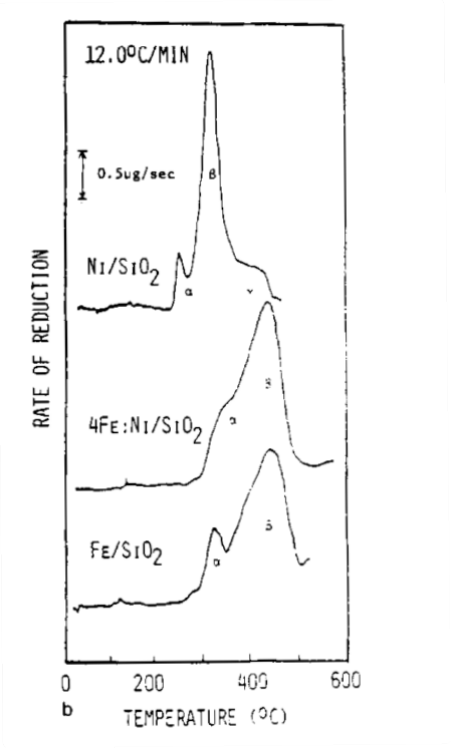

Figure 2.2.1 – A comparison of TPR profiles for three catalysts: Ni/SiO_2, $4Fe : Ni/SiO_2$ and Fe/SiO_2. The reduction was conducted at 425℃, H_2, 1 atm. and 12h. The shift of the reduction curve of $4Fe : Ni/SiO_2$ shows the decrease of reduction temperature. The important point is that the reduction completion is increased compared to monometallic Fe. [62]

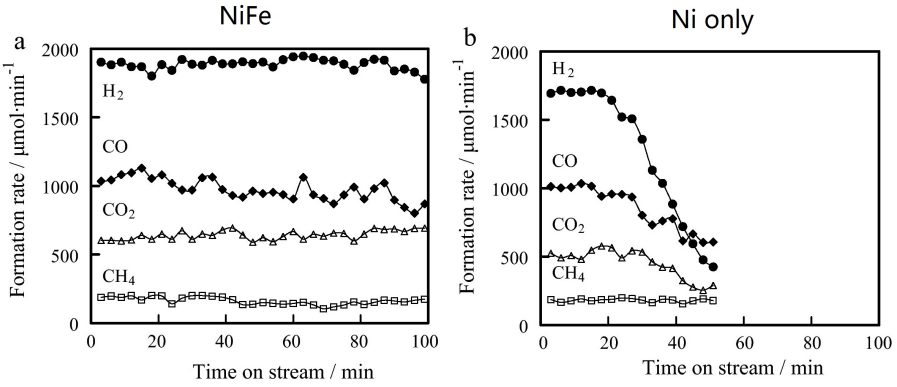

Figure 2.2.2 – Life test in steam reforming of tar wood at 873K. Figure a) shows the result of $Ni-Fe/Al_2O_3(Fe/Ni$=0.5) and figure b) shows Ni/Al_2O_3. [16]

In general, methane is the most common hydrocarbon feedstock used in steam reforming along with Ni based catalysts [64, 65]. Recently, Wang et al. reported that biomass could be steam reformed to produce syngas [16]. They used an $Fe-Ni$ (Fe/Ni=0.5) based catalyst and found it had a better stability compared to monometallic nickel as shown in Figure 2.2.2.

This study claimed that Fe had a higher affinity for oxygen, and Fe atoms act as a donor

of oxygen during the reaction to boost performance. Mizushima et al. conducted EXAFS research on silica-supported bimetallic iron nickel catalysts [66]. In this, they focused on two catalyst production methods: alkoxide method (alkoxide method was based on a hydrolysis of a mixed solution of ethylsilicate and nickel and iron ethylene glycolates) and a co-impregnation method, both requiring calcination and hydrogen reduction during fabrication. This then could be treated as a decomposition and reduction cycle. The study reported *Fe* enrichment on the surface of the particles, especially for the sample prepared by the alkoxide method. This was attributed to the difference of the reduction rate of Fe and Ni after calcination. Ni reduced faster, forming the core whilst Fe took longer to reduce and hence formed the shell. In addition, Wang et al. reported Fe surface enrichment during oxidation and reduction cycle analysed in EXAFS [16]. However, this result should be treated with caution because the difficulties of distinguishing Fe and Ni EXAFS signals due to their close atomic numbers.

In work reported by Matsuyama et al. [67], a unique way to determine the surface composition of a bimetallic system has been investigated. In this, Cu-Ni, Fe-Ni and Co-Ni bimetallic alloys with various compositions were tested for ethylene hydrogenation and the Ni distribution within the alloys investigated by detecting the β-ray emissions from a $_{63}Ni$ tracer. The results of this study showed a low surface content of Ni compared to the average composition in all alloy systems, which cannot be explained by thermodynamics (including melting point, the free energy of alloy formation, the frequency factor), the activation energy of self-diffusion, or volume diffusion of metal atoms, given the observed persistence of Ni deficiency in all those different systems. This work combined with Mizushima, Ishihara and Wang's work shows nickel deficiency of the surface to be common. However, Matsuyama's work, as mentioned, suggests that surface segregation is equally sensitive to sample preparation method and thermodynamics. As a summary, some reactions that can use Fe-Ni catalytic systems are listed in Table 2.2.1.

Another system investigated in this thesis is the NiCo bimetallic system. NiCo has been found to catalyse various reactions, which are listed in Table 2.2.2. Carbon dioxide reform-

ing of methane gas is the most reported NiCo catalyst application to date. Ni itself can be an effective catalyst for this reaction, but it is prone to the formation of graphite, which diminishes its effectiveness as a catalyst [68]. Adding Co into Ni has been reported as one way to reduce the coke formation [69]. Takanabe et al. using X-ray Diffraction (XRD) and X-ray Photoelectron Spectrometry (XPS) reported that $NiCo$ particles in a bimetallic $NiCo/TiO_2$ system were homogeneously alloyed after hydrogen activation and subsequent carbon dioxide reforming of methane [68]. Adding Ni into Co reduced the formation of CoO dramatically, and increased the CH_4 conversion rate when comparing to pure Co counterparts. Wu et al. also confirmed that Co was mixed with Ni during preparation of $xNiyCo$/SBA-15 (x + y =5%, x/y =0/5–5/0, mass ratio) catalysts, used for the same reaction [70]. The formation of Ni_xCo_yO during preparation was pointed out as being vital to obtain a catalyst with high performance.

In conclusion to this section, the FeNi and NiCo catalytic systems have the potential to catalyse a large number of important reactions. Manufacturing processes of these catalysts have been found to affect catalytic performance by causing phenomena such as surface segregation, influencing particle stability, carbon formation etc. Calcination (oxidation) and reduction are more than often involved in these manufacture processes. Therefore, a general review to the oxidation behaviour of Fe, Ni, Co, FeNi and NiCo systems is presented in the subsequent sections to obtain further understanding.

2.2.1.2 Oxidation behaviour of Fe, Ni, Co, FeNi and NiCo

Knowledge of the various phases formed within Fe, Ni, Co, FeNi and NiCo metals is a prerequisite to fully understand their oxidation behaviour. Various research groups have investigated the phase diagram of FeNi and NiCo alloys by calculation and experiments. Swartzendruber et al. [85] summarised the field of FeNi alloys, and the phase diagram is shown in Figure 2.2.3. In the figure, there exists: (1) a liquid phase, (2) (δ Fe) solid solution based on the high temperature face centred cubic (fcc) Fe, (3) (γ Fe,Ni) solid solution based on fcc Fe and Ni, (4) (α Fe) solid solution based on the low-temperature body centred cubic

Reaction	Reactants	Products	Catalyst
Fischer-Tropsch [71]	Syngas	various hydrocarbons depends on catalysts	Fe50Ni50 wt.% based
CO disproportionation reaction[33]	CO	carbon and CO_2	75wt.%Ni-25wt.%Fe
Steaming reforming of toluene and phenol[72]	Toluene+steam	CO and hydrogen with CH_4,CO_2 and benzene	Ni-Fe mixed with Mg/Al oxides (Fe/Ni=0.25)
Steaming reforming biomass[16]	Cedar wood (Biomass)	CO and hydrogen with CH_4, CO_2, tar, coke and char	Ni-Fe/Al_2O_3(Fe/Ni=0.5)
Hydrodechlorination of trichloroethylene[13]	Trichloroethylene	even-numbered saturated hydrocarbons	1:3 Ni:Fe
Synthesis of narrow-diameter carbon nanotubes[73]	Acetylene	narrow-diameter carbon nanotubes	Ni-Fe/Al_2O_3 , Iron to Nickel ratio varies
Steam reforming methane[74]	Methane	CO and hydrogen	Fe-Ni metal foil (up to 60 wt.%)
CO_2hydrogenation[75]	CO_2+hydrogen	Methane	Ni-Fe/Al_2O_3 (Ni75Fe25)
Conversion of furfural to methylfuran[76]	Furfural	2-methylfuran	Ni-Fe/SiO_2 (5.wt% of Ni and 0-5 wt.%Fe)
Hydorgenation of acetophenone and benzonitrile [77]	acetophenone and benzonitrile	cyclohexyl ethanol and benzylamine	Ni-Fe/SiO_2 varying ratios

Table 2.2.1 – A brief summary of reactions catalysed by Fe-Ni catalytic system

(bcc) Fe and (5) the $FeNi_3$ intermetallic compound [85]. By contrast, the NiCo system is relatively simple as shown in Figure 2.2.4. Ni and Co exhibit a complete solid solubility in the $\alpha Co, Ni$ phase. The dashed line between $\alpha Co, Ni$ and εCo is the hypothetical transition line between fcc and hexagonal close packed (hcp) phases [86]. At room temperature, it is believed that fcc structure is the stable phase once the Ni percentage exceeds 50 at.% [87].

In terms of the thermodynamics of oxide formation of monometallic Fe, Ni, and Co, the free energies of formation (in kJ) and standard entropies of iron oxides, cobalt oxides, and nickel oxide are listed in Table 2.2.3 [88]. The Gibbs free energy for forming oxides at certain temperatures can be obtained from Ellingham diagrams [89]. At a temperature

Reaction	Reactants	Products	Catalyst
Carbon dioxide reforming of methane to syngas[70]	CO_2,CH_4	Syngas	90wt%Ni-10wt%Co/SBA-15
Carbon dioxide reforming of methane to syngas [78]	CO_2,CH_4	Syngas	Co-Ni bimetallic aerogel catalyst
Biogas reforming for hydrogen production [79, 80]	CO_2,CH_4	Hydrogen	Ni-Co/La_2O_3/Al_2O_3
Methanol oxidation [81, 82]	Methanol, O_2	CO_2, H_2O	CoNi-decorated graphene
Bioethanol steam reforming[83]	CH_3CH_2OH,H_2O	Hydrogen, CO_2	ZnO supported Co-Ni
Fischer-Tropsch [24]	Syngas	various hydrocarbon depends on catalysts	Co based
Hydrolytic dehydrogenation of amine borane[84]	$MeNH_2 - BH_3$,H_2O	H_2,$(MeNH_3)BO_2$	$Co_{0.9}Ni_{0.1}$/graphene

Table 2.2.2 – A brief summary of reactions catalysed by Ni-Co catalytic system

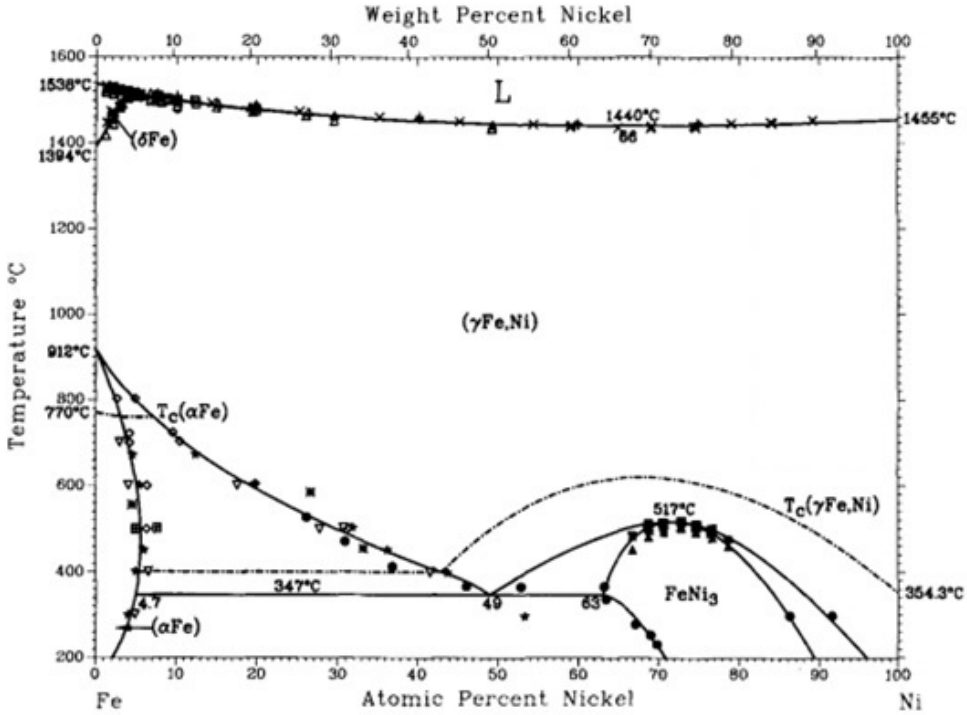

Figure 2.2.3 – Phase diagram of Iron-Nickel system [85]

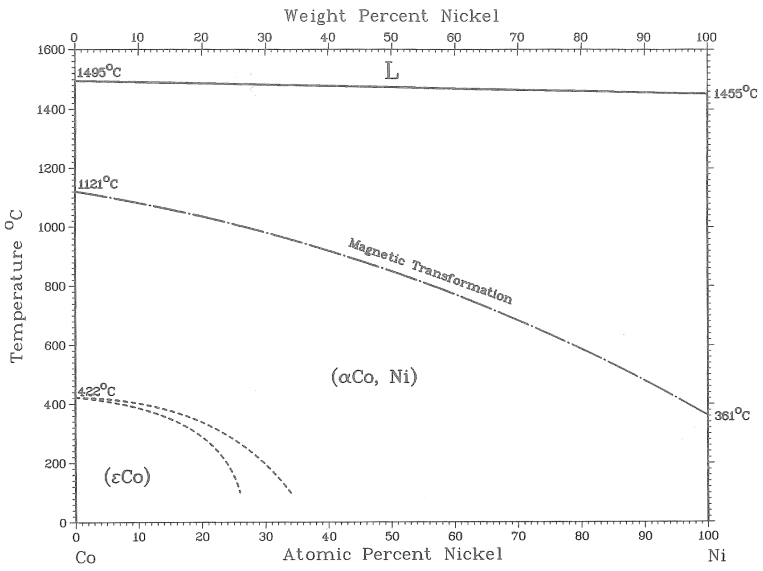

Figure 2.2.4 – Phase diagram of Nickel-Cobalt system [86]

353K(80°C)		
Transformation	Free energy $\Delta G/kJ \cdot mol^{-1}$	$P_{O_2}/log\ bar$
$Fe \rightarrow FeO(I)$	-	-
$Fe \rightarrow Fe_2O_3$	-483.75	-71.619
$Fe \rightarrow Fe_3O_4$	-496.5	-73.507
$Fe \rightarrow Fe_{0.95}O$	-490.625	-72.637
$Ni \rightarrow NiO$	-410.375	-60.756
$Co \rightarrow CoO$	-435.6	-64.4
$Co \rightarrow Co_3O_4$	-398	-58.9

Table 2.2.3 – Thermodynamic data of forming iron oxide, cobalt oxide and nickel oxide at 353K. The unit is kJ/mol for oxide formed with 1 mole oxygen (O_2). The lower the value, the more favoured the formation of oxides. [89]

of 80°C, which is used to oxidise samples in this thesis, formation of Fe_2O_3, Fe_3O_4 and $Fe_{0.95}O$ are favoured compared to the formation of NiO. Also, CoO is favoured over NiO but this is not the case for Co oxidation to Co_3O_4. However, it should be understood these data do not take the surface effect into account, and that most experimental investigations carried out on flat systems are not necessarily representative on metal particles.

General oxidation mechanism The general mechanism of metal oxidation is introduced here before expanding to the specific metal oxidation. When metal combines with an atom or with a molecular group and loses electrons, an oxidation reaction has taken place [90]. In the context of this thesis, it is the oxidation involving metal losing electrons combing with oxygen atoms. Thermodynamics of oxide formation is the fundamental driving force and the equation is:

$$\triangle G = -RTln\frac{1}{p'_{O_2}} - RTlnp''_{O_2} \tag{2.2.1}$$

where p'_{O_2} is the oxygen pressure at equilibrium and p''_{O_2} the initial oxygen pressure at the beginning of the reaction. While thermodynamic indicates the more stable reaction product, it is the kinetics of oxidation control the ultimate form of oxide. In an oxidation involving oxygen gas, the oxygen molecule is firstly dissociated into oxygen atoms, chemisorbing on the metal surface [91]. This oxygen chemisorbtion continually accumulates until it reaches a saturation coverage, where the heat of oxide formation is equal to the heat of chemisorbed layer formation (critical coverage) [92, 93]. Oxide nucleation happens once exceeding the critical coverage and grows rapidly on the metal surface until reaching the full coverage [94].

Oxidation rates are usually used to describe the mathematical relationship between the oxide thickness y and oxidation time t. Initial oxidation, which is considered as thin film, has logarithmic relationships as following:

$$y = K_1 logt \tag{2.2.2}$$

$$\frac{1}{y} = K_2 - K_3 logt \tag{2.2.3}$$

$$y = K_4\,(1 - exp\,[-K_5 t]) \tag{2.2.4}$$

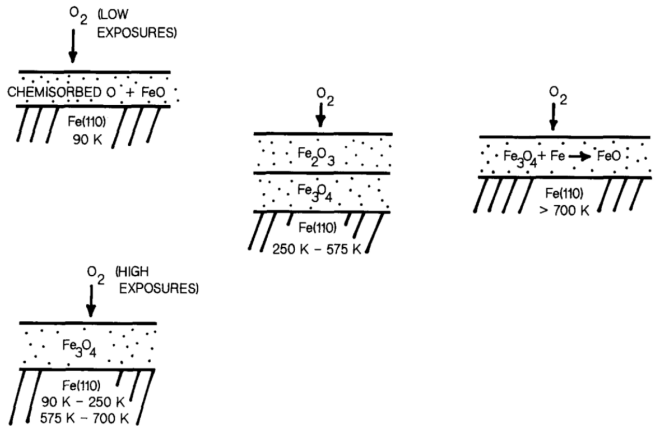

Figure 2.2.5 – Schematic illustrating the behaviour of Fe(110) surface during oxidation [97]

where K_1-K_5 are constants. With thicker oxide growth, the oxidation rate is more often parabolic:

$$y^2 = K_6 t \tag{2.2.5}$$

or linear :

$$y = K_7 t \tag{2.2.6}$$

where K_6 and K_7 are constants. For the initial oxidation, the new formed oxide on the surface has a potential of the order of a volt [90], and the oxide film has a thickness about $1-4nm$. The field pulls metal ions through the film. However, as the film thickens, further growth is diminished as the field drops drastically. Oxide growth will be more governed by ion diffusion [95]. In a general understanding, the oxidation of Fe, Ni and Co all have the effect that metal ions diffuse through the formed oxide scale on the oxide-gas surface whilst oxygen inner diffusion can also occur along fast diffusion paths, such as grain boundaries, scale cracks and etc. [96].

Fe oxidation Iron and related steel oxidation is a vast field that has been summarised by Uhlig, Evans and West[98–100] . There is an immense variety of conditions that lead to the

corrosion/oxidation of iron, however in this section only direct oxidation of Fe by oxygen will be reviewed. Evans summarised the basic structure of a typical iron oxide formed under high temperature (above 700°C) as: $FeO \rightarrow Fe_3O_4 \rightarrow Fe_2O_3$ from the metal-oxide interface to the oxide-air interface [101]. Pignocco et al. reported a very surface sensitive investigation of oxidation on (011) Fe using low energy electron diffraction (LEED) [102]. They found that FeO formed at room temperature, in a UHV atmosphere of 10^{-8} Torr oxygen. Smentkowski et al. conducted an Auger electron spectroscopy (AES) study on the Fe (011) surface oxidation, shown in Figure 2.2.5 [97], finding that oxide formation depends as expected on both oxidation temperature and oxygen partial pressure. With the increase of oxidation temperature from 90K to 700K, oxides structure started with FeO, then changed into Fe_3O_4, then Fe_2O_3 overlayer on Fe_3O_4. When temperature is above 700K, FeO forms by a solid-state reaction between Fe_3O_4 and Fe substrate. Similarly, Busch et al. analysed oxide formation on Fe (011) by AES [103], and confirmed FeO formation on $Fe(110)$ direction with 10^{-8} mbar O_2 at a constant temperature of 420 K. They found the long range order of formed oxide was poor once 3-5 layers formed. Lattice mismatch effect was claimed to be the reason to cause such problems.

In terms of the kinetics of Fe oxidation, Cornell et al. found that the oxide was governed by a two-stage linear and parabolic growth law [104]. On a clean surface of iron, the reaction with oxygen is initially fast and a linear growth rate dominates. With further development of the oxide, a parabolic law takes over once the whole surface is covered by oxide. As mentioned above, oxides formed having a thin haematite, then thin magnetite, and then thick wüstite layer, which means the oxygen inward diffusion is significantly slower than iron cation outwards diffusion [105].

Ni oxidation Ni oxidation is believed to be relatively simple by comparison with Fe [99]. NiO was reported as the only form of oxide during oxidation < 900 °C at 1 bar oxygen [106]. The formed oxide layer has a good adhesion with the underlying metal matrix. Similar to Fe, the diffusion mechanism of the oxidation process, i.e. the outer diffusion of nickel ions

or the inner diffusion of dissociated oxygen, is generally believed to be nickel ion diffusion outwards [99]. Grain boundaries may also be pathways for 'leaking' oxygen to increase the oxidation rate at 450K due to the high defect density on grain boundaries. [99, 107].

Wagner [108] discussed the initial oxidation of Ni at 250°C. In this, dissociation of molecular O_2 was believed to be the rate determining step. The dissociation rate was determined to be inversely proportional to the square of the thickness of the NiO film, which should be less than 1μm. The oxidation kinetics of Ni and Ni based alloys have also been investigated. In the work by Graham et al. [107], a three-stage oxidation kinetics mechanism was reported on samples oxidised from 23°C to 450°C. The first stage in this is oxygen adsorption forming a layer on the surface, then logarithmic growth forming a oxide layer of 0.8-3nm, before a third stage of parabolic growth for thicker oxide films. A more recent work on Ni nanoparticle oxidation confirmed these results, whereby Jeangros et al. [109] reported TEM in-situ observation of the oxidation of a nickel particle. They found that NiO growth occurs very rapidly on fresh nickel particle surfaces. Most interestingly, they further found transverse crack formation on the oxide, which could be a result of geometrically induced stresses.

Some related research from the field of Ni superalloys is also relevant to examining. It has been recognised that a NiO, Al_2O_3 and Cr_2O_3 forming alloy does not only have Al_2O_3 on the utmost oxidised surface, despite the fact that its formation is most energetically favoured [110]. NiO with a high void concentration is also present in the formed oxide layer, which could be a source of microcracking [110]. England et al. reported research on the oxidation kinetics of Haynes 230, Inconel 625, Inconel 718 and Hastelloy X, all of which are Ni based alloys [111]. Oxidation of these materials was conducted at 800-1100°C for thousands of hours and a parabolic growth law was confirmed. These alloys were also oxidised at 700-1000°C under a wet hydrogen atmosphere [112], with parabolic growth law again confirmed. Overall, oxidation research on Ni based superalloy can give general information about the oxidation kinetics of Ni but results should be cautiously interpreted, as the oxidation times often exceed hundreds of hours at very high temperature (<1000 °C),

in addition to these alloys having complex compositions.

Co oxidation Co as a transition metal has moderate oxidation behaviour. It has been reported that Co has three forms of oxides, Co_2O_3, Co_3O_4, and CoO. CoO and Co_3O_4 can form directly by oxidising Co metal. The Gibbs free energy of such formation is listed in Table 2.2.3. Co_2O_3 however, can only be prepared by precipitation method of Co^{3+} with OH^-, not by direct oxidation of Co [113]. Co oxides have various stability under high temperatures. Co_2O_3 is stable in atmosphere up to 1164K; above this, it decomposes into CoO, Co_3O_4 and O_2 [114]. Similarly, Co_3O_4 becomes unstable above the same temperature and decomposes into O_2 and CoO [115]. Also, further oxidation of CoO in O_2 can only form Co_3O_4 [116]. On fresh metal surfaces, the structure of oxide formed follows: $metal \rightarrow CoO \rightarrow Co_3O_4$ when oxidising Co in air (385-800°C). The thickness of CoO is dominant compared to Co_3O_4 and no Co_3O_4 species are seen above 1164K as mentioned previously .

It is also important to understand the formation mechanism of such oxides and the rate of oxide formation, i.e., oxidation kinetics. Carter et al. concluded that Co diffusion outwards through formed oxides is the fundamental mechanism [117]. Co diffusion outwards from CoO to Co_3O_4 during oxidation has also been identified by gold marker as shown in Figure 2.2.6 [116]. The growth of Co_3O_4 on CoO has also been reported to follow a parabolic law between 600-910°C [118]. Przybylski et al. conducted oxidation of a CoO (100) surface and observed a parabolic growth law with a Co diffusion coefficient in Co_3O_4 calculated as $D_{Co} = 3.0 \times 10^{-12} cm^2/sec$ [116]. Defects within alloys can also change the oxidation behaviours of Co metals. Phase changes of Co between hcp/fcc at 690K could induce a high level of defects into the alloy structure. Matsuyama et al. reported that oxidation formation by O_2 inner diffusion through formed oxide scale on a Co (0001) surface, which had undergone hcp/fcc change 30 times [119]. Such diffusion however was not observed on samples without extensive hcp/fcc change, indicating that defects are the driving force for oxygen inner diffusion.

For the oxidation of Fe, Ni and Co, there are many similarities. Oxide formation on the

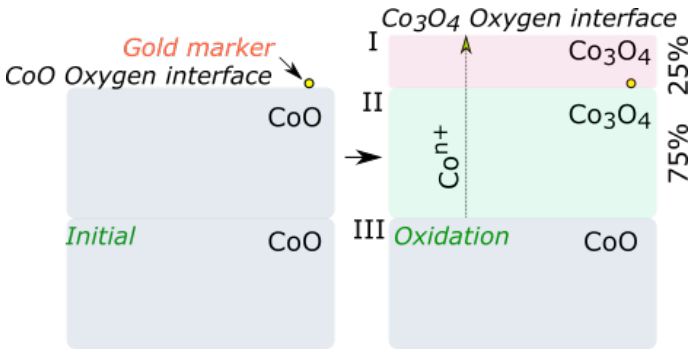

Figure 2.2.6 – Schematic model for CoO oxidation. Designation I is the interface of Co_3O_4/O_2; II initial position of CoO surface and III, CoO/Co_3O_4interface. One mole of Co_3O_4 grows at the Co_3O_4/O_2 interface by outward diffusion of cobalt to react with O_2 and 3 moles of Co_3O_4 are formed from the reaction of 12 moles of CoO. [116]

surface has one or more phases due to their available valence states. Ion out-diffusion is the main mechanism during the formation. Defects, such as the voids in the formed oxide and grain boundaries, also affect the oxidation behaviour.

FeNi alloy oxidation Oxidation of FeNi alloys has been investigated since 1918 due to the variety of applications for this alloy. For example, the Invar alloy, the composition of which is Fe64Ni36, is notable for its low thermal expansion coefficient [120]. It has therefore been used to produce instruments, such as vacuum components, where high dimensional stability is required. Permalloy, with about 20% iron and 80% nickel content, has a very high magnetic permeability, which is used extensively as magnetic core material in electronic equipment [121]. The oxidation behaviour of samples with varying composition across the Fe-Ni phase diagram was investigated, at oxidation temperatures varying from 500-1100°C [122, 123]. Foley [124] summarised the progress up to 1962 and arranged the data into three categories: 0-30wt% Ni, 30-75wt% Ni and 75-100wt% Ni. For 0-30wt% Ni, the results show Ni enrichment both around the metal-oxide interface and in the $NiFe_2O_4$ spinel within the oxide layer developed. More interestingly, the addition of Ni reduces the alloy oxidation rate. In a particular example, a 10.38wt% Ni alloy has an oxidation rate many orders of magnitude slower than pure iron determined by thermogravimetric reduction measurement. It is believed that Ni can inhibit the formation of FeO, which is the

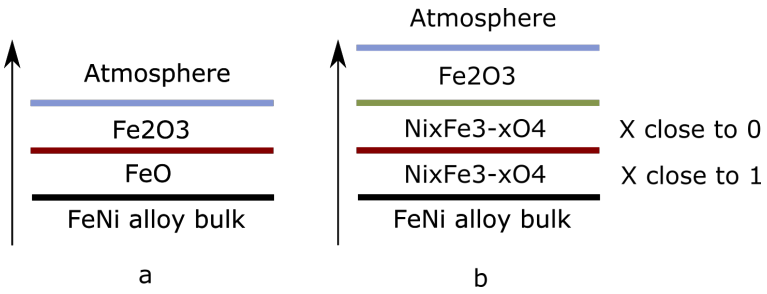

Figure 2.2.7 – The growth of oxide Fe-Ni alloy, which has a Ni content ranging from 30-75wt%. (a) oxidation for short time (up to 60 min and 600-1000℃) (b) oxidation for a prolonged time (3h and 500-1100℃) [124]

fastest growing oxide phase. Foley also claimed Ni contents over 30wt% have no further impact on the oxidation rate. For the oxidation of 30wt%-75wt% Ni alloys, initial preferential oxidation of Fe was reported. However, during the development of this outer iron oxide, $Ni_xFe_{3-x}O_4$ forms beneath the outer layer. Near the metal-oxide interface, the composition of the spinel is close to $NiFe_2O_4$ and close to Fe_3O_4 near the oxide-atmosphere interface. In those oxides, Ni is oxidised into Ni^{2+} and replaces Fe^{2+} in the spinel. A schematic illustration of the oxide formation is shown in Figure 2.2.7. For the 75wt%-100wt% Ni contained alloys, most of the oxidation products were Ni containing spinels. This was attributed to Fe_2O_3 and NiO undergoing a solid-state reaction above 600°C to form the $NiFe_2O_4$ spinel.

Subsequently, Cater et al. [125] investigated the oxidation behaviours of a Fe-1wt%Ni alloy. They oxidised an Fe-1wt%Ni alloy at 800°C up to 11h and found that different annealing pre-treatments affect the formation of oxides. FeO was only found to form on the surface of hydrogen-annealed samples. For the vacuum cleaned sample, two phases were detected, Fe_3O_4 and Fe_2O_3. They believed the presence of hydrogen stabilised FeO and therefore in a hydrogen annealed sample it would be easier to form FeO. Also, this study investigated oxide formation under various pressures and found the hydrostatic pressure (oxygen and nitrogen) rather than the oxygen partial pressure influenced the adherence of the formed oxides. In terms of Ni enrichment, no prominent enrichment occurred in the bulk oxide, but there was a Ni enrichment at the interface between oxide and metal.

Inaba et al. [126] reported research on the effects of varying annealing conditions on the oxidation behaviour of FeNi alloys. In this, an Invar Fe-36Ni alloy was annealed under

vacuum or hydrogen before oxidation at temperatures from 500 to 800°C for 600 s, 1800 s and 3600 s. Generally, they found that the oxide growth rate follows a parabolic law, and the thickness of the oxide is under one micrometer. However, the growth rate of oxide on an initially hydrogen-annealed sample is two to three times higher than in a vacuum annealed sample. The interesting point of this work is that it shows that different microstructures induced by different annealing conditions can affect oxidation behaviours. However, it also should be mentioned that the material used in this work contained a number of other elements, such as silicon and chromium and so on, any of which could affect the oxidation behaviour significantly.

Wandelt et al. [127] reported work on oxidation of polycrystalline Fe/Ni samples at 550°C. The techniques used were AES and a surface X-ray technique known as Appearance Potential Spectroscopy (APS). In this work, alloys with less than 70% Ni showed surface enrichment of iron oxide (Fe_3O_4), whilst spinel $NiFe_2O_4$ was found on the oxidised alloys with more than 70% Ni. The result is interesting since the techniques used therein are surface sensitive, which means only few nanometres of oxide layers within field of view. However, the oxidation experiments were carried out in a vacuum chamber at a pressure < 10^{-5} Torr, which means the comparison of this work to those mentioned above is difficult due to a large difference in experimental conditions. Similar work by Pollak et al. [128] also showed iron enrichment on the top 1 nm of oxide. They analysed an 81wt%Ni-Fe permalloy exposed in laboratory air for three weeks. They reported that the structure of the oxide, from the atmosphere to the material bulk, consisted of: 1. A chemisorbed layer; a complex surface layer with the thickness of the order of one monolayer, 2. An oxide layer about 1.2 nm deep, enriched with oxidised Fe and poor in nickel, 3. An interfacial layer about 1.2 nm, enriched with Ni and deficient in Fe, 4. The bulk alloy. A schematic drawing of this oxide is shown in Figure 2.2.8.

This work, as compared to that of Wandelt et al. mentioned above, differs in that the sample used by Pollak at al. work was oxidised under atmospheric pressure and ambient temperature. However because the sample was oxidised in air not pure O_2, therefore con-

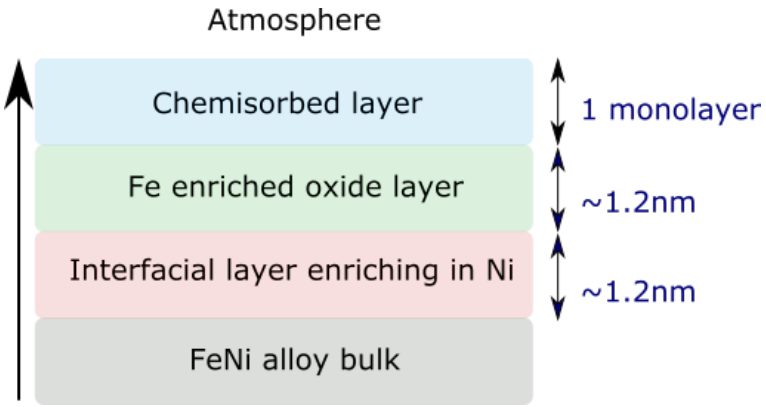

Figure 2.2.8 – Schematic drawing of the oxide formed on permalloy. [128]

tamination, such as water vapour, may influence the segregation, and thus this data must be interpreted with caution.

Brundle at al. [129] investigated the interaction of oxygen with a 76wt%Ni24wt%Fe alloy surface at 293 K, thus also in ambient conditions. The techniques used were LEED and XPS. The results show Fe partial segregation towards the outermost 0.4 nm forming an iron oxide, the dominant state of which is Fe^{3+}. Ni was found predominantly in metallic form, with little Ni^{2+} present. However, they also reported that Ni^{2+} could be reduced back to Ni^{0} just by heating, although the heating temperature was not stated. This provides useful information on the very outermost 1-4 atomic layers of NiFe alloy oxidation. However, when comparing to other works, it must be considered that since the oxidation was at low temperature and the oxidation pressure was extremely low in the analysis chamber, some variability may arise.

Olefjord et al. [130] reported on an XPS study of a Ni-25at%Fe single crystal. Oxidation experiments were conducted at 25°C and 500°C at a pressure of oxygen = 10^{-4} Torr. They found that Fe segregation was observed upon oxidation at both conditions. The oxide formed at 500°C was determined to be $NiFe_2O_4$. However, the authors state that sulphur contamination within the steel can segregate towards the sample surface if initial sample annealing is conducted at 800°C or higher.

Overall, as a conclusion to this section, a majority of research has found Fe based oxide forming on the surface of Fe-Ni alloys. However, the oxidation pressure, temperature and

even the purity of the oxidising gas can drastically affect the oxide formed. In addition, pre-treatment on Fe-Ni alloys is also an important factor for oxide formation. Some important questions in this field still need to be addressed. For example, low temperature oxidation (273K-500K) has not been systematically investigated, along with the effect of impurities during oxidation.

NiCo alloy oxidation NiCo catalysts have gained extensive attention towards their application towards renewable fuels production [68, 79, 131]. Alloying Ni with Co has been reported to lead to better oxidation resistance during reforming reactions, which increases the catalyst lifetime during operation [132]. Oxidation of such alloys is also of interest for catalyst research, since surface changes during oxidation could alter the active catalytic sites. There is, however, a necessity to consider the crystal structure of this alloy system. As illustrated in Figure 2.2.4, as mentioned, the Gibbs free energy of formation for CoO is slightly lower than that of NiO. Therefore, the formation of Co oxide is thermodynamically favoured. Co oxide was reported to form on NiCo alloy surface leaving an Ni enriched region under initial oxidation, the conditions of which were 1 atm oxygen, 600°C and 10 min [133]. Also, it was found that NiCo alloys oxidise faster than Ni metal, and this rate increases with higher Co contents. In Figure 2.2.9, the structural diagram of NiCo oxide is shown, in which growth above a grain boundary and a mixed oxide with Ni and Co are illustrated. However, the scale was well developed with a thickness ~200nm (which is considered relatively thick with regards to the scope of this thesis), although Chattopadhyay et al. claimed the aim of research was early stage oxidation. It was also found that it is possible to have a more noble (respecting to oxidation) metal in the oxide formed in the early stages (in this case Ni oxidised before Co oxidation), if its scale growth rate is fast enough. In this case, NiO was found together with CoO in the oxide that formed initially. In addition, Co was enriched onto the surface once CoO overgrew NiO due to higher diffusion rate of Co^{2+}over Ni^{2+}through oxide formation.

Extensive XPS studies of NiCo(50%) oxidation were conducted both at high and low en-

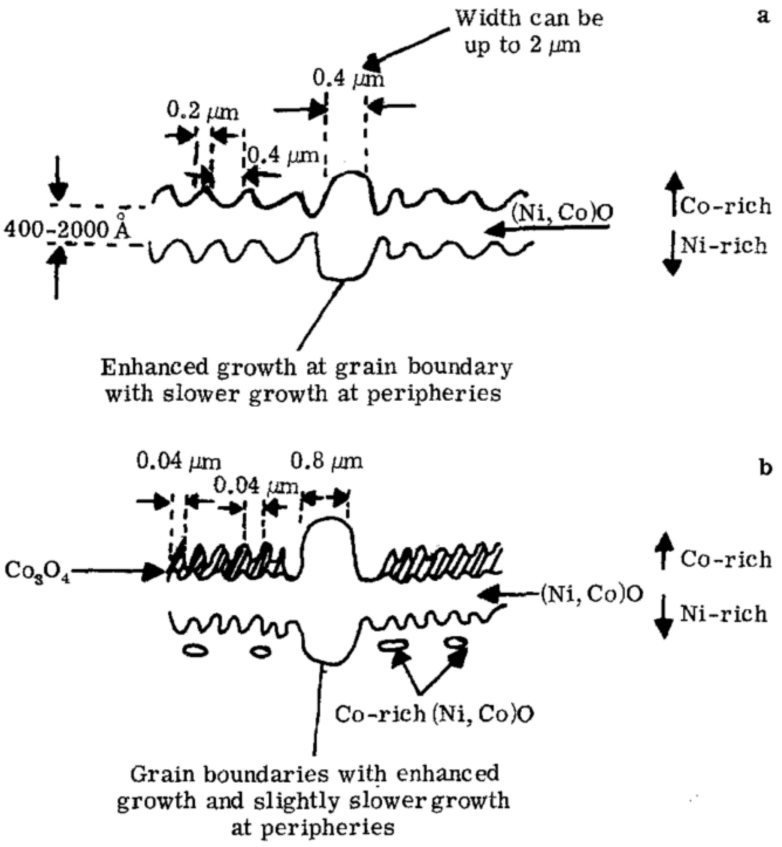

Figure 2.2.9 – Schematic representation of the cross-section diagram of oxide film on NiCo alloy grown in 1atm oxygen at 600℃ a) Ni-5at%Co, 10min, b) Ni-20at%Co, 10min [133]

vironmental pressure [134]. The results of a sample cleaned by Ar^{+}plasma and oxidised at 5×10^{-7}mbar oxygen and at 670K showed initial Co segregation towards the surface within 5 min before slowly reaching a developing plateau. Law at al. claimed Ni was depleted in the oxide in the case of low pressure oxidation. Oxidation with higher oxygen partial pressure (0.5 atm) was performed and it was again discovered that *Co* segregates towards the surface. Despite this finding of Co surface segregation, it is however important to realise that this is based on measuring the mean binding energy of the two elements, therefore it is not a direct observation. Following this work, Law et al. also conducted low pressure oxidation of Ni-Co layers (5 min heating at 773K in $1 \times 10^{-6} mbar$ oxygen) using synchrotron-based Photoelectron Emission Spectroscopy (PES) [135]. Again they found Co segregation over

Ni. Given the sample thickness was only around 1nm and that the signal strength was weak, such segregation was not however prominent. Hajcsar et al. used scanning Auger microscopy to investigate initial oxide islands forming on a clean 79 wt.% Ni-Co alloy surface [136]. Oxide growth was observed following the Holloway-Hudson model, in which oxide islands nucleate at one point in time and then grow at a rate determined by the rate of gas impingement at the island perimeters, surface crystallographic orientation, and the temperature. Co segregation towards these islands was observed in this study.

Overall, oxidation of non-noble metals has been summarised in this section. It is worth to conclude that the oxidation mechanism is rather complicated even when relative simple compositions are examined. Apart from the composition, manufacture process also determines the overall oxide development. Also, thermodynamics has been identified as being only one important factor among several others affecting the oxidation process. In the next section, noble metals, in particular Au, relevant to this thesis are discussed.

2.2.2 Noble metal Au-based alloys

2.2.2.1 Catalytic behaviour

Au-based materials were long considered as catalytically inert materials until 1980s. However, unique catalytic properties were discovered once Au could be processed into the form of very small particles of only few nanometres in diameter [2]. There are two major reactions reported in which Au is an exceptional catalyst: a) low temperature (< -70°C) oxidation of *CO* (over Au catalyst on silica) was first discovered by Haruta et al. [1, 27, 137]; b) the application of Au based catalyst for alkyne hydrochlorination to vinyl chloride [138, 139]. A recent review covering the high reactivity of Au particles pointed out that a decrease of particle size has the most prominent effect on performance, at least for the *CO* oxidation reaction [140]. Figure 2.2.10 shows this dramatic effect; only Au particles less than 5 nm in diameter possess a high catalytic ability for converting *CO* [141].

It has also been pointed out that Au atoms with low coordination numbers are the key sites for reactions [140], although the support also acts in a manner to alter reaction rates

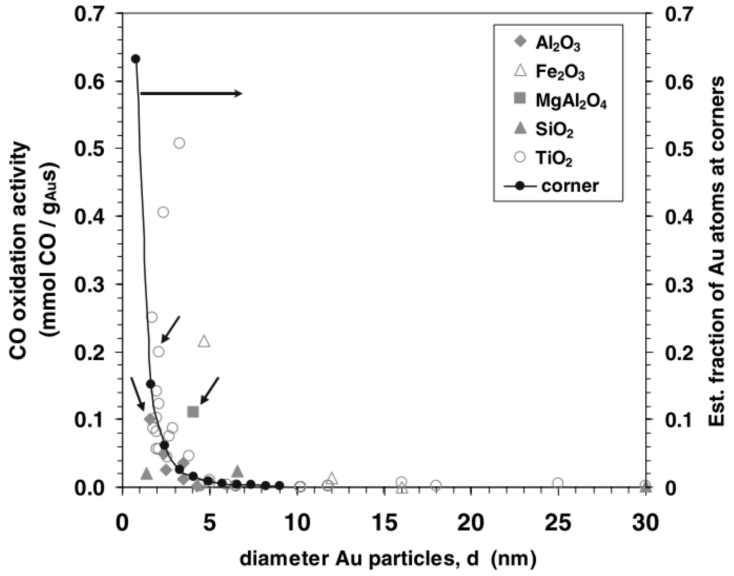

Figure 2.2.10 – Size effect of Au catalyst reactivity towards CO oxidation. Au catalysts were tested with various supports. [141]

[142]. The ability to drive CO oxidation is very important in industries involving hydrogen. Most hydrogen used industrially is produced by steam reforming, which also produces CO as a side product. However, CO is a poison for various reactions, such as ammonia synthesis, and it must be eliminated. Au based catalysts show the best sensitivity to CO oxidation, converting to CO_2 from the gas stream [143]. Similarly, hydrogen without CO is also essential for fuel cell systems in particular using methanol as the H_2 source [144]. Another important reaction is alkyne hydrochlorination, which is the main reaction to produce vinyl chloride, one of the most used industrial chemicals. This reaction has been previously catalysed by mercuric chloride supported on carbon [139], which is highly toxic for the environment because the sublimation temperature of Hg is low. Au particles on carbon were thereafter developed as an alternative [145]. Apart from the monometallic Au particle catalysts, bimetallic ones have attracted considerable attention since they allow fine tuning of the catalytic properties [146]. AuCu is one such alloy that has been studied by a few research groups, and the catalysed reactions are listed in Table 2.2.4. AuCu bimetallic particles show an improved conversion rate for CO oxidation at lower temperature compared to pure Au

Reaction	Reactants	Products	Catalyst
Acrolein synthesis [148]	propene	acrolein	$AuCu$ on silica
Propene epoxidation [149]	N_2O	propene oxide	$AuCu_3$ on TiO_2
CO selective oxidation[147]	CO	CO_2	$AuCu/TiO_2$
Benzyl alcohol to benzaldehyde [150]	benzyl alcohol	benzaldehyde	$AuCu/SiO_2$sample with AuCu weight ratio of 4 : 1
Borohydride oxidation[151]	borohydride	hydrogen	$AuNi/C$
Steam reforming [152]	CH_4 and steam	hydrogen and CO	Au modified Ni surface
Hydrolysis of ammonia borane[153]	ammonia borane	hydrogen	AuNi NPs 3–4 nm diameter embedded in silica

Table 2.2.4 – A brief summary of reactions catalysed by Au based catalytic system

particles [147]. However, the exact effect of the Cu addition is not yet clear. Apart from the driving force of potential performance increases, the major factor of adding Cu and Ni is to reduce the load of precious metal and in turn reduces the overall costs.

2.2.2.2 Au based particles

As described in the previous section, Au has superior catalytic abilities for certain reactions. These abilities are strongly related to the particles local chemistry, structure, and stability. In the following section, studies about various Au based particles are presented. Phase diagrams of AuNi and AuCu systems are shown in Figure 2.2.11. AuNi is a very simple system only containing two phases: liquid and fcc-A1 phase. Similarly, AuCu system is one of the simplest system since Au and Cu can mix with each other regardless of the proportion. Three common intermetallic phases can be found in this system, which are $AuCu$, Au_3Cu and $AuCu_3$.

Composition Adding more than one element into the monometallic particle results in much more complexity; the distribution of elements can now become phase separated such as core-shell structure, chemically ordered, Janus structures (nanoparticles whose surface

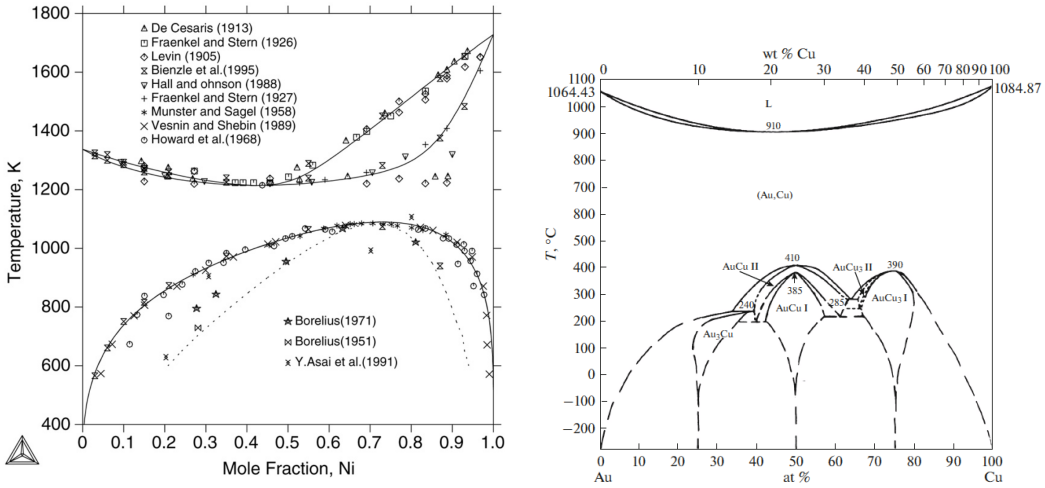

(a) **(b)**

Figure 2.2.11 – a)The Au–Ni phase diagram (solid line) and spinodal line (broken line) calculated from the present thermodynamic description in comparison with experimental measurements [154] b) AuCu phase diagram with a extended calculation into the low temperature region [155]

have two or more distinct properties) or higher order mixtures [156]. Xiang et al. [157] observed oxidation-driven segregation of Ni to the surface of an AuNi particle under ambient atmosphere, 300°C for 30 min, by High Resolution Transmission Electron Microscopy (HRTEM). They found that Au migrated into the centre of the particle during the oxidation and a corresponding Density Functional Theory (DFT) calculation showed Au reduced the dissociation energy of oxygen and helped Ni oxidation. Hydrogen reduction on such oxidised particles resulted in an amorphous AuNi layer formed on the outside while the NiO layer collapsed. Formation of such AuNi alloyed layers on the surface has also been observed by Molenbroek et al. [158]. They stated that the resistance of coke formation on the particle surface is enhanced by Au incorporation into Ni. Also, the mechanism of coke resistance was interesting as they identified that Au segregation to the highly reactive Ni edge and kink sites through Monte Carlo simulation. For the AuCu system, experimental evidence for weak Au segregation to the surface of Cu has been reported [159]. Sinfelt et al. examined Cu-25at. %Au (Au_3Cu), Cu-50at.%Au ($CuAu$), and Cu-75at.%Au (Cu_3Au) nanoparticles under oxidising and reducing environments and found that Au segregated to the surface in a reducing hydrogen environment, whilst segregating towards the core in a

oxidising environment [50].

Structure The structure of *Au* based particles is also very important in terms of the catalytic reactivity. As mentioned *Au* atoms that have a low coordination number show unique catalytic properties, therefore structures with high numbers of edges and corners are favourable for catalytic reactions [160]. Before going into details about particle structure, it must be understood that there is no simple answer concerning how a particular material at a given size may have structure 'A', which changes to 'B' as conditions change [161]. For a micro-size particle, the minimum energy shape for a given volume is determined by the Wulff construction, mathematically proved by C. Herring [162]. If only considering the material surface energy, particle morphology should be independent of its size [163]. Particle deformation when contacting supporting materials has been observed, which was believed to be due to the free energy of adhesion [164] and/or elastic deformations. In some extreme cases, Au particles can be incorporated into the substrate such as *Au* particles sinking into an *MgO* substrate [164]. Molecular Dynamic (MD) modelling also confirmed similar phenomenon by showing that *Au* particles smelt on a silicon (001) surface [165]. Despite these factors that alter the particle shape and structure, relatively little research has been carried out to date. *Au* particles freely standing have several possible structures as illustrated in Figure 2.2.12. The exact shape is dependent on factors such as particle size and temperature. A phase diagram showing this relationship is illustrated in Figure 2.2.13.

Darby et al. conducted research on the structure of *CuAu* intermetallics. Pure *Cu* particles have an icosahedral packing with lowest energy, whilst pure *Au* clusters tend to form less symmetrical structures. However, Darby et al. reported that even single *Cu* atom replacement in pure Au cluster can change from an amorphous structure into an ordered one, using computational analysis [167]. Darby et al. also tried to determine the structure and composition that minimised energy by computational methods, and found that *AuCu* particles exhibit icosahedral packing, $CuAu_3$ clusters tend to form layered structures and Cu_3Au shows greater Cu-Au mixing.

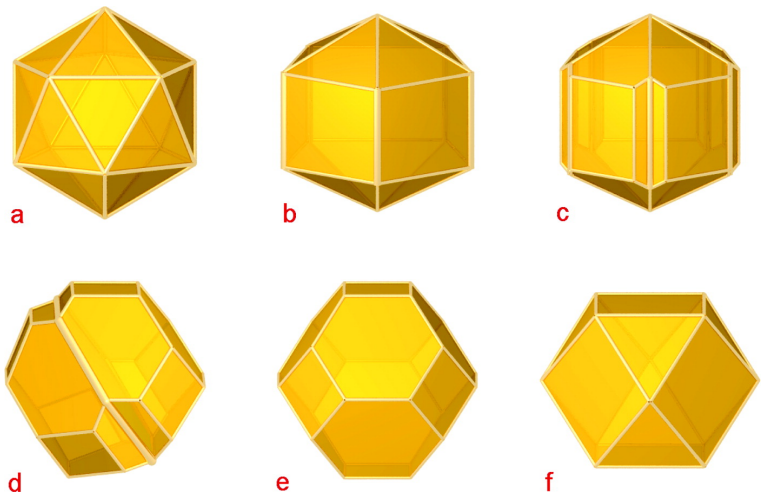

Figure 2.2.12 – Various shapes exhibited by gold nanoparticles: the Mackay icosahedron (a), the Ino (b) and Marks (c) decahedra, the symmetrically twinned truncated octahedron (d), the ideal truncated octahedron (e), and the ideal cuboctahedron (f). [166]

In conclusion, it is important to know that local composition of AuNi and AuCu particles changes under changing environments and/or conditions. It therefore important to get insight into the local arrangements between metal atoms in multimetallic nanoparticles.

2.3 TEM, FIM and APT study of catalysts

Development of nanoparticles would be not possible without methods to probe their structure and composition, revealing why they are effective for particular applications. Various techniques are available for this purpose. For example, XPS is used to understand the chemical composition of the outermost surface region (a few nanometres) [168]. XRD is used to understand the crystal structure [146]. EXAFS is used to probe the atomic distance between elements within particles [49–51]. In this thesis, TEM, FIM and APT are the three main techniques utilised, and hereafter this literature review is focused around their contributions to understand catalytic materials.

2.3.1 TEM Research on nanoparticles

Transmission electron microscopy (TEM) is a well-established way to investigate nanoparticles [166, 169–173]. The resolution of modern TEM, which is at the sub-nanometre

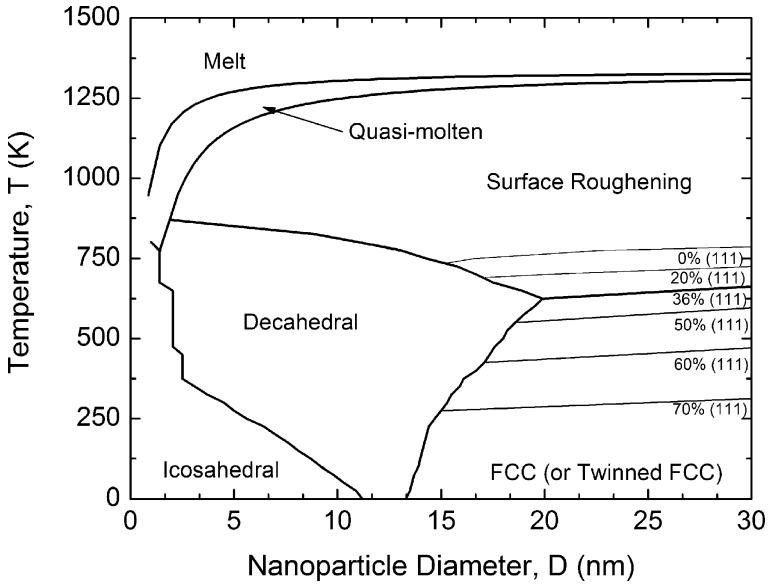

Figure 2.2.13 – Quantitative phase map of gold nanoparticles, based on first principles calculations. [166]

level, is sufficient to reveal the shape and lattice structure of nanoparticles, whose sizes are normally between few nanometres and hundreds of nanometres [174]. Chemical information from nanoparticles can also be detected by TEM. High Angle Annular Dark Field (HAADF), Electron Energy Loss Spectroscopy (EELS) and X-ray Energy Dispersive Spectroscopy (XEDS) are used to reveal the chemical information within small particles [175–180]. Although TEM provides a great tool for particle research, this technique still faces some challenges under some particular situations. The major difficulty is dimensional mismatch. TEM normally produces 2D projections, which are not sufficient enough to represent nanoparticles with features in 3D. 3D HAADF with a spatial rotational holder [181, 182] and imaging with varying focal length [183, 184] have been both been applied to try to probe nanoparticles in 3D. However, at this stage, these 3D techniques are still mostly limited to provide images only. EELS and EDS are powerful methods to probe chemical composition together with TEM, but the scanning speed is slow and the signal intensity is significantly affected if the particle size is relatively small. HAADF combined with EELS and EDS is promising to directly give 3D structure but again with limited resolution [185].

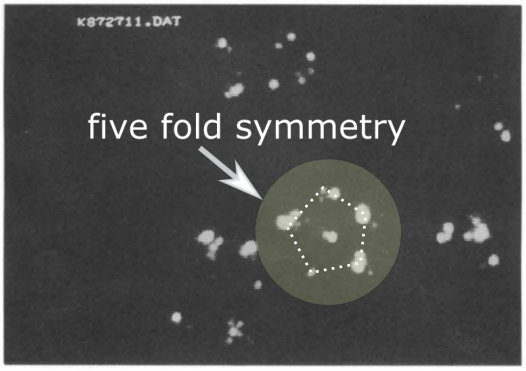

Figure 2.3.1 – A He ion image of Au clusters on a tungsten tip at 77 K. The conditions to produce clusters was adjusted to yield particle with a diameter of 2 nm. The five-fold symmetry of the cluster located in the centre of the image is clearly resolved. [186]

2.3.2 Field Ion Microscopy and Field Emission Microscopy

Nanoparticles have attracted attention among scientists in the area of field emission research. Substantial work has been conducted using Field Ion Microscopy (FIM) and field emission microscopy (FEM). Castro et al. [186] reported work investigating Au nanoclusters under FEM, FIM and also Scanning Tunnelling Microscopy (STM). In this work, a multiple expansion cluster source was used to fabricate clusters. By this method, a metal source was vaporised and subsequently condensed by injection of He or Ar gas. The condensed clusters were then driven by a pressure differential and finally projected onto substrates [187]. The field ion emission image is shown in Figure 2.3.1. Particle agglomeration was directly observed using FIM, together with the five-fold symmetry, which is characteristic of the icosahedral configuration. The size of the produced particles was 1.5-3 nm determined by FIM. Clusters tended to agglomerate due to the high imaging field and Castro et al. claimed they were not able to image individual clusters. However, in the images they presented (as shown in Figure 2.3.1 and 2.3.2), it is apparent that an individual particle could be observed. In addition, the melting temperature of the Au clusters, which was found to be 450 ± 75°C, is substantially lower compared to bulk Au (1060°C). This is a well-known phenomenon, where a monotonic lowering of melting temperature with decrease in particle size is found [188]. The FIM results showed this melting phenomenon quite clearly by comparing Figure 2.3.1 and 2.3.2.

Castro et al. further conducted an investigation on cluster melting temperature based on FIM [189]. They observed the solid-liquid transformation of Au clusters on a tungsten tip

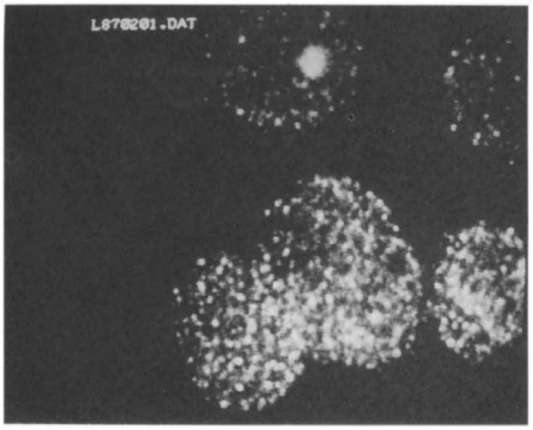

Figure 2.3.2 – A He ion image of the cluster covered tip shown in Figure 2.3.1 after heating the tungsten substrate to 450 ± 75 ℃. The melting of the individual clusters is clearly evident from this image. The image was taken at 77 K.[186]

and also pointed out the potential of using FIM to systematically analyse the melting temperatures of supported clusters with other compositions. Following that, Castro et al. [190] also examined gold and silver nanoparticles with sizes larger than 2 nm. They observed that the melting temperature of such clusters was size dependent and in agreement with a thermodynamic model for cluster melting. The thermodynamic model took into consideration the coexistence between the solid and liquid cluster along with some general thermodynamic relationships. In that model, the large internal stress is the pressing factor to depress the melting temperature of a cluster. On the other hand, Lovall et al. [191] investigated the atomic structure of supported nano-clusters. By combining Molecular Dynamics (MD) simulations of Field Ion Emission and FIM images of supported Au clusters, they claimed to resolve the lattice structure of Au nano-clusters on W, Pt and a Pt/Ir tips. MD simulation, which was used to simulate the field emission process, was of great value helping to determine the crystallographic information of emitting tips. Some of the simulation and FIM image are shown in Figure 2.3.3.

Aside from metallic nano-clusters, Lin et al. conducted FEM research on supported C_{60} particles [192]. The investigated C_{60} was attached to a tungsten tip. The emission of the sample was successfully obtained and the result indicated that C_{60} has a steady electron emission with a narrow electron energy distribution.

Discussion will now switch from the study of particles to acicular tips. The semi spherical shape of the tip is a good analogy between the surface of the tip and the surface of a

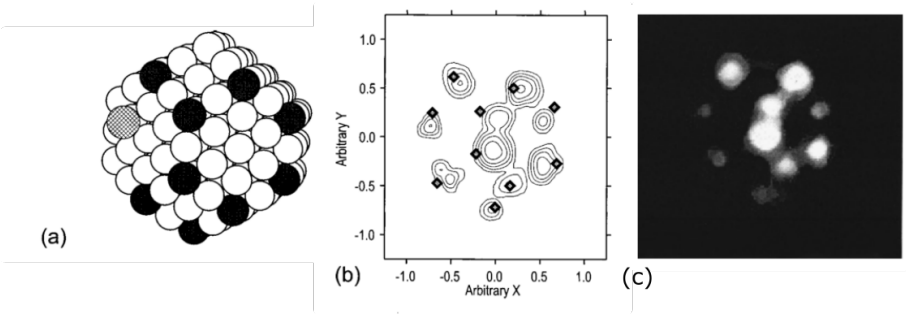

Figure 2.3.3 – (a) A 202-atom cluster shown in the orientation that best fits the experimental image in (c). The darkened atoms represent the atoms imaged in the experiment. The atom shaded with a cross-hatched pattern represents an atom added onto a surface facet to improve the fit to the experimental image. (b) Comparison of a simulated FIM image of a 202-atom cluster to the experimental image in (c). Figure (c) A field-ion image from a ~1.5 nm Au cluster, annealed before deposition at a temperature of 1200 K, cooled to 300 K, and landed on a W tip. The imaging gas is Ar and the temperature of the tip and cluster is 100 K. [191]

large nanoparticle. The following discussion is around FIM, FEM and APT.

FIM and FEM have also been used to reveal the field changes before and after chemisorption on metal surface [193–197]. Since surface chemisorption has been identified as one of the crucial step for catalytic reactions, direct observation of this effect would be of great importance, especially seeing differentiated behaviours among various zone axes on a stepped surface. Gaussmann et al. observed surface reconstruction using FEM [198]. In this work, Pd surface reconstruction happened after exposure to 1hPa CO and between $300K - 400K$. FEM images before and after exposure showed that surface reconstruction was only about one atomic layer thick. With the development of the research method, Bär et al. [199] conducted NO dissociation reaction on Ag surfaces with a dose of 150L (1L = $1.3 \times 10^{-4} Pa \cdot s$) and 400K. Reconstruction was again observed on the surface (as shown in Figure 2.3.4), with crystal coarsening occurring during reaction with NO gas. The <100> zone was dark under FIM after exposure to NO, but the brightness reappeared after field evaporation of only a few layers. This affect was believed to be a result of subsurface embedded oxygen atoms formed during NO decomposition since this behaviour was not observed in the case of specimens that were analysed subsequent to plasma cleaning.

Visart de Bocarmé et al. [200] conducted similar experiment but with Rh in an oxygen/hydrogen mixture and considerable surface morphological changes were observed in-

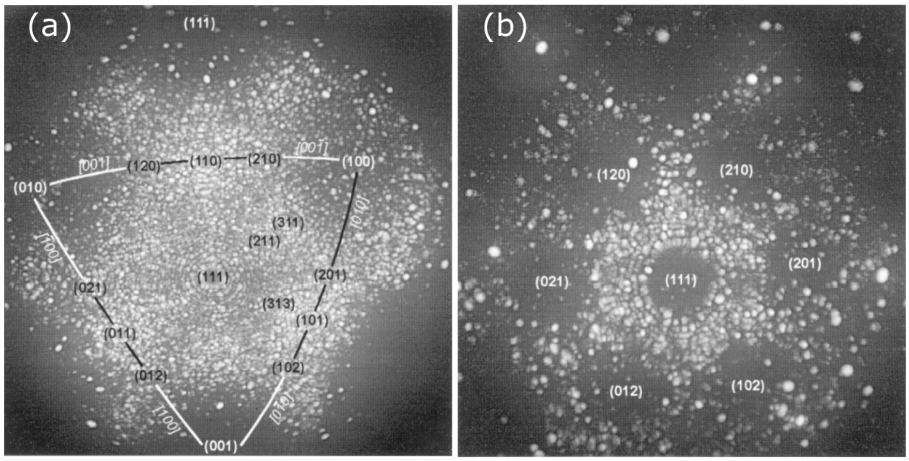

Figure 2.3.4 – (a) Field ion micrograph of a clean [111] oriented Ag tip sample; the image was taken in hydrogen with $p_{H_2} = 1.0 \times 10^{-3} Pa$, T= 57 K (with an estimated tip radius of 87 nm, the field strength is about 22 V/nm). (b) H_2^+ field ion micrograph of the same Ag sample as in (a) after field-free exposure to 150 L NO (1 L=$1.3 \times 10^{-4} Pa \cdot s$) at T=400 K; [199]

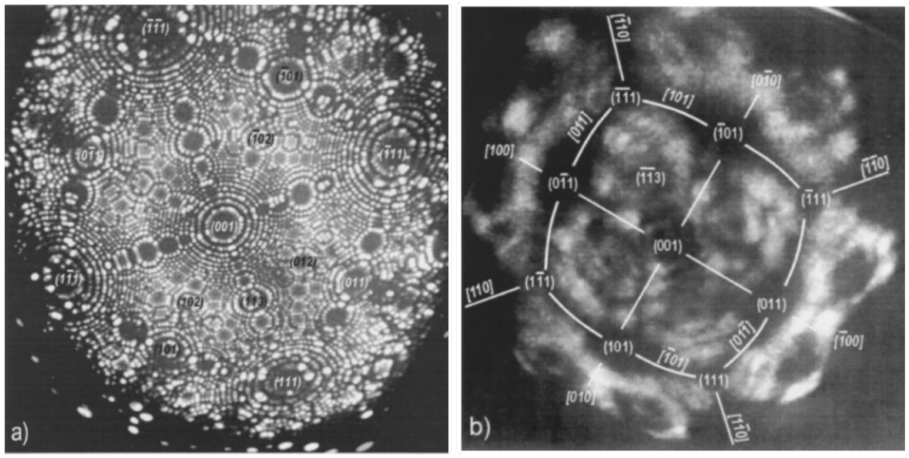

Figure 2.3.5 – (a) FIM micrograph of a clean [001] oriented Rh tip imaged in neon at 60 K and 37 V nm^{-1}. (b) Same tip at 505 K imaged in a mixture of $H_2 - O_2$ (2:1) at $4.5 \times 10^{-3} Pa$ and $13 V nm^{-1}$.[200]

cluding facet formation along the <110> zone lines. The experiment was conducted between 400 and 500 K and total pressures up to $10^{-2} Pa$. In Figure 2.3.5, a Rh surface is shown before and after heating at 505K in $H_2 - O_2$ (2:1) atmosphere. The significance of this work however was mainly the direct observation of surface changes in real time; removal of hydrogen in the gas mixture resulted in a delayed surface reconstruction.

Such FIM experiments mentioned above should inevitably consider the effect of high field induced. McEwen et al. [201] compared oxidation of Rh with DFT calculation. This

confirmed that oxidation of Rh is promoted under an applied field due to reduction of the barrier for oxygen incorporation into the surface of an oxide layer. It is therefore also of interest to examine oxidation without the interference from the electrical field. Bocarmé et al. [193] conducted such field free surface segregation experiments on Au-Pd alloys in NO environments at temperatures ranging from 300-573K. A considerable surface enrichment in Pd (to ~80at%) was observed, which was believed due to the strong Pd-O bonds at the surface. A point to address in this work is that the reaction was conducted in a separated reaction chamber, which was attached to the main FIM instrument [202]. This allowed surface reaction to be conducted at a pressure much closer to real-world reaction condition (from 10^{-5}mbar region to few 100mbar region). Barroo et al. [195] ingeniously exploited brightness changes during FEM experiments to investigate oscillations of chemical reactions. In this, they followed the dim and bright cycle of platinum surface emission when reducing NO_2. In Figure 2.3.6, different points in the cycle are clearly apparent in c and d. Through a careful analysis of image brightness, they discovered that there were modal and bimodal oscillations depending on H_2/NO_2 ratios. Barroo et al. [203] then attempted to track the behaviour of a [012] facet only along with a similar experimental setup. They found that the oscillations were strongly related to phase diffusion, which describes small systems where noise manifests itself. Furthermore, they attempted similar experiments on a $Pt-17.4at\%Rh$ alloy [204], concluding that the robustness of the oscillation reaction was determined by the nature of the chemical reaction itself, and only slightly influenced by the alloy composition.

Overall, FIM and FEM are very effective tools to investigate reaction mechanisms down to regions of single zone axes. However, they cannot detect the chemical composition changes during or after reaction. Therefore, another complementary technique: atom probe is introduced in the following section.

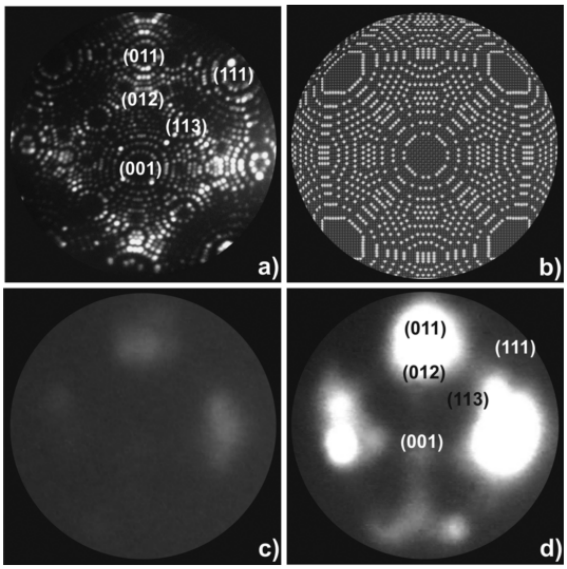

Figure 2.3.6 – FIM and FEM Images of a platinum nanocrystal surface before and during reaction with NO_2. a) FIM image of a platinum model surface imaged by Ne at 55K. b) ball model of a reconstructed fcc crystal lattice. c) Field emission micrograph during the reaction, which has low brightness due to surface chemisorbtion oxygen atoms. d) Field emission micrograph after the reaction. Chemisorbed oxygen formed water and desorbed from the surface. [195]

2.3.3 Atom probe research on catalytic alloys and nanoparticles

Atom probe is a technique with atomic-scale chemical detection capability. Initial apparatus developed in 1967 was only able to detect signal ions from specific regions of interest, and was therefore known as 1D atom probe [205]. However, subsequent ongoing instrumentation development, such as delay-line detectors and various electronic & computational advances, culminated in atom probe having a full 3D detection ability in 1988 [206] and the technique now known as Atom Probe Tomography (APT). Building upon further advances, the Local Electrode Atom Probe (LEAP) series of instruments manufactured by CAMECA Inc. is now the latest in commercial atom probe technology with high detection efficiency, improved yield and a wide field-of-view [207].

In this section, mostly metal surface analyses and nanoparticle analyses are reviewed, intermixed with the development of atom probe sample preparation methods for nanoparticles. In terms of surface analyses, oxidation work is reviewed together with other gaseous reactions. FIM studies are covered first, before focusing on APT driven experi-

ments in an approximately chronological order.

FIM and 1D atom probe approach The first report on the initial stages of oxidation via 1D atom probe was authored by Ng et al. [208]. In this work, pure Fe, Co and Ni wires were oxidised in both pure oxygen and air and then analysed by atom probe. As it was the first research reported to analyse oxide under atom probe, the results were novel. They found that the elements revealed in the mass spectra were not the same as the known stoichiometric oxide chemistry. They suspected the high electric field present during analyses was decomposing molecular ions in a complex fashion, and thus biasing the result. Nevertheless, they detected FeO^+, FeO_2^+, FeO_3^+, O^+, O_2^+, Fe^{2+} and Fe^+ ions for the analysis of the oxidised Fe sample, whilst NiO^+, NiO_2^+, O_2^+, O^+, Ni^{2+} and Ni^+ ions were found to be field evaporated in the oxidised Ni samples (lists are not in order of abundance). Cobalt oxide layers field evaporate as CoO^+, Co^{2+}, O_2^+, and O^+ ions as well as a small number of Co^+, $CoOH^+$, and CoH^+ ions. Apart from this, they also found higher metal concentrations at the very start of experiments, counter to the expectations for seeing purely single-phase oxides. They explained this phenomenon through a theory of the formation of a space-charge layer with metal ions driven to the surface to cater for the depletion of vacancies. However, it is worth mentioning that the volume of data was relatively small compared to modern local electrode atom probes and this surface enrichment could be site specific. Also, the high field around the apex of the sample may be playing a role in terms of influencing which ions evaporate first. Nevertheless, this work opened a new field of study and the results demonstrated the power of atom probe techniques in surface oxide investigations. Following this work, Cranstoun at al. [209] used atom probe to investigate ruthenium oxides. In this work, the oxide formed on exposure of Ru to oxygen at temperature of 850-900K, and it was believed to be RuO_2 via counting the numbers of Ru^+, O^+, RuO^+, RuO_2^+ ions. Additionally, oxides formed on various crystallographic facets were individually analysed and the result showed the distinctive chemical composition of oxides on each facet. For example, such as O/Ru ratio was 1.8 along $10\bar{1}0$ axis and 2.0 along

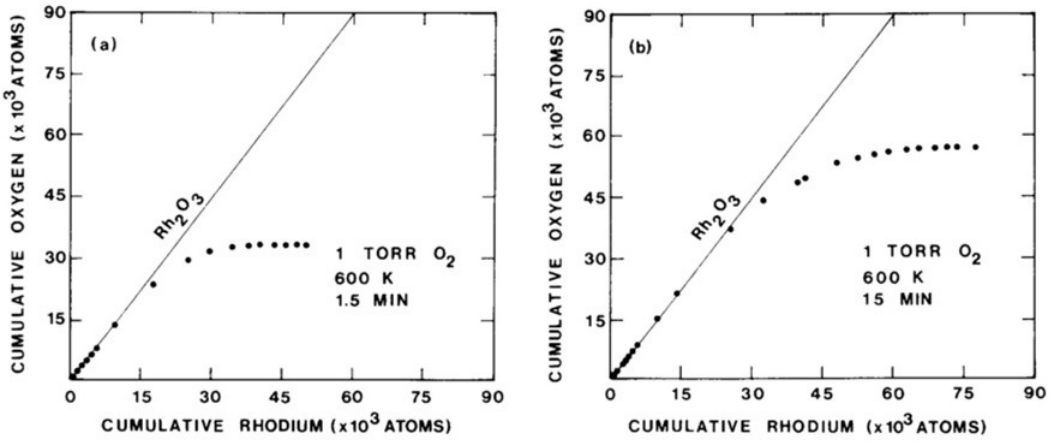

Figure 2.3.7 – Plots of the cumulative number of oxygen atoms versus the cumulative number of Rh atoms obtained from imaging atom-probe mass spectra from samples heated to 600K in 1 Torr 0_2 for (a) 1.5 min and (b) 15 min. The initial slopes of the plots indicate that the oxide is stoichiometric Rh_2O_3 [210]

$11\bar{2}0$ axis. In general, this work combined with the work of Ng et al. [208] formed a key foundation of atom probe research on oxides.

In a later work conducted by Kellogg in 1986, initial oxidation and reduction on the surface of Rh was investigated [210]. The initiative for this work was to understand the deactivation mechanism of Rh for catalysing CO oxidation to CO_2. In this, the author used a plot of cumulative Rh atom count versus cumulative O count to determine the stoichiometric composition of the oxide, which was Rh_2O_3 (as shown Figure 2.3.7). Oxide growth was preferential. Also in this study, a comparison between FIM and 1D atom probe showed that oxide was observed almost half thinner comparing to the atom probe composition calculation, which was due to the non-uniformity of oxide as shown in Figure 2.3.8, in which oxide on [100] direction was totally evaporated initially.

3D atom probe approach The research discussed above was mainly conducted on FIM and using 1D atom probe. With the invention of 3D atom probe in 1988 [206], offering a wider field of view and improved detection capabilities, these instruments have now allowed a number of groups to add new insights to oxidation behaviour. Bagot et al. [196, 202, 211, 212] reported a series of works both on the instrumentation and precious

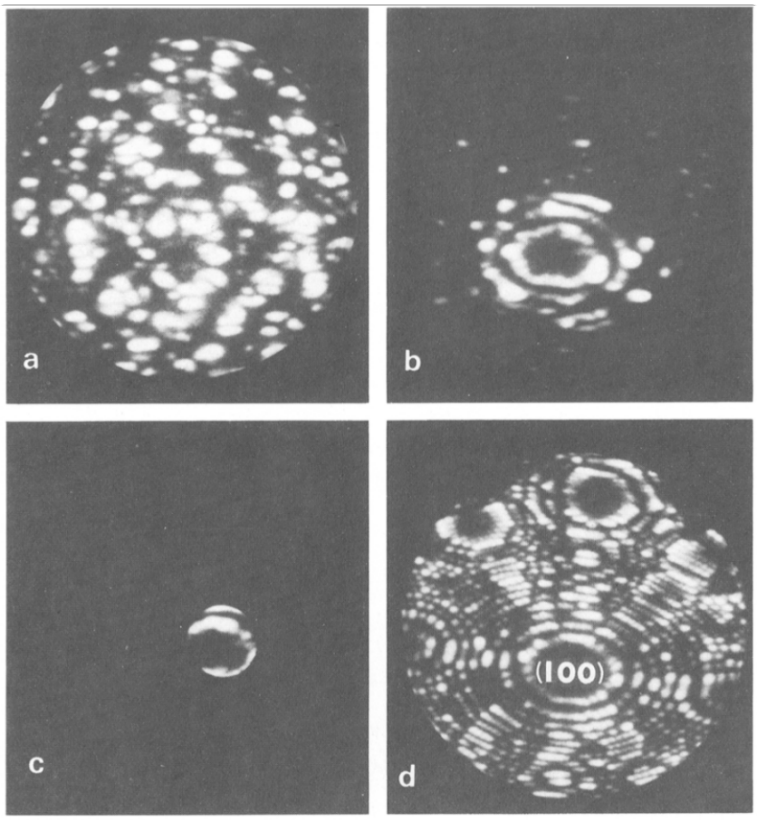

Figure 2.3.8 – Field ion images of a Rh sample after it had been heated to 500 K in 1 Torr O_2 for 15 min. The sequence shows images of (a) the surface oxide, (b) the Rh substrate after removing the oxide indicating a protrusion, (c) the surface with a probe hole placed over the protrusion, and (d) the surface after the protrusion was field evaporated. [210]

group metals. In their initial work, new instrumentation was designed and made specifically for catalytic alloy research as shown in Figure 2.3.9 [202]. The instrument consisted of a reaction cell, attached to the preparation vacuum chamber of a 3D atom probe. A gas rig was attached to admit various gases into the reaction cell. The benefit of this system is that samples can be analysed directly after surface reactions without being exposed to atmosphere. Contamination free environments are crucial for any successful surface research. By using this instrument, Bagot et al. observed Rh surface enrichment of a Pt-Rh alloy reacting with NO at 300°C. More recently, an updated version of the reaction cell has been built by Dumpala et al. at Iowa State University. The preliminary results from this system indicate prominent contamination reduction on the obtained mass spectrometry, compared to conventional oxidation in a furnace and subsequent transfer to the atom probe [213],

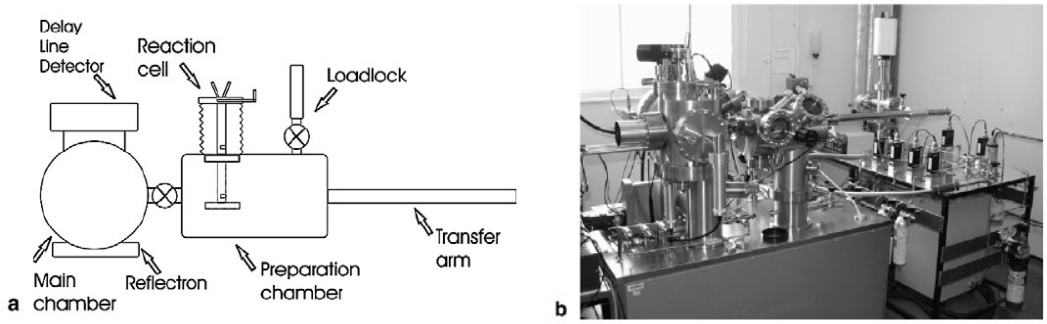

(a) (b)

Figure 2.3.9 – Reaction cell (a) schematic drawing of the reaction cell designed by Bagot et al. and (b) the configuration of gas rig sitting aside to a 3D atom probe [202]

along with segregation behaviour in oxidised Pt-Ir and Pt-Rh-Ir alloys.

Furthermore, Bagot et al. [196] reported a comprehensive research on Pt and Pt-Rh alloys oxidised under NO, NO+CO and O_2+NO. One finding utilising FIM analysis was that NO could alter the surface morphology of pure Pt samples, but more pronounced surface faceting was observed for a Pt-17.4at%Rh alloy after exposure to 10 mbar NO for 15 min (Figure 2.3.10). The depth of faceting is about 10 atomic layers, which illustrates the typical surface reconstruction of a catalyst during reaction. More importantly, it proves the ability of the FIM to reveal subtle surface characteristics. Another important point in this work was that the authors evaluated the influence of the high field from FIM on the gas metal surface absorption by Field Emission Microscopy (FEM). By taking FEM images at -0.6kV after FIM at +1kV, +2kV, +3kV and +4kV, no changes to the structure of the treated sample after applying high fields were confirmed. This was the first-time experiments could show that the surface segregation of Pt-Rh alloy is dependent on both temperature and crystallographic orientation.

Furthermore, Bagot et al. [211] reported research on the ternary alloys: Pt-Rh-Ru and Pt-Rh-Ir. The research methodology was the same as the works mentioned above: using a modified APT known as the Catalytic Atom Probe (CAP) and admitting NO gas to investigate surface changes. The results indicate different surface segregation behaviours are imposed by adding Ru and Ir into Pt-Rh alloys, and again that segregation trends are

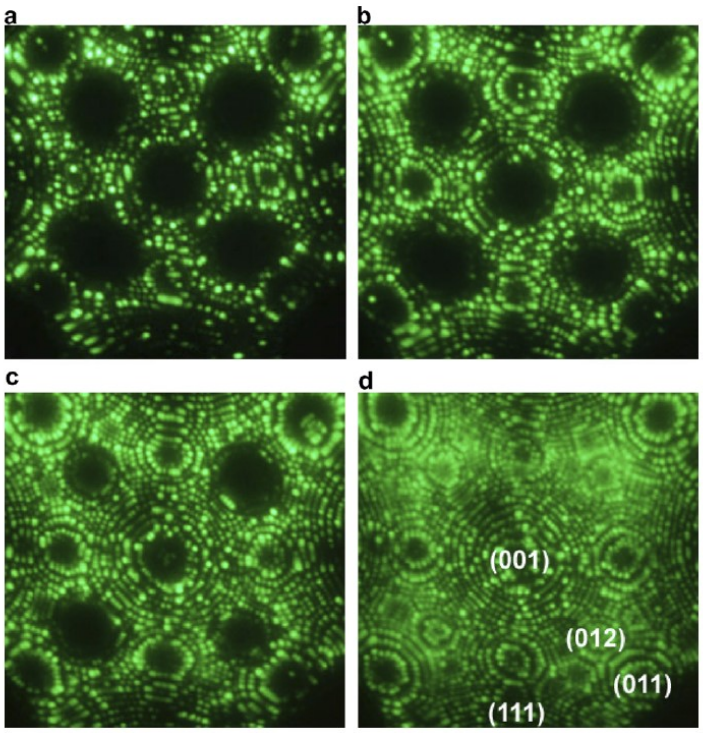

Figure 2.3.10 – FIM image of Pt-17.4at%Rh following a treatment of 15 mins NO at 10 mbar, 300℃. Image shown in (a) no atoms have been removed, successive images show approximately 2-3 atomic layers removed each time. [196]

strongly related to crystallographic directions. The importance of this work clearly shows that the composition of facets controls the reactivity.

In addition to the catalytic atom probe work, some work has been carried out on oxidation-reduction cycles of Pt-Rh alloys by Li et al. [214]. In this study, a Pt-22at%Rh alloy was oxidised at 873K, 973K and 1073K for 5 h in 1 bar oxygen. In a separate experiment, some specimens were oxidised at 1073K for 1 h and then reduced at 673K for 1.5 h in 1 bar of hydrogen. The results indicated a stoichiometric oxide formation of Rh_2O_3, the growth rate of which is controlled by the outwards diffusion of Rh. This work also calculated diffusion coefficients of Rh in Pt-Rh system from the Rh depletion profiles. In terms of sample after hydrogen reduction, a thin layer of Rh was found at the sample surface. This suggests oxidation-reduction cycle on metal altered the surface composition, information which that can be used to tune compositions in the development of future nanoalloys and nanoparticles.

Subsequent to this, Li et al. published works on Pt-Ru, Pt-Rh-Ru and Pd-Rh alloys

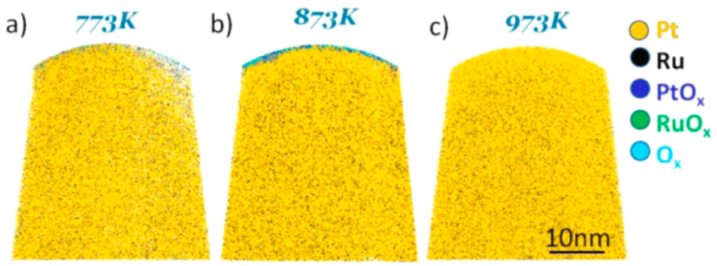

Figure 2.3.11 – APT reconstructions of Pt–Ru specimens oxidized for 300 min at different oxidation temperatures: (a) 773, (b) 873, and (c) 973 K. [215]

[215, 216]. Both of these works were designed to investigate surface segregation behaviour under oxidation-reduction cycling. In the Pd-6.4at%Rh alloy investigation, PdO was observed on the surface after initial oxidation [216]. Interestingly, Rh segregation, forming a ($PdRhO_2$) oxide, was also observed. In the following reduction experiment, Rh enrichment persisted even after all the oxide had been reduced back to the metal state. By comparison with the previous Pt-Rh work, this work clearly shows the difference in oxidation-reduction behaviours of the two alloys. Although similar Rh surface segregations were observed, the oxidation temperature was substantially lower (873K) and time was shorter (maximum 180 min) for the Pd-Rh system. In Pt-8.9 at%Ru and Pt-23.9%Rh-9.7at%Ru alloy investigation [215], Ru and Pt oxides were found at the surface, however metal segregation remained after reduction. Ru segregation in oxides was observed only at 773K but depletion at 873K and 973K. The surface oxide layer vanished at higher temperature leaving Pt-rich surface as shown in Figure 2.3.11. Grain boundary diffusion was significant for initial oxidation on Pt-23.9%Rh-9.7at%Ru alloy. Also Rh and Ru depletion was evident near oxide regions.

Based on previous works, Li et al. [217] directly investigated Pt alloys in a direct comparison with other PGM alloys. Three distinct regimes were found for the Pt-31at%Pd alloy. For oxidation experiments at 673-1073 K, surface enrichment was initially in Pd and then switched to Pt above 873K as shown in Figure 2.3.12. Li believed that PdO was dissociated leaving enriched Pt surface. The comparison among three Pt-Rh, Pt-Pd and Pd-Rh alloys shows fundamentally different surface segregation behaviours. This work provides a fundamental understanding of oxidation behaviours of noble alloys at near atomic scales and has

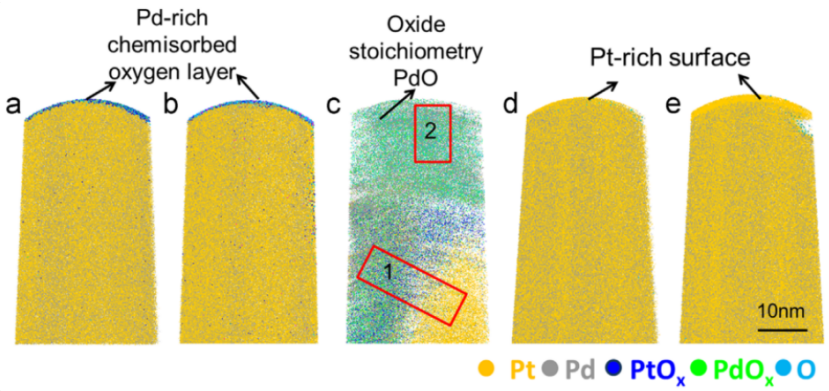

Figure 2.3.12 – Cross-sectional APT reconstructions of a Pt-31 at% Pd alloy oxidized for 5 h in 1 bar O2 at (a) 673 K, (b) 773 K, (c) 873 K, (d) 973 K and (e) 1073 K. [217]

clear implications for working catalysts.

Local Electrode Atom Probe approach A significant improvement in 3D atom probe instrumentation occurred with the introduction of the LEAP [207, 218]. These instruments offered advantages including better data collection speeds, laser pushing, larger field-of-view, yield improvement, ease of operation. LEAP systems have been extensively used to investigate local chemistry features within alloys, such as the composition of particle inclusions, clusters from initial nucleation, chemical segregation induced by irradiation [219–225]. In these works, features are of the size of a few nanometres, and their compositions were revealed by APT with high chemical resolution. Therefore, it is natural to consider utilising LEAP to directly observe nanoparticles.

Initial work towards this goal started in the Oxford atom probe group, with Li et al. using APT to analyse Ag@Pd nanoparticles synthesised by a wet chemical reaction [42]. The particles were candidate alloys for the decomposition of formic acid to the selective production of hydrogen and CO, a very important reaction for fuel cell applications. The thickness of the Pd shell, which is crucial to the performance of such kinds of catalysts, was therefore examined by APT. The results clearly indicate a monolayer coverage of Pd on an Ag core, which is difficult to observe via other techniques.

A novel sample preparation method utilising electrophoresis was applied to enable quick sample preparation. The basic working steps of this method are depicted in Figure 2.3.13a.

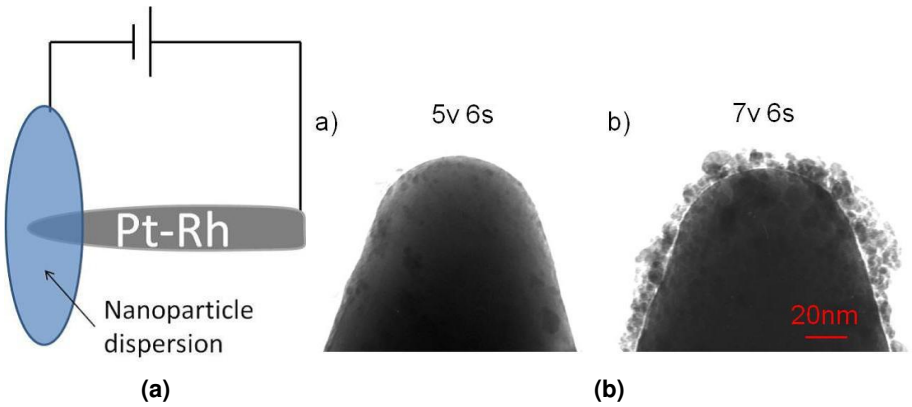

Figure 2.3.13 – (a) A Sketch showing electrophoresis method to deposit nanoparticle to the Pt-Rh specimen. (b) A TEM picture of a Pt-Rh tip before and after attaching nanoparticles [226]

Basically, a Pt-Rh substrate needle is inserted into a nanoparticle-containing solution, and then a DC current is applied for a time period ranging from a few seconds to dozens of minutes. This directly deposits a layer of nanoparticles onto the substrate needle apex. The outcome is depicted in Figure 2.3.13b. This method is a quick and relatively easy way to make the sample, however the disadvantage is that the subsequent APT analysis and reconstruction is difficult. This is because the tip after electrophoresis is very different from the ideal needle shape assumed in reconstruction algorithms, and thus ion spatial trajectory aberrations can cause a large distortion of shapes and distances in the analysis. However, despite these limitations with the reconstruction, Li et al. were able to demonstrate a monolayer coverage of Pd on an Ag core, restricting analysis to individual nanoparticles near the apex in a region of higher data quality.

Furthermore, other nanoparticle systems have been investigated based on this electrophoretic deposition method. Yu et al. analysed a $CuZnGaO_x$ catalyst [227], as this material is believed to be able to reform methanol into hydrogen and carbon dioxide. For this particular catalyst, there is believed to be an inverse relationship between Cu cluster size and the methanol-reforming activity. Therefore, APT was used to analyse Cu clusters within the bulk particle catalyst. APT data showed a good match with HADDF-STEM and XPS data, identifying two different types of Cu clusters. Furthermore it was found that the smaller clusters, with diameters around 2-2.5 nm, were more catalytically effective.

Li et al. conducted additional work characterising commercial carbon-supported Pt, Pt/Co alloy and Ir@Pt core shell structured nanoparticles [228]. These particles are smaller than 10 nm, and electrophoresis was again used to attach them in their supported form onto the apex of APT needles. While the reconstructions were again not straightforward, the atom maps of these nanoparticles and their relative spatial distributions indicated Na and Cl contamination as shown in Figure 2.3.14. In addition, Ir@Pt core shell particles were detected with significant structural intermixing. Overall, this work further proved the viability of using APT as a quality control method in catalyst industry, and efforts to build on this area appear promising.

The previous works are based on the specimen preparation method of electrophoresis, the advantage of which is the relative ease for making samples. However, the reconstruction remains problematic and the optimum electrophoresis conditions need to be determined for each system. As a result, not all nanoparticles from the work of Tedsree et al. [42] could be properly reconstructed. Finding a way to embed nanoparticles within APT needles, in order to achieve a higher quality reconstruction, is therefore desired, although this may require sophisticated sample preparation procedures. The most straightforward approach for this is to use an existing FIB lift-out procedure, as was originally explored by Larson et al.[229]. The preparation procedure is described in Figures 2.3.15, and it was designed for making specific samples, such as those containing a grain boundary. In this particular application, nanoparticles are embedded into the region very close to the apex of the needle. The reconstruction of the APT data is therefore much more accurate compared those from electrophoresis experiments.

Xiang et al. [230] published research on nanoparticles using the FIB-based sample preparation method. They investigated *CoCuMn* core-shell particles, which could be used in heterogeneous CO hydrogenation catalysis. Their detailed structure and chemical composition is shown in Figure 2.3.16. A core-shell structure of the particle is clearly observed with an indication of a faceted structure. The importance of this work is that a relatively good reconstruction of the nanoparticle is presented and the lift-out method for sample preparation

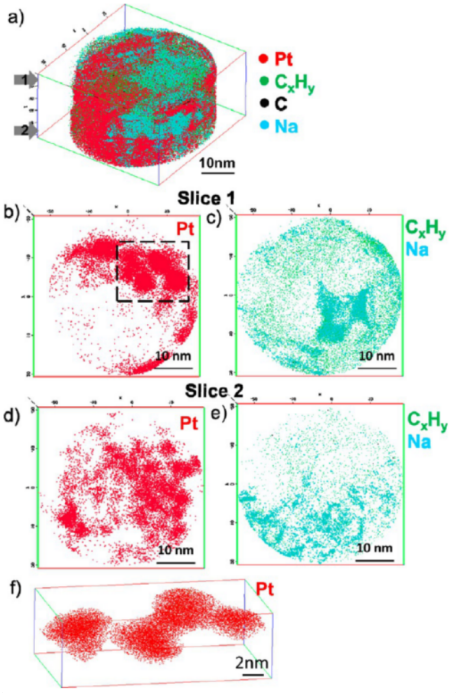

(a) (a) APT reconstruction of Pt nanoparticles on carbon support showing all species, (b) APT reconstruction (X–Y view) of the top 5 nm cross-sectional region marked 1 in part a showing ~7nm diameter Pt particles, (c) APT reconstruction (X–Y view) of slice 1 showing $CxHy$ and Na, (d) APT reconstruction (X–Y view) of the bottom 5 nm cross-sectional region marked 2 in part a showing ~3–4 nm diameter Pt particles at deeper porous structure, (e) APT reconstruction (X–Y view) of slice 2 showing $CxHy$ and Na, and (f) APT reconstruction of ~3–4 nm diameter Pt particles from the dashed rectangle box in part b. The Pt nanoparticles on carbon support were deposited onto the APT substrate at 20 V for 20 s.

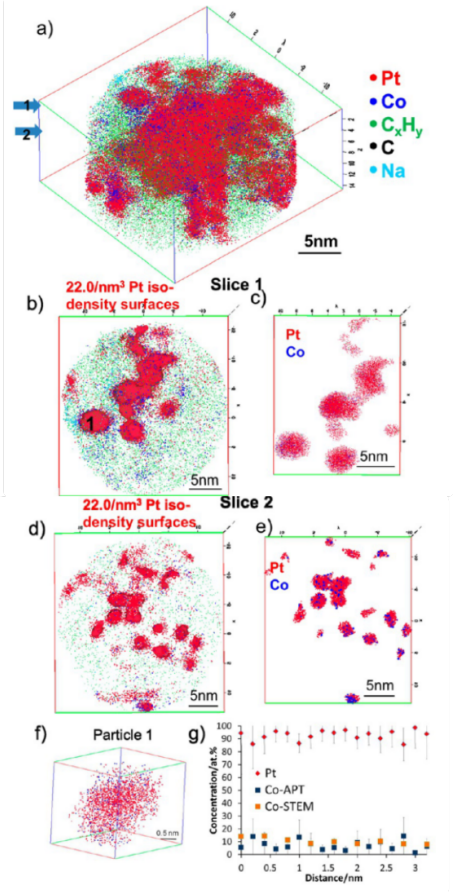

(b) (a) APT reconstruction of Pt/Co nanoparticles on carbon support with all species, (b) APT reconstruction of the top 3 nm cross-sectional region marked 1 in part a showing all species and Pt isodensity surfaces (53.0/nm3), (c) APT reconstruction of Pt/Co nanoparticles inside Pt isodensity surfaces in part b, (d) APT reconstruction of region 2 (z = 7.8–8.6 nm) marked in part a showing all species Pt isodensity surfaces (53.0/nm3), (e) APT reconstruction of Pt/Co nanoparticles inside Pt isodensity surfaces in part d, (f) particle 1 marked 1 in part b, and (g) 1D concentration profile of particle 1 in part f and separate STEM/EDX line analysis of particle 1 in Figure 1d for comparison. The Pt/Co nanoparticles on carbon support were deposited onto the APT substrate at 20 V for 15 s

Figure 2.3.14 – Carbon-supported Pt, Pt/Co commercial catalysts analysed by APT. [228]

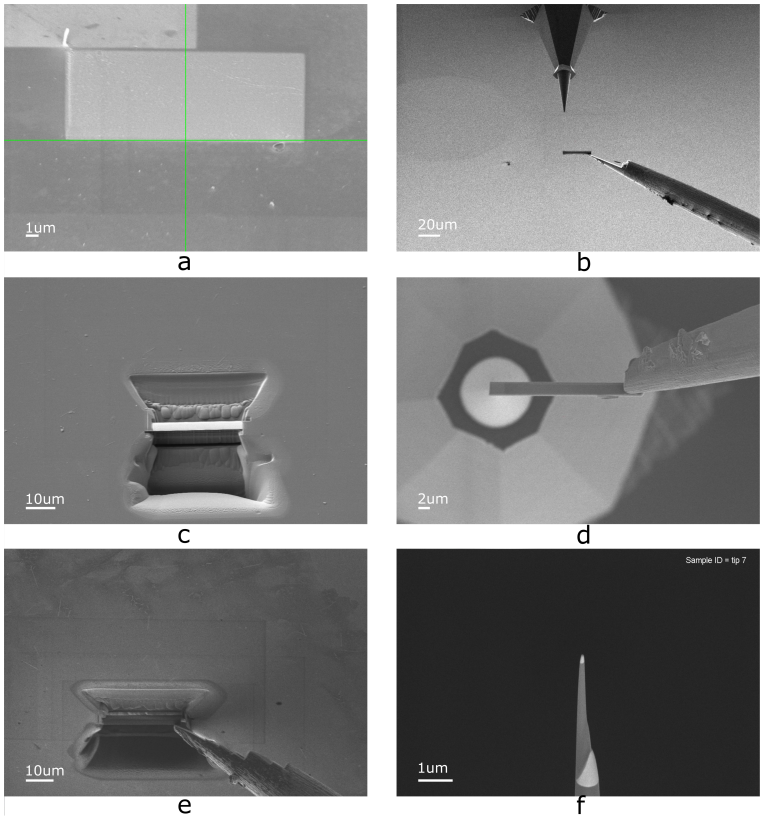

Figure 2.3.15 – FIB lift-out procedure shown in SEM

was proven to be viable although there was no direct report on the reproducibility of such sample preparation.

In the work by Felfer et al. [231] Au@Ag catalysts were investigated. The method used to mount the nanoparticles was similar to the procedure described in Figure 2.3.15. However, the orientation of the lift-out bar was changed by 90 degrees to make the deposition layer parallel to the direction of needles. This approach was aimed at maximising the number of nanoparticles which could be analysed through this way, due to the asymmetry in APT reconstructions, which are typically longer than in the horizontal direction. The nanoparticles themselves had a diameter around 20 nm, and Ag atoms were observed more concentrated on the areas of nanoparticles with high surface curvature. In addition, Na and N were also detected as contamination of the surface. Ag-rich regions were detected within the particle itself, although this could be an artefact since Ag can be highly mobile under

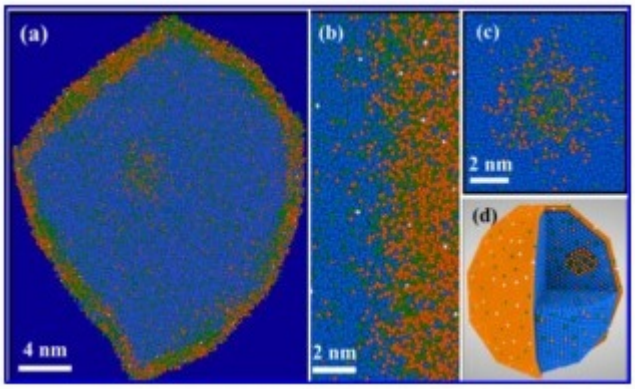

Figure 2.3.16 – The reconstruction of $CoCuMn$ nanoparticle. The blue colour ball indicates Co atom, the orange ball indicates Cu atom and the green colour ball indicates Mn atom. In (a), a cross-section of the nanoparticle is shown indicating a distinct core-shell structure. In (b), the magnified picture indicates the thickness of the shell is around 2nm. In (c) and (d), the small cluster formed within the core is shown (A simulation diagram) [230]

high fields [190].

A development of the FIB lift-out method was used by researchers involving direct particle deposition and encapsulation [232]. Inert gas condensation was used in both work. Folcke et al. made samples by continuous deposition of $PtFe$ nanoparticles and Cr. Larson et al. further developed this approach [233]. They utilised a technique called Atomic Layer Deposition (ALD) to produce encapsulation layers as shown in Figure 2.3.17. The composition of the layer (Al doped ZnO film) was tuned to match the evaporation field of these embedded nanoparticles. Felfer et al. also summarised a series of related sample preparation methods [234]. In Figure 2.3.18, nanoparticles were spread onto a fractured edge of a silicon wafer, as the faceted fracture surface of Si effectively produces a series of organised steps. Particles retained on these steps were then encapsulated and milled into samples. In Figure 2.3.19, a micro gripper was used to locate particles onto a Si cleaving step.

Other preparation methods include the direct growth of catalyst nanotubes, which was investigated by Moutanabbir et al. [235]. In this, a silicon nanowire whose growth was catalysed by aluminium nanoparticles was obtained, and the wire was subsequently investigated by atom probe. In the data analysis, one dimensional concentration profiles both along and perpendicular to the silicon nanowire indicated that Al was uniformly distributed in both directions (as shown in Figure 2.3.20). This work also reveals Al as a catalyst that could

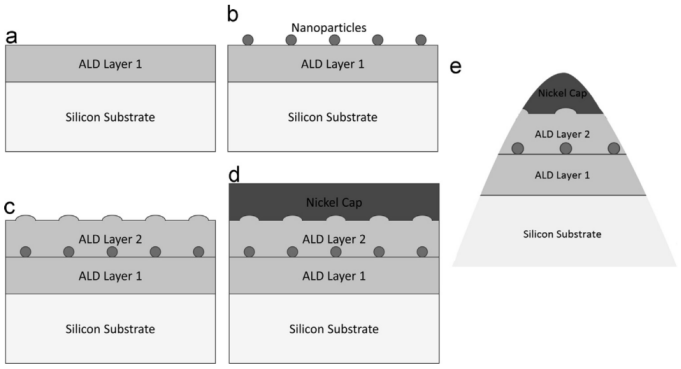

Figure 2.3.17 – Scheme showing method of encapsulation of nanoparticles using atomic layer deposition. In (a) an initial layer is deposited onto which the particles are deposited (b). (c) shows the second ALD layer which encapsulates the particles and an optional additional protective cap material (e.g. nickel) is shown in (d). The final structure after focused ion beam milling is shown in (e) [233]

uniformly dope silicon nanowires into a P-type semiconductor.

Apart from the research on various nanoparticles, Devaraj et al. [236] investigated the effect of the various evaporation fields between the analysed particle and its support, usually in a form of oxide. Due to the different evaporation fields, local magnification artefacts exist, which can induce inaccurate assessment of nanoparticle compositions [237]. It was therefore suggested the necessity of applying a locally variable evaporation field to correct the aberrations. Oberdorfer et al. investigated preferential evaporation phenomena by field evaporation simulation [238]. The aberrations were very prominent, and a more accurate reconstruction algorithm is needed to reveal the true sample shape. In addition, Vurpillot et al. claimed a thorough understanding of both the evaporation field and tip geometry evolution is necessary for a true reconstruction [239]. TEM correlative research is another feasible way to achieve suitable APT reconstructions [240, 241], where TEM images of features in pre-analysis atom probe tips can correct the reconstruction of atom probe data, an example of which is shown in Figure 2.3.21.

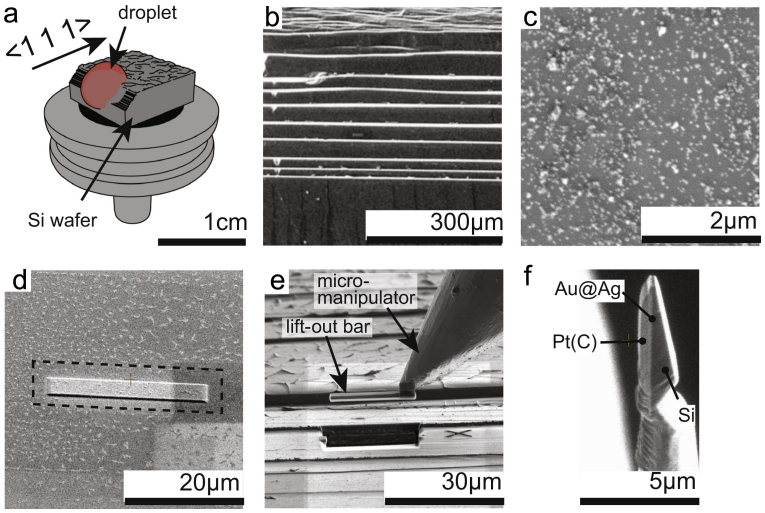

Figure 2.3.18 – Fabrication of atom probe samples from agglomerates of nanoparticles. (a) The experimental setup inside the FIB-SEM system. (b) Small particles agglomerate. (c) Particle agglomerate, lifted out and attached to Mo grid. (d) The sample after initial Pt(C) deposition, pyramid and annular Ga^{+} milling combined with deposition of Pt(C). (e) Final atom probe tip, imaged in SEM (SE) and TEM. Two larger particles are marked in the image. (f) Typical shape of a fractured atom probe sample produced by this technique. [234]

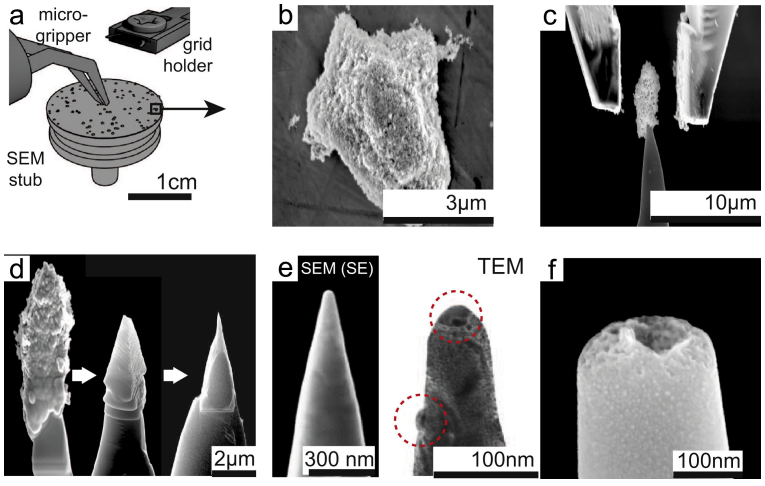

Figure 2.3.19 – Fabrication of atom probe samples from a dispersion of Au@Ag nanoparticles. (a) The experimental setup for the nanoparticle incubation. (b) Part of the Si wafer with cleaving steps. (c) An image showing the nanoparticle distribution. (d) The surface of a wafer step after deposition of 200 nm of Cr and a strip of ~400 nm of Pt(C). (e) Lifting out a bar of material, which is sliced into individual atom probe samples. (f) An individual sample on a Mo grid post, ready for final milling. [234]

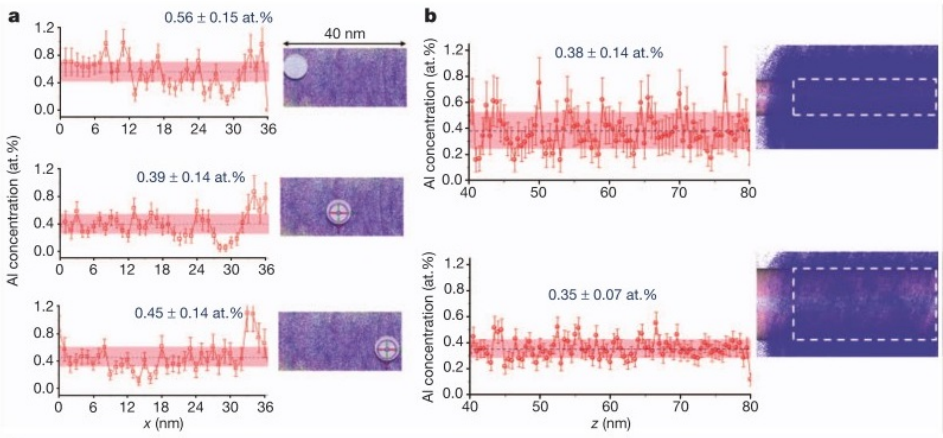

Figure 2.3.20 – Al concentration profiles in individual nanowires. (a), Al radial concentration profiles (left) measured in different regions of a Si nanowire. Each concentration profile is taken from a cylindrical segment having a diameter of 8 nm, as indicated in the images (right). (b), Al axial concentration profiles (left) measured for cylindrical segments (right) with a diameter of 10 nm (top) and 20 nm (bottom). The horizontal dashed line in all concentration profiles denotes the average concentration, which is given as blue numerals; the shaded band is the uncertainty interval; and error bars in (a) and (b) represent ±1s.d. The number of Al atoms in the sampling volumes varies between 2,000 and 4,500. [235]

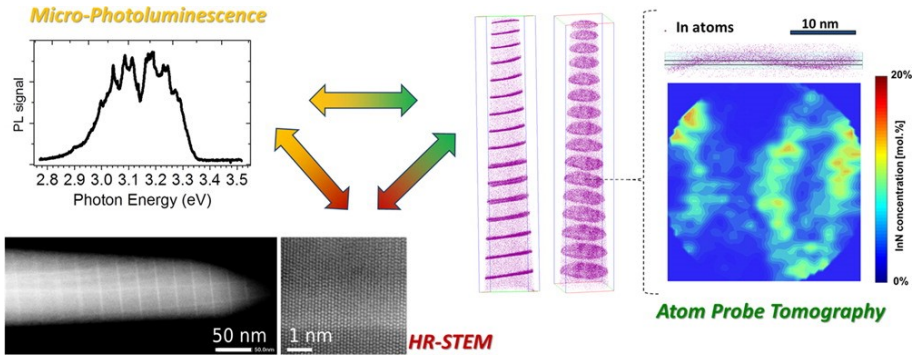

Figure 2.3.21 – A correlative research of TEM and APT on InGaN/GaN Multiquantum Well System [241]

2.4 Summary

In this literature review, Fe, Ni, Co and their alloys have been reviewed in terms of chemical reactions they can catalyse, surface oxidation of these metals and techniques used for probing these surface characteristics. As the major technique involved in this thesis, a comprehensive review of FEM, FIM and APT on nanoparticle research and tip research is presented. Through the literature, surface oxidation of alloys is summarised with some emphasis on the oxide composition and structure. For the nanoparticles, their structure and

composition segregation are also reviewed.

However, limitation of atomic level knowledge of the surface reconstruction and composition change is reported. Similarly, local composition segregation of nanoparticle is also of great importance. Therefore, further pursuit of atomic information of metal surface and nanoparticles is the main goal of this thesis. The particular technique involved is APT and with other complementary methods giving a deeper view of metallic surface and nanoparticles. A further challenge lies in the preparation and characterisation of nanoparticles, in order to limit artefacts in the analysis of the data.

Chapter 3

Materials and Experimental methods

This chapter is divided into two sections; the first section covering the details about sample preparation and the second describing the experimental methods used to analyse the produced samples. Two distinct forms of samples were investigated, acicular samples (i.e. needle-shape specimens) and nanoparticles. Preparation of these materials, to the stage where they were ready for analyses, is described in detail.

In the section describing experimental methods, operational parameters of all techniques utilised are detailed. This includes the field emission and field evaporation based-techniques of FIM and APT, respectively. Conventional atom probe image processing and data analysis is discussed. Other methods used to support analyses, including TEM, AFM, XPS, LEIS, and the relative benefits of all methods used for characterisation of catalytic materials are presented.

3.1 Materials and Sample Preparation

There are two main forms of materials which have been used as samples in this thesis: alloy wires and nanoparticles.

3.1.1 Alloy wires

In the case of the wire samples, *NiFe* and *NiCo* wires have been used with four distinct compositions. All wires were obtained from *Goodfellow* and their nominal compositions are listed in Table 3.1.1. Apart from Fe52Ni48, which was commercially available, the other three alloys were made by commission. The wire diameter is c.a. 0.5mm, which is an appropriate size for subsequent electrical polishing to prepare APT specimen. No thermal treatments were applied to the as-drawn wires before the electropolishing process.

Nominal composition wt.%	Ni90Fe10	Ni48Fe52	Ni10Fe90	Ni50Co50
Order status	By commission	Commercial	By commission	By commission
Contaminations	No	minimal	No	No

Table 3.1.1 – Four wire alloys investigated in this thesis. The contamination level information is from the supplier. no contamination means beyond the detection limit of APT upon on a dataset containing 10 million data points.

To transform the wire into a needle-shaped specimen on which oxidation/reduction experiments could be performed, a first step of electropolishing was applied. Setup of the electropolishing followed a conventional rota with two stages of electropolishing [242, 243]. A double-layer method was used for the first stage rough polishing. In the setup, Galden® (PFPE) was chosen as the inert layer, on top of which a 0.5 cm layer of the electrolyte was placed. This configuration of electropolishing enabled the formation of a bottleneck region in the middle of a wire specimen as illustrated in Figure 3.1.1. To create an ideal shank angle and sharpness, the sample was continuously moved up and down around the formed bottleneck region until the wire sample finally broke into two needles. After that, the samples were cleaned by distilled water and ethanol and then dried by compressed N_2 gas. The samples were then checked under optic microscope with up to X25 magnification.

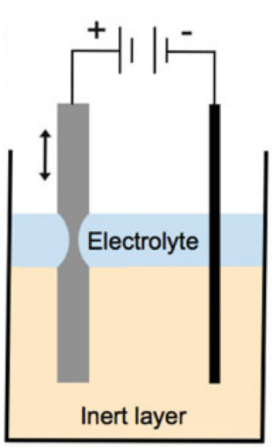

Figure 3.1.1 – Electropolishing setup for wire alloys in FIM/APT analyses. The double-layer method was used for the rough polishing.

If there was no observation of a round termination of the tip, the sample was considered sharp enough for subsequent analysis. If not, the sample was subjected to a secondary electropolishing under microscope. The details can be found in Gault et al. [242].

The conditions used for the first and second stage of electropolishing, respectively, are listed in Table 3.1.2. After electropolishing, the radius at the apex of the tip is expected to reach less than 100nm [243]. At this stage, the sample was ready to be analysed either via APT or to be imaged and cleaned via FIM. As an example of the tip size, TEM image of a polished Ni10Fe90 sample is shown in Figure 3.1.2. In this image, the tip radius is around 55nm, which is suitable for high field experiment. However, oxide species can be observed at the tip surface. This is a common phenomenon after electropolishing involving strong oxidising acid. The thickness of the oxide is about 4nm, which is sufficient enough to interfere with any subsequent oxidation experiment. Therefore, those oxides must be removed. The process of oxide removal is done by field evaporation via FIM.

Oxide cleaning is conducted by FIM using an Oxford Nanoscience 3DAP instrument. The as-polished sample mentioned above was loaded into the 3DAP vacuum chamber immediately after electropolishing to minimise oxide formation induced by air. After introducing the sample into the instrument, the load-lock of the 3DAP was pumped to UHV condition for subsequent analysis. The UHV condition also acted as a method to prevent

Polishing stages	Time	Voltage (DC)	Current(A)	Polishing Solutions
Stage 1	20 min	15-25V	0.01A	20vol% perchloric acid + 80vol% acetic acid*
Stage 2	5 min	10V	not measured	2vol% perchloric acid +98vol% 2-butoxyethanol

Table 3.1.2 – Electropolishing conditions used for preparing alloy wire samples. * For Ni abundant wires, 10 vol.% perchloric acid was used in stage 1 polishing to avoid surface pitting

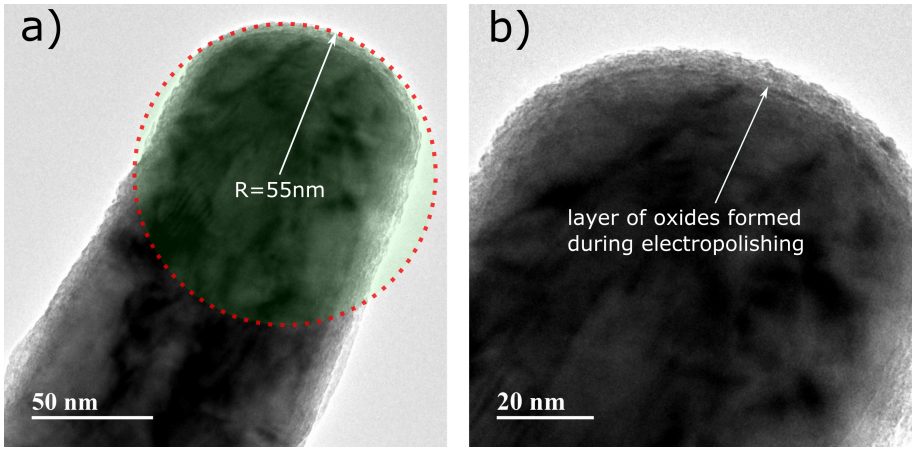

Figure 3.1.2 – TEM images of an electropolished Ni10Fe90 sample. The tip has a radius of c.a. 55nm as being marked in sub-figure a) and there is a layer of oxide formed on the sample surface shown in b). Identification of the oxide is based on the morphology difference between the layer and substrate. In addition, APT investigation confirms the existence of oxide.

further oxidation of those tips. Parameters used for the surface cleaning were: 50K base temperature, Ne imaging gas, base pressure $2 \times 10^{-5} mbar$, and high voltage with pulse functionality. Depending on the sharpness of the tip, the applied voltage used to trigger field evaporation varied from 3 to 8kV. The pulse applied was 1kHz and the magnitude ranged from 100 to 1000V. In Figure 3.1.3, an example of surface cleaning of Ni90Fe10 sample is shown. During the process, surface oxide was removed progressively and the metallic structure was revealed. According to the simulated FIM image, [1 1 1] zone axis was located in the image centre initially as shown in Figure 3.1.3a and then $<1\ 1\ \bar{1}>$ zones were revealed during cleaning as shown in Figure 3.1.3b.

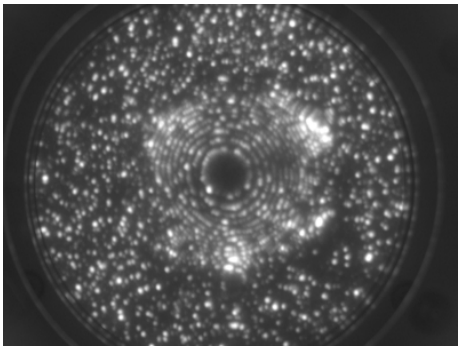

(a) Start of field evaporation. 50K, He, 4.1kV

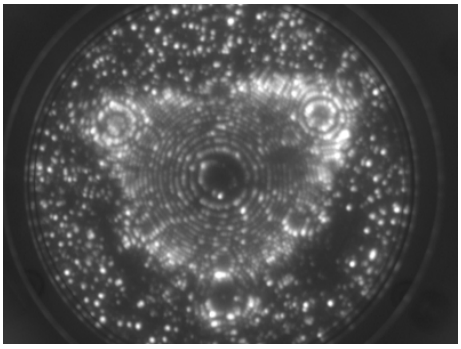

(b) Later on of field evaporation. 50K He, 5kV

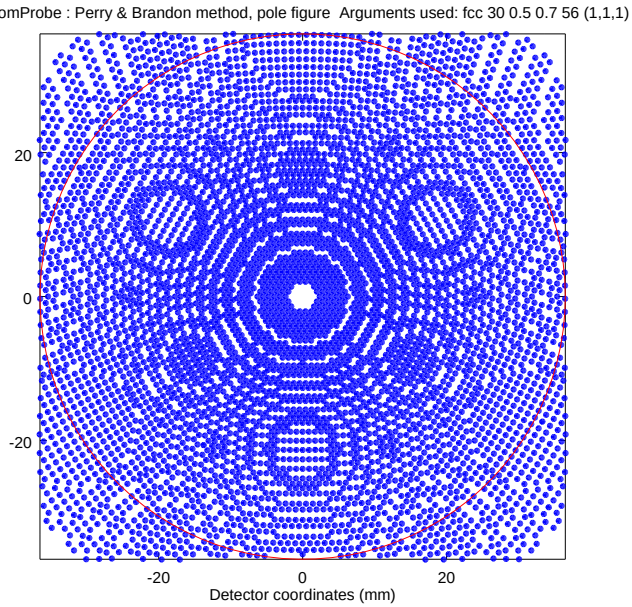

(c) Simulation FIM image of [1,1,1] direction of fcc structure. The red line in the figure indicates the nominal outline of the detector, which is 73mm in this case.

Figure 3.1.3 – FIM images from analysis of Ni90Fe10 sample during field evaporation cleaning process. Sub-figure a) and b) shows the progress of the cleaning process. With the reference shown in sub-figure c), the development of the fcc structure during the cleaning procedure is evident for oxide removal.

After the surface cleaning, samples were transferred to a specially designed reaction cell, which is attached to the 3DAP as shown in Figure 3.1.4. The transfer of the cleaned sample was under UHV condition; therefore no further contamination occurred at the sample surface [202, 213]. The sample after oxidation was then directly introduced into Cameca

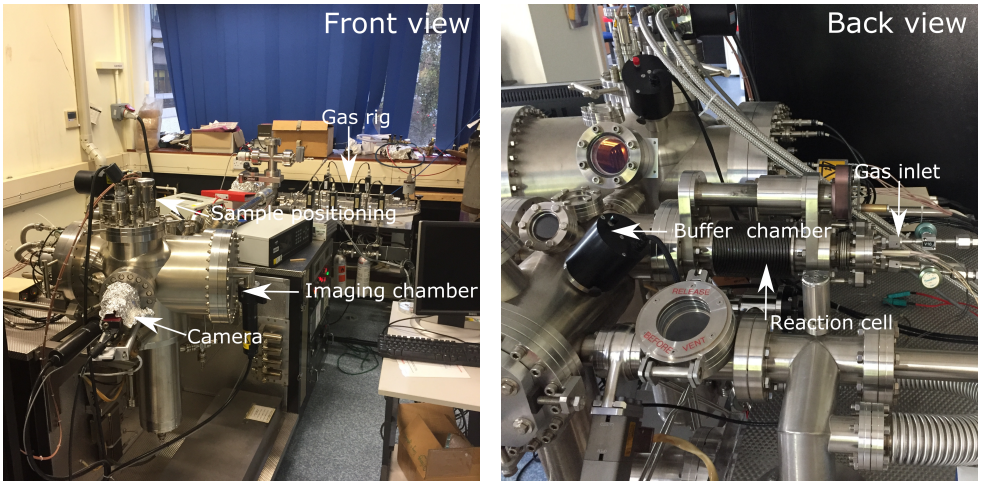

(a) Front view of 3DAP and reaction cell gas rig

(b) Back view of 3DAP with reaction cell

Figure 3.1.4 – 3DAP equipment utilised in this research together with the view of the attached reaction cell. [202]

LEAP 3000X HR or 5000XR for atom probe analysis.

3.1.2 Preparation of nanoparticles by chemical synthesis

Nanoparticles synthesised by chemical methods were used both to compare atom probe observations with alloy wire samples, and more generally to seek a controlled fabrication route for producing nanoparticles suitable for routine APT analysis. Deposition Precipitation by Urea (DPU) was the method involved for producing bimetallic particles with controlled size and composition. Ni-Fe based and Ni-Co based nanoparticles were fabricated by collaborators at University of Lille and UPMC, following the procedures that had been designed by them and that are conventional in heterogeneous catalysis [244–247]. Catalysts were supplied for the study thereafter. In Figure 3.1.5, particle samples produced are indexed with numbers.

The Ni-Fe silica-supported catalysts were all prepared via DPU. In a typical deposition precipitation process, metal salts are dissolved into an acidic solution and at room temperature. Acidity of the solution maintains the salt dissolved in the solution. By altering the pH value of the solution, metal containing salts will precipitate onto substrate. In this thesis,

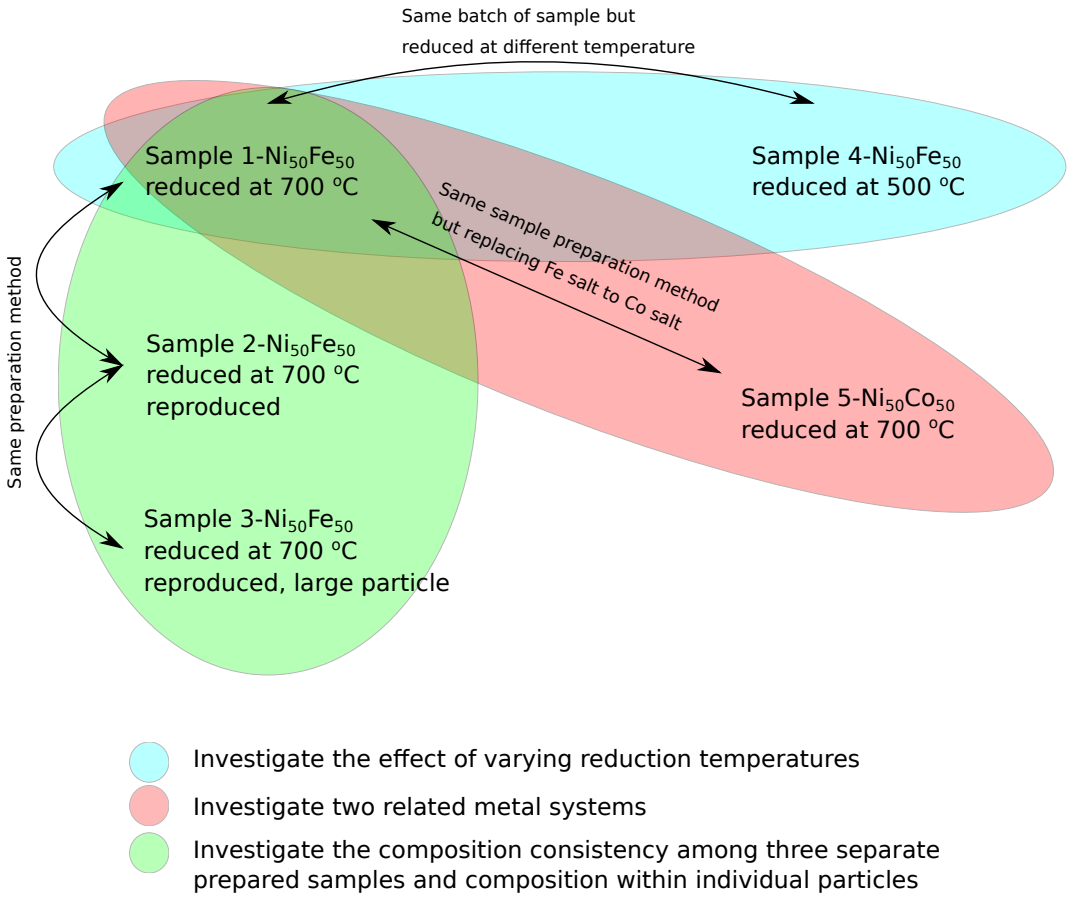

Figure 3.1.5 – Nanoparticles synthesized by DPU methods. There are 5 samples investigated for three tasks as indicated by three coloured circles

urea was used to adjust the solution pH value. Urea starts decomposing around 80°C and changes the solution pH value homogeneously in the solution. Therefore, the precipitation process was uniform within the solution. It is important to note that all the metals introduced in the solution do not necessarily deposit onto the support during DPU.

For producing $Fe50Ni50$ nanoparticles, a 150 mL aqueous solution of 0.84M urea (7.57 g), 0.02M sulphuric acid (0.16 mL, 96 wt%), and a total of 0.28M divalent metal salts was mixed in a flask with 1.14g of silica (Sipernat-50, Degussa, 475 $m^2.g^{-1}$). Metal salts used were iron (II) sulfate heptahydrate (99% normapur) and nickel (II) sulfate hexahydrate (99% Aldrich) (5.84 and 5.52 g respectively, for a Ni/Fe = 50/50 catalyst). All materials were used without further purification. The iron salt was added last to minimise Fe^{2+} exposure to potential oxidants, after a few hours of degassing of the aqueous suspension with Ar

bubbling. The suspension was continuously stirred under Ar bubbling and slowly heated to 80°C, resulting in urea decomposition, a rise in the pH to 5.3 after 5 h, and precipitation of Fe^{2+} and Ni^{2+} hydroxides and silicates onto the support. The solution was then kept at 80°C for 16-20 h. Absence of Ar degassing and bubbling (or presence of oxidizing species such as nitrates) would result in the oxidation of Fe(II) into Fe(III) upon heating, and in the precipitation of goethite $FeOOH$ at pH 2.6 (as detected by XRD), which later reduces into very large Fe nanoparticles. After cooling to room temperature, the solid was recovered by centrifugation (2 x 8000 rpm, 10 min), washed three times with degassed distilled water, then dried. When a dried system was kept in air without precaution, the catalyst turned from green initially to orange, indicating the oxidation of Fe(II) to Fe(III). The green colour was preserved longer when the system was dried under Ar flow and kept under Ar, however oxidation still occurred but very slowly (6 weeks). The catalysts were reduced by heating in 10% H_2/He (flow rate $55 cm^3.min^{-1}$) at a rate of $5°C.min^{-1}$ up to 500 or 700°C (plateau of 2 h), without any intermediate calcination. The total metal content was 22-25 wt%, as confirmed by Inductively Coupled Plasma Mass Spectrometry (ICP-MS). Similarly, the preparation for $Ni50Co50$ sample (marked as Sample 5) was made by the same method but replacing iron (II) sulfate heptahydrate with cobalt(II) sulfate heptahydrate. Only metal sulfates were used as the precursors because, unlike nitrates, sulfate ions did not oxidise iron (II) into iron (III), otherwise a vast difference in precipitation pH between Ni^{2+} and Fe^{3+} would induce preferential precipitation of iron(III) hydroxides.

Those as-fabricated nanoparticles were then analysed by TEM by the author in Oxford. In order to prepare a TEM sample, the catalyst grains were dispersed into methanol to a low concentration via ultrasonic mixing. Then, a small proportion of suspension was transferred to a Cu grid coated with 400 mesh carbon film by pipette. Then, the grid was dried at room temperature until methanol evaporated. After that, these grids were kept in vacuum until TEM analysis.

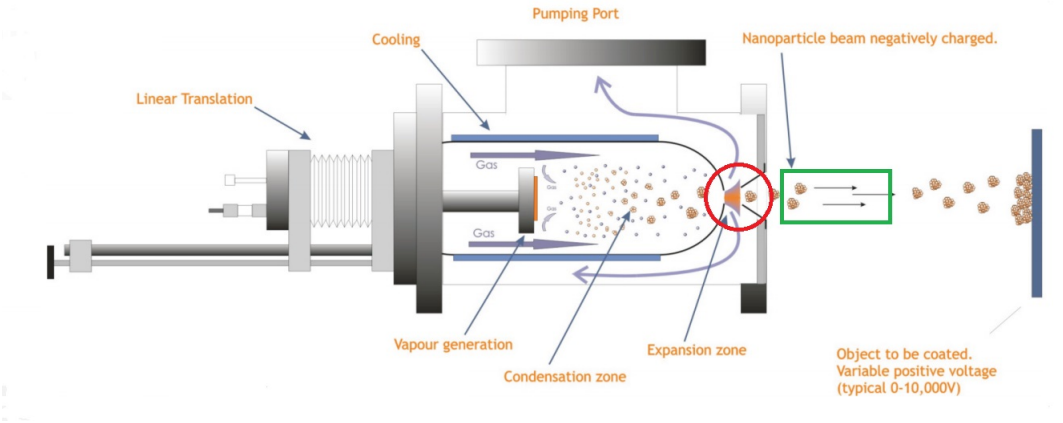

Figure 3.1.6 – Schematic configuration of the Mantis Nanogen 50 source. The circled red area is the zone where pressure drop occurs and particles are expelled. The rectangular green area indicates the location of mass spectrometer, used to filter charged particles. (Courtesy Mantis Deposition Ltd.)

3.1.3 Preparation of nanoparticles by physical deposition

Monometallic and multimetallic nanoparticles were prepared by Inert Gas Condensation method (IGC) with collaboration with Mantis Deposition Ltd. [248–251]. The motivation for the use of this method is to seek an optimised sample preparation route compared to chemical methods for atom probe nanoparticle research. In detail, IGC is a technique based on physical deposition under vacuum. A schematic diagram of the IGC apparatus is shown in Figure 3.1.6 [252, 253]. As shown in the figure, the deposition apparatus is a vacuum system comprising a plasma region, condensation region and deposition region. In the plasma region, magnetron plasma created by inert gas (Ar and/or He) was used to bombard a metallic target forming metal ion plasma (the detailed configuration of the metal target loading head is shown in Figure 3.1.7). A DC power supply is used to sustain the plasma. Metal ion plasma is then driven through confined aperture via differential pumping. Through this process, metal ions nucleate together forming nanoparticles. The formed particles further travel towards the substrate, during which mass filter is applied to select nanoparticles with desired size. Overall, the advantage of IGC is that particle composition and size can be controlled to a high level.

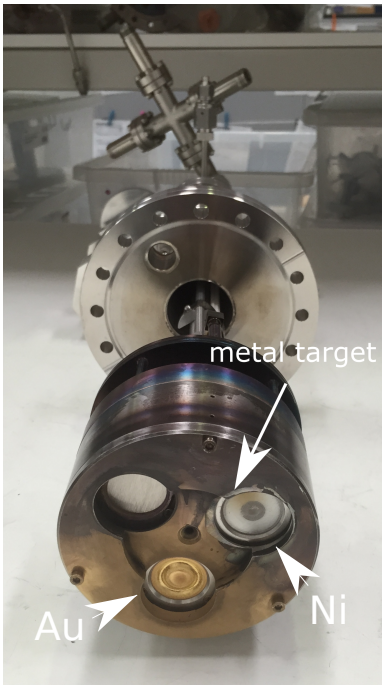

Figure 3.1.7 – Plasma head with two metal targets loaded to produce bimetallic nanoparticles. Metal target of yellow colour on the picture is gold and Ni is the silver coloured target.

In this thesis, one single target, two targets and three targets were activated respectively to create monometallic and multimetallic nanoparticles. Mixing of these plasmas occurs in the condensation region. A constriction in the outlet of the condensation zone creates an elevated stagnation pressure inside the chamber on the order of a few tens of Pascals, equivalent to a mean free path of a few tens of micrometres. The large number of collisions in this region thermalises the vapour, promoting the nucleation and subsequent coalescence of nanoparticles. An expansion zone (circled in red in 3.1.6) creates a rapid pressure drop where excess carrier gas is pumped away through the differential pumping port, and a nanoparticle beam emerges. A number of available parameters were explored to understand their influence for APT samples including sputtering power, aggregation length, inert gas flow rate, stagnation pressure, and chamber wall temperature. Parameters used to fabricate nanoparticles in this thesis are listed in Table 3.1.3. In these manufacturing processes, the same power input on individual metal targets was used in an attempt to reach balanced compositions. However, caution was taken as power input is merely one of those factors affecting final particle composition. To simplify the context, techniques used to probe those as-produced nanoparticles are also listed in Table 3.1.3.

Batch No.	1*	2	2	3	3	3
Running Conditions	Ag	AuCu	AuCuMo	AuNi	AuNi with He	AuNiMo
Base Pressure	4×10^{-6}mbar	1×10^{-6}mbar	3×10^{-6}mbar	4×10^{-7}mbar	3.7×10^{-7}mbar	4×10^{-7}mbar
Argon flow rate	100sccm Ar	60sccm Ar	60sccm Ar	60sccm Ar	40sccm He	60sccm Ar
Pulsed DC Power	20kHz, 1μs, 100W (0.34A, 298V)	Au-60mA, Cu-60mA	Au-60mA, Cu-60mA, Mo-20mA	Au-60mA, Ni-60mA	Au-60mA, Ni-60mA	Au-60mA, Ni-60mA, Mo-60mA
MesoQ filter	10nm	6nm	-	-	-	-
Substrate Bias	0.5kV	-	-	-	-	-
Deposition Rate	60ng/s	2.4ng/s	3ng/s	0.24layer/min	0.17layer/min	0.2layer/min
Deposition Time	45s	4.6min	4.5min	3.25min	4.5min	4min
HRTEM imaging	-	✔	✔	✔	✔	✔
EDX	-	✔	✔	-	-	-
APT	✔	✔	✔	✔	✔	✔
LEIS	-	-	-	✔	✔	✔
AFM	-	-	-	✔	✔	✔
XPS	-	-	-	✔	✔	✔
SEM	✔	-	-	-	-	-

Table 3.1.3 – Operation parameters of IGC for preparing nanoparticles in this thesis. 6 batches of nanoparticles were made, from monometallic to multimetallic types. *Sample of batch 1 was deposited by Dr Paul Bagot in 2012.

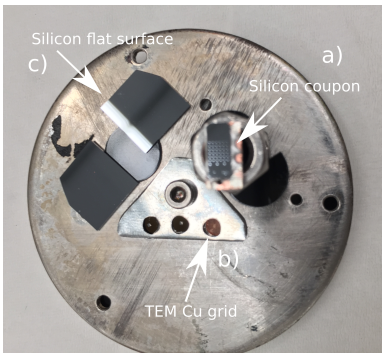

Figure 3.1.8 – Sample loading stage for AuNi and AuNiMo particle deposition via IGC method. There are three sample formats produced a) Silicon coupon for atom probe research b) TEM grid for TEM and c) silicon flats for AFM, LEIS and other techniques. It is important to realise that all the analyses later on are based on the same batch of particles, so the results are directly comparable.

Size selection One of the advantages of this method is having accurate mass selection of as-produced nanoparticles [254]. The mechanism that allows the size selection is explained as follows. During the fabrication process, a large fraction of nanoparticles becomes charged as the consequence of passing through a plasma in the condensation area. The resulting charge state is a function of the experimental conditions, but generally a large proportion of the nanoparticles (>70% for Ag case) have a single negative charge, meaning the total flux remains quite high even after mass filtering. A quadrupole can therefore be used to filter nanoparticles by their mass-to-charge ratio [255]. The quadrupole mass filter is attached after the expansion zone (represented as a green rectangle in 3.1.6). In order to mass-select nanoparticles, AC and DC voltage was applied to four straight metal rods inside the quadrupole. Any ionised nanoparticle passing through the rods is forced into an oscillating path. For a given AC frequency and amplitude, only one mass (within the resolution of the instrument) continues on a stable oscillating path and other masses are rejected. In this way, particles having a mass-to-charge-ratio match with a predetermined value will make their way through the quadrupole and on to the substrate. During th operation, the mass filter scans through the entire mass distribution range, creating a deposition with controlled particle size distribution. Detailed threshold set parameters are listed in Table 3.1.3. To collect the particles, the sample stage was loaded with various substrates into the vacuum deposition chamber, directly under the path of particle cluster beam. In Figure 3.1.8, a silicon flat surface (for AFM, LEIS), silicon coupon (for APT) and TEM Cu grid were loaded together. A variety of experimental investigations can thus be carried out on the exactly same batch of particles. The mass filter used in this thesis is produced by Mantis Deposition ltd. with a brand name Meso-Q. Its filting range is $350 - 10^6$amu with a resolution $\pm 2\%$.

Controlling the coverage onto the substrate surface during particle deposition is crucial for accurate characterisation. As shown in Figure 3.1.9, particles were deposited onto the surface at less than 100% coverage. This was designed to prevent particle overlap with each other, which might create voids between particles during subsequent coating steps.

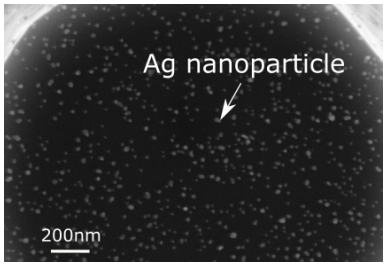

Figure 3.1.9 – SEM image of Ag particles deposited on the top-flat surface of a new silicon coupon. The distribution of Ag on the top is kept sparse intentionally.

The formation of voids is unfavourable for atom probe analysis and results in significant detriment to the data quality [233]. The most effective way to control the deposition was to use a quartz crystal micro-balance (QCM) [256]. A QCM measurement was taken prior deposition, from which the rate of the deposition was calculated (ng/s). Then, the deposition time was calculated for forming a sheet with a sparse distribution of particles. However, it also requires that particle loading should be sufficient so that the mean nearest neighbour distance should be smaller than typical analysis dimensions for an atom probe experiment.

For AFM, XPS, LEIS and TEM analyses, as-made samples can be analysed directly without any further process whilst additional coating and FIB milling are required for APT. During the nanoparticle manufacturing procedure, particles were directly deposited on the top of a silicon post, making the post as a ready-made specific site for specimen preparation. An Ag coating was then applied by either magnetron deposition or ebeam deposition (normal operation conditions), as shown in Figure 3.1.10. The decision to select Ag as the coating layer is due to: a) Ag has only two isotopes available and neither overlap with Au, Ni and Cu peaks in the APT mass-to-charge-state spectrum; 2) Ag has a low evaporation field relative to the materials of the particle or substrate layer 3) Ag is not vulnerable to oxidation and hence can protect the capped particle from oxidation. After application of a pre-coating Ag layer, only FIB sharpening is required to derive analysis-ready samples.

FIB-SEM has been a commonly utilised method by which to produce atom probe tips with site-specific requirements [229, 257]. In a Dual Beam FIB system, there are two sources to image the sample from two angles (54º apart): electron beam and Ga^+ beam. The electron beam is extracted via thermic emission of LaB_6 crystal. Ga^+ ions are extracted from a liquid metal source and usually accelerated by 30kV within an ion column, focused

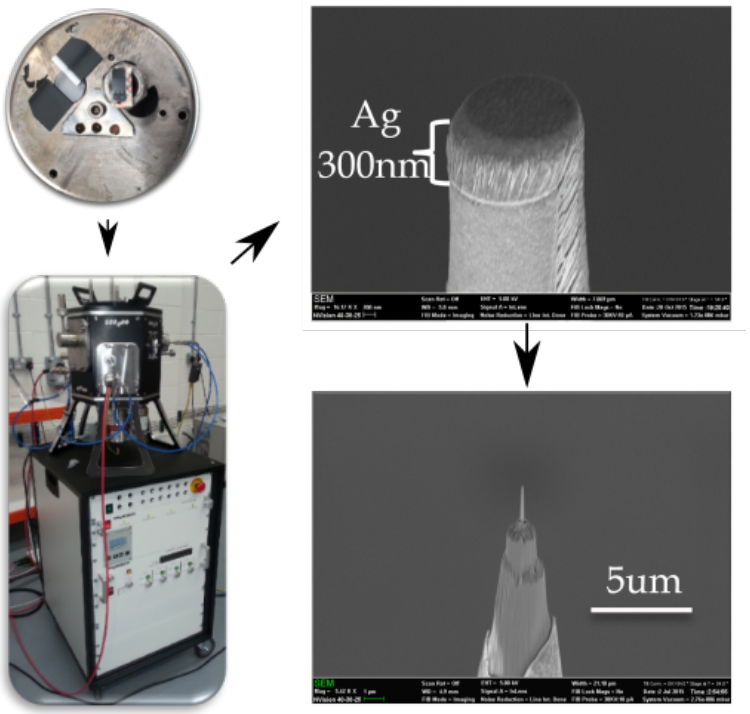

Figure 3.1.10 – Sample coating procedure for the nanoparticles. Silicon post after deposition was placed upside down in the deposition machine. Magnetron coating was applied to the silicon post having a thickness c.a. 300nm. FIB milling applied to the flat surface producing a shape tip with a radius less than 100nm.

and projected onto sample surface by electrostatic lenses. The imaging mechanism of these two beams are the same. The beam is guided by electromagnetic lenses to perform scanning across sample surface, generating secondary electrons to form images. Depending on the area that the beam scans, varied resolution could be achieved. In this research, a 5kV accelerated e-beam was used to conduct imaging. Similarly, 30kV Ga^+ beam was used to do imaging with similar working mechanism. However, because of the high kinetic energy of the Ga^+ ions, atoms of imaged sample could be sputtered under impact, the result of which is that Ga^+ beam is instead used as a milling tool. During a typical operation, the ebeam is used to observe the milling process to ensure accurate sample cutting. It should be noted that the more intensive lift-out procedure was not utilised in this thesis due to the simplification of particle deposition directly onto silicon posts. A Zeiss Nvision dual beam FIB-SEM was used in this thesis. There were three steps involved during the milling

Step	Voltage	Current	Time	Profile
1 doughnut shape cutting	30kV	150pA	250sec.	line width $1.8\mu m$, height $5\mu m$
2 annular milling	30kV	10-40pA	dwelling 1-$10\mu s$	outer radius $2\mu m$, inner radius $0.1\mu m$
3 low energy cleaning	2kV	10pA	varies	light cleaning subject to conditions

Table 3.1.4 – Parameters used for FIB to mill embedded nanoparticle samples.

process: 1) doughnut shape cutting 2) feature milling (annular milling) and 3) low energy cleaning. The parameters used are listed in Table 3.1.4.

3.2 Field Ion Microscopy

Field Ion Microscopy (FIM) is a technique that can reveal the structure of materials at the atomic level. It involves high field emission which can be understood most readily in its predecessor, Field Emission Microscopy (FEM) [258]. Fowler et al. [259] predicted that an electron tunnelling effect in hydrogen could happen once the field strength exceeds $10 V nm^{-1}$. However, it is not common to obtain such a high field. A sharp tip can enhance field emission, by production of a very high electric field at its apex through an applied high voltage. In 1935, Müller applied high negative voltage on very sharp tip (radius less than 100nm) in vacuum, obtaining strong field enhancement and creating field emission of electrons. The field, F_0, at the apex of a sharp needle-shaped specimen is given by

$$F_0 = \frac{V_0}{k_f r_0} \tag{3.2.1}$$

where V_0 is the applied potential, r_0 is the end radius of the tip and k_f is known as the field factor, accounting for the shape of the specimen, and usually has a value of approximately 3 in this case [260]. With the specimen biased negatively, the field is sufficient to trigger electron emission by quantum tunnelling. Emitted electrons are projected onto a fluorescent screen located a few centimetres away from the sample tip in the vacuum system converting

the electron current into a visible pattern representative of the arrangement of atoms on the surface at the apex of tip. The technique was coined as field emission microscopy (FEM)[258]. Normal conditions for the FEM experiment are : a local field of the order of $1 V nm^{-1}$, and an apex radius in the order of 10^{-6}m.

Further development of FEM led to the invention of FIM. FIM involves a setup similar to FEM and incorporates high field ionisation of an imaging media, usually noble gas molecules, such as He, Ne or Ar. Ionisation of these noble gas molecules is believed to occur by electron quantum tunnelling when they are adsorbed onto a positive-biased surface under a high electric field. To image, the inert gas is introduced into the UHV chamber to a pressure around $10^{-5} mbar$. The gas molecules become polarised under the high electric field and are attracted to the sample surface. During this process, the molecules lose a fraction of their kinetic energy and become increasingly thermally accommodated to the surface at the apex region of the sample. As a result a layer of gas molecules progressively forms above the sample surface, especially as the sample temperature is held at typically cryogenic conditions. Adsorption created by this process is thus stronger than pure physical adsorption. When the electric field is sufficiently strong, quantum tunnelling can occur and imaging gas atoms from within the closest layer to surface become ionised. Ionised gas molecules are removed from the surface by the intense electric field, and projected by the highly diverging field lines onto a detector, in the form of a micro channel plate (MCP) fluorescence screen, revealing an image of the specimen surface. A schematic diagram is shown in Figure 3.2.1, along with a FIM image of a Ni50Co50 alloy sample, investigated in this thesis. Each single bright spot on the image represents the signal emitted from a single atom. The emitted bright spots form concentric rings, which represent the atomic terraces of prominent crystallographic planes at the surface due to the very high local curvature of the sample. High spatial resolution is thus achieved by this technique, such that individual atoms are able to be resolved. The limit to spatial resolution of FIM is dependent on several factors including size of the ionisation zone (i.e. the highest above the surface in which ionisation can be induced), lateral velocity of the imaging gas, and positional uncertainty

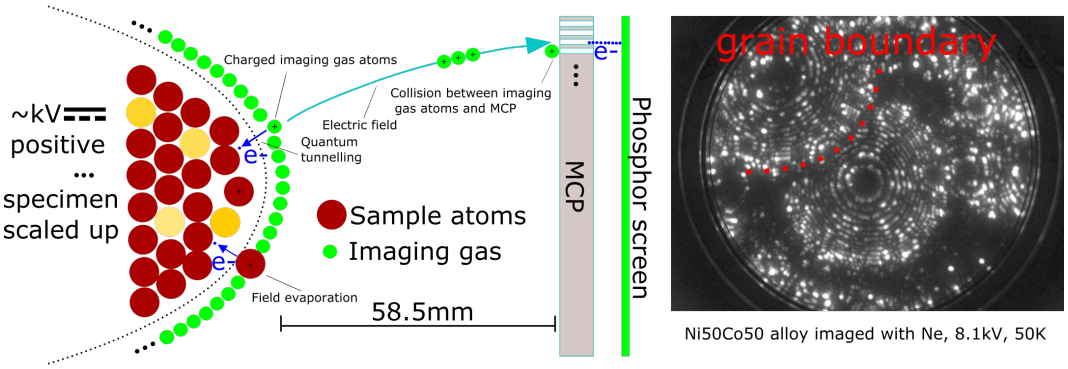

Figure 3.2.1 – Working mechanism of FIM and resulting image of a Ni50Co50 alloy tip. The distance between the tip and MCP is representative for Oxford Nanoscience 3DAP. A grain boundary is revealed between two major crystallographic poles.

[261]. Temperature has strong effect on the positional uncertainty and therefore should be kept as low as possible. In general, a higher electric field and smaller tip radius will lead to better resolution. The best FIM resolution (on metal sample) normally achievable is about 0.2nm with He at 20K [242].

3.3 Atom Probe Tomography

3.3.1 Basic principles

Atom Probe Tomography (APT) is a technique based on field ionisation and evaporation. The basic working mechanism is similar to FIM but imaging gas is not utilised in APT. Instead, a slightly higher standing voltage along with a voltage or laser pulse is applied to trigger field evaporation of the outer surface sample constituent atoms. In Figure 3.3.1, the relationship between the effective evaporation field (in grey) with field pulsing and thermal pulsing is illustrated. Field pulsing is created by pulsing the applied voltage to a local electrode (Fig. 3.3.3) located in front of the sample, while thermal pulsing is achieved by directly illuminating the tip with a nanosecond-pulsed laser beam.

During analysis, a high (~2-10kV) voltage is applied to the sample to maintain a base electric field on the sample tip, the amplitude of which is not sufficiently strong to trigger

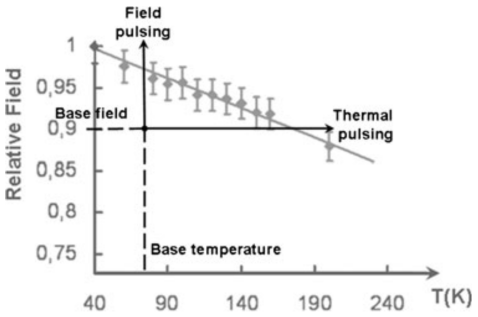

Figure 3.3.1 – Schematic diagram of field with relationship to sample temperature, field pulsing and thermal pulsing. The grey line represents effective evaporation field, above which field evaporation could be triggered. [242]

field evaporation. The pulse (either voltage or laser-based) is supplied to create conditions necessary for field evaporation. Usually, the intensity of the field is moderated such that only one evaporation event is triggered amongst several pulses. For the particular pulse that generates a field evaporation event, the time is measured between the initiation of the pulse and when the position-sensitive digital detector receiving an ion signal. Since the path that a single ion needs to travel from the tip to the detector is fixed, the mass-to-charge-state ratio of that ion can be calculated through equation 3.3.1.

$$\frac{m}{n} = M \approx 2eV(\frac{t_{flight}}{L})^2 \tag{3.3.1}$$

where m/n is mass-to-charge-state ratio (M), V is the electric potential between the sample and electrode, t_{flight} is the flight time of ions, and L is the flight path from the tip to the detector. Initial development of atom probe could only allow ions emitted from confined location on the sample to be analysed and thus it was called 1D atom probe [262]. The introduction of position sensitive detectors then enabled the measurement of 2D lateral coordinates of where evaporated ions strike the detector [206]. The information of each evaporated ion is recorded including X_D, Y_D coordinates, time-of-flight, and sequence of evaporation. Based on this information, the relative real-space 3D ion positions from within the original sample can be estimated utilising a reconstruction algorithm. In general, the reconstruction procedure is a two-step process, in which the lateral positions are computed prior to the z coordinate [263]. In Figure 3.3.2, a prominent early protocol proposed by Bas et al. [264]

is shown, where the determination of the lateral coordinates is presented. The first step is to determine the magnification (assuming ξR term is too small comparing to L):

$$M_{proj} = \frac{D}{d} = \frac{l + \xi R}{\xi R} \approx \frac{L}{\xi R} \tag{3.3.2}$$

where L is the distance between the tip and the detector, ξ is known as the image compression factor, and R is the radius of the tip. The algorithm assumes ions are projected along a straight path once departed from the sample, and hence the real-space location of the ions on the surface (x, y) can be derived from the detector position (X_D, Y_D) with a relationship as:

$$x = \frac{X_D}{M_{proj}} \; and \; y = \frac{Y_D}{M_{proj}} \tag{3.3.3}$$

ξ in function 3.3.2 is an effect to the ion trajectories due to the electrostatic environment and can be estimated using :

$$\xi \approx \frac{\theta_{crys}}{\theta_{obs}} \tag{3.3.4}$$

where θ_{crys} is the theoretical angle between two crystallographic zone axes, and θ_{obs} is this same angle as observed on the APT detector, which is derived from function:

$$\theta_{obs} = arctan\frac{D}{L} \tag{3.3.5}$$

Finally, R in function 3.3.2 (the radius of the tip) can be determined from the function:

$$R = \frac{V}{k_f F_e} \tag{3.3.6}$$

where k_f is the field factor and F_e is the evaporation field for a given material. k_f is usually assumed to be constant for one experiment and it is strongly associated with the sample's shank angle [265]. By monitoring the voltage, the radius can be estimated instantaneously throughout the experiment.

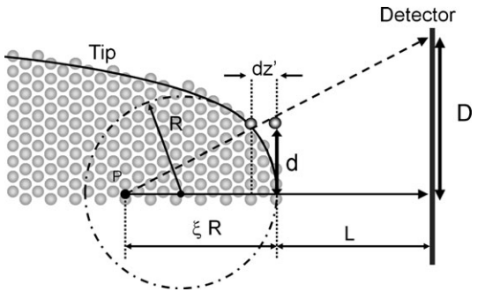

Figure 3.3.2 – Bas et al. Protocol for atom probe data reconstruction. [264]

After deriving the lateral coordination, Z coordinates are calculated. As one of the crucial input, the tip radius is needed and there are two methods to calculate it: one uses the local field which is shown in Equation 3.3.6 and the other is by introducing a parameter called shank angle α. This approach is based upon estimating how the specimen evolves as atoms are systematically removed from the surface [266] and the function is:

$$R = R_0 + \frac{sin\alpha}{1 - sin\alpha} z \tag{3.3.7}$$

where R_0 is the initial radius, z is the coordinate and α is the shank angle. Then, z direction is derived assuming that ions are from the emitting tip surface with a position Z_{tip}. The emitting surface progressively retreats with a small increment dz proportional to a nominal atomic volume Ω . The could be expressed as:

$$Z_{tip}^{(i+1)} = Z_{tip}^{(i)} + dz = Z_{tip}^{(i)} + \frac{\Omega}{\eta w_v(z)} \tag{3.3.8}$$

where η is the detector efficiency, $w_V(z)$ is the increase in the volume of sample that has been analysed. Discussion in the existing literature about reconstruction focuses significantly on various estimation of $w_V(z)$. η is highly dependent on the instrument. In this research, both LEAP 3000X HR and LEAP 5000XR were used and η values is 37% and 52%, respectively. According to Bas et al. protocol, $w_V(z)$, which is represented by S_a, is derived utilising small angle approximation :

$$S_a = \frac{S_D}{M^2} \tag{3.3.9}$$

where S_D is the area of the detector. In this protocol, ion positions are constructed in the plane normal to the specimen apex. A term is added to accommodate the curvature of the specimen, which is named the curvature correction dz', as:

$$dz' = R(1 - \sqrt{(x^2 + y^2)/R^2}) \tag{3.3.10}$$

And finally, the in-depth coordinate is

$$z = (\sum dz) + dz' \tag{3.3.11}$$

To improve the accuracy, Geiser et al. developed a methodology without small angle approximations but utilising shank angle α, which is a term to describe the sample geometry [264]. In Gault et al. protocol has a further extension on the Bas et al. protocol and provides a amended estimation of $S_a = 2\pi R^2(1 - cos\theta_D)$, where θ_D represents total field-of-view for the semi-spherical tip geometry [267]. In this thesis, it is the Gault et al. protocol used for data reconstruction in the Cameca IVAS programme.

These formulas summarise the core working mechanism for reconstructing data from a modern atom probe. There has been also major improvement in recent years to the instrumentation, especially the application of local electrodes [207, 268, 269], reflectron lens (as shown in Figure 3.3.3) [270], laser pulsing [271, 272] and wide-field-of-view detectors [206]. The implementation of a local electrode, which is the counter electrode placed close to the tip. As the result, the electric field produced at the specimen apex by given voltage is enhanced [273]. The electric field applied on the specimen creates a force and courses mechanical stresses, which causes the sample fracture prematurely. As the field is reduced by the implication of local electrode, sample fracture rate is then reduced [274]. A reflectron acts as an electromagnetic lens that focuses ions in time and space by providing energy compensation to ions according to varying mass-to-charge-state ratios. A schematic diagram of the reflectron is shown in Figure 3.3.4. Considering an ion with mass m, charge ne, initial acceleration potential V_t and small energy variation δ, the ion energy can be expressed as:

$$E = \frac{1}{2}mv^2 = neV_t(1+\delta) \tag{3.3.12}$$

Given the incident angle of ion α_{inc}, then the speed of ion along with axial of the lens is:

$$v_x = v\,cos\alpha_{inc} = \sqrt{\frac{2neV_t}{m}}\sqrt{1+\delta}\,cos\alpha_{inc} \tag{3.3.13}$$

Therefore, the flight time of ion within the reflection is:

$$t_r = 4d_r\frac{V_t}{V_r}\sqrt{\frac{m}{2neV_t}}\sqrt{1+\delta}\,cos\alpha_{inc} \tag{3.3.14}$$

Where d_r is the distance travelled within the reflectron and V_r is the potential within the reflectron. The distance the ion travels outside the reflectron is $ds = d_1 + d_2$ and the total time the ion travels can be written as:

$$t \approx \frac{d_s}{cos\alpha_{inc}}\sqrt{\frac{m}{2neV_t}}(1+4\frac{d_r}{d_s}\frac{V_t}{V_r}cos^2\alpha_{inc} - \frac{\delta}{2}\left[1-4\frac{d_r}{d_s}\frac{V_t}{V_r}cos^2\alpha_{inc}\right]) \tag{3.3.15}$$

When $V_r = 4V_t\frac{d_r}{d_s}cos^2\alpha$, the impact of energy variation δ is no longer affecting the total travel time and therefore increases the mass resolution [270].

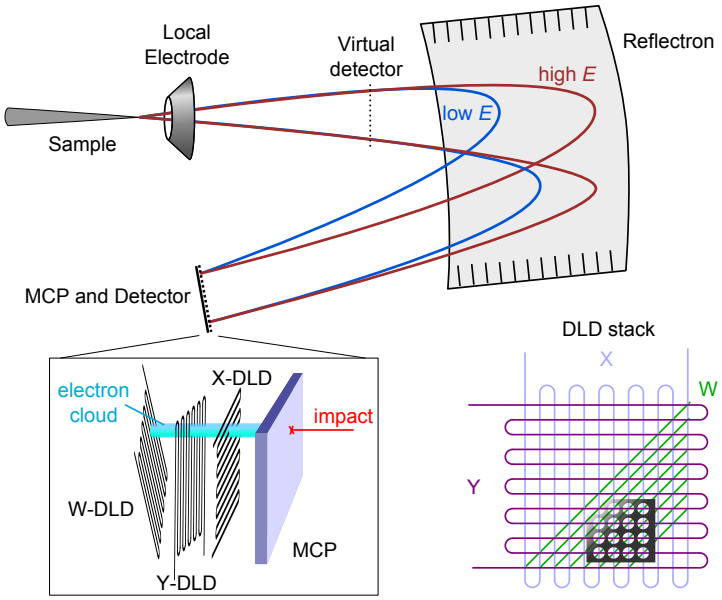

Figure 3.3.3 – Schematic diagram of a modern LEAP with reflectron and delay-line detector. (Picture of Dr. Andrew London)

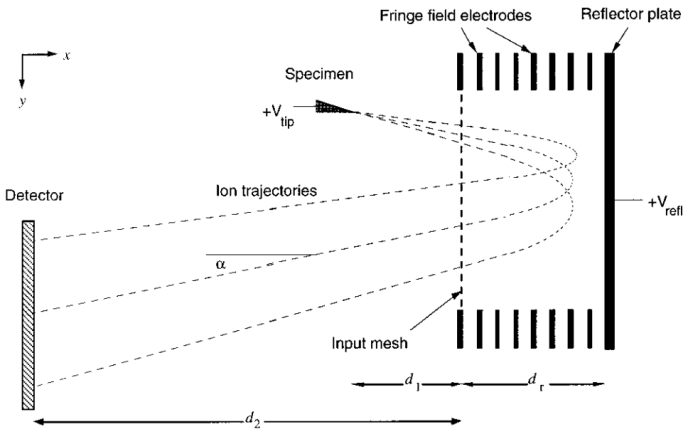

Figure 3.3.4 – Schematic diagram showing the basic layout of the energy compensated three-dimensional atom probe. [270]

As mentioned, the other significant improvement to atom probe was the development of laser as the excitation source. Laser has enabled analyses of non-metallic samples by enabling thermally induced field evaporation. The laser pulse essentially creates a localised heated zone on the apex of a tip, which imposes kinetic energy to the surface atoms. The development of ultra-high frequency laser together with low temperature sample stage (nor-

mally around 50K) enables thermal evaporation but without systematic temperature increase of the sample itself [272]. This advance is of great importance for catalyst research. Laser pulsing enables the evaporation of catalytic materials which more than often incorporate non-conductive compositions.

Apart from the general improvement of the atom probe instrument, the development of the in-situ reaction cell is particularly important to catalyst research [202]. In this work, the reaction cell as shown in Figure 3.1.4 is used for surface reaction on the cleaned sample. The reaction cell is attached to the atom probe buffer chamber, which is at a pressure of $8 \times 10^{-9} mbar$. The cell can be heated with a 600W heater, which has been monitored by two thermocouples passed symmetrically down the inner cell. Gas supply is attached to the cell and controlled by pressure and/or flow rates. This control is provided by mass flow controller (MKS), diaphragm pump (Vacuubrand) and leakage valves.

3.3.2 Data reconstruction protocol

Reconstruction of raw experimental data produced by atom probe is essential for subsequent imaging and analyses. Reconstruction using the purpose-built Cameca IVAS software follows several fixed steps of data refinement. Among those steps, there is the selection of several key parameters; tip radius, shank angle, imaging compression factor and field factor. In the following context, the method to derive the parameters mentioned above will be presented. Data reconstruction of oxidised samples follows a common reconstruction protocol in this research in order to eliminate systematic errors from reconstruction. Due to the field differences between that needed to evaporate surface oxides as compared to metallic substrate, there is often a voltage surge when analysing through the interface between the oxide and metal, as shown in Figure 3.3.5, as the instrument attempts to maintain a constant evaporation rate [275]. The plateau and subsequent surge of voltage is evident, showing the transition between oxide and metal. Therefore, reconstruction based on voltage history for an instantaneous measure of tip radius during the experiment will create erroneous abrupt changes in shape in the resulting reconstruction. To avoid this, a strategy of using shank

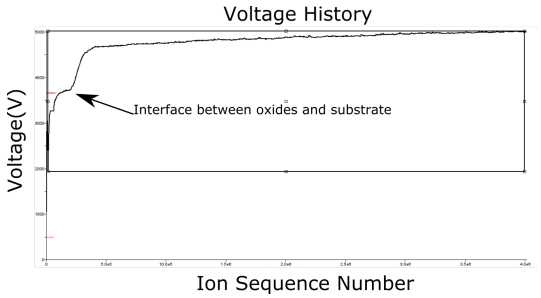

Figure 3.3.5 – Voltage history of a oxidised Ni50Co50 sample across an APT experiment. There is a plateau and increase of voltage after initial analysis, which is caused by oxide-metal transition.

angle mode reconstruction, which estimates the instantaneous radius based an initial characterisation of the tip shape and an estimate of the cumulative amount of material evaporated from the specimen at each point in the experiment, was applied, in an attempt to have all reconstructions directly comparable and avoid aberrant shape changes in the resulting atom maps.

Here, an oxidised Ni50Co50 sample is used to illustrate the detailed procedure of reconstruction, which is shown in the Figure 3.3.6. The first step was to make a reconstruction excluding any oxide containing regions of the data. A typical way to do this was to select the data after the voltage surge as shown in Figure 3.3.5. This sub-section of data resulted in a 2D desorption map (a histogram of the distribution of detected events across the face of the detector) as shown in Figure 3.3.6, in which there are high density regions representing various zone axes. In some cases, the desorption map did not clearly reveal the location of zone axes. In such cases, filtering the data to consider only single hits (eliminating multi-hits which can lower data quality) is useful. In this particular sample, an fcc structure was pre-identified through XRD analysis and FIM analysis. Therefore, the distance between two crystallographic planes of atoms along the [1 1 1] direction should have a characteristic value. An initial reconstruction is generated using the default values of initial radius and shank angle. Using spatial distribution map (SDM) analysis (a distribution function measuring atomic offsets along a specific direction [276, 277]) the plane spacing can be measured along a specific crystallographic pole in the reconstructed data. The reconstruction can then be calibrated by selecting a combination of initial radius and shank angle that will result in this observed crystallographic plane spacing matching that theoretically expected for this

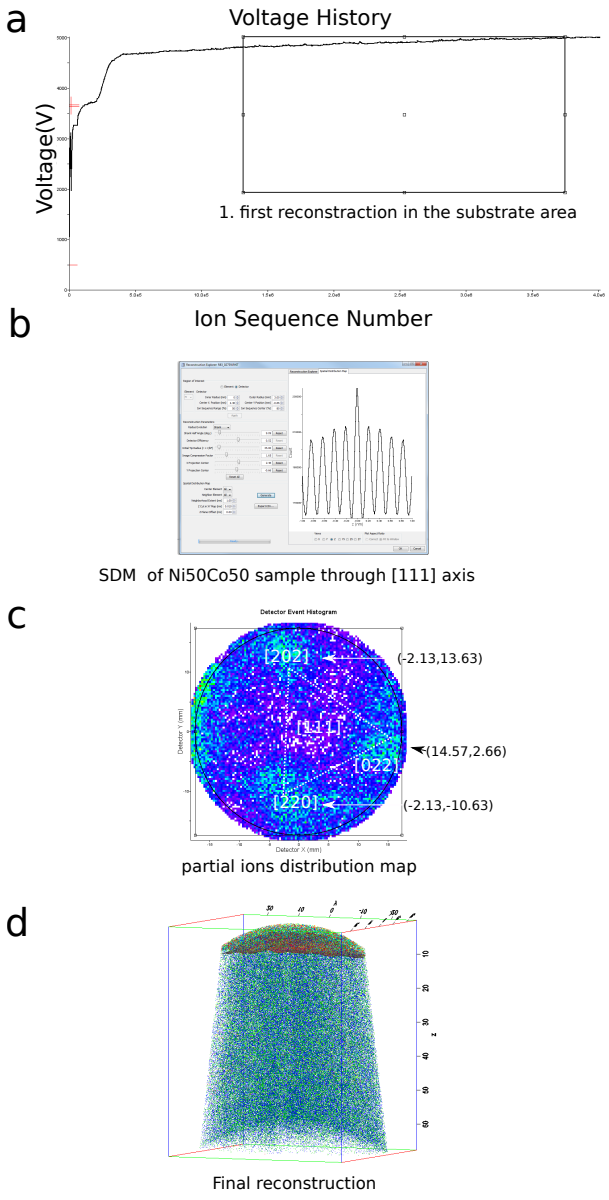

Figure 3.3.6 – Reconstruction procedure for determination of the shank angle, tip radius. a) the voltage history of a Ni50Co50 sample is shown. There are two distinct regions, representing the analyses of oxide and metallic substrate. The rectangular region represents the selected region used to determine reconstruction parameters. b) Ion detection map is shown with <220> axes. According to the stereographic projection, [111] axis is in the middle of those <220> axes. The x,y coordinates of the high intensity areas are recorded and used as the inputs for the following SDM analysis. c) SDM map of selected region of recorded zone axis. distance of selected ions along with the selected zone axis is plotted. By using the distance from XRD results as a reference and changing the plotting parameters of tip radius and shank angle, a right match is found. d) Data reconstruction of the Ni50Co50 sample is shown, in which a layer of oxide is on the tip.

material.

Image compression factor, which has been mentioned in equation 3.3.4 was set to the standard default value as 1.65. This is because improvement of the reconstruction was found not to be substantially affected by this parameter.

3.3.3 Mass labelling protocol

Peak identification in the mass-to-charge-state spectrum is one of the most critical steps in APT analysis since it determines the result of any compositional measurements. In this work, peak identification was involved during the analyses of as-received alloys and these alloys after gaseous exposure.

For the as-received alloys, peak identification is straightforward. Ni and Fe have five and four isotopes, respectively, however there is one mass overlap at 58 Da. As the mass 58 Da is only includes 0.28 at.% of total iron abundance, it is therefore associated to Ni in this research. Taking consideration of NiCo alloy, since Co only has one isotope at 59 Da, there are no mass overlaps with Ni. However, peak identification of oxidised samples can be significantly more difficult because various combinations of oxygen and metal molecular ion species at varying charge states can be detected. Furthermore, relatively small peaks with low detected ion counts, representing the ion species originating from the initial surface of the oxidised sample can change the surface composition significantly. The difficulties of obtaining a correct identification of these ions come from: a) overlapping of mass-to-charge-state ratio for molecular ion species; b) low ion counts of these oxide species limiting information on which to base identification; c) field evaporation of complex molecular ion species that can assume multiple charge-states, together with dissociation of these ions under intense electric field post-evaporation. In this research, multiple software tools have been used to optimise accuracy of mass spectrum peak-labelling. The tools include: *Weights, RangeCheck and AtomProbeLab 0.04. Weights* is used to help to identify unknown peaks by supplying possible options by which a given peak might be identified as based on analysis of potential existing elements in the alloy, target peak mass-to-charge-state ratio, a predefined number of ion combinations (i.e. limited to molecular ion size), tolerance of mass-to-charge-state ratio shift in defining the position of the peak, and maximum allowable charge state. *RangeCheck* is used to check the theoretical viability of a given labelling selection by examining isotopic ratios. *AtomProbeLab 0.04* is used to conduct global (entire reconstruction) and local (sub-regions of the reconstruction) deconvolution of

relative contributions to overlapped peaks using known isotopic abundances and the results are used to facilitate the decision of subsequent peak labelling [278]. As an example, the details of fitting the mass spectrum of Ni10Fe90 sample is presented below.

A mass spectrum of typical high complexity from the analysis of an oxidised Ni10Fe90 sample is shown in Fig. 3.3.7. Between 33 Da and 55 Da, is a region containing mostly double charged FeO^{++} and NiO^{++} ions. The peak at 44 Da is usually considered as CO_2^+. Due to the relatively low ion counts in some peaks, it is not possible to identify all the peaks in this region. The single charged oxide species are mostly located beyond 63 Da. The full map of potential overlapping peaks is identified by using Atom Probe Lab with a setting of minimum abundance of 0.2. The result is shown in Figure 3.3.8. There are four separated relationships containing overlapping information and they are connected by coloured lines which indicate the difficulty to de-convolute the peaks. The Maximum likelihood method is involved to calculate the difficulty of deconvolution and the darker the connecting line, the more difficult the two species can be isolated under the information given. As shown in the Figure 3.3.8, there is an overlap of one Ni isotope and O_2^+ at 32 Da. Decision to label it as O_2^+ has been made based on the calculated fit as shown in Figure 3.3.9a. The amount of Ni in this particular peak is minimal with respect to the contribution of the oxygen signal through the calculation. One of the other overlap peaks is at 63.9 Da, where Ni^+ and Fe_2O^{++} overlap. As shown in Figure 3.3.9b, it can be clearly shown that Fe_2O^{++} is the dominant species given the intensities of adjacent isotope peaks. It is also important to point out that there are still unidentified peaks in the oxide region since the calculated relative intensity of the species does not match the actual intensity from the data (as shown by the black X mark in the figure). However, the author has exhausted all potential combinations of Fe, Ni and O without a satisfactory outcome. Overall, the total list of identified peaks is presented in Table 3.3.1. It is important to note that there is a compromise in terms of labelling the peaks when some of these overlapping peaks contain equal amount of different species but in the end only one ion could be assigned to these peaks.

Figure 3.3.7 – Identification of peaks from a typical oxidised Ni10Fe90 sample. Peaks representing oxide species are closely located with each other between 32 Da to 43 Da and 63 Da beyond. There is however little overlap between the peaks representing metallic species and oxide species. Specis labels here are for indication puerpose and the detailed information is listed in Table 3.3.1

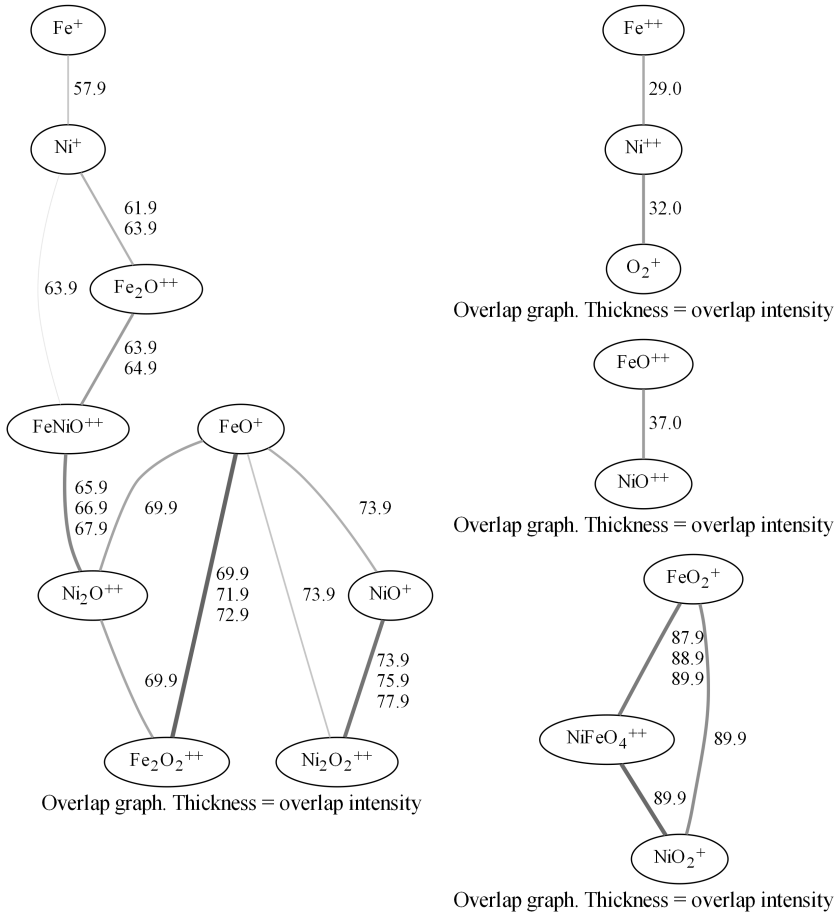

Figure 3.3.8 – Relationships between overlapping peaks identified by mass ranging of a oxidised Ni10Fe90 sample. Within the circle, the name of identified peak is listed. Between the circles, lines connect overlapping isotope peaks together at the indicated mass-to-charge-state ratio (Da).

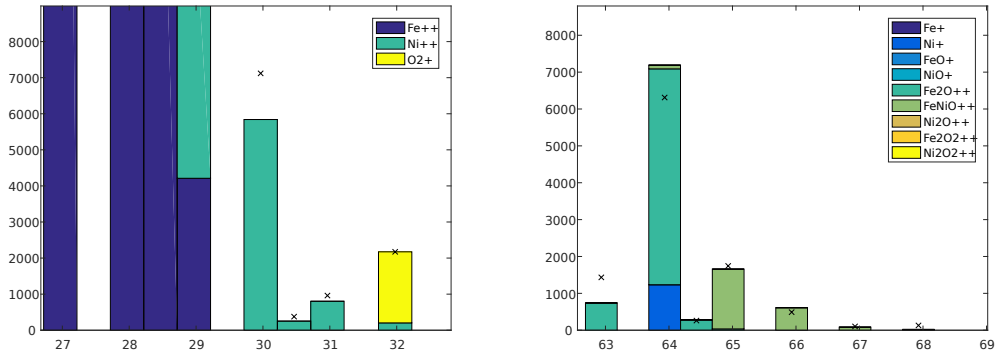

(a) Da 32 identification

(b) Da 32 identification

Figure 3.3.9 – Peaks deconvolution of typical oxidised Ni10Fe90 sample. Maximum likelihood method has been applied to the calculation.

Da	Ions	Da	Ions	Da	Ions
14.0	$^{14}N^{+}$	44.0	$^{16}O^{16}O^{12}C^{+}$	70.0	$^{54}Fe^{16}O^{+}$
16.0	$^{16}O^{+}$	54.0	$^{54}Fe^{+}$	71.0	$^{54}Fe^{56}Fe^{16}O^{16}O^{2+}$
18.0	$^{16}O^{1}H^{1}H^{+}$	55.0	$^{55}Mn^{+}$	72.0	$^{56}Fe^{16}O^{+}$
24.0	$^{16}O^{16}O^{16}O^{2+}$	56.0	$^{56}Fe^{+}$	72.5	$^{56}Fe^{57}Fe^{16}O^{16}O^{2+}$
27.0	$^{54}Fe^{2+}$	57.0	$^{57}Fe^{+}$	73.0	$^{57}Fe^{16}O^{+}$
28.0	$^{56}Fe^{2+}$	58.0	$^{58}Ni^{+}$	74.0	$^{58}Ni^{16}O^{+}$
28.5	$^{57}Fe^{2+}$	59.0	$^{59}Co^{+}$	75.0	$^{58}Ni^{60}Ni^{16}O^{16}O^{2+}$
29.0	$^{58}Ni^{2+}$	60.0	$^{60}Ni^{+}$	76.0	$^{60}Ni^{16}O^{+}$
30.0	$^{60}Ni^{2+}$	62.0	$^{62}Ni^{+}$	78.0	$^{62}Ni^{16}O^{+}$
31.0	$^{62}Ni^{2+}$	63.0	$^{54}Fe^{56}Fe^{16}O^{2+}$	86.0	$^{54}Fe^{16}O^{16}O^{+}$
32.0	$^{16}O^{16}O^{+}$	64.0	$^{56}Fe^{56}Fe^{16}O^{2+}$	90.0	$^{58}Ni^{16}O^{16}O^{+}$
35.0	$^{54}Fe^{16}O^{2+}$	64.5	$^{56}Fe^{57}Fe^{16}O^{2+}$	91.0	$^{58}Ni^{60}Ni^{16}O^{16}O^{16}O^{16}O^{2+}$
36.0	$^{56}Fe^{16}O^{2+}$	64.5	$^{56}Fe^{57}Fe^{16}O^{2+}$	92.0	$^{58}Ni^{62}Ni^{16}O^{16}O^{16}O^{16}O^{2+}$
36.5	$^{57}Fe^{16}O^{2+}$	65.0	$^{56}Fe^{58}Ni^{16}O^{2+}$	94.0	$^{62}Ni^{16}O^{16}O^{+}$
37.0	$^{58}Ni^{16}O^{2+}$	66.0	$^{56}Fe^{60}Ni^{16}O^{2+}$	102.0	$^{54}Fe^{16}O^{16}O^{16}O^{+}$
38.0	$^{60}Ni^{16}O^{2+}$	67.0	$^{56}Fe^{62}Ni^{16}O^{2+}$	104.0	$^{56}Fe^{16}O^{16}O^{16}O^{+}$
39.0	$^{62}Ni^{16}O^{2+}$	68.0	$^{58}Ni^{62}Ni^{16}O^{2+}$	105.0	$^{57}Fe^{16}O^{16}O^{16}O^{+}$

Table 3.3.1 – Peak identification table for Ni10Fe90 sample including as-received and oxidised samples. This Table is plotted with isotopeList.m from A. London. The tables for the other alloys can be found in appendix.

3.4 Transmission Electron Microscopy

Electron interaction

In all Transmission Electron Microscope (TEM) working modes, the information obtained comes from an interaction between the electrons and atoms of the analysed samples [279]. The average distance that an electron travels within the sample without interaction is called the mean-free path λ. In Figure 3.4.1, the interaction volume of the incident electron and characterised TEM specimen is shown. Sample thickness t is around few nanometre up to few tens of nanometres. Interaction volume is marked in blue colour. As shown in the figure, R is the samllest distance between two volumes in the speciment for EDX analysis.

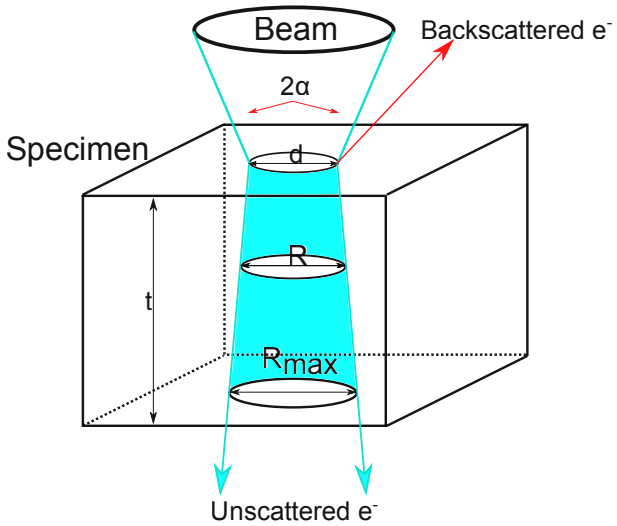

Figure 3.4.1 – Schematic of the interaction volume between incident electrons and TEM specimen sample. The blue region is the interaction volume between the beam and sample. t is the thickness of the sample, d is the incident-beam diameter. R is the smallest distance between two volumes in the specimen for EDX analysis. R_{max} is the diameter of the exit-probe. [279, 280]

Elastic scattering and Inelastic scattering

Electrons penetrating the analysed sample atoms experience deflection, which includes elastic and inelastic scattering. For the elastic scattering, only the momentum changes without affecting energy. An electron with energy E_0 to be elastically scattered at an angle α is described by relation :

$$p(\alpha) \propto \frac{1}{E_0 sin^4 \alpha} \tag{3.4.1}$$

It is clear that small scattering angles are much more likely to occur. Also, with the increase of the atomic mass (Z), the scattering is more likely to happen. For the inelastic scattering, the energy of an incident electron changes. The electron can excite photons, lattice vibrations etc. It is the characteristic energy spectrum of the excited photons that is examined, the technique name of which is called Energy-dispersive X-ray spectroscopy (EDX).

TEM working mechanism

TEM is a versatile research tool for catalytic particle research. There are two modes used in this thesis: Bright Field Imaging (BF) and High Angle Annular Dark-Field imaging (HAADF) together with EDX. For the BF imaging, the electron beam is used to illuminate a relatively large area of a specimen. Crystallographic properties and defect structure can be imaged. The resolution of BF can normally reach sub-nanometre resolution. In Figure 3.4.2a, schematic diagram of a TEM for the BF imaging is shown. The HAADF imaging is the based on the scanning TEM (STEM) which is illustrated in Figure 3.4.2b. In STEM mode, the electron beam is rasterised across the sample via scan coils. Incoherently diffracted electrons are collected using a high angle annular detector. The number of these reflected electrons is largely related to the size of the nuclei through the illuminated spot. Therefore, Z-contrast images can be obtained by HAADF.

Imaging

200KeV TEM observations were made using JEOL JEM-2100 fitted with LaB_6 source (JEM-2100) and JEOL ARM200F (ARM200). JEM-2100 was used for the general observation and to check the particle distribution. ARM200F was used to conduct subatomic observation and diffraction. Additionally, STEM was conducted by JEOL JEM-3000F FEGTEM (JEM-3000) JEOL ARM300F (ARM300). The ARM200F and 300F were fit-

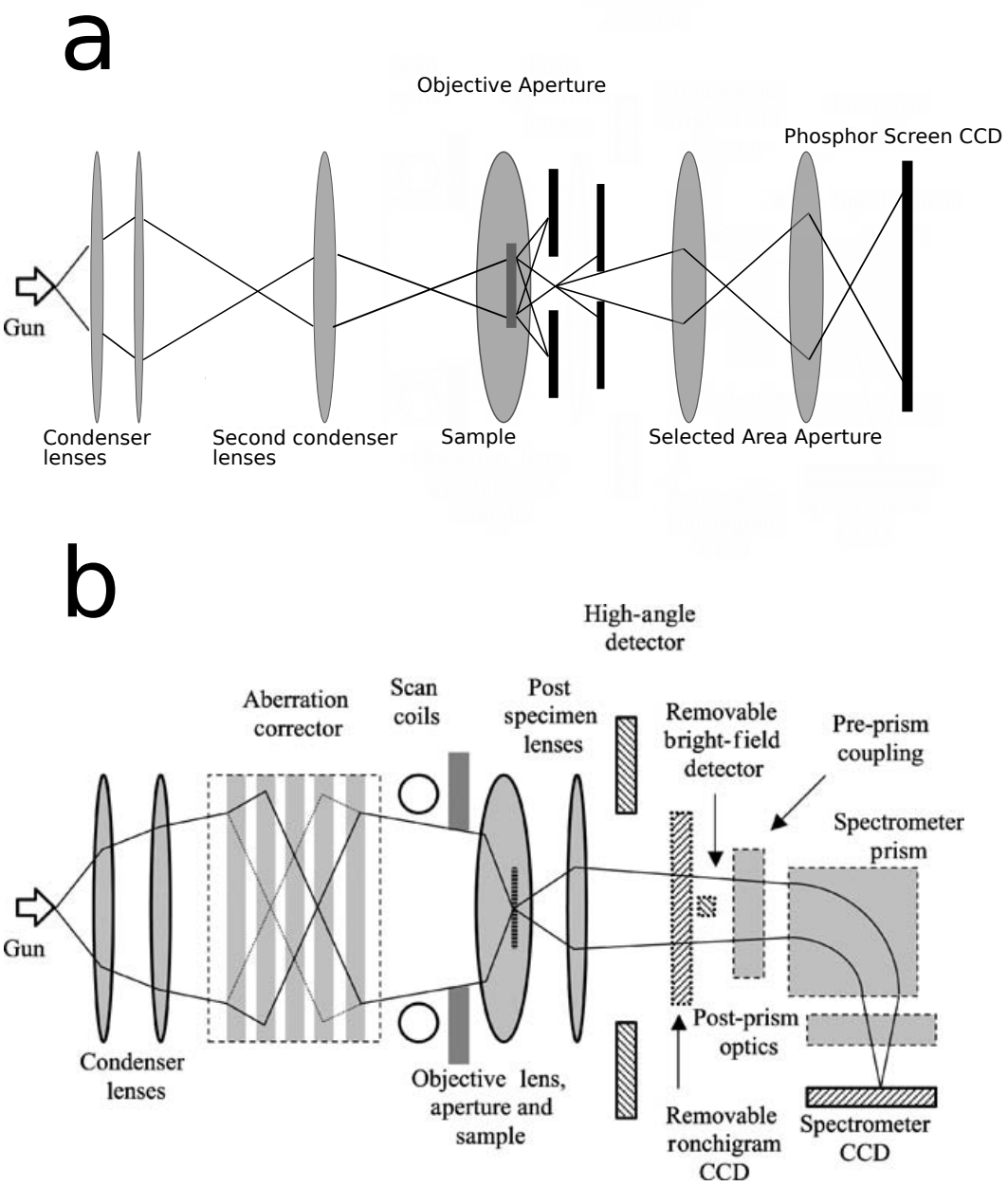

Figure 3.4.2 – a) Scheme of a TEM for the set-up for bright-field imaging. b) Simplified schematic of an aberration-corrected STEM; examples of electron trajectories are indicated. In the (quadrupole-octupole) aberration corrector, the different trajectories in the XZ and YZ planes are indicated with dotted and solid lines, respectively. The electrons are accelerated from the gun; condenser lenses are used to adjust the beam current and beam coherence and to couple to the aberration corrector. The objective lens focuses the probe, which is scanned across the sample by the scan coils. The high-angle detector collects electrons scattered to high angles. Removable bright field and Ronchigram detectors are shown as well as the important components of the spectrometer. [281]

ted with a spherical aberration STEM probe corrector, a Centurion EDX detector, and Gatan GIF Quantum 965 ER featuring Dual EELS. In this thesis, the author mainly operated JEM-2100 and JEM-3000F. Aberration Corrected TEMs were used with the support from Dr Neil Young in Oxford Materials Department and Dr Mohsen Danaie from High Resolution TEM centre in Diamond, Harwell.

EDX

EDX probing was mainly carried out for chemical information. JEM-3000 was used mostly for probing those particles made by chemical methods. An Oxford instrument EDX detector fitted with a super atmospheric thin window (SATW) detector and an INCA processor was used. Ebeam size was selected to 1.2nm and data collection time for single point was less than 45 seconds. EDX quantification involves various factors which can induce random and systematic errors in the final results. Random error come from statistical fluctuation and systematic errors could come from samples, which includes factors: thickness (interaction volume), homogeneity, sample stability, conductivity and etc., and they also come from the instruments, which includes beam current, EDX detector and etc. Cliff&Lorimer proposed k factor to describe the accurate elemental composition:

$$\frac{C_A}{C_B} = k_{AB}\frac{I_A}{I_B} \tag{3.4.2}$$

where C_M is the atomic fraction, I_M is the measured X-ray intensities [282]. It requires a known composition specimen to be analysed as the reference for subsequent actual specimen measurement. k factor is still used as the primary method for the EDX quantification since it is embedded within majority of commercial software [283]. Those k factors based on first principle calculation could contains significant systematic errors more than 10% [283, 284]. In this thesis, EDX analysis conducted as 'standardless analysis' and it is the standards of the Inca software that are used for quantification. In the Chapter 5, the errors given for particle composition are standard deviation based on multiple measurements. But the errors for multiple measurements on single large particles are counting error.

3.5 LEIS and XPS

Low energy ion scattering (LEIS) and X-ray photoelectron spectroscopy (XPS) are both surface sensitive methods used to probe sample surface composition [285, 286]. XPS is a mature technique for surface composition analysis, with a detection limit down to 0.1 at.%. During analysis, X-rays with specific wavelength are fired towards the sample surface. Specific electrons of the surface atoms absorb energy from the X-rays and become excited before being emitted. The kinetic energies of the emitted electrons are measured, and because the incident energy of the X-rays is known, the binding energy of the electrons in the material is calculated by the difference. The binding energy is directly associated to a particular element and its oxidation states. For the experiment in this research, XPS analyses were performed on the samples made by the IGC method (Batch as listed in Table 3.1.3) using a Kratos Analytical Axis UltraDLD spectrometer equipped with a monochromatic aluminium source (Al K_α = 1486,6 eV) in UCCS University of Lille. The analysed area was approximately $300\mu m \times 700\mu m$. The depth of the area examined was about 10nm into the sample, with a resolution of about 0.1at% for elements apart from hydrogen and helium.

The LEIS is installed together with an inline oxygen plasma. LEIS was performed with charged He^+ ions bombarding the sample surface. Due to the difference of atomic weight, reflected He^+ ions will lose certain energy characteristic of the scattering element. By analysing the energy loss, elements can thus be identified. LEIS is a very surface sensitive method and only the top surface is analysed in normal conditions. However, some incident ions inevitably penetrate deeper than the first layer of atoms and return to the detector. These ions result in shadow peaks on the low energy loss side to the main peak of the sample, which indicates ions detected on the surface also exist beneath atoms atop. LEIS is also a quantitative method since the intensity and width of an energy loss peak is a direct reflection of the abundance of atoms on the surface. By calculating the area under all detected peaks, a surface composition can be obtained. However, this composition determination requires standardised reference, which is not extensively available. Therefore, LEIS is only used

as a qualitatively rather quantitatively in this thesis. One other important fact is that LEIS is a destructive method since ion bombardment on the surface removes atoms gradually. Therefore, it can reveal composition in depth by designing multiple scans on the same area.

In the past, the LEIS ion gun was fitted in a XPS chamber. Ion beams enters and exits the sample surface following a fixed path. Therefore, there was a substantial limitation in traditional LEIS experiment due to the low single collecting efficiency: only one data collecting angle/direction was allowed, and the angle was not optimised due to the installation angle of the gun. Modern commercial LEIS instruments, such as that used in this thesis, have a source and detector configured in an optimised position as shown in Figure 3.5.1. An accelerated ion source, which normally uses He, Ne or Ar, is projected onto the sample surface perpendicularly. Reflected ions are collected only at the optimised angle of 104°. In addition to that, a tulip shaped detector collects all reflected ions from that specific angle. The efficiency of this machine is orders of magnitude higher than the traditional configuration. Reflected ions travel through the electromagnet lenses to resolve their energy distributions. The detection limit of LEIS is related to the ion used and the weight of probed atoms. Light elements which are lighter than the incident ions cannot be revealed in the spectrum. On the other hand, heavy incident ions could give better resolution towards energy loss on elements closely located in the periodic table. For the heavy elements (transition metals), the detection limit can reach ppm level, while for light elements it can reach down to 1at%.

LEIS experiments were performed for the analysis of nanoparticles fabricated by the IGC method (labelled as batch No. 3 in Table 3.1.3). During the analysis, initial scanning revealed that carbon contamination on the sample surface was present. Thus, oxygen plasma was used to clean the surface. The plasma was applied for 10 min with a partial pressure of $1 \times 10^{-5} mbar$. After the cleaning, C was not detectable anymore in reference scanning. Then, the homogeneity of the sample was first checked in five different areas to ensure data was representative, given that each scan covers an area of $1000\mu m \times 1000\mu m$. He^+ ions were used as the plasma source. The accelerating voltage was set as 3kV and the current was set to 5nA. During a typical analysis, one scanning spectrum was the average of five single

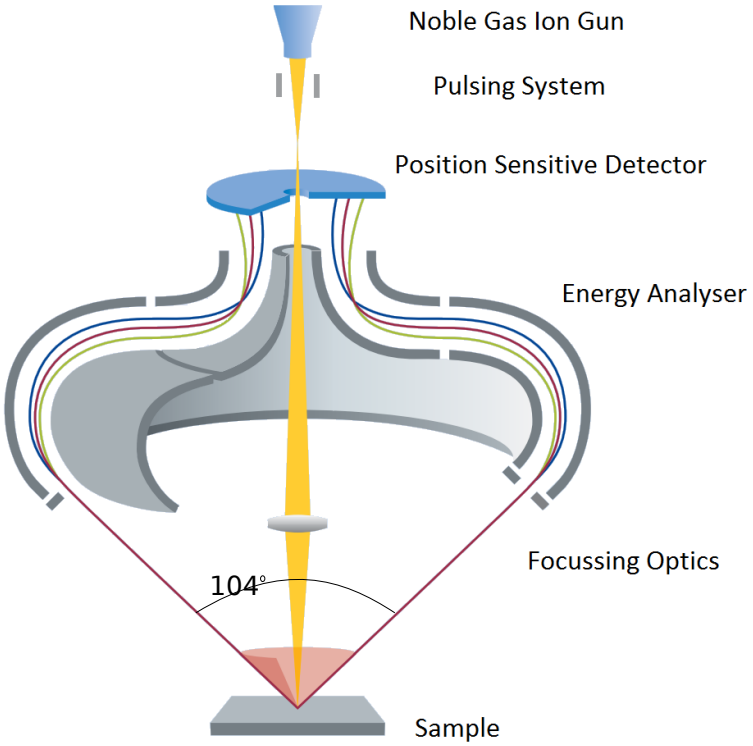

Figure 3.5.1 – Illustrated structure of LEIS detector. Incident ions are sent above the sample. The collection angle is fixed with 104°.

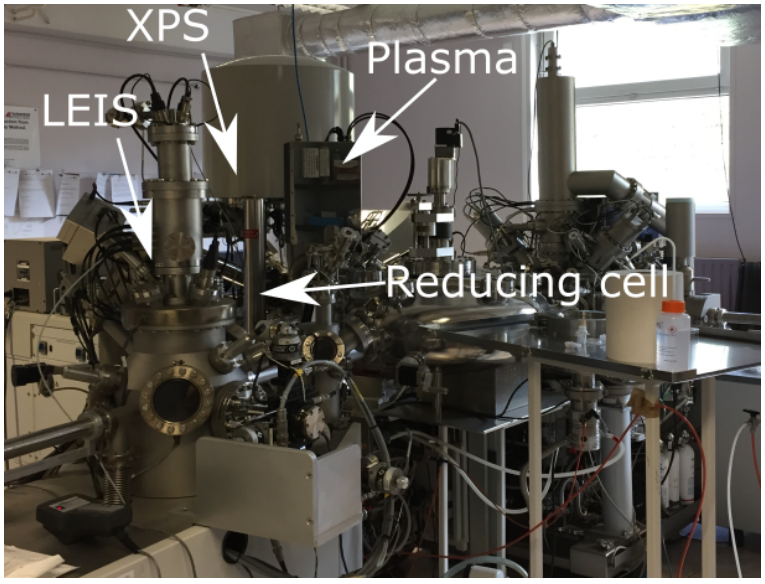

Figure 3.5.2 – LEIS instrumentation installation in University of Lille. The unique setup of the instrument is that it is attached to a surface analysis platform common to LEIS, XPS and TOF-SIMS analysers.

scans. As mentioned, LEIS is a destructive method and therefore compositions within the nanoparticles can be revealed with prolonged scans, which was the case in this study.

3.6 AFM

The Atomic Force Microscopy (AFM) is a traditional tool for understanding material surface at nanoscale or atomic level [287, 288]. The Atomic Force Microscopy (AFM) images of surfaces were recorded using a commercial MultiMode® 8 Scanning Probe Microscope from Bruker Corporation in UPMC, France. In order to avoid tip and sample damages, topographic images were taken in the Peak Force QNM® mode. Silicon tips on nitride levers (resonance frequency of ~50-70 kHz, force constant of 0.4 N/m) were used. The AFM mode used was tapping mode, but force measurements were also recorded as the piezoelectric can re-equilibrate automatically. Images were obtained at a constant speed of 1 Hz with a resolution of 512 lines of 512 pixels each. The raw data were processed using the imaging processing software Nanoscope Analysis v.1.20. from Veeco Instruments Inc., mainly to correct the background slope between the tip and the surface.

3.7 XRD

X-ray Diffraction (XRD) was used to probe the crystallographic structure and lattice parameters for alloy wires in the chapter on the *alloy work*. XRD is a traditional technique using the elastic scattering of the X-ray on individual atoms. Following Bragg's law [289],

$$2dsin\theta = n\lambda \tag{3.7.1}$$

where d is the spacing between diffracting plane, θ is the incident angle, n is any integer and λ is the wavelength of the X-ray. In this thesis, XRD was conducted by collaborators at the University of Lille. A Rigaku Smartlab diffractometer equipped with a 9kW copper rotated anode (wavelength=1.5418 angstrom) was used to collect the patterns of the samples. To

minimize the effects of sample shape of the wires, the parallel reflection geometry was used through a parabolic multilayer mirror. Diffracted intensities were integrated using a 1D PSD DTEX detector covering 2° in 2 thetas, and the energy of the detector was optimized to minimize the fluorescence effects of Co, Ni, Fe.

Chapter 4

APT Characterisation of Oxidised Bimetallic Alloys

In this chapter, surface composition changes of model catalytic alloy tips exposed to oxidising conditions are investigated via FIM and APT analyses. Three FeNi alloys and one NiCo alloy were selected as the materials to be characterised in this study. Analysis of the experimental results provides essential information relating to the initial oxidation behaviour, which is crucial to understand how real catalysts may evolve during exposure to their working environment.

4.1 As-received alloys

The properties of as-received alloy wires were investigated in the first step. For this, the major goals are to determine the lattice structure, lattice parameter and the composition (including contaminants) of the respective alloy wires. The lattice structure and the lattice parameter are used as the inputs for calibration of the 3D data reconstruction using IVAS, as detailed in Section 3.3.2. Composition information of the as-received alloy wires is essential to properly interpret the controlled oxidation experiments. In this chapter, four alloys wires were analysed, Ni10Fe90, Ni48Fe52, Ni90Fe10, Ni50Co50 (all wt.%).

4.1.1 Crystallography

XRD In Figure 4.1.1, XRD results from the four wires are shown. Ni90Fe10, Ni48Fe52 and Ni50Co50 samples have an fcc structure, as confirmed by three characteristic peaks around 45°, 52° and 76° [290]. In comparison Ni10Fe90 has a bcc structure, identified by two characteristic peaks around 45° and 65° [291]. It is clear that mixing of Fe and Ni in varying proportions results in a transition between fcc and bcc structures. Also, the increasing amount of Ni shifts the diffraction peaks to the high angle side, which is similar to previous observation [291]. According to the FeNi phase diagram, shown in Fig. 2.2.3 on page 21, three phases could be present in the NiFe wires: a bcc αFe solid solution, fcc $\gamma(Fe,Ni)$ phase and a $FeNi_3$ intermetallic [85]. The XRD results confirm that each sample studied here only contains a single kind of crystallographic structure, either bcc or fcc, but not mixture of both. Therefore, Ni10Fe90 takes the form of bcc αFe solid solution, and that the Ni48Fe52 and Ni90Fe10 wires are both a fcc $\gamma Fe,Ni$ solid solution. Furthermore, the lattice parameters have been calculated and are listed in Table 4.1.1. With 10 wt.% addition of Ni into Fe, the lattice parameter has a significant decrease. However, with further addition of Ni, the lattice parameter increases due to the change from a bcc to an fcc structure. The value of the lattice parameter in fcc alloys is decreased by further Ni loading. For NiCo, only an fcc $\alpha Co,Ni$ phase is present in the Ni50Co50 alloy, and the lattice parameter is close

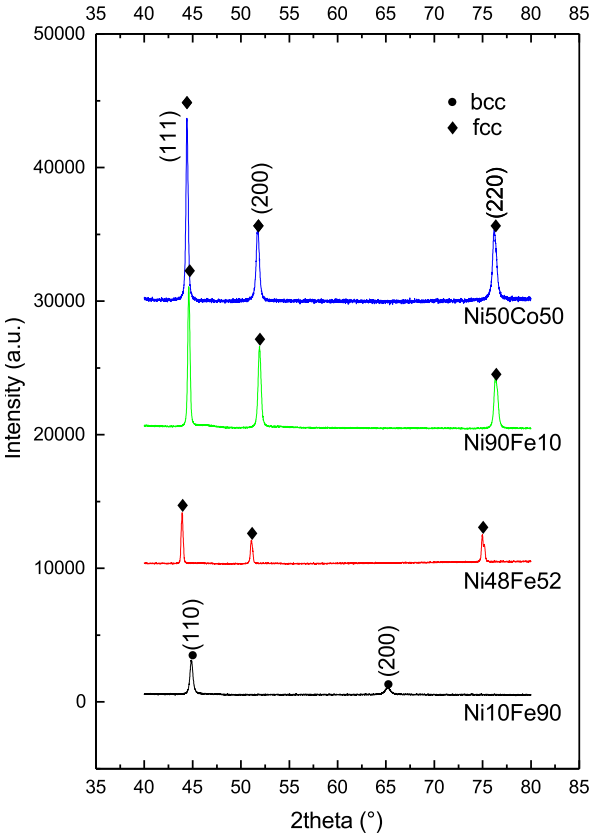

Figure 4.1.1 – XRD results of four analysed wires (Ni10Fe90, Ni48Fe52, Ni90Fe10 and Ni50Co50). The data show that Ni90Fe10, Ni48Fe52 and Ni50Co50 have an fcc structure whilst Ni10Fe90 has a bcc structure. A lattice parameter shift is evident with the changes of Ni and Fe contents.

to both Ni and Co, as indicated in Table 4.1.1. Overall, the application of XRD represents an important insight into the sample homogeneity and the derived lattice information is essential for subsequent spatial reconstruction of the APT data.

FIM FIM cleaning (experiment parameters are shown in 3.1.1 on page 65) of the surface of the as-polished alloy wires is essential to ensure that oxidation/reduction experiments are conducted on a contamination-free surface. During the cleaning procedure, FIM can also reveal the surface structure at an atomic level, providing information which is directly related to the surface structure. Characteristic FIM images after cleaning are shown in Figure 4.1.2 for all four alloy wires. The fcc structures of Ni90Fe10 and Ni50Co50 are

	Fe(ref.)	Ni10Fe90	Ni48Fe52	Ni90Fe10	*Ni(ref.)*	Ni50Co50	*Co(ref.)*
Crystal structure	*bcc*	bcc	fcc	fcc	*fcc*	fcc	*fcc*
a(nm) calculated from 1st peak	*0.2886*	0.2857	0.3571	0.3518	*0.3524*	0.3533	*0.354*
a(nm) calculated from 2rd peak	-	0.2862	0.3576	0.3522	-	0.3534	-

Table 4.1.1 – Calculated lattice parameters from XRD results. Note that the data from mono-metallic systems are from reference [88].

apparent in Figure 4.1.2a and 4.1.2d whilst a bcc structure of Ni10Fe90 is demonstrated in Figure 4.1.2c. The identification of the poles in these images have been determined by referring to the stereographic projections (stereograms) of the theoretical bcc and fcc structure, respectively [242]. For Ni50Co50, a grain boundary within the analysed material is observed, indicating subsequent oxidation experiments may be carried out on a multi-crystallographic surface. Such grain boundary features are not only present in Ni50Co50, multi-crystalline features were also observed in the other FIM images of the three alloys. In Figure 4.1.2b, there is no obvious structural information in Ni48Fe52, apart from the concentric rings in the centre indicating the location of the sample tip. Combining the XRD and FIM results of the Ni48Fe52 sample however, it can be concluded that Ni48Fe52 has an fcc structure. Furthermore, minor contamination within the Ni48Fe52 could be the reason of such non-clear surface structure.

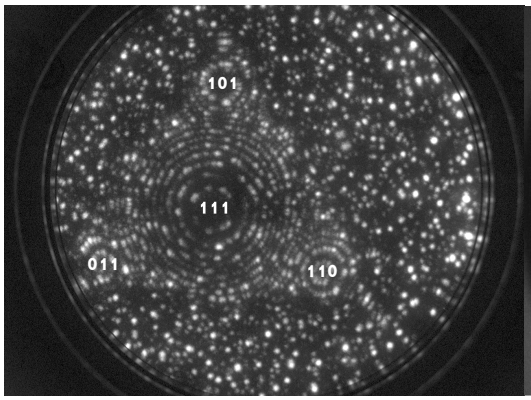

(a) Fcc structure-Ni90Fe10 sample. Imaging gas Ne, 8.1kV and 50K.

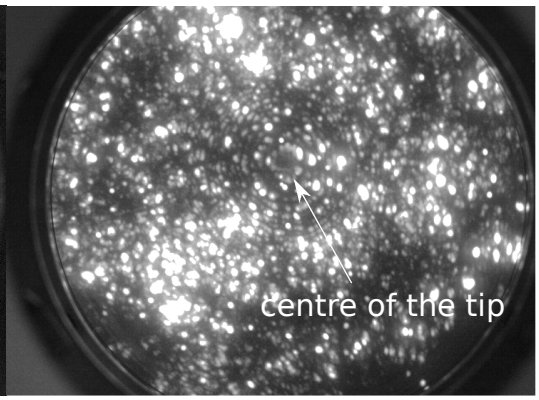

(b) No FIM-based identification-Ni48Fe52 sample. Imaging gas Ne, 5kV and 50K.

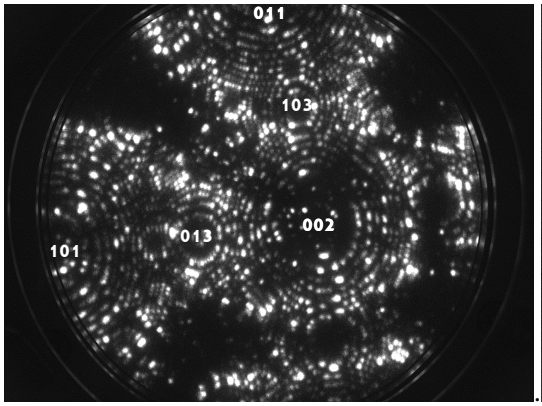

(c) Bcc structure-Ni10Fe90 sample. Imaging gas He, 6kV and 50K.

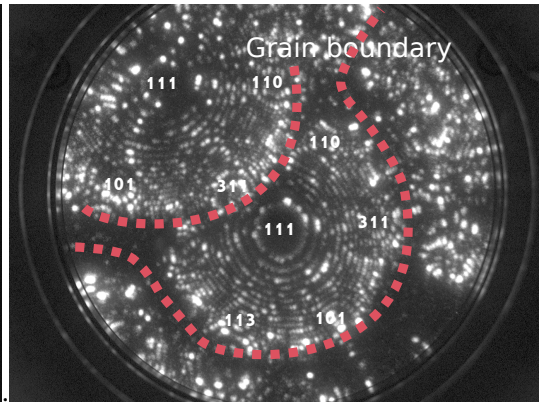

(d) Fcc structure-Ni50Co50 sample. Imaging gas Ne, 8.2kV and 50K.

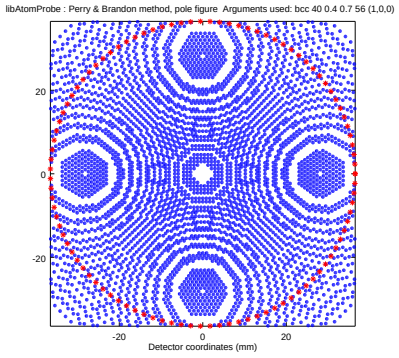

(e) Simulated bcc structure, with the [2,0,0] direction in the centre

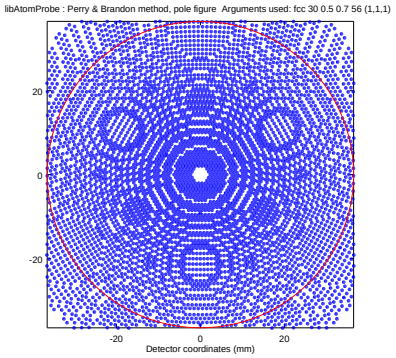

(f) Simulated fcc structure, with the [111] direction in the centre

Figure 4.1.2 – FIM images of the cleaned surface of four alloy samples. Ni90Fe10 and Ni50Co50 show fcc structures whilst Ni10Fe90 shows a bcc structure. There is no direct structural identification possible for the Ni48Fe52 sample. The pole identifications are made by referring to the stereographic projections of bcc, fcc structures. In the sub-figure e and f, simulated bcc and fcc structures are shown, which are used to help the identification of the crystallographic orientations. [242].

4.1.2 Chemical compositions and contaminations

The chemical compositions of the four alloy wires were investigated by APT in order to characterise any deviations from the nominal compositions, along with the level of any contamination. In Table 4.1.2, APT analyses on the four alloy wires are shown (each composition is determined by datasets containing more than 10 million data points). There is no significant variation between the nominal composition and the detected composition, within a maximum 1 wt.% tolerance. In terms of contamination, no unexpected elemental species in Ni10Fe90, Ni90Fe10 and Ni50Co50 were detected. However, there are observed C, Si and Ti traces in the Ni48Fe52 sample at ppm level, possibly attributed to it not being custom made with lower control over purity during processing.

	Ni10Fe90	**Ni48Fe52**	**Ni90Fe10**	**Ni50Co50**
Nominal Composition (wt.%)	Ni10Fe90	Ni48Fe52	Ni90Fe10	Ni50Co50
APT result (wt.%)	Ni9Fe91	Ni47Fe53	Ni89Fe11	Ni50Co50
APT result (at.%)	Ni9Fe91	Ni54Fe46	Ni89Fe11	Ni50Co50

Table 4.1.2 – Chemical compositions of four alloy wires analysed by APT. The composition variation is below the 1wt.% tolerance.

4.1.3 Compositional measurements along zone axes and cleaned surfaces

Variations across the atom probe hit maps were examined in order to explore limitations of the APT technique, while also revealing further details of the specimen crystallography. During the analysis of the Ni90Fe10 sample under voltage mode, there is a clear composition variation visible along different zone axes. As shown in Figure 4.1.3, Fe preferentially evaporates along the [111] axis, while Ni is concentrated more along <200> axes. The composition variation is identified along the [111] axis, where a $3nm \times 3nm \times 64nm$ region-of-interest (ROI) cylinder is aligned. The measured Fe content is 16.5 wt.% within this ROI. It is particularly interesting to observe such evaporation effects since the evaporation fields of Fe and Ni for doubly charged ions are almost the same under the Image Hump Model

prediction [242]. However in the actual analysis, there is a clear preferential evaporation. Similarly, it has been found that Ni is preferentially evaporated from both the [002] axis and <113> axes in the Ni50Co50 sample. The level of the preferential evaporation for Ni reaches 52 wt.%, illustrating a lesser extent of variation than the Ni90Fe10 sample. However, such preferential evaporation is not observed in either the Ni48Fe52 nor Ni10Fe90 samples. A summary of the preferential evaporation is shown in Table 4.1.3. Although all the preferential evaporation behaviours are confirmed under voltage mode of APT analysis, it is still an important information for the oxidation/reduction experiments where evidence is needed to fully quantify reaction-induced surface segregation.

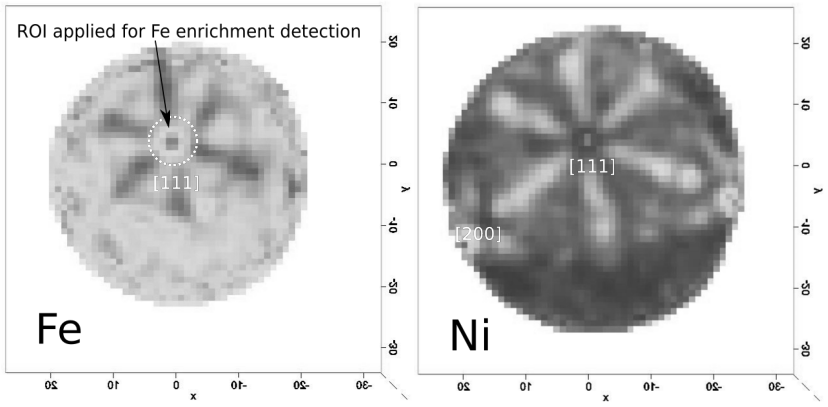

Figure 4.1.3 – Local preferential evaporation along the zone axes of a Ni90Fe10 sample (fcc structure). Fe is concentrated more along the [111] axis whereas Ni is enriched along the <200> axes. Note that “pole” and “axis” are used interchangeably in the following context unless specification is put.

	Preferential evaporation behaviours
Ni10Fe90(bcc)	No observation
Ni48Fe52(fcc)	No observation
Ni90Fe10(fcc)	Ni is abundant along <200> and Fe is abundant along <111> axes
Ni50Co50(fcc)	Ni is abundant along [002] and <113> axes

Table 4.1.3 – Summary of the preferential evaporation behaviours of the four alloy wires under the voltage mode of APT analysis. Only Ni90Fe10 and Ni50Co50 shows the preferential evaporation. These observations are present in multiple assessments.

As the nature of the experiments probes the sample surface, the very initial surface

composition in the APT analysis is also investigated before exposure to various gas environments. This experiment is undertaken to elucidate the possibility of having surface segregation induced purely by intense fields generated in the APT analysis. This was done by first analysing reference samples in the atom probe until reaching a depth such that no contamination was detected. The experiment was halted, for 30 minutes and then restarted analysing the same sample (laser mode of APT). After this process, across all the four alloys, no field-induced surface enrichment of any element was detected.

4.2 Oxidation of alloys

4.2.1 Oxidation of Ni10Fe90 alloy

Oxidation of Ni10Fe90 samples were conducted under the experimental parameters listed in Table 4.2.1. The oxidation temperature selected was mainly at 353K (instead of room temperature) for two reasons: this temperature is just above room temperature and can be easily controlled and secondly this temperature can activate oxidation process of interest. Oxidation at the higher temperature of 473K was also conducted, mainly to seek kinetic information. The oxidation pressure was chosen as 45 mbar (pure oxygen). Comparing to other surface sensitive techniques, this pressure is sufficient to mitigate the so called "Pressure gap". This term refers to the vast difference between the working pressure of the catalysts (> 1 bar) and pressure in characterisation instruments (< 10^{-6} mbar) [202]. However, given that the reaction cell is mounted on a UHV chamber, this pressure is also safe to prevent a potential breach of the vacuum system. Oxidation times ranged from 30 min to as long as 720 min. At each oxidation condition, typically one successful dataset was acquired. This low final sample yield was due to the fragility of the oxide layers, as well the stringent cleaning process required to form suitable pre-oxidised samples limiting the number of specimens that could be attempted.

Oxidation temp.	Oxidation time		
	30 min	60 min	720 min
353K	1	1	1
473K		1	

Table 4.2.1 – Oxidation parameters for Ni10Fe90 samples. 3 samples were oxidised at 353K and 1 sample oxidised at 473K. The oxidation was done in the in-situ reaction cell with 45mbar oxygen.

Employing the dedicated mass peak labelling detailed in section 3.3.3, a typical reconstruction of an oxidised Ni10Fe90 sample is shown in Fig. 4.2.1. In the reconstruction, oxides located at the top of the tip of this Fe-rich alloy indicate oxidation occurring at the surface. Various ion species are detected such as: FeO^+, NiO^+, Fe_2O^+, Ni_2O^+, FeO_2^+,

NiO_2^+ and $FeNiO^+$. The detection of iron oxides dominates compared to Ni oxide species as shown in the figure. Overall, the ion distribution map shows a well-mixed NiFe substrate and distinct development of oxide on the top of the surface.

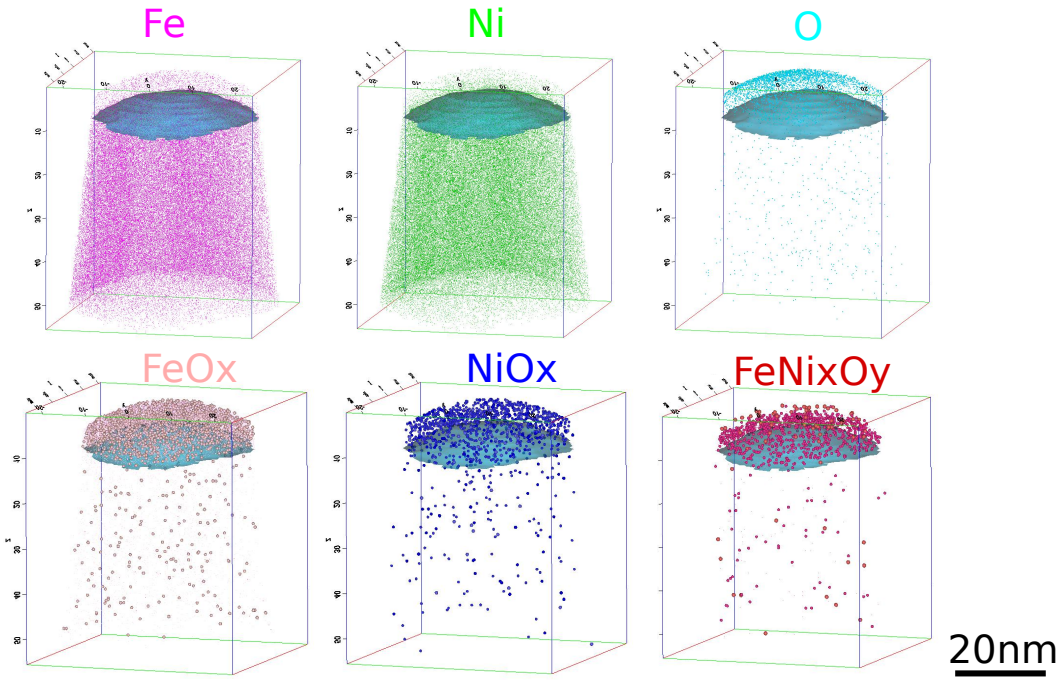

Figure 4.2.1 – Ion maps of a Ni10Fe90 sample oxidised at 353K for 30 minutes in 45 mbar O_2. Iso-surface plane indicates the boundary of oxides and substrate.

Detailed analysis of the oxide phase above the oxide-metal interface was performed using the proximity histogram method [292]. For this, the O concentration was used to construct the iso-surface defining the measurement, setting it at 5 at.%. In Figure 4.2.2, proxigrams of samples as listed in Table 4.2.1 are shown. Across all the samples with increasing oxidation times, the measured thickness of the oxides is always less than 5nm. It therefore seems that there is a barrier for the continuous development of oxides. On the other hand, a composition variation through the oxide layer (in the z direction) is also evident. Firstly, it can be confirmed that there is a multi-layer structure within the oxide formed and they are labelled as surface oxide, intermediate oxide and Fe-depleted region, respectively.

Fe-depleted region Beneath the substrate-oxide interface (towards the substrate side), Fe shows a decreasing profile, which is evidence for the outer diffusion of Fe during oxide formation. The thickness of the diffusion depth varies from 1 nm to 4 nm. There is a small increase of Ni content from 10 at.% to 15 at.% on the metal-oxide surface in the 30 minutes oxidised sample (as shown in Fig. 4.2.2a), which is believed to be caused by Fe out-diffusion to the oxide layer, leaving the region Ni enriched.

Intermediate layer In all measurements shown in Fig. 4.2.2, oxide formed directly above (towards the oxide side) the substrate-oxide surface has the same composition, which is 60 at.% Fe, 10 at.% Ni and 30 at.% O. These concentrations do not match any stoichiometric oxide, and it is proposed that Fe and/or Ni are not fully oxidised at this stage. The composition is consistent within a short depth, which is 1 nm for oxide formed at 353K and 2nm for oxide formed at 473K. Higher temperatures appear to facilitate the development of this intermediate layer.

Surface Oxide Above the initial intermediate oxide layer, oxygen content is increased while the fraction of metallic ions decreases. The Ni content decreases to almost 0 at.% as shown in Fig. 4.2.2a and 4.2.2c). The Ni content in the 473K oxidised sample is kept steady either due to higher temperature or grain boundary diffusion, which is discussed later. On the gas-oxide interface, Ni enrichment is observed on the very surface, 0.5nm thick (as shown in Fig. 4.2.2a). This enrichment is not however across the entire surface but only concentrated on certain crystallographic pole directions, which will also be discussed in detail later. Overall, through the application of iso-surface analyses, it can be considered that the formation of an initial intermediate $Fe_{60}Ni_{10}O_{30}$ layer acts as a barrier to further oxidation development. With the increase of oxidation time, there is no change in the composition of this initial layer, but the oxygen content increases on the very oxide surface whilst the metal loading decreases, a clear sign of further oxidation of metal ions.

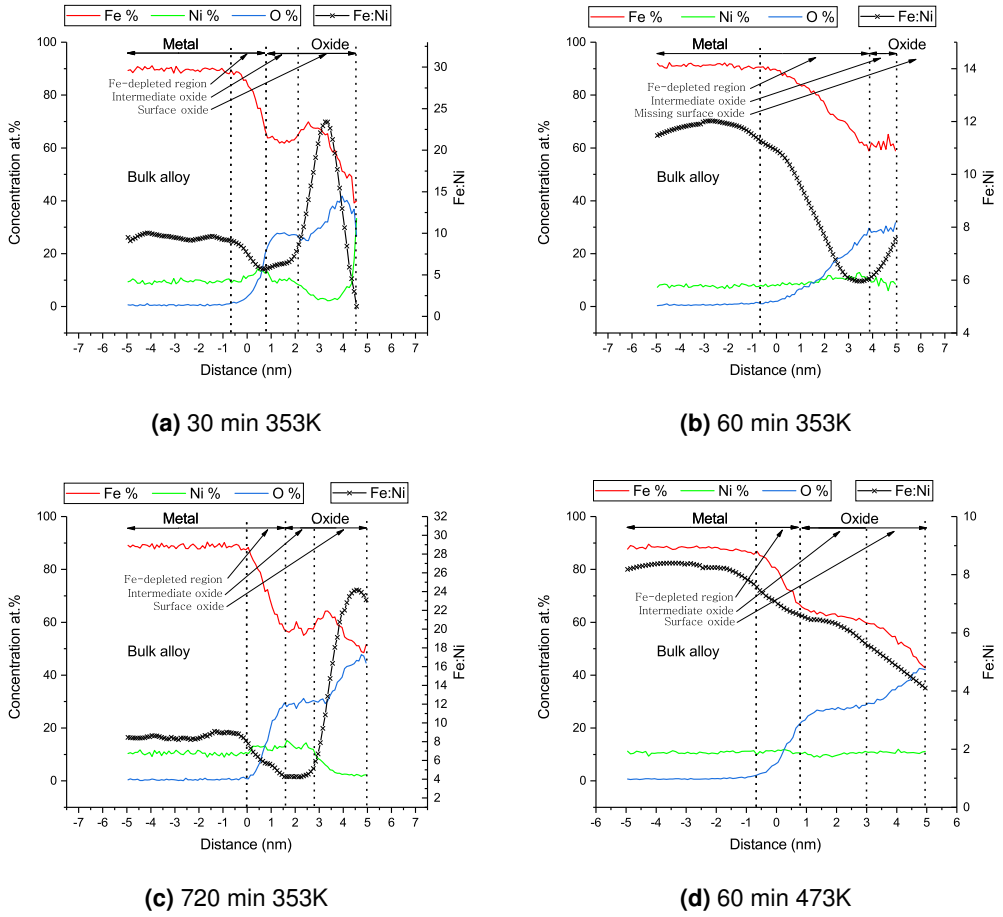

(a) 30 min 353K

(b) 60 min 353K

(c) 720 min 353K

(d) 60 min 473K

Figure 4.2.2 – Proximity histograms of oxidised Ni10Fe90 samples based on iso-surfaces defined by 5 at.% oxygen concentration. Note that sample d contains grain boundary, which facilitates Ni outer-diffusion.

With further localised analysis, the surface enrichment of Ni as shown in Fig. 4.2.2a is mostly located on [110] pole. The location of this [110] pole is determined by the ion density projection as shown in Figure 4.2.3. The low-density region in the centre of the data is identified as the [110] direction through an SDM calculation during the reconstruction procedure. Three respective 1D concentration analyses defined by $6nm \times 6nm \times 60nm$ cylinders are applied to this particular reconstruction (30 minutes oxidised Ni10Fe90). The first ROI cylinder is positioned through the [110] pole and the other two are in close proximity but not on any particular crystallographic feature. The results of these 1D concentration profiles are plotted in Fig. 4.2.4. There is a clear difference in terms of the top surface composition.

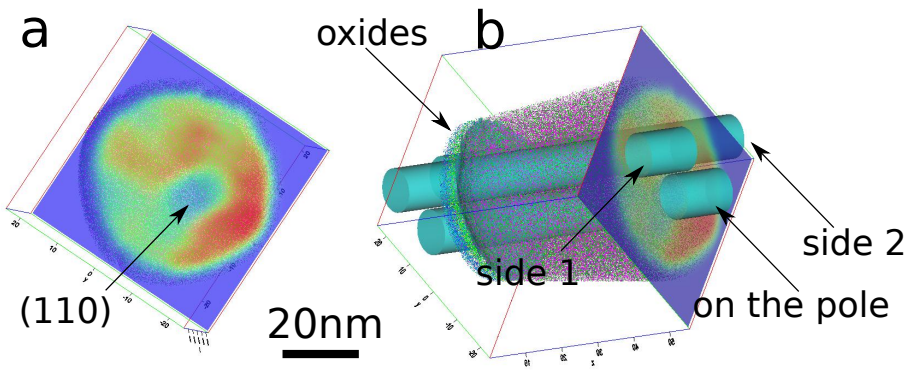

Figure 4.2.3 – 1D concentration analyses on the 30 min 353K oxidised Ni10Fe90 sample. a) density of the Fe ions within the sample b) 1D concentration analyses on three different locations. One is on the [110] pole and the other two are reference points.

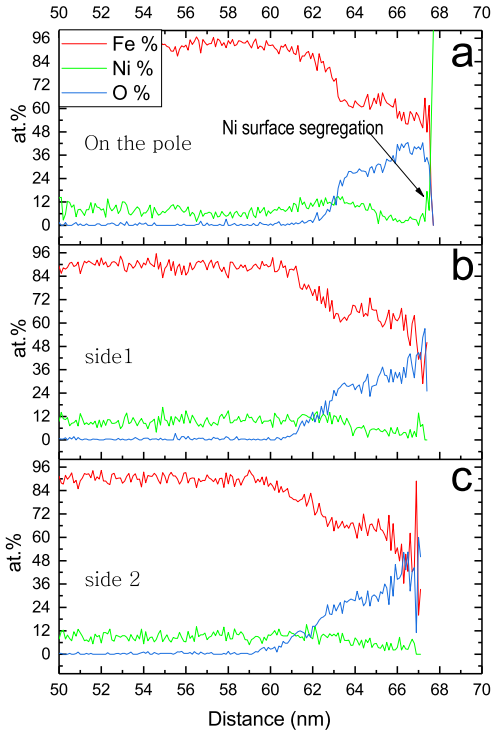

Figure 4.2.4 – 1D profiles of the three regions marked in Fig. 4.2.3. a) profile on the pole b) profile of the side 1 c) profile of the side 2. The base composition is clearly shown as 90 at.% Ni and 10 at.% Fe. Surface enrichment of Ni is observed on the [110] pole whereas there are no such features on the other two control analyses.

Ni enrichment (green curve) is observed on the [110] pole whereas the other two reference analyses show no significant Ni enrichment. Although the 100 at.% Ni reading at the top as shown in Figure 4.2.4a is unlikely to be an accurate measurement due to the small sampling size, the trend of rising Ni content should however be authentic. Considering the control experiments done on the as-received samples (Table 4.1.3), this Ni enrichment should not be an artefact of preferential evaporation.

Such Ni surface enrichment is also observed in the 720 min 353K oxidised sample, but on different crystallographic poles. In Fig. 4.2.5 a and b, the [002] and <013> poles are identified via the atom probe detector hit maps and the application of a Fe density iso-surface to the reconstructed data, respectively. In Figure 4.2.5 c, an iso-surface is defined by 13.8 at.% Ni. The high Ni content is observed overlaid on the <013> poles, leaving the [002] pole depleted with respect to bulk Ni. Ni thus seems more likely partition along the high indexed poles in this sample. In the 1D concentration analyses shown in Figure 4.2.6, the Ni enrichment is confirmed on the very surface (about 0.5nm thick as seen in bar 1-4), while there is no such enrichment on the control profile (bar 5).

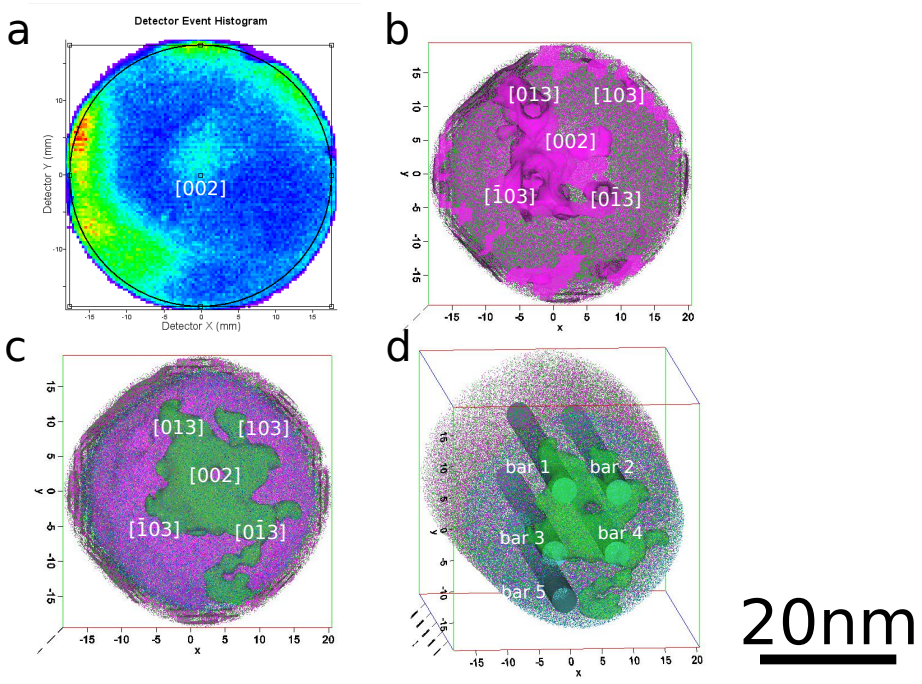

Figure 4.2.5 – Surface segregation of Ni on a 720 min 353K oxidised Ni10Fe90 sample (bcc). a) [002] pole has identified in the hit map. b) 4 <013> poles are identified via iso-surface of Fe density. c) Ni enrichment in the oxide is identified via iso-surface of dissociated Ni ions d) The exact locations of 1D concentration ROI cylinders used in the analysis.

Apart from Ni segregation along various poles to the oxide surface, grain boundaries embedded in the tip region also acts as a fast diffusion path for Ni during oxidation. In a 60 min 473K oxidised sample, a grain boundary is identified as shown in Fig. 4.2.7. The iso-surface, shown in green created by$log_{10}(Fe/Ni)$ 0.8, highlights the grain boundary for iden-

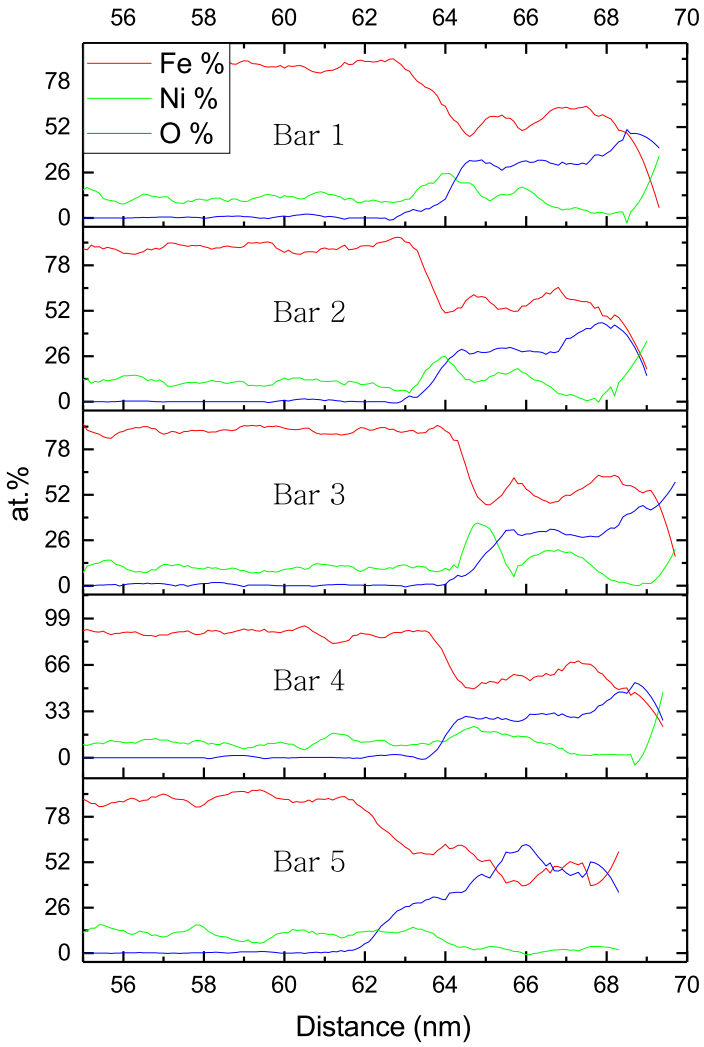

Figure 4.2.6 – 1D concentration profiles of the five bars (4nmx4nmx60nm) as shown in Fig. 4.2.5d. Ni enrichment on the very surface is evident from the results of bar 1-4 whereas no such evidence is shown in bar 5.

tification. It is clear that the grain boundary is perpendicular to the sample surface. In order to understand the segregation behaviour, a 1D concentration bar ($30nm \times 30nm \times 100nm$) is applied perpendicular to the grain boundary, as shown in Fig. 4.2.7b. The result is plotted in Fig. 4.2.8. Enrichment of Ni along the grain boundary is evident, with the concentration of Ni changing from 10 at.% to 14 at.%, while the Fe concentration decreases accordingly. Adjacent to the enrichment area, a decrease of Ni concentration below the nominal 9 at.% is observed whilst the Fe content increases. Ni is therefore believed to be diffusing to the

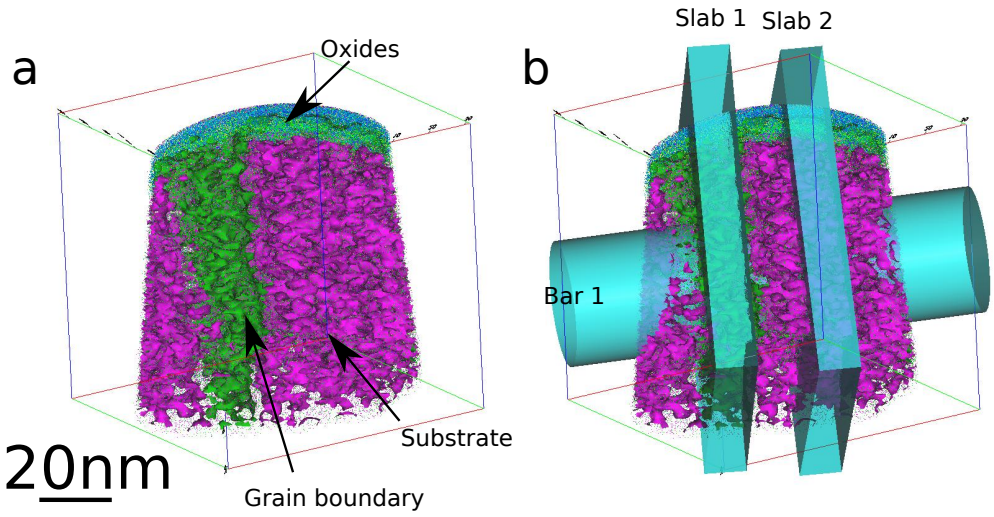

Figure 4.2.7 – a) Grain boundary identified in a 60 min 473K oxidised Ni10Fe90 sample. The Grain boundary is directly connected to the region of surface oxide. b) ROIs applied to the oxidised sample are labelled as Bar 1, Slab 1 and 2.

grain boundary during the oxidation process. The total diffusion distance is 20nm, counting from both sides of the grain boundary. Furthermore, an anisotropic diffusion profile across the grain boundary is observed. In Fig. 4.2.8, the left side of the grain boundary has a more gradual and longer diffusion zone whereas a shaper profile is on the right side. This difference could reflect different diffusion coefficient values in different crystallographic directions existing on the two sides of the grain boundary.

In order to understand the microstructure parallel to the grain boundary (from the surface to the material inside), two slab-like ROIs are placed on the grain boundary and close-by as a second reference point (both shown in Fig. 4.2.7b). The size of the slab is $10nm \times 80nm \times 80nm$. The 1D concentration profiles (along the z axis) of the 2 ROIs are plotted in Fig. 4.2.9. Ni enrichment towards the sample surface is clearly observed in both results, which is not unexpected since Ni diffusion along grain boundary is identified. In the slab 1 profile, the Fe content is about 84.7 at.% and the Ni content is about 14.2 at.%. In comparison, the Ni content from the slab 2 profile remains at 10 at.% except at the very surface. Through this comparison it is again clear that Ni is enriched on the grain boundary. In addition, this enrichment along the z axis shows a linear profile compared to the controlled analysis. A linear fit is applied from 20nm to 65 nm, and the slope indicating the

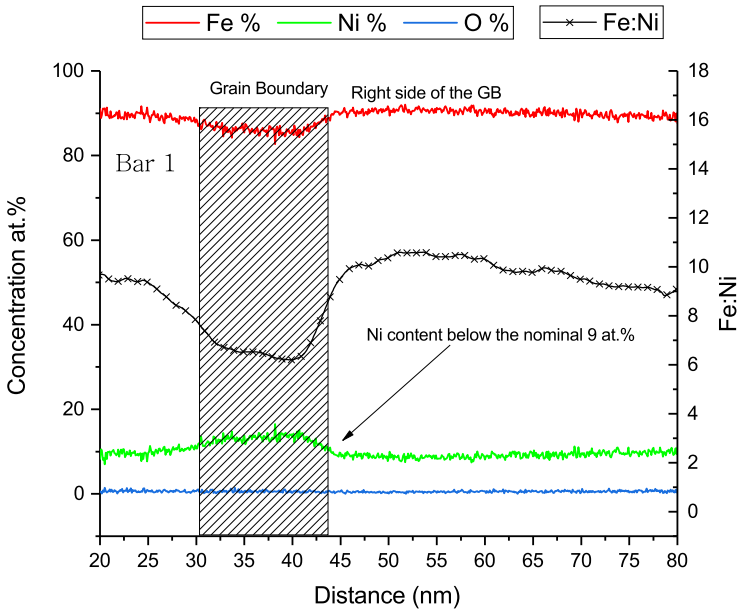

Figure 4.2.8 – 1D concentration profile perpendicular to the grain boundary, which is identified in Figure 4.2.7 (Ni10Fe90 60 min 473K oxidation). The size of the bar is $30nm \times 30nm \times 100nm$. Ni enrichment is seen in the grain boundary. Low Ni content (below 10 at.%) on the right side of the grain boundary is seen indicates Ni outer diffusion through the grain boundary towards the surface. (right Y axis represent Fe:Ni ratio)

rate of change of Ni concentration is -0.027 at% per nm for slab 1 and -0.008 at.% per nm for slab 2). Assuming the rest of sample is in similar configuration (i.e. APT analysis did not incorporate the entire grain boundary), the diffusion depth of Ni is as deep as 250nm, much higher than the diffusion depth on any crystallographic surfaces analysed. From the data isolated within slab 1 and slab 2, it is also observed that the O, Fe and Ni contents are similar on the sample surface regardless of the existence of grain boundary. Ni, which is fast diffusing along the GB, also move fast laterally once it reaches the surface.

Overall, oxidation of the Ni10Fe90 samples shows that oxidation development is limited to a thin layer under the experimental conditions applied in this study. The composition of the oxidation scale is consistent (detailed information will be included in the discussion section together will other alloys). The <110>, <103> axes and grain boundaries act as the fast diffusion routes for Ni migrating towards the sample surface. The effect of the grain boundary is substantially stronger than any partitioning along the zone axes.

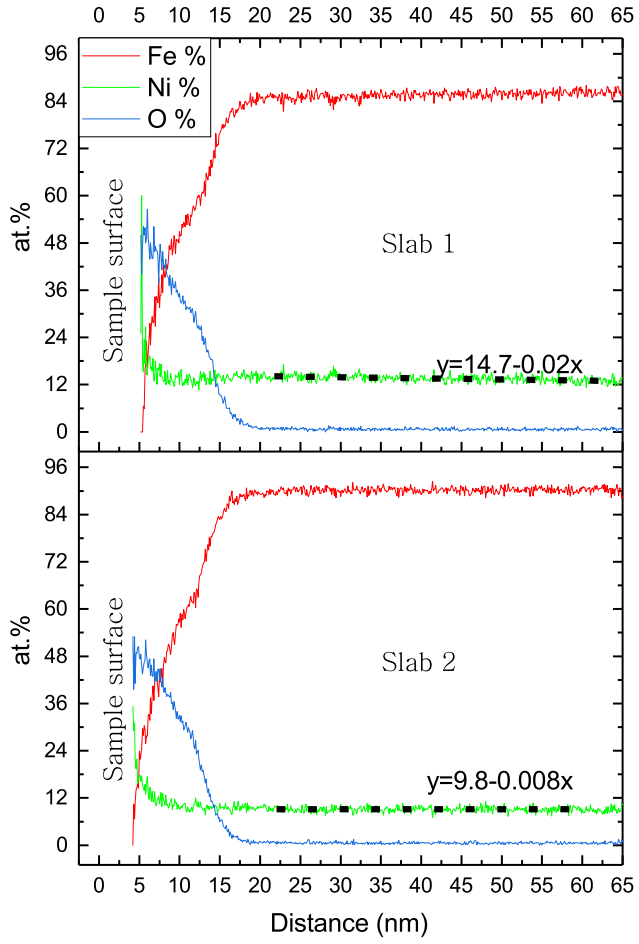

Figure 4.2.9 – 1D concentration profiles of slab 1 and slab 2. Each slab has a dimension of $10nm \times 80nm \times 80nm$. Slab 1 is placed overlapping the identified grain boundary and Slab 2 is placed close-by as reference.

4.2.2 Oxidation of Ni48Fe52 alloy

Oxidation of Ni48Fe52 samples is conducted in the same manner as the Ni10Fe90 samples. The detailed experiment list is shown in Table 4.2.2. Due to the low yield of successfully analysed samples, there are again only 4 usable datasets. However, the results obtained still provide important information about the development of oxidation.

Oxidation Temp. 353K	Oxidation time/min	30	360	1200
	Number of experiments	1	1	1
Oxidation Time 240min	Oxidation temp./K	493		
	Number of experiments	1		

Table 4.2.2 – Ni48Fe52 oxidation in 45mbar oxygen at 353K and 493K. There are 3 successful runs on 353K oxidised samples and one on 493K oxidised sample. The oxidation was carried out under 45mbar oxygen after FIM surface cleaning.

Oxide development is observed with the increase of oxidation time at a 353K for this alloy composition. The results are presented in Figure 4.2.10. Iso-surfaces, defined by 1.57 at.% FeO^+ and shown in red, are used to mark the boundary between developed oxide and substrate in the APT datasets. It is clear that oxidation develops significantly with increasing oxidation time. In Figure 4.2.10 a, oxide occurs on just one corner at the surface. In the slightly longer 360 min oxidation, oxide covers the entire top surface and its thickness has developed significantly to 7nm. The following 1200 min oxidation shows further oxidation both on the top and side of the dataset. The thickness of the oxide increases to 14 nm in average. Through these three datasets, it is clear that oxide development in Ni48Fe52 at 353K is dependent on exposure time, unlike that observed in the case of Ni10Fe90.

Inspection of the oxide composition can also provide insight into the oxidation development. Proxigrams based on the iso-surfaces as shown in Fig. 4.2.10 are plotted in Fig. 4.2.11. For the initial 30 min oxidation, oxygen content increases towards the surface with a decrease of Ni and Fe, showing that oxygen is mixed with the metallic elements. Because of the limited volume of oxide available for analysis, it is not clear about any preferential diffu-

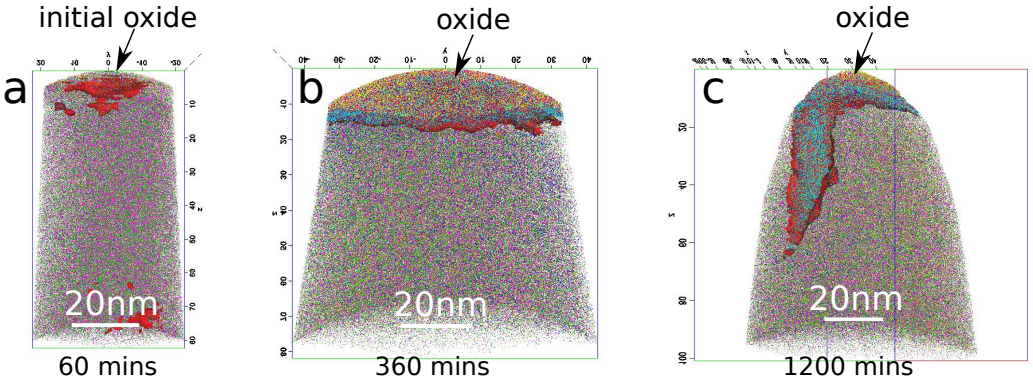

Figure 4.2.10 – Oxidation evolution of Ni48Fe52 samples at 353K. a) 30 min oxidation b) 360 min oxidation and c) 1200 min oxidation. All the oxidation is conducted under 45 mbar oxygen after FIM cleaning of these sample surfaces. Oxidation development with increasing time is evident among these three samples.

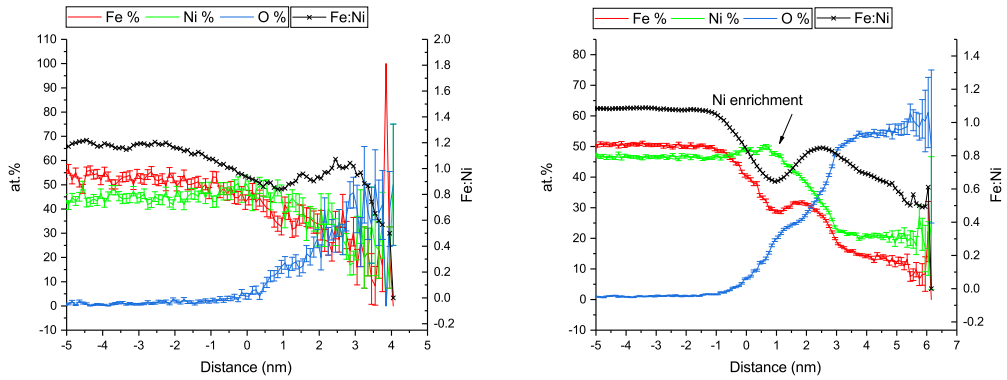

(a) 30 min

(b) 360 min

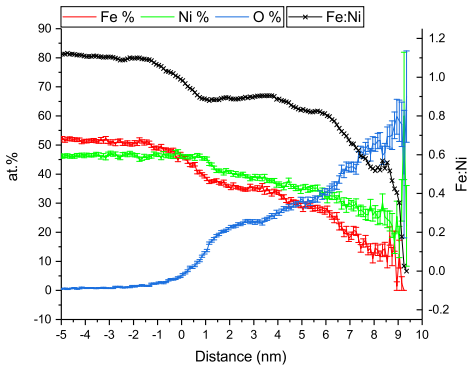

(c) 1200 min

Figure 4.2.11 – Proxigrams based on FeO^{+} iso-surface of Ni48Fe52 samples 353K. The samples were oxidised under 45 mbar oxygen after FIM surface cleaning.

sion of either Ni or Fe. In the following 360 min oxidation, an oxide with a layered structure is observed. On the substrate-oxide interface, there is a strong Ni enrichment, reaching 50 at.%. This Ni enrichment (also presented in a longer oxidation as shown later on in Figure 4.3.2b), is the evidence of the preferential diffusion behaviour of Ni and Fe. Above this layer, the formation of an oxide with composition of Fe_2Ni_2O is observed but only having thickness around 1 nm. Further close to the surface, the oxide seem to reach a stable composition, which is 14 at.% Fe, 20.8 at.% Ni and 54 at.% O in this case. This composition is similar to the Fe, Ni spinel composition: $FeNi_2O_4$ ($Fe_{15}Ni_{30}O_{60}$). This spinel-like composition is also obvious in the 1200 min oxidised profile shown in Fig. 4.2.11c. The element content of the outermost oxide layer is 13.8 at.% Fe, 29.2 at.% Ni and 59 at.% O, which is the stoichiometric composition of the spinel. Comparing the respective Fe profile for both the 360 min and 1200 min oxidation exposures, it appears that the levels of Fe in the outermost $FeNi_2O_4$ is less than Ni, which is indicative of the Ni enrichment on the surface with respect to Fe. Furthermore, an additional feature is that the spinel-like region has a constant thickness, about 3nm, in both the 360 min and 1200 min oxidised samples but the intermediate oxide layer directly above the substrate has a substantial increase in thickness for the 1200 min oxidised sample, of approximately 10nm.

It is also of interest to investigate the relationship between zone axis and preferential diffusion. In Fig. 4.2.12, the [111] pole has been identified via an Fe density iso-surface (the density value is set as $17 atoms/nm^3$). An Ni ion iso-surface is also applied (as Ni concentration 40 at.%) indicating the position of the pole running vertically through the middle of the reconstruction. In the analysis, there is no enrichment of Ni in the oxide directly above the pole. Combining this with the observation as listed in Table 4.1.3, it can be seen that there is no preferential diffusion along zone axes.

In the 1200 min oxidised sample, the oxide detected in the reconstruction develops in two locations: top oxide and side oxide (as shown in Fig. 4.2.13a). In most oxidized APT tips investigated in this thesis, oxide only forms on the top of the tip, which is along the APT analysis direction. APT has a well-known aberration along the z-axis due to preferential

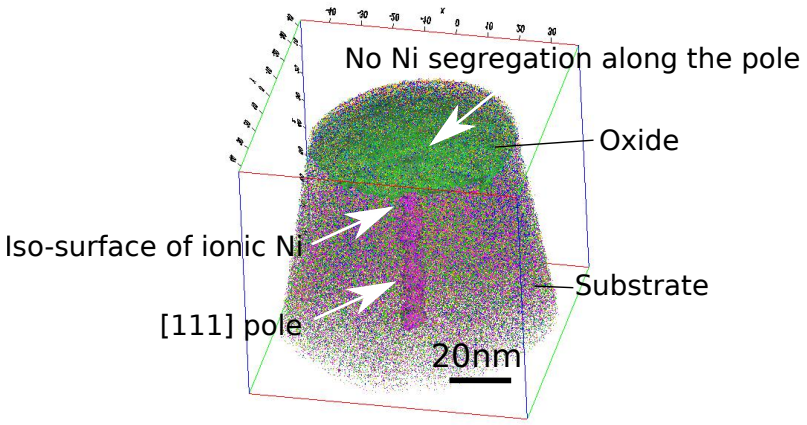

Figure 4.2.12 – Pole identification and Ni iso-surface identification of the 360 min 353K oxidised Ni48Fe52 sample. There is no evidence of preferential oxidation along the pole direction.

evaporation, which can induce errors into the accurate spatial positioning in this direction [293]. Therefore, having oxides present at both the top and side of the reconstruction represents a unique chance to perform oxide analyses from two different orientations to verify the integrity of the measured oxide composition. In Fig. 4.2.13a, two analysis cylinders are placed perpendicular to both top oxide and side oxide. Their resulting profiles are plotted in Fig. 4.2.13b and c. The $FeNi_2O_4$ spinel is shown in the "bar 2" profile, extracted from the top oxide, together with an intermediate oxide layer between the spinel and metal substrate. In comparison, the profile derived in "bar 1" from the side oxide shows a thick oxide layer, the composition of which is closer to the intermediate layer identified in "bar 2". This could be interpreted that the observed side oxide belongs as part of a larger well-developed oxide, the top section of which is however not sampled by the APT analysis. Overall, this could be interpreted that there is no difference induced in the composition measurements with respect to particular oxide species from different analysis directions. This confirmation is crucial to understand other oxidised samples.

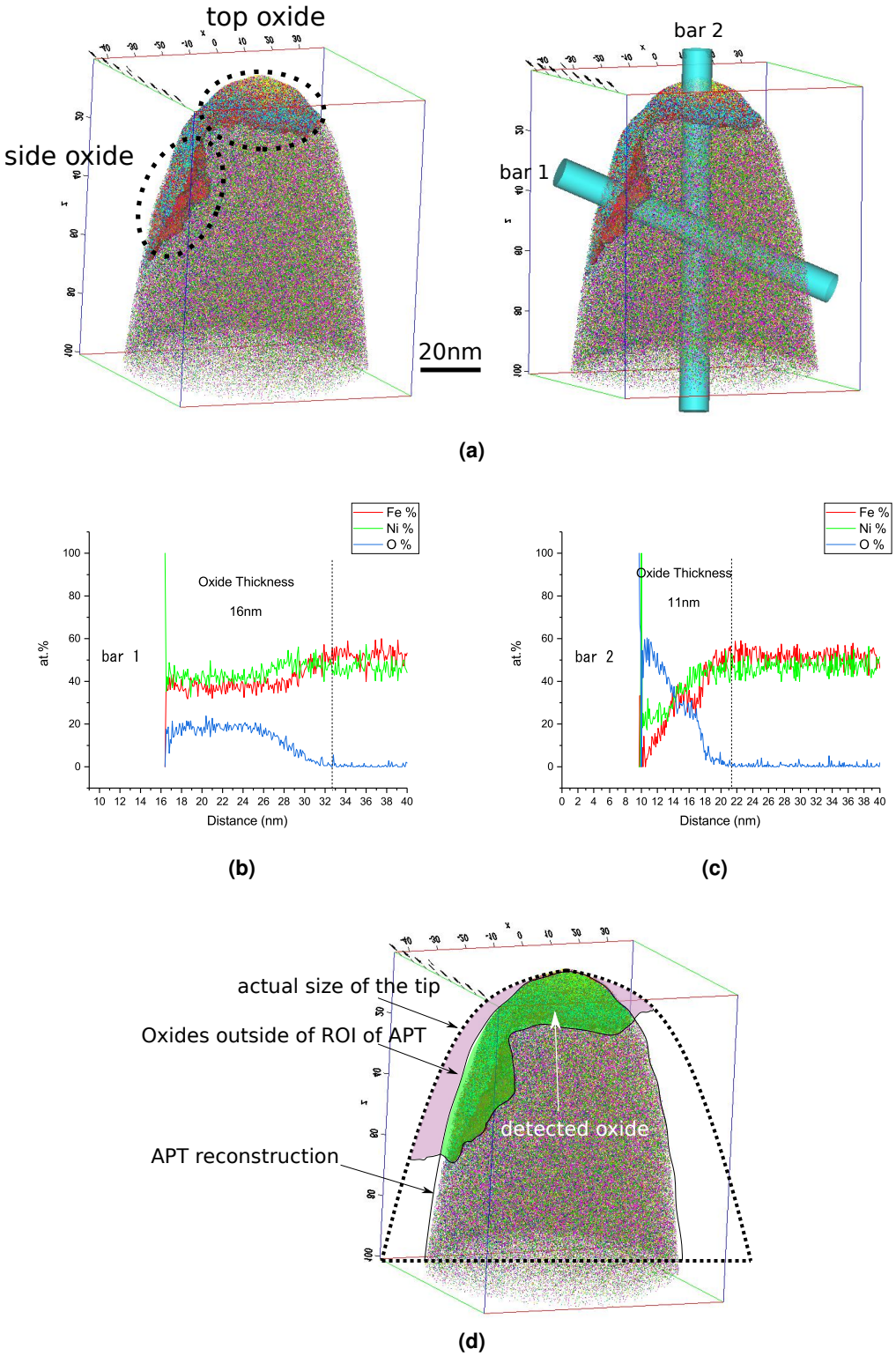

Figure 4.2.13 – Oxidation development on the 1200 min 353K oxidised sample. a) tip oxide and side oxide have been identified. Two 1D concentration bars are located on the side oxide and top oxide b) 1D concentration profile of bar 1 c) 1D concentration profile of bar 2. d) a schematic view of the actual oxidised tip versus APT reconstruction

4.2.3 Oxidation of Ni90Fe10 alloy

Similar oxidation experiments for the Ni90Fe10 samples were performed, as detailed in Table 4.2.3. With this particular composition, there are two series of experiments conducted: various oxidation times at constant temperature, and various oxidation temperature at a constant time. The initial oxidation behaviour of this composition is of particular of interest due to the inconsistency of oxide formation. Therefore multiple repeat experiments were conducted under the conditions of 30 min and 353K. However there is hardly a discernible trend in the oxide development of Ni90Fe10. The oxide thickness changes not according to the oxidation time nor to the temperature in the limited measurements. Therefore, each individual analysis is presented .

Oxidation Temp. 353K	Oxidation time/min	30	60	120	360	1000
	Number of experiments	3	1	1	1	1
Oxidation Time 60 min	Oxidation temp./K	353	393	433	473	673
	Number of experiments	1	1	1	2	2

Table 4.2.3 – Ni90Fe10 oxidation in 45 mbar oxygen. There are two batches of experiments: various oxidation times at constant temperature (353K) and various oxidation temperatures at constant time (60 min).

30 min 353K oxidation The APT reconstruction of a 30min 353K oxidised sample is shown in Fig. 4.2.14. The development of the oxide is located on the top surface of the reconstruction. Judging from the reconstruction, the thickness of the oxide is about 2nm. The blue iso-surface is created to illustrate the difference between the oxide and substrate defined by O 1.52 at.%. Proxigram analysis from this iso-surface shows oxygen clearly on the sample surface (in Fig. 4.2.14b). The composition on the surface is Ni 60 at.%, O 22 at.% and almost no Fe. It is clear in this oxide, Ni is not fully oxidised into the form of NiO, which might be a result of the short oxidation time. Profiles of Fe and Ni show that the process is Ni diffusing outwards, forming the oxide. Fe also participates during the oxidation, since there is a low Fe content within the oxide region. However, the

development of this oxide is not at all similar to another observation of a 30 min oxidised sample. The reconstruction of the second oxidised sample is shown in Fig. 4.2.15. One of the major differences is the thickness of the oxide scale. The oxide development in this second observation is about 17nm, much thicker than the previous one. In terms of composition, the two cases present quite similar measurements. The second analysis after 30 min has a surface composition of 60 at.% Ni, 30 at.% O and 7 at.% Fe. Overall, it is seen that the composition is consistent under these initial oxidation conditions, with Ni not fully oxidised. The Fe content is low/negligible in the formed oxide, indicating Ni diffusing towards the surface is the main mechanism for the oxide formation.

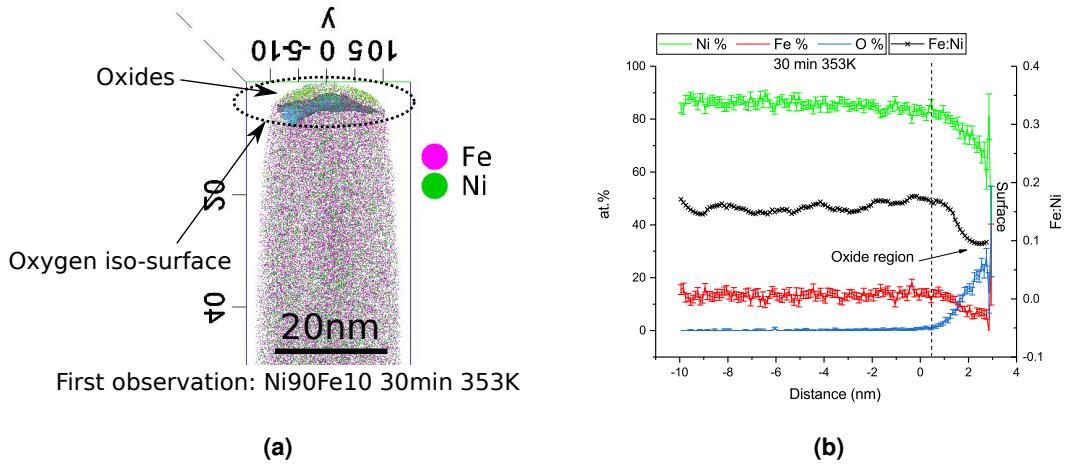

Figure 4.2.14 – a) 30min 353K oxidation of a Ni90Fe10 sample. The oxide only develops on the top surface of the reconstruction. An iso-surface was applied based on the O decomposed ions and the level is set as 1.52 at.%. b) Proxigram based on the oxygen ion iso-surface.

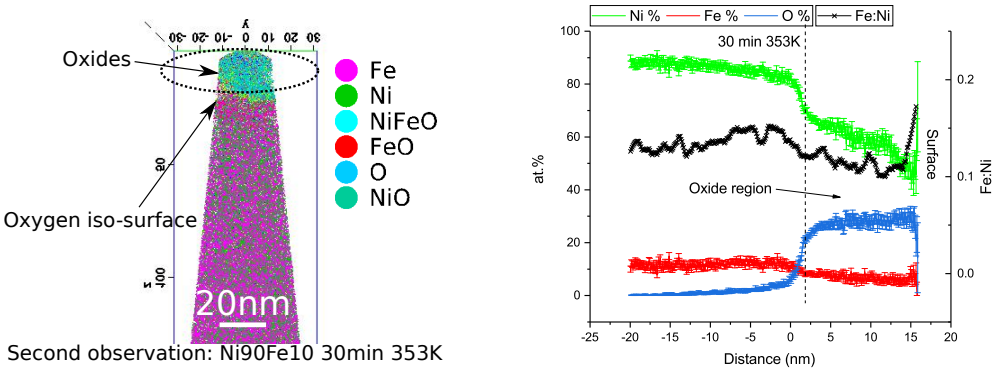

Figure 4.2.15 – a) Second observation of a 30min 353K oxidation of one Ni90Fe10 sample. The oxide develops on the top surface of the reconstruction with a thickness about 17 nm. An iso-surface was applied based on the O decomposed ions and the level is set as 8.63 at.%. b) Proxigram based on the oxygen ion iso-surface.

60 min 353K oxidation Oxidation for a longer period of 60 min was conducted and the result is shown in Figure 4.2.16. In the reconstruction, it is apparent that there is an excess of Ni on the top section of the reconstruction (~80nm). On the very top of this reconstruction, oxide species are found with a thickness of 5-10 nm. In order to understand the composition more clearly, a 1D concentration analysis is applied through the reconstruction as shown in the figure ($30nm \times 30nm \times 180nm$). This shows a substantial enrichment of Ni towards surface with almost no Fe. Oxide development is minimal, with only a thickness of 6nm. It is however interesting to observe the diffusion of O into the Ni enriched region. Although, the average concentration of O is only about 3 at.%, it does penetrate into the sample to a depth of about 80nm. Overall, the oxidation mechanism presented in this observation is clearly unique. An enriched Ni layer facilitates the inner diffusion of O into the metal region.

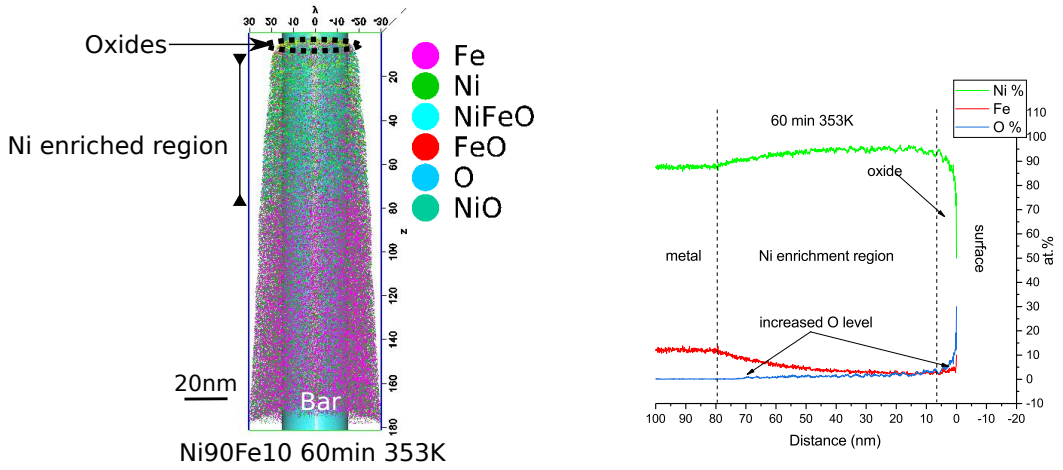

Figure 4.2.16 – a) An observation of a 60 min 353K oxidation of one Ni90Fe10 sample. The oxide develops on the top surface of the reconstruction with a thickness about 6 nm. However the Ni enrichment is as thick as 80 nm. b) 1D concentration analysis through the bar placed in the middle of the reconstruction.

120 min 353K oxidation A 120 min oxidation was conducted to further explore the oxidation trends under increasing oxidation time, and the result is shown in Figure 4.2.17. In Figure 4.2.17a, the reconstruction shows that entire dataset is oxide. The height of the reconstruction reaches about 80nm, indicating the oxide at least has a thickness of 80 nm (analysis length limited by sample fracture). In the 2D density plot of atomic Ni (i.e. decomposition of all Ni containing ions), a high-density region within the reconstruction is apparent, which could be an indication of a particular oxide developing path. The 1D concentration analysis through the z-direction is shown in Figure 4.2.17b. This confirms that the oxide has the nominal composition of NiO. Slight Ni enrichment is observed on the surface ~2nm, which could be contributed from the Ni enrichment region as shown in the density plot. Another 1D concentration analysis from the side direction (xy) confirms the NiO stoichiometry is genuine but with a small fluctuation of O content. A slightly higher content of Ni over O is apparent on the right side of the figure. However at the other end of the profile, the O content is higher than that of the Ni. This variation is mostly due to the existence of an Ni enrichment region within the dataset. From the two profiles, it is clear

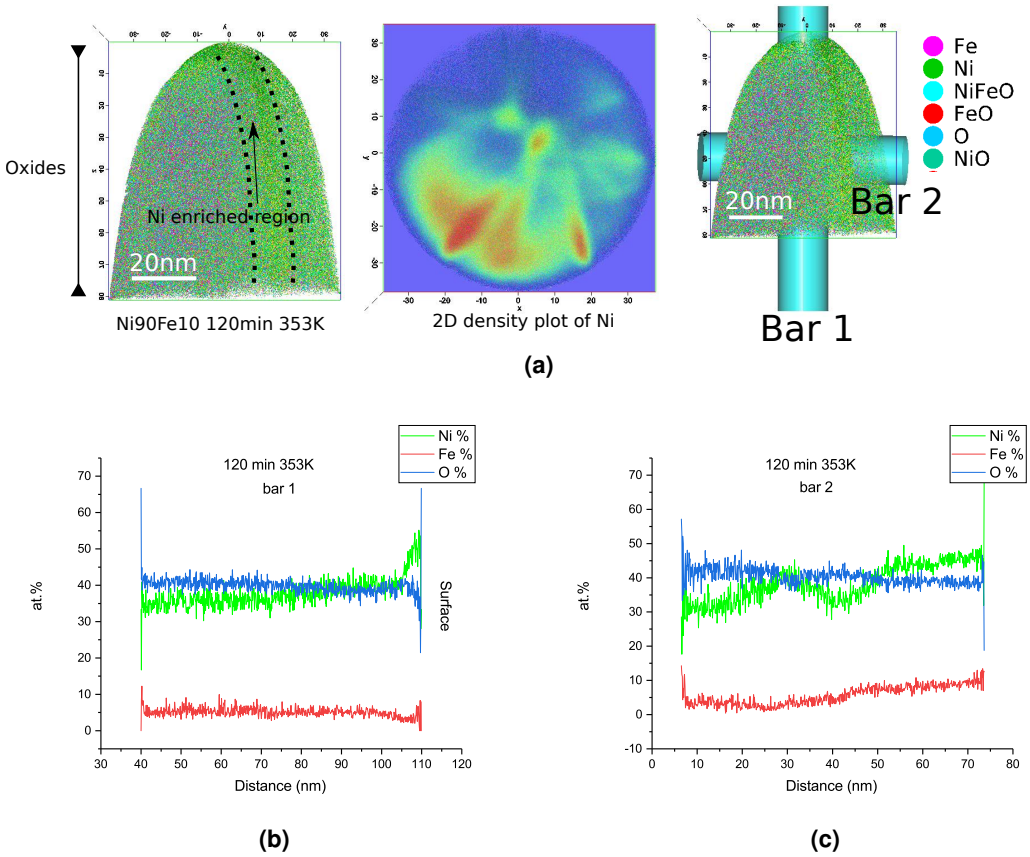

Figure 4.2.17 – a) Analysis of a 120min 353K oxidised sample. The entire reconstruction is made of oxide containing 5M data points. Local variation of oxide composition has been found within the oxide. b) 1D concentration analysis along the z direction of the reconstruction and c) 1D concentration analysis along the x direction.

that the development of oxide even within the formed *NiO* is not uniform and it strongly depends on the local sample defects.

360 min 353K oxidation Since it is hard to make firm conclusions about the oxidation behaviour of Ni90Fe10 from the previous short oxidation times, an even longer oxidation was conducted (360 min) and reconstruction of this APT analysis is shown in Figure 4.2.18a. Oxide development occurs on the top and side of the tip. An *NiO* ion iso-surface was applied to separate the oxide and substrate, and a proxigram based on this iso-surface is plotted in Figure 4.2.18b. The profile shows a similarity to the 30 min and 120 min oxidised samples, having an oxide composition of Ni 60 at.%, O 30 at.% and Fe 10

at.%. Ni diffusing outwards is the apparent mechanism for the oxide formation. However, it is more interesting to discover that there is a difference when analysing the oxide from two different directions, shown as bar 1 and bar 2 in the figure. Bar 1 is placed along the z axis while bar 2 is placed perpendicular to the identified *NiO* iso-surface. Comparing the two profiles in c) and d), there is no difference in the oxide composition on the surface, but the out-diffusion profile of Ni from the side is substantially thicker, reaching 25nm whilst the oxygen profile is similar in both directions. The thick Ni diffusion region may indicate anisotropic oxide development, dependent on different directions of the grain/sample.

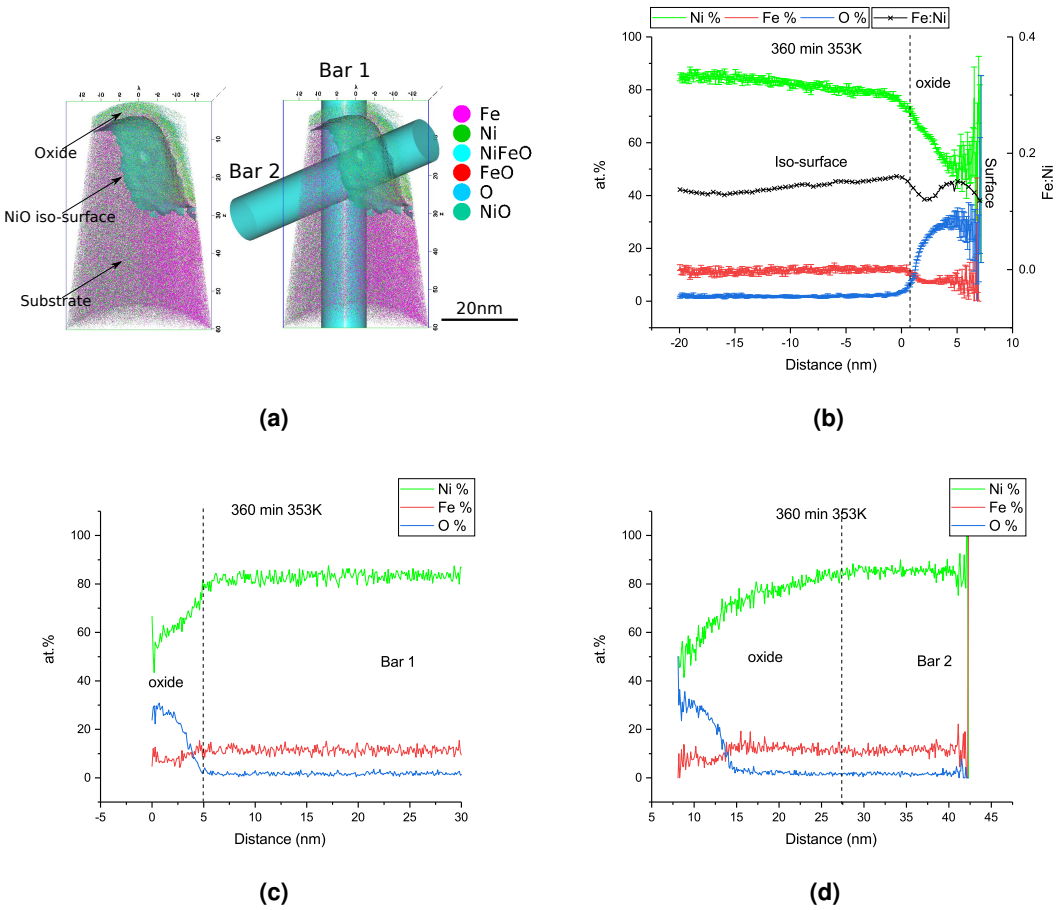

Figure 4.2.18 – a) An observation of a 360 min 353K oxidised Ni90Fe10 sample. The iso-surface is set as *NiO* concentration at 4.5 at% b) Proxigram based on the iso-surface c) and d) 1D concentration profiles of bar 1 and bar 2 as shown in the sub-figure a.

1000 min 353K oxidation A 1000 min oxidation also at 353K, was conducted and the APT reconstruction is present in Figure 4.2.19a. There is only minimal oxide development on the top of the surface. The oxide is about 5nm thick and the composition is again Ni 60 at.%, O 30 at.% and 10 at.% Fe.

In summary, despite all the information gathered about oxidation of Ni90Fe10 over various oxidation times, a clear trend in oxidation behaviour for this alloy composition is not apparent. A thin oxide layer of ~ 5nm, with a typical composition of $Ni_{60}Fe_{10}O_{30}$ is commonly observed for most analyses. However, there are variations if any rapid oxide development mechanism is present and when NiO is detected. Local features, such as different crystal orientation, could also influence the Ni diffusion profiles and affect oxide formation.

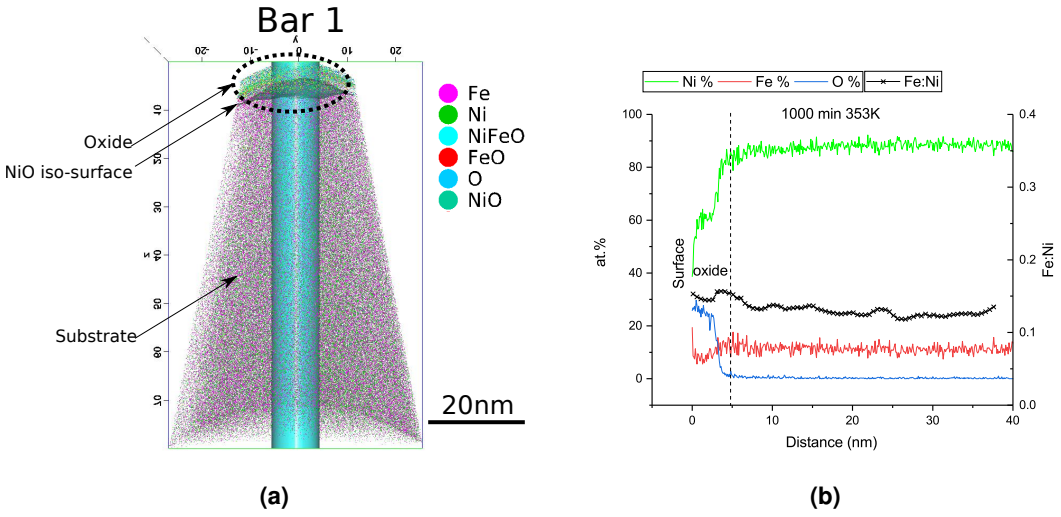

Figure 4.2.19 – a) An observation of 1000min 353K oxidised Ni90Fe10. b) 1D concentration based on bar 1 shown in a).

393K 60 min oxidation Having established experiments with constant oxidation temperature, it is also of interest to observe oxide development as a function of increasing oxidising temperatures. An observation of 393K 60min oxidised sample is shown in Figure 4.2.20. Increasing the oxidation temperature seems have direct impact on the development of the surface oxide, which is about 18nm thick (as measured by the distance of the iso-surface to tip surface). There is a unique feature isolated by applying the iso-surface, which is a protrusion of a less oxidised region located in the middle of the oxide. By applying a 1D concentration profile through this feature and for comparison an adjacent volume, in Figure 4.2.20b and 4.2.20c, it is clear that less oxide has developed along this feature. In terms of composition, $Ni_{60}O_{30}Fe_{10}$ is observed again in both profiles. Given the shape of the protrusion, it is easy to associate it to a crystallographic pole direction running through the length of the sample, although difficult to assign to a specific orientation in this dataset. However, oxidation development on a featureless surface may also experience a difference in the oxidation rate.

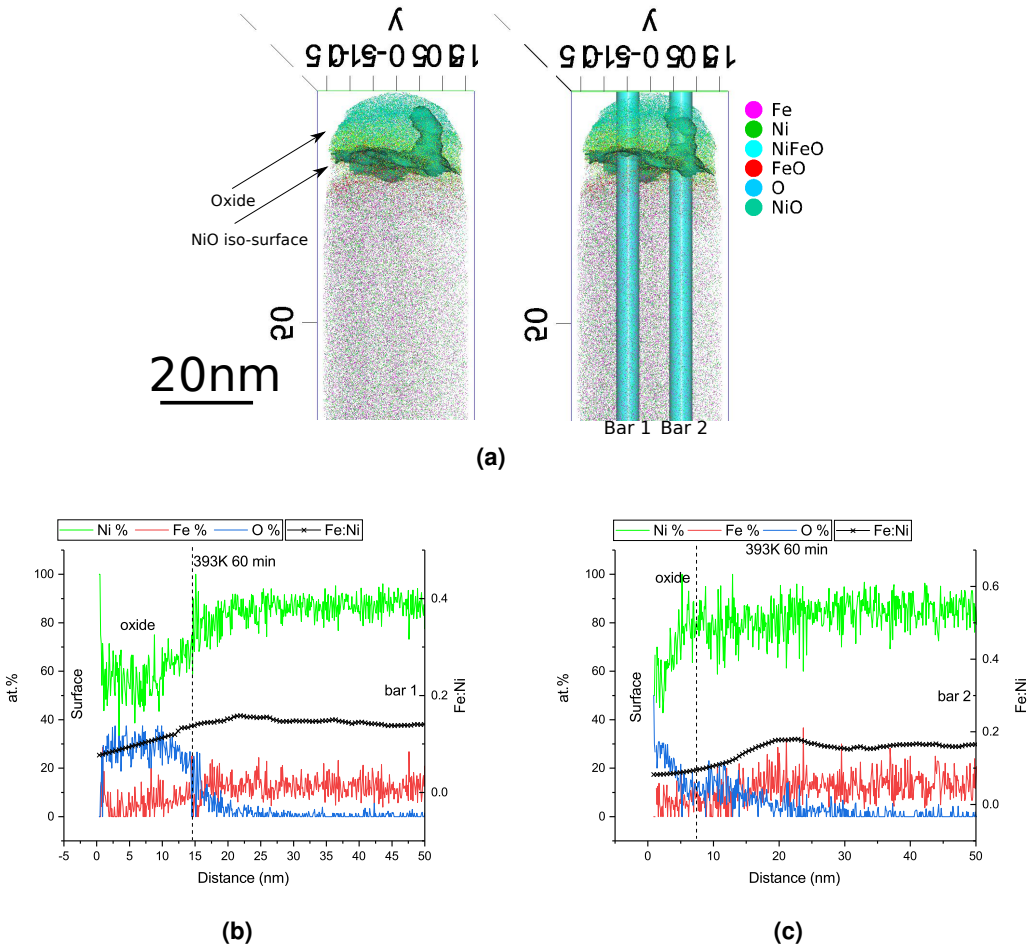

Figure 4.2.20 – a) Analysis of 393K 60min oxidised Ni90Fe10 sample. Iso-surface is created with NiO concentration at 9.9 at.% b) and c) are 1D concentration profiles based on bar 1 and bar 2 illustrated on the reconstruction image.

433K 60 min oxidation Further increasing the oxidation temperature to 433K produces the APT reconstruction shown in Figure 4.2.21. Apart from a slight increase of the oxide thickness (30nm), the composition of the oxide remains the same as in previous lower temperature observations. However, there is one interesting feature at the top of the reconstruction which is that the Ni content and O content begin to converge, although not reaching an NiO stoichiometry. On the very surface, there is a surge of Ni concentration, which mostly originates from the decomposition of localised oxide ions containing high amount of Ni.

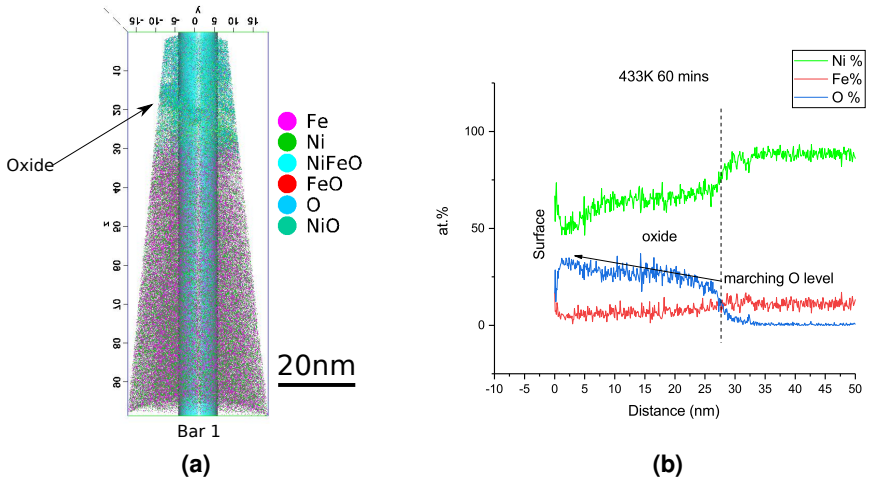

Figure 4.2.21 – a) An observation of 433K 60 min oxidised Ni90Fe10. b) 1D concentration profile on the bar shown in the reconstruction figure.

473K 60 min oxidation Oxidation at an even higher temperature of 473K however, does not continue the trend of increasing oxide thickness with increasing oxidising temperature, as shown in Figure 4.2.22 and 4.2.23, in comparison to the reconstructions of the specimens oxidised at 393K and 433K. The thicknesses of the oxide and also the compositions are very similar to samples oxidised at 353K. It is believed that oxidation observations made here are the oxidation process on a feature-less sample surface, on which a homogeneous oxide layer can be developed. Oxide composition is still $Ni_{60}O_{30}Fe_{10}$, which is the stable composition in both observation.

673K 60 min oxidation Oxidation at the upper limit of 673K was also conducted and the reconstruction is shown in Figure 4.2.24. One significant feature in this oxidised sample is the discovery of Cu species in the dataset, which is likely contamination from the sample holder. 673K appears high enough to initiate the movement of Cu from the specimen holder along the shank of the sample to the tip. The 1D concentration profile in 4.2.24b shows that the major composition of the oxide has reached the stoichiometrically balanced NiO composition. Cu is segregated to the side of the reconstruction, which fits with the assumption about migration of Cu ions up the shank of the sample during the

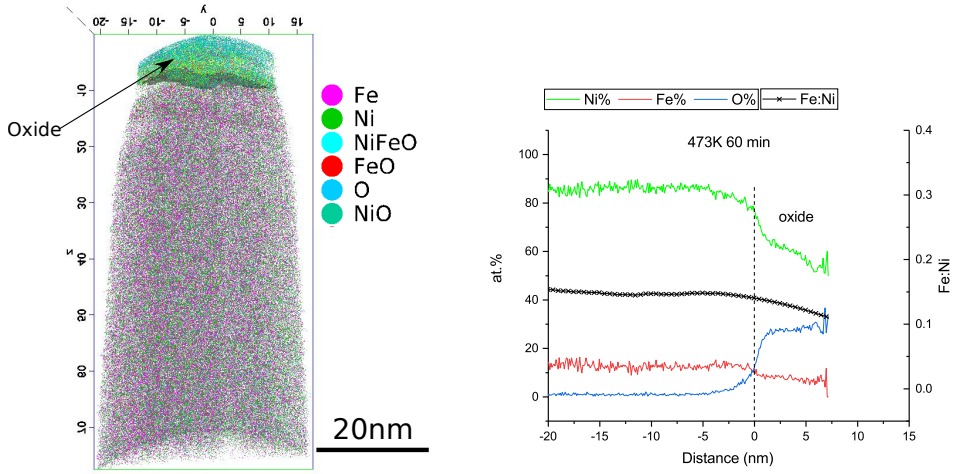

(a) (b)

Figure 4.2.22 – a) First APT analysis of a 473K 60 min oxidised Ni90Fe10 sample with iso-surface created based on the NiO concentration at 6 at.%. b) proxigram based on the NiO iso-surface.

experiment. In another 1D profile through the z direction (as shown in Figure 4.2.24c), it is clear that the entire reconstruction is oxide, having a composition of approximately NiO together with incorporating a small amount of Fe. On the top of the tip, Cu oxide replaces Ni and Fe as the dominating species. Overall, it has been observed that 673K is high enough to fully oxidise Ni90Fe10, forming stoichiometrically balanced NiO. The presence of Fe in the oxide layer is also detected in the form of complex oxide ions. Cu migration to the sample surface could have an initiation temperature between 473K to 673K as it has been reported that there is a difference of several order of magnitude at low and high temperatures [294, 295]

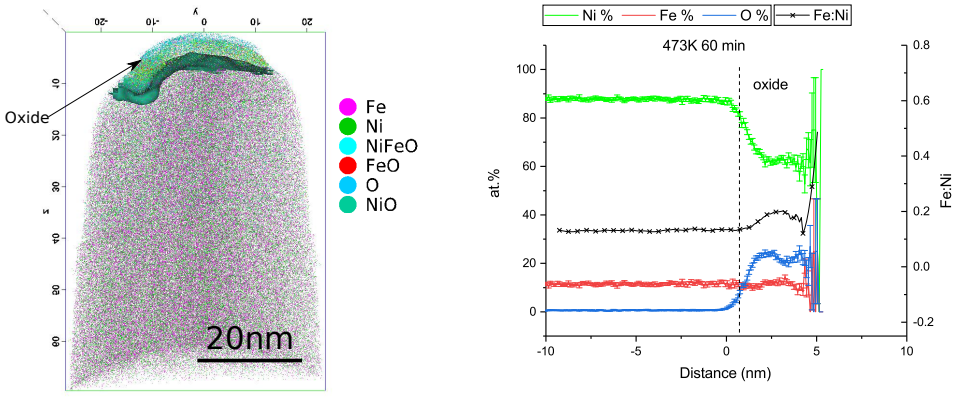

(a) (b)

Figure 4.2.23 – a) Second APT analysis of a 473K 60 min oxidised Ni90Fe10 sample with iso-surface created based on the NiO concentration at 2 at.%. b) proxigram based on the NiO iso-surface.

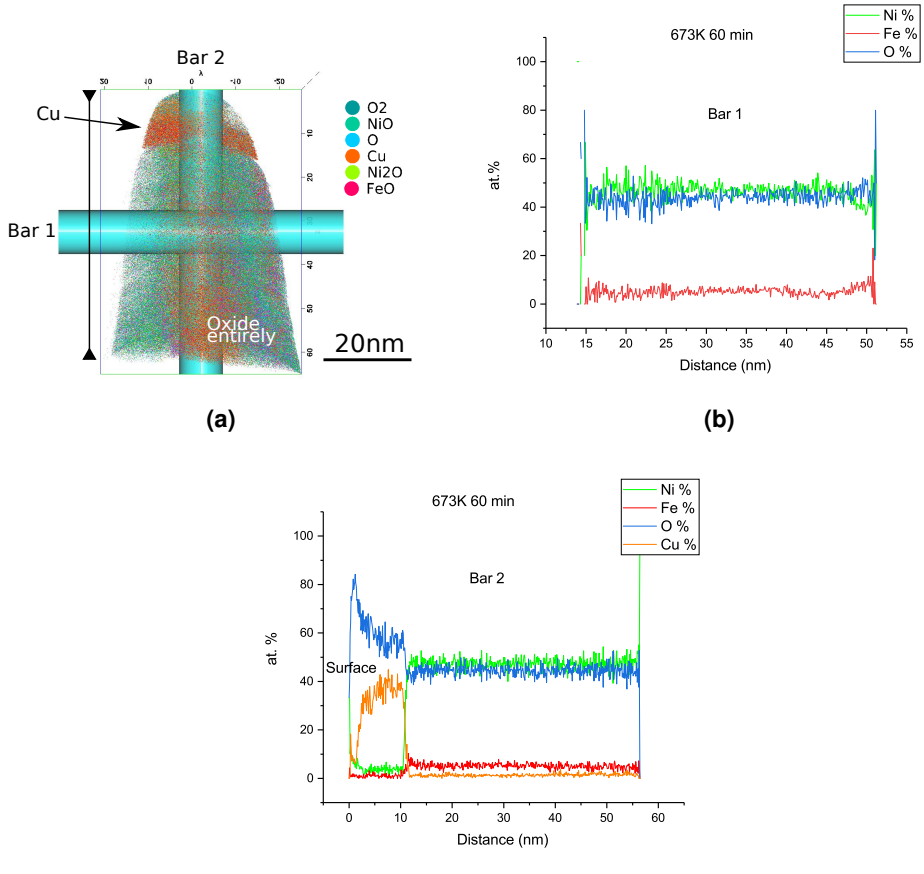

(a) (b)

(c)

Figure 4.2.24 – a) An APT analysis of 673K 60min oxidised Ni90Fe10 sample. b) and c) 1D concentration profiles through the x direction and z direction of the reconstruction, respectively.

4.2.4 Oxidation of Ni50Co50 alloy

The oxidation behaviour of a Ni50Co50 alloy has also been investigated since it is similarly an important catalytic material as described in section 2.2.1. Co only has one isotope at 55.8 Da and only has one potential oxide (*CoO*) existing at the designated oxidation temperatures (353K-473K) investigated in this study. In table 4.2.4, all successful APT experiments conducted on the oxidised Ni50Co50 are listed.

Oxidation Temp. 353K	Oxidation time/min	120	240	280	2100
	Number of experiments	1	1	1	1
Oxidation Time 60 min	Oxidation temp./K	473			
	Number of experiments	1			

Table 4.2.4 – Ni50Co50 [011] oxidation in 45mbar oxygen at 353K.

Similar to the FeNi alloys, oxidation at various oxidation times at 353K were conducted together with a 473K (higher temperature) oxidation. A typical APT reconstruction of a 280 min 353K oxidised Ni50Co50 sample is presented in Figure 4.2.25. The reconstruction shows oxide development: an oxide layer is uniformly developed onto the fresh surface with Ni oxide species and Co oxide species evenly distributed in the oxide layer. Similar results in term of oxide distribution are seen in all observations. Limited surface oxidation development occurs on this particular material, which is not surprising since Ni and Co are both reported as forming protective layers with respect to Fe during oxidation [296]. The composition and thickness of the oxide is clearly shown in the proxigrams from 5 at.% O the iso-surfaces, as shown in Figure 4.2.26. The oxide has a composition of *NiCoO* in all cases. Only in one instance, which is the 280min 353K oxidised sample, is surface enrichment of Ni observed in comparison to Co. It is also of interest to evaluate the composition at the interface between oxide and substrate. Again making use of iso-surface composition plots, Figure 4.2.26 shows an enrichment of Ni at this interface on the oxide side, which may indicate the preferential movement of Ni towards the surface. This trend is most prominent in the 60 min 473K oxidised sample, in which Co concentration declines more steeply from

substrate into the oxide in comparison to Ni, which has a steadier decrease in concentration profile diffusing outwards. In terms of the oxide thickness, oxide formed on the Ni50Co50 sample has a limited development. It reaches a thickness of 5nm regardless of the oxidation time at 353K and it only has 3 nm for the 473K oxidised sample.

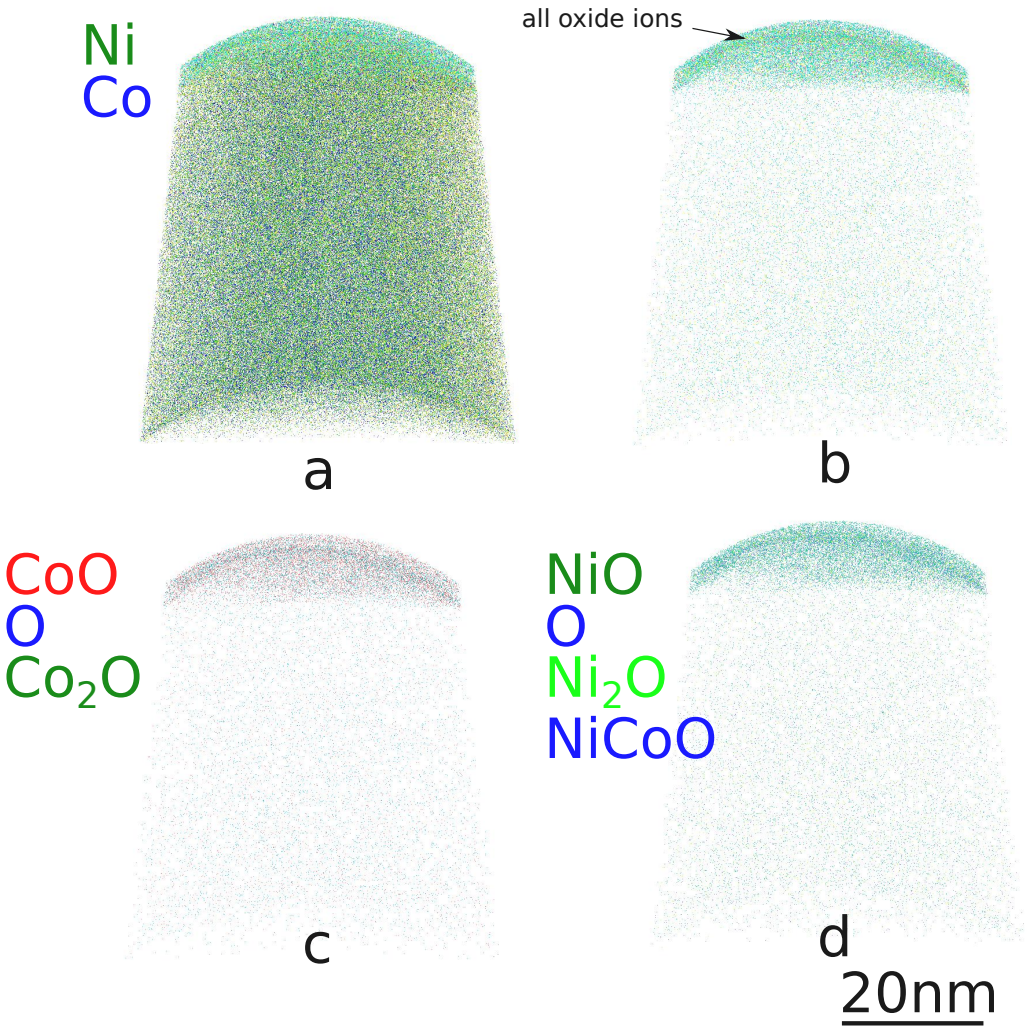

Figure 4.2.25 – Reconstruction of a 280 min 353K oxidised Ni50Co50 sample. a) ion map contains all the ions b) ion maps only contains oxide species c) ion map contains Co species and d) ion map only contains Ni species

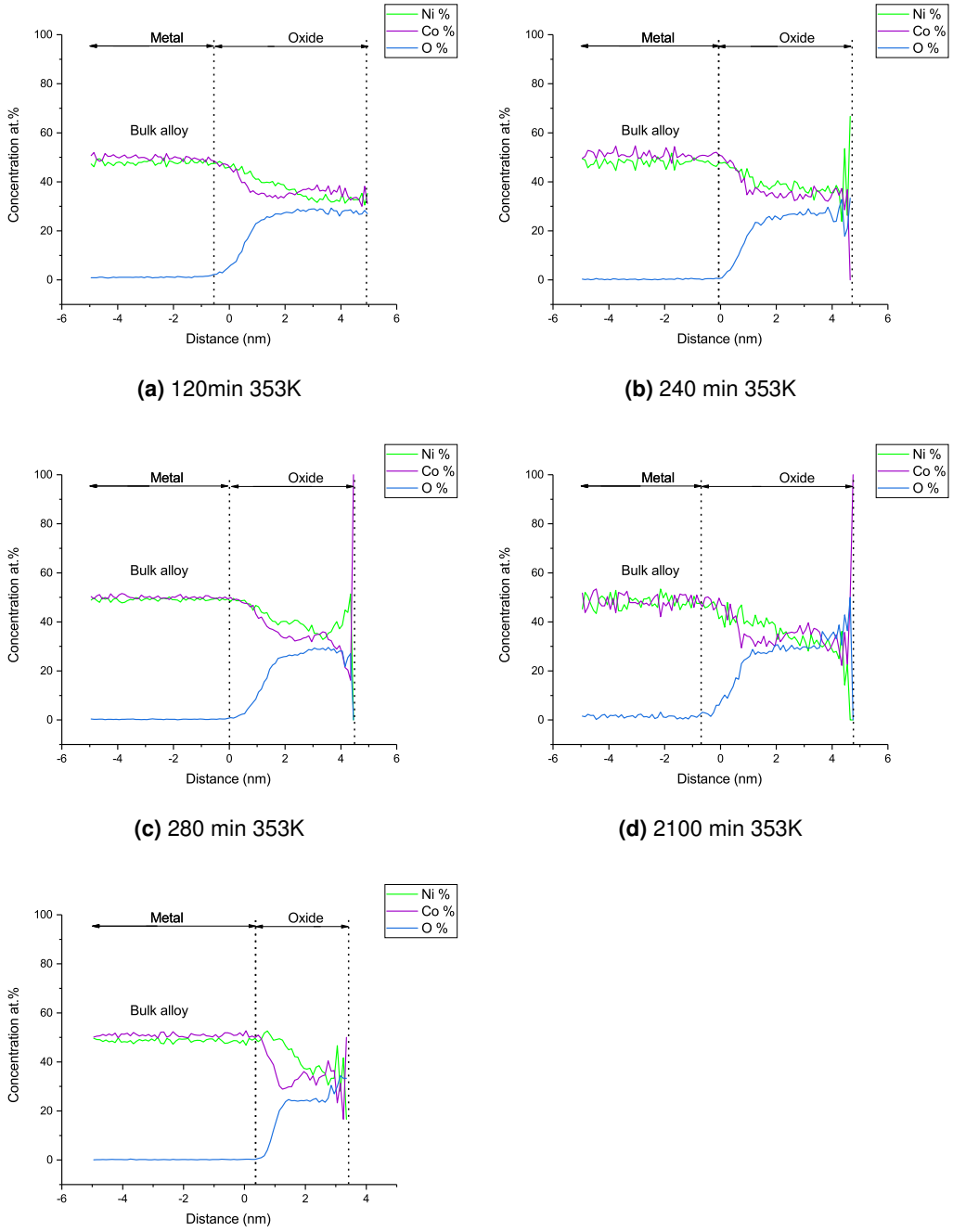

(a) 120min 353K

(b) 240 min 353K

(c) 280 min 353K

(d) 2100 min 353K

(e) 60 min 473K

Figure 4.2.26 – Proximity histograms of oxidised Ni50Co50 samples based on iso-surface created by 5at.% oxygen concentration. There are five samples, four oxidised at 353K and one at 473K. Oxidation with various times were conducted for the 353K oxidation.

4.3 Reduction of alloys

4.3.1 30min 773K H_2 reduction on Ni10Fe90

Reduction experiments were conducted to further evaluate the nature of the observed surface Ni enrichment after oxidation. In the Ni10Fe90 experiments presented above, surface partitioning of Ni has been observed along either the [110] pole and/or <013> poles. Ni enrichment is even more prominent in the 473K oxidised sample, covering the entire surface of the sample facilitated by fast diffusion along a grain boundary. However, all of these observations are directly from APT oxidation measurements and it is important to understand the stability of any surface segregation. Hydrogen reduction of oxidised samples was conducted to investigate this issue. The result of a 30 min 773K H_2 (3 vol.%) reduction on 600 min 353K oxidised Ni10Fe90 sample is shown in Figure 4.3.1. In the sub-figure a, the reconstruction of the APT dataset is presented and there is an abrupt change in the distribution of Ni (green) and Fe (pink/red), which also correlates to a mini fracture of the specimen during the analysis. Before the mini fracture, there is very limited Fe signal. After the mini-fracture, an intense Fe signal emerges showing the original substrate composition. The segregated location of Fe in the reconstructed ion map is caused by the irregular tip shape and is proposed to be an artefact resulting from the mini fracture. In the sub-figure b, Fe and Ni concentration along the ROI is plotted, in which the surface enrichment of Ni is apparent. Despite the fracturing of the tip, analysis of the data prior to this event shows the surface of the oxidised sample has been reduced and the enrichment of Ni on the surface is confirmed.

4.3.2 30min 773K H_2 reduction on Ni48Fe52

Similar to the Ni10Fe90 sample, a 1440 min 353K oxidised Ni48Fe52 sample was reduced under the same reduction conditions (30 min 773K H_2 (3 vol.%) reduction). The APT reconstruction and a 1D concentration profile along the z axis are shown in Figure 4.3.2. The 1D profile highlights a composition change of the surface oxide. In the profile, the

outer surface still has a composition of $FeNi_2O_4$, similar to these of the oxidised samples, but the thickness of the $FeNi_2O_4$ layer is thin, only 2 nm in depth. Right beneath this thin oxide, there is a layer of $FeNiO_2$, with a thickness of 11 nm. Further beneath this layer, a diffusion zone is observed with an increasing level of Ni relative to Fe. Overall, this reduction experiment has not fully reduced the sample to a metallic state. It is possible that oxygen species have been present during the intended reduction stage, influencing the final surface state. Comparing the oxide to the one not exposed to the reducing environment (shown in Figure 4.2.11c), similar trend of oxide development has been observed, with Ni enriched in the region right above the substrate. However, the $FeNiO_2$region is unique and it could be the result of the exposure to H_2 at 773K.

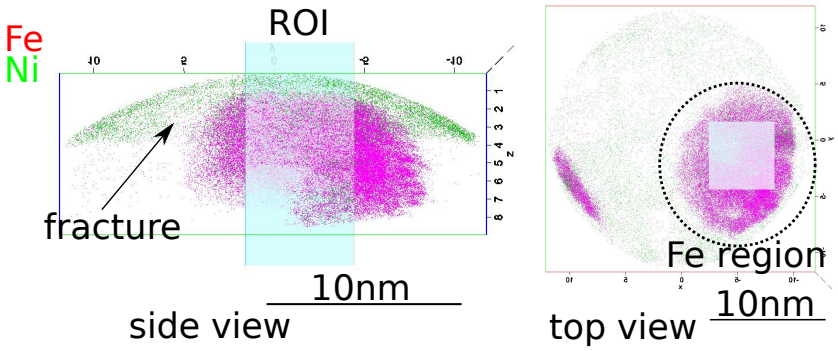

(a)

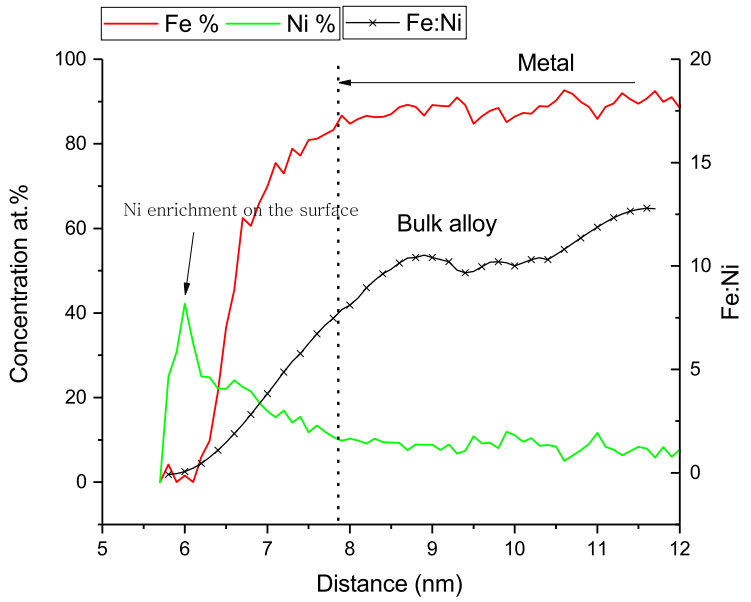

(b)

Figure 4.3.1 – Reduction experiment on a 600 min 353K oxidised sample. a) There is a mini fracture in the reconstruction, which is reflected through the vast change from Ni ions to Fe ions. In the reconstruction ion map, red/pink colour represents Fe ions and the green colour represents Ni ions. b) The Fe and Ni concentration of the ROI is plotted, in which the surface enrichment of Ni is evident. (Similar sample which was not hydrogen treated has been shown in Figure 4.2.2c)

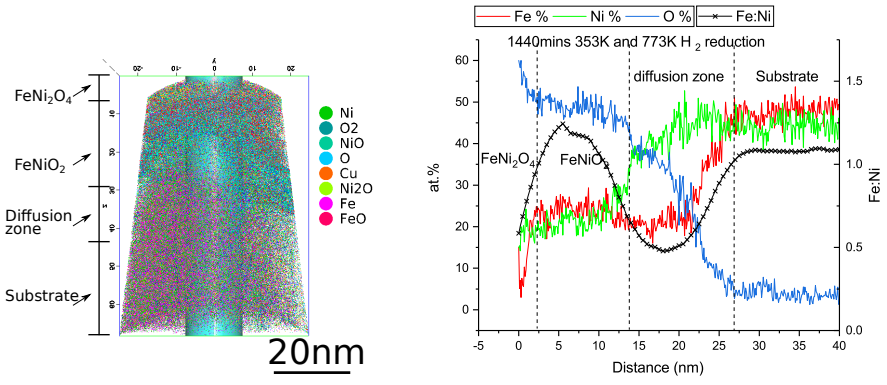

(a) **(b)**

Figure 4.3.2 – Reconstruction of the 773K hydrogen reduced Ni48Fe52 sample, which has been oxidised for 1440 min at 353K in 45mbar oxygen. (Similar sample which was not hydrogen treated has been shown in Figure 4.2.26)

4.4 Discussion and summary

4.4.1 Oxide composition

A major goal of the oxidation experiments is to investigate the composition of the initial oxides developed at low temperature within short oxidation times. To summarise the experimental data described previously, a schematic diagram of oxide composition is presented in Figure 4.4.1.

Transition region All analysed oxidised samples display a transition layer directly above the metal substrate, which is labelled as the "transition region". In this layer, moving out from the metal substrate, the oxygen signal steadily increases coinciding with a decrease of metal signals. However the amount of O concentration is low, and no stoichiometric oxide composition can be reached in any of the four alloys. Also in this layer, the ratios of Ni:Fe and Ni:Co starts to deviate from the bulk ratio due to element diffusion towards the surface. This phenomenon is well observed in other oxidation analyses [297].

This enrichment could be the result of initial oxide formation. Judging from the thermodynamic of the formation of NiO and Fe_3O_4 in the case of the oxidation of $Ni10Fe90$ and literature of long-time oxidation [128], Fe should be favoured forming the initial oxide on the surface. Hence Fe in the metal substrate continuously diffuse to the oxide region leaving a Ni enriched region behind [105, 123]. This speculation is supported by the APT observations, in which a lower Fe:Ni ratio respecting to the bulk is observed above this Ni enriched transition layer in the $Ni10Fe90$ samples.

For the similar working mechanism, the Ni enriched transition region exists for the $Ni48Fe52$ samples. But, this enrichment cannot be the result of merely diffusion since Ni enrichment is present through the entire oxide region. A path for Ni moving towards the surface should also exist.

In contrast, the transition region for $Ni90Fe10$ samples is enriched with Fe and this enrichment is with relative low intensity. In the case of $Ni50Co50$ alloy, Co is thermody-

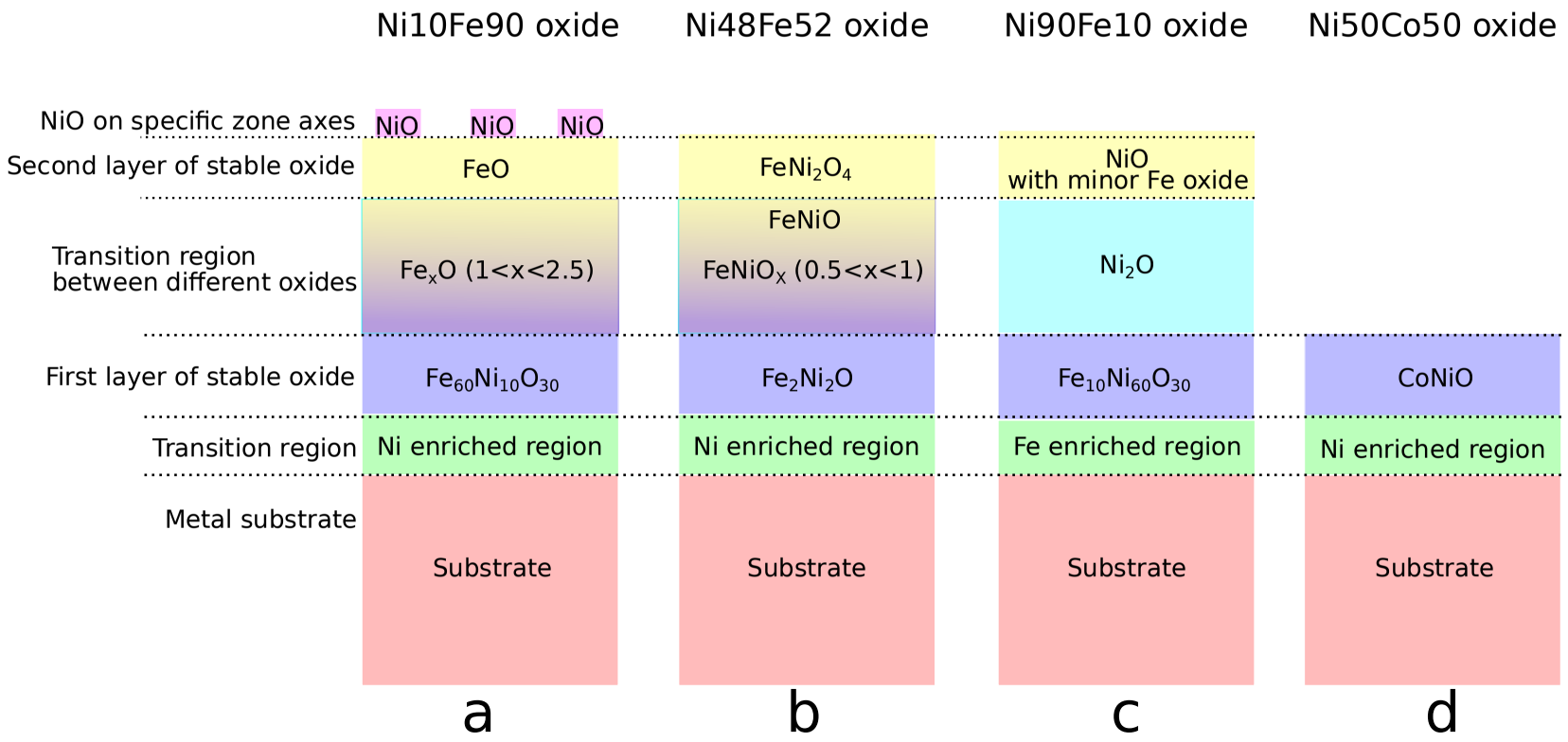

Figure 4.4.1 – Schematic diagrams of the oxide composition developed on the surface for a) Ni10Fe90 b) Ni48Fe52 c)Ni10Fe90 and d) Ni50Co50. The thickness of the coloured block is just a qualitative representation for the oxide thickness. A precaution should be put about the terminology about the ' enriched region ', which is based on the particular element. It could be the depleted region in regard to the counterpart element.

namically favoured to form oxide over Ni. In the APT observation, a slight Ni enriched region is observed, which could be the result of two effects: a) an oxide formed having a higher level of Ni over Co or b) Co ions diffuse to the surface forming oxide and leaving a enriched Ni region. Taking into the results observed at higher temperature oxidation [133], it is believed that the Ni enriched region in the APT result is caused by Co outwards diffusion.

First layer of stable oxide Above the transition region, stable oxide compositions are detected, which are strongly dependent on the substrate composition. As there is another stable oxide layer closer to the surface, this layer is termed the "first layer of stable oxide". For the Ni10Fe90 sample, an oxide of composition of $Fe_{60}Ni_{10}O_{30}$ formed. In contrast, $Ni_{60}Fe_{10}O_{30}$ forms on the Ni90Fe10 sample. By comparing $Ni10Fe90$ and $Ni90Fe10$, the composition of this layer clearly depends on the alloy substrate composition and appears as less affected by the thermodynamics of oxide formation [89]. Similarly for the Ni48Fe52 sample, the composition of the layer above the transition layer has a composition of Ni_2Fe_2O, again reflecting the bulk content of the alloy. $Ni50Co50$ alloy follows similarly in terms of this relationship to the bulk composition of the alloy. The oxide has a balanced Ni and Co content with respect to the bulk. However, due to the limited oxidation states of both Ni and Co, there is no further development of the oxide (single layer) of $Ni50Co50$. Overall, it seems oxide composition in the first layer of stable oxide is driven by the composition of the substrate.

Transition region between the first and second layer of stable oxides Oxide composition in this transition region above the first layer of stable oxide is still affected by the composition beneath. The general trend is that oxygen concentration in this layer increases and composition shifts from M_2O to MO. The trends in the three NiFe alloys are similar, developing an oxide form that is deficient in oxygen to one having increased oxygen level as reported in the literature (as NiO and FeO) [102, 103].

In addition, iron abundant alloys are observed to undergo a further oxidation. Compos-

ition transitions from $Fe_{2.5}O$ to FeO in the $Ni10Fe90$ sample and Fe_2Ni_2O to $FeNiO$ in $Ni48Fe52$ sample. On the other hand, there is no composition variation in the transition region of $Ni90Fe10$, keeping a stable Ni_2O. This observation of a single steady no-changing layer of Ni_2O could be the result of insufficient levels of Fe, which has two oxidation states and could result into a variation of O content with respect to the different level of exposure, assuming a gradual change of Fe(II) to Fe(III) oxidation state.

Second layer of stable oxide The second layer of stable oxide observed in this study exhibit stoichiometric compositions. FeO is the surface oxide in the Ni10Fe90 samples whilst NiO exists on the surface of Ni90Fe10 samples. The formation of FeO, is similar to that observed in other studies conducted at low temperature (90K) [97, 102, 103]. NiO formation is also expected as it is the only oxide Ni can form in oxidation <1173K [106]. However, the formation of an $FeNi_2O_4$ spinel on the Ni48Fe52 sample has not been often reported in the literature. Echoing on the previous discussion, Ni enrichment in the oxide of $Ni48Fe52$ suggested that diffusion of Fe is not the only cause for the Ni enrichment in the transition region. There must be other mechanism for Ni surface diffusion.

NiO on specific crystallographic axes The observation of an NiO region on the oxidised $Ni10Fe90$ samples is of interest. Ni is observed to move to the surface through the [110] and <103> zone axes and grain boundaries [298–301]. This observation matches the literature, in which rapid Ni oxidation is consistently observed on [001] and <110> axes [300, 302, 303].

APT results here provide a more detailed oxidation profiles for the initial oxidation of bimetallic NiFe and NiCo alloys. Although these are fundamental engineering materials, new aspects pertaining to the fine details of their oxidation behaviour, especially at low temperature, are clearly revealed. Comparing to existing literature, in which FeO and NiO are often reported as the very first layer of oxide developed on the fresh surface, significant new insights into the oxidation mechanism details have been added through the use of APT

in this study.

4.4.2 Ni enrichment

Ni enrichment on the surface of Ni10Fe90 sample is detected. Due to the small quantity of Ni surface enrichment in the APT reconstruction of this oxidised alloy, a thorough analysis has been conducted to verify this observation. This starts with the analysis of the as-received Ni10Fe90 samples (section 4.1.3). The concentration plot of Ni across the reconstruction does not indicate any segregation along the crystallographic axes. In addition, no excess of Ni on the surface was observed after field evaporation cleaning. Thus, it can be concluded that there is no Ni surface segregation before any oxidation experiment. In the APT analyses, particular attention has been paid to the identification of the 32 Da peak in the resulting mass spectra, at which a potential overlap occurs between doubly charged $^{64}Ni^{+}$ and singly charged $^{32}O_2^{+}$. After a deconvolution calculation, to investigate the relative contributions of these ions to this peak in the mass spectra, using maximum likelihood method, 32 Da has been labelled as oxygen, which therefore excludes the potential of any erroneous interpretation Ni surface enrichment due to mistakenly considering oxygen as Ni. The last step but most decisive observation comes from the reduction experiment of the oxidised sample as mention in section 4.3.1 on page 141. Ni is still detected on the surface after the hydrogen reduction stage. Together, these three measures lead to the firm conclusion that the Ni surface segregation along zone axes is an authentic observation.

4.4.3 Oxidation Kinetics

Fast diffusion along zone axes The speed and the scale of oxide development is an important factor in the development of catalyst material. However, there is one important difference between the oxidation on acicular tips in this research and on typically flat surfaces as reported in the literature. The first point is the exposure of crystallographic facets on the tip highlighting a variety of zone axes. For example, there are [001] and <103> axes co-existing on the spherical surface (bcc structure) whereas only one axis exists on a flat

surface of single crystal. Also, the adhesion of formed oxide is different between a curved and flat surface, which can affect the oxide development process. Bonfristo at al. [301] and Herchl et al. [300] reported that Ni oxide has a faster development along [001] than [111] directions due to the high grain boundary formation owing to the epitaxial relationship difference between NiO [001] and Ni [001] directions. However, observation in this work finds that Ni is enriched on [110] and <103> axes, suggesting Ni diffusion is fastest on these surfaces. This could be attributed to the surface curvature as the result of the APT sample shape. As it has been claimed the high level of mismatch of NiO formed on [001] axis causes Ni fast diffusion and therefore fast oxide formation. It therefore can be proposed that <103> axes on the APT tip contains more protruded sites due to the curvature and oxide development is facilitated.

Ni10Fe90 In this research, the development of oxide thickness of the analysed materials appears to terminate after the oxide achieves a certain thickness. This is especially the case for the Ni10Fe90 samples, whose oxide thickness is about $5.4nm \pm 0.38nm$ in all observations. Even an increase of exposure temperature from 353K to 473K has little impact on the oxide development. Ni enrichment on the interface between substrate and oxide appears to act as a protection layer. This phenomenon has been reported in high temperature oxidation of NiFe alloy, where the enrichment decreases the Fe diffusion activity [123, 125]. This phenomenon is confirmed also works for oxidation at low temperature.

Ni48Fe52 Oxidation of Ni48Fe52 sample however shows the trend of increasing oxide thickness with exposure time. For 30 min, 360 min and 1200 min oxidations at 353K, the oxide thicknesses are 1nm, 7nm and 10nm, respectively. The development of $FeNi_2O_4$ on the surface could act as a partial barrier since this particular layer has the same thickness, about 3nm in both 360 min and 1200 min oxidised samples. The region below the $FeNi_2O_4$, which has a composition of Fe_2Ni_2O, has the most important development with increasing oxidation time. Also, the increase of the thickness of this Fe_2Ni_2O layer is most prominent from the side of the tip rather from the top as shown in Figure 4.2.13, suggesting

that the growth of oxide is anisotropic. However, it is hard to conclude if that is based on the crystallographic direction or not due to limited information about the substrate itself.

Ni90Fe10 In the case of the Ni90Fe10 samples, the manner of oxidation development is the least consistent across repeated observations. The formation of a Ni_2O layer on the surface has been observed both in 353K oxidised samples (with different oxidation times) and also at higher temperatures (393K, 433K and 473K). It has been observed that only Ni_2O can act as the protecting layer. Once the surface is protected by such an oxide layer, the thickness of the total oxidation is controlled within 10 nm. However, NiO is also observed as the dominant oxide composition in one 30 min/353K and another 60 min/673K oxidised samples. It is not surprising to observe the formation of NiO in the 673K oxidised sample, since it has been reported that NiO is the only oxidation product formed by Ni below 900°C [99]. However the formation of NiO at 353K indicates there is a mechanism which can speed up the oxidation at low temperature. As shown in Figure 4.4.2, a high-density region of oxygen is distributed within the oxide, clearly defined running through the length of the specimen. This could be highlighting a fast diffusion pathway for diffusion of oxygen into the substrate. Although APT analysis can erroneously create such high-density region of species during high field analysis, there is no such feature observed in the analyses of other similar oxides. Therefore, it is believed the observation is not due to trajectory aberrations. Also, this observation echoes the study showing that grain boundary is the fast diffusion pathway and can facilitate Ni oxidation [107].

Ni50Co50 For the oxidation of Ni50Co50, the oxide layer has a cap of up to 5 nm thick. The development of the initial oxide, which is $NiCoO$, acts as the barrier layer for further oxide development. Comparing to other three alloys, this alloy only develops a single composition within the oxide. Ni enrichment on the interface between substrate-oxide is also observed in a 60 min exposure at 473K, which indicates the diffusion of Co towards the surface during the oxidation [134]. Similarly, the remaining Ni enriched region prohibits the Co diffusion and therefore reduces the oxidation speed [304, 305].

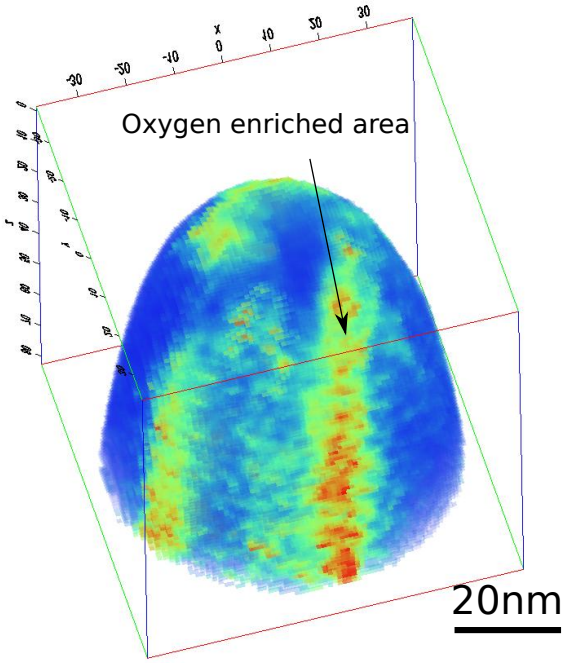

Figure 4.4.2 – Density map of oxygen in the reconstruction of a 360 min 353K oxidised Ni90Fe10sample. The high-density region represents the pathway of oxygen inner diffusion.

4.4.4 Future work on alloy experiments

Direct oxidation on atom probe tips were initially conducted by Tsong et al. [306] and later on further investigated by Kruse et al. [307–309], Bagot et al. and Li et al. [196, 211, 212, 214–216], Barroo et al. and Visart de Bocarmé et al. [194, 195, 203, 204, 310, 311]. Surface changes on various materials under different environments have been evidenced, and the results help to understand the catalysts under working conditions. In this thesis, transition from noble metals to base metals has been made for the purpose of understanding alternative catalytic materials. Important information about the initial oxidation of FeNi alloys has been obtained on semi-spherical samples. A protocol has been established for oxidation investigations, which includes initial surface cleaning via FIM, followed by in-situ oxidation and then high resolution APT analysis. The gap in the current understanding of oxide formation at the sub-nanometre scale has been investigated. Nevertheless, there is also opportunity for improvement. In the current research, an extremely low yield of samples

successfully analysed by atom probe has been experienced, which is due to complicated sample making and cleaning procedures. FIM is a great tool to conduct the surface cleaning but it relies on human experience and judgement about the finishing states. It would be more efficient to conduct the cleaning step in the atom probe instrument, which can indicate the finish of a successful cleaning stage definitively without over-cleaning and pre-mature fracture. Also, the involvement of laser analysis can substantially reduce the specimen fracture rate, since surface contamination is most often in the form of oxide, which is an insulator and not best suited for voltage-pulsed field evaporation. The potential experiment route, which includes: atom probe cleaning, in-situ oxidation, and atom probe analysis, is feasible provided that a similar setup of an in-situ reaction cell is available on the dedicated atom probe instrument. Examples of these are now becoming more common [213, 312].

In terms of experimental parameters, higher oxidation temperatures and longer oxidation times could be investigated, assuming the yield of successful APT analyses is sufficiently high. The main focus of the work in this thesis is on the low temperature oxidation and very few experiments were conducted at high temperature. Also, while the initial development of the oxide has been explored, information about element diffusion would further add to the understanding of the fundamental oxidation process. Due to the low oxidation temperature, diffusion profiles are not obvious in the current dataset. However, an important result is that an anisotropic growth of the oxide resulting from oxygen or metal diffusion along preferential pathways seems to occur in several of the systems investigated here.

In addition, there are other alloy systems could be explored, for example NiPd, NiPt alloys and etc., all of which have catalytic functionalities but without being fully explored in terms of surface composition involvement under reactive environments.

Chapter 5

Initial attempt: a TEM inspection of multimetallic nanoparticles fabricated by chemical method

After successful APT analyses of the oxidised and reduced model alloys (NiFe, NiCo bimetallics), in this chapter, attention is turned to systems more closely resembling industrially relevant catalysts for realisation of the benefits of the APT technique. The primary focus of this work is on chemically synthesised NiFe and NiCo nanoparticles studied after exposure to air. The goal here is to determine to what extent a local analysis of the nanoparticles composition is possible using "conventional" characterisation instrumentation. TEM has been selected as the primary tool to conduct the composition investigation in this chapter. As the result, important information has been derived relating to the particle size, particle distribution on the substrate and composition of individual particles. Overall, there is benefit here to show the primary results on these particles synthesised by chemical methods to illustrate the advantages and disadvantages of TEM and also of this specific synthesis approach.

5.1 Inspection of Ni50Fe50 particles reduced at 700℃

As the model alloys analysed in the previous chapter comprise NiFe and NiCo alloys, nanoparticles with similar formulations are studied here. The preparation method involved is called DPU (Deposition Precipitation by Urea) and the particles were prepared on a silica support, which has been described in detail in section 3.1.2 on page 68 and is summarised here in Figure 5.1.1.

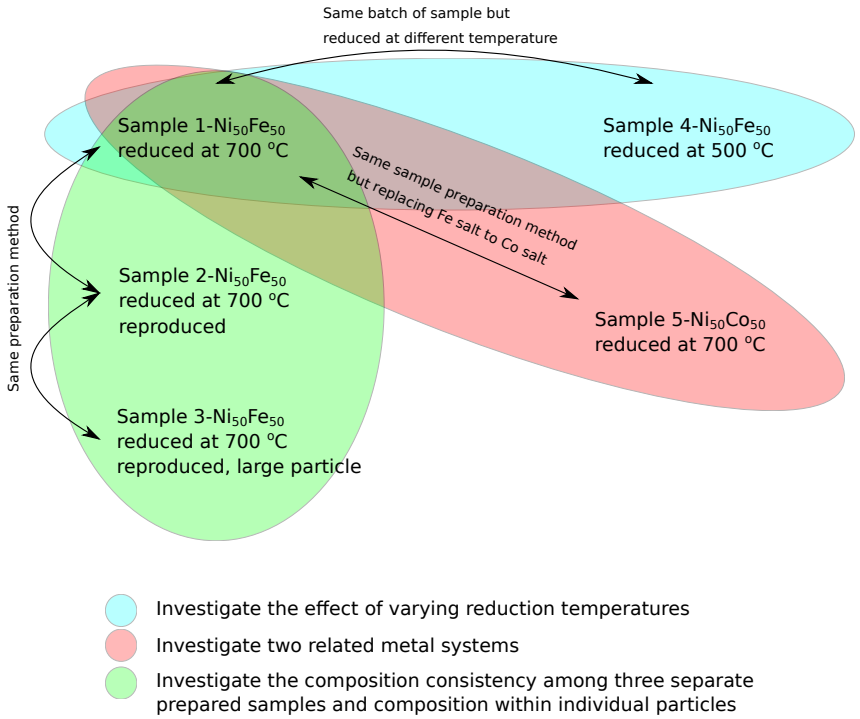

Figure 5.1.1 – Nanoparticles synthesized by DPU methods. There are 5 samples investigated for three tasks as indicated by the three coloured circles, respectively.

Ni50Fe50 particles reduced at 700°C were made to confirm if a composition and size control is effective upon preparation by DPU. Two batches of samples were made separately with the same methodology and conditions, and are labelled as Sample 1 and Sample 2 (more information about sample labelling to see Figure 3.1.5 on page 69). The particles are examined by TEM. In Figure 5.1.2, BF images of the Sample 1 are shown. As illustrated, both metal particles and silica support are observed. The particles have a round shape with clear defined edge. Agglomeration of particles is not observed, instead the produced

particles are evenly distributed on the silica substrate. Figure 5.1.2 a to d show different magnifications of the produced particles, confirming a high level of consistency across various sampling areas. The separation between individual particles is clearly shown in the Figure 5.1.3 a and the separation distance is on average 5 nm as measured from Figure 5.1.3 b and c. The size distribution of these individual particles was measured manually using the information from the BF images. In Figure 5.1.3, a histogram of the size distribution measured in the Sample 1 shows that most particles have a size around 5.4 nm, spanning across a range from 2.5-9 nm, with a standard deviation of 1.3 nm. It is therefore evident that DPU allows a tight control of the particle size. In order to substantiate conclusions from these initial observations, a second batch of Ni50Fe50 particles was investigated as a cross-check (Sample 2). A HAADF image and particle size measurement of sample 2 are shown in Figure 5.1.4. The distribution of metallic particles on the silica substrate is more distinctively revealed in the DF image as shown in Figure 5.1.4. It is due to the large Z contrast between the NiFe particles and SiO_2 substrate. Again, the particles are evenly distributed on silica and no agglomeration is observed. In terms of size distribution, the size of the particle is 3.6 nm with a standard deviation 0.8 nm. The span of the particle size distribution is however even smaller, from 2 nm to 5.5 nm as shown in Figure 5.1.4b. Comparing Sample 1 and Sample 2, the sizes of the particles are very similar, both around 3-5 nm. In addition, the narrow distribution on the two samples shows that the DPU method is able to produce high quality nanoparticles.

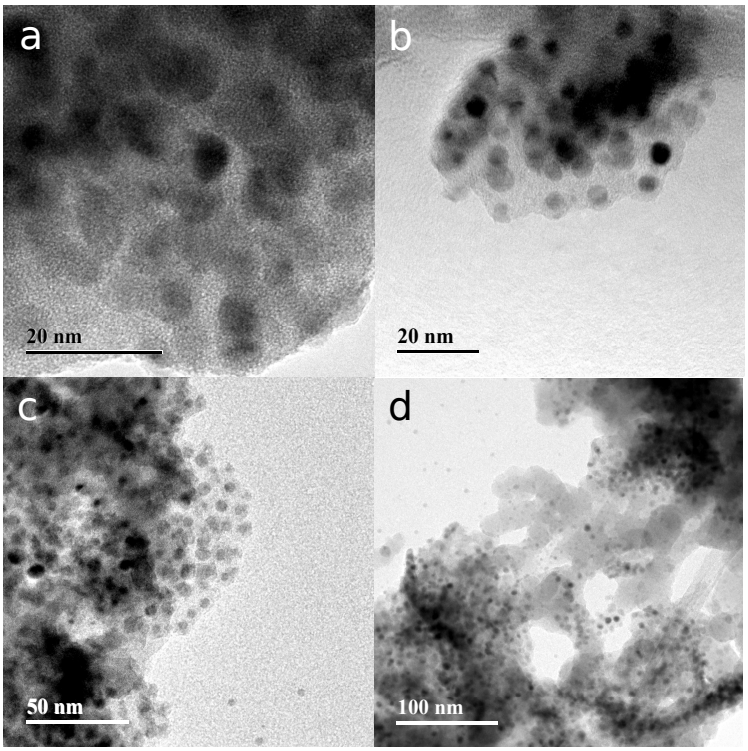

Figure 5.1.2 – BF images of the first batch of silica supported Ni50Fe50 particles reduced at 700℃ (Sample 1). Magnification is reduced from a to d. The results show a uniform distribution of round shape particles regardless of the level of magnification.

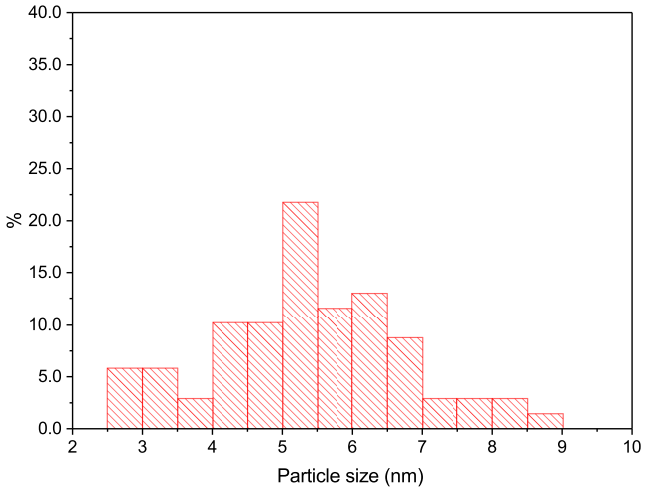

Figure 5.1.3 – Size distribution of Ni50Fe50 particles reduced at 700℃ (Sample 1). Size measured manually and the result is 5.4 nm with standard deviation 1.3 nm. The analysis volume is based on 5 areas with 100 data points.

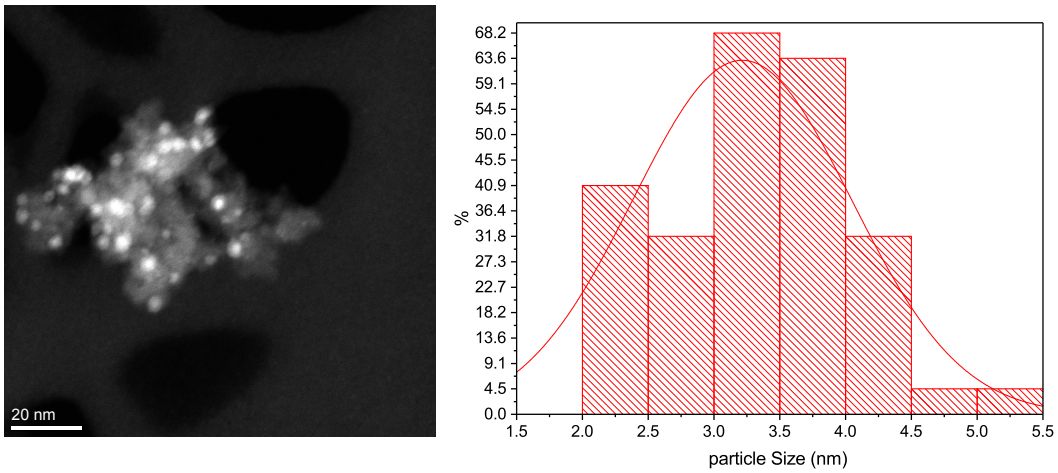

Figure 5.1.4 – a) HAADF image of the duplicated Ni50Fe50 particles reduced at 700 °C (Sample 2). b) Size distribution of particles measured on the support substrate. A slightly smaller particle size was observed which could be the result of DF imaging because DF is only based on electrons that diffract out of the particles, limiting the visibility of the particles edge. The result is 3.6 nm with standard deviation 0.8 nm. The analysis volume was based on 5 areas with 100 data points. [313]

In addition to the size distribution, the composition of individual particles is another important aspect. EDX 2D map scans and point scans associated with STEM were conducted on individual particles from both Sample 1 and Sample 2. In Figure 5.1.5, the EDX map scan on several individual dispersed particles of Sample 1 is shown. Ni and Fe are well dispersed at the level of a few nanometres. Even for particle sizes as small as 2 nm, both Ni and Fe signals are detected. This observation shows that particles made under DPU method have a very good consistency of composition down to the level of an individual particle. Point scan results (more than 30 point scans were applied on each batch) show the composition for the Sample 1 is: Fe 24.6 at.% Ni 75.4 at.% (standard deviation of 7.7 at.%). For Sample 2, the measured composition is Fe 20.5 at% Ni 79.5 at.% (standard deviation of 8.2 at.%). Thus the overall compositions are reasonably consistent across the two batches of samples, which indicates that the DPU method can deliver reproducible results. However, the measured composition is somewhat different from the nominal Ni50Fe50 composition, demonstrating a deficit of Fe content.

Another independently prepared Ni50Fe50 reduced at 700°C (Sample 3) was analysed.

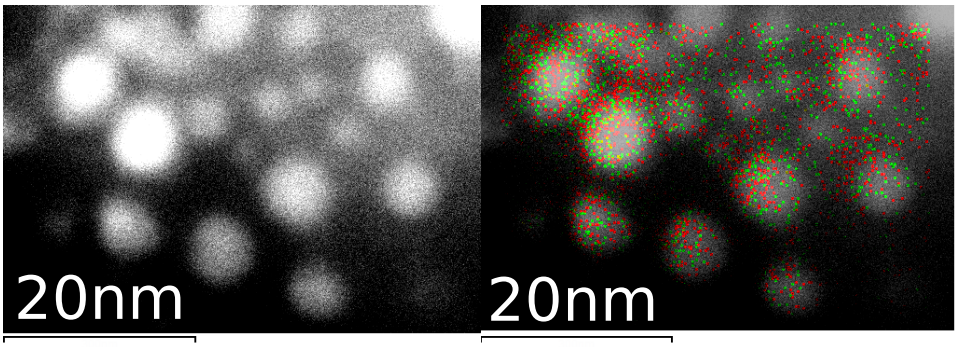

Figure 5.1.5 – EDX map scan of Ni50Fe50 samples reduced at 700℃ (Sample 1). Red represents Fe and green is Ni. An even distribution of Fe and Ni inside detected particles is observed in particles as small as 2 nm in diameter, despite that the signal intensity is low.

It was possible to examine a few larger particles in this batch and the results are shown in Figure 5.1.6. The large particles are roughly around 40 nm in size. Point scans show a good consistency with the nominal composition, having the Ni 50 at.% and Fe 50 at.%, along with a slight signal of Si from the substrate, matching well with the loading of the metal salts. No local composition variation between Fe and Ni is observed inside the particles, where each spot analysis was about 5 nm apart. Compared to Sample 1 and 2, the increase in the size of particles observed in Sample 3 seems to generate a composition closer to the expected nominal value. A link between the particle size and composition is possible.

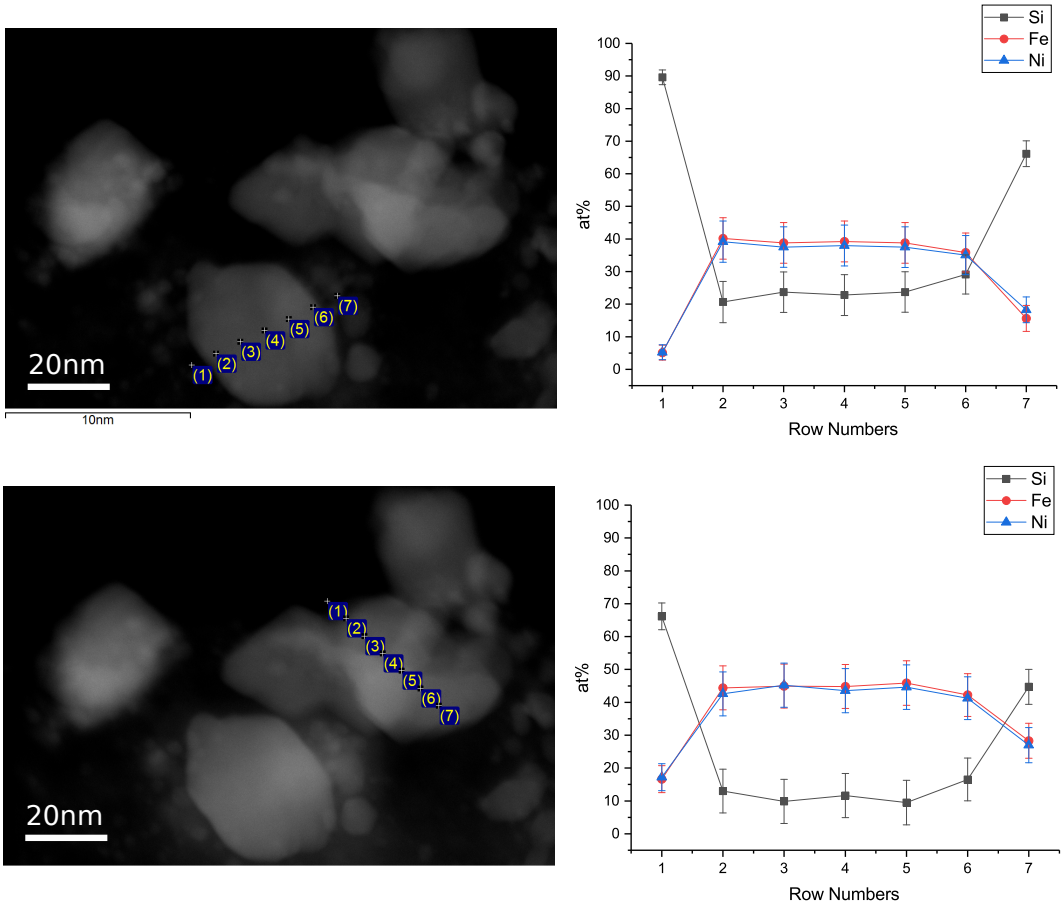

Figure 5.1.6 – Point scans on large particles of Ni50Fe50 reduced at 700 °C (Sample 3). Each data point is about 5 nm spatially apart. The result shows that there is an equal amount of Fe and Ni within the large particles. Error bar is calculated by counting error.

5.2 Investigation of effect of reduction temperature on Ni50Fe50 particles

The reduction temperature could play a role in the particles in terms of the resulting composition and/or shape. Therefore, material from the same batch of material prepared by DPU which was subsequently reduced at 700°C to produce Sample 1, was instead reduced at 500°C to generate Sample 4. In Figure 5.2.1, BF images of Sample 4 are shown. The particles still have a round shape and they are evenly distributed on the substrate, which is especially evident in sub-figures c and d. Compared to Samples 1 and 2, there is only one distinct difference, which is the star-shape folded material highlighted in the Figure 5.2.1 b. This feature is routinely observed, for example more are shown in Figure 5.2.2. It is believed that these features are regions of sample that have not fully reduced at this lower reduction temperature (500°C). EDX analysis on these regions also detected Si and O, confirming the silicate species. It is believed that it contains metal ions in these regions as well but with no direct observation.

Based on the BF images, the size distribution of the particles is measured, and the result is shown in Figure 5.2.3. The particles have an average diameter of 5.1 nm with standard deviation 0.9 nm. Compared to those particles reduced at 700°C (Sample 1 and 2), the decrease of reduction temperature does not change the particle size distribution significantly. There is however a moderate increase in the number of those produced with size smaller than 5.1 nm. This observation could be explained by the fact a low reduction temperature does not allow the same extent of growth of the particles. The elemental distribution of both Fe and Ni was also examined by EDX mapping. In Figure 5.2.4, the distribution of Ni and Fe is shown. Once more the two elements are evenly distributed within the individual particles. Fe and Ni signals are mostly confined within the particles with no signals from the surrounding SiO_2 substrate. The composition of the particles is Fe 31 at.% Ni 69 at.% (standard deviation of 8.4 at.%).

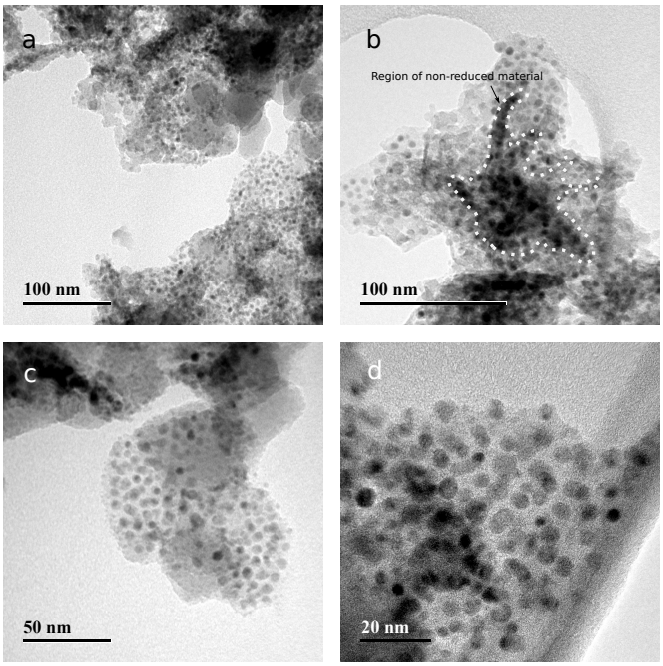

Figure 5.2.1 – BF images of the Ni50Fe50 particles reduced at 500℃ (Sample 4). The particles have a round shape and they are evenly distributed on the support. Region of non-reduced material is highlighted in b. EDX point scan was also conducted on the feature but there is no direct signal of either Ni or Fe but only SiO_2.

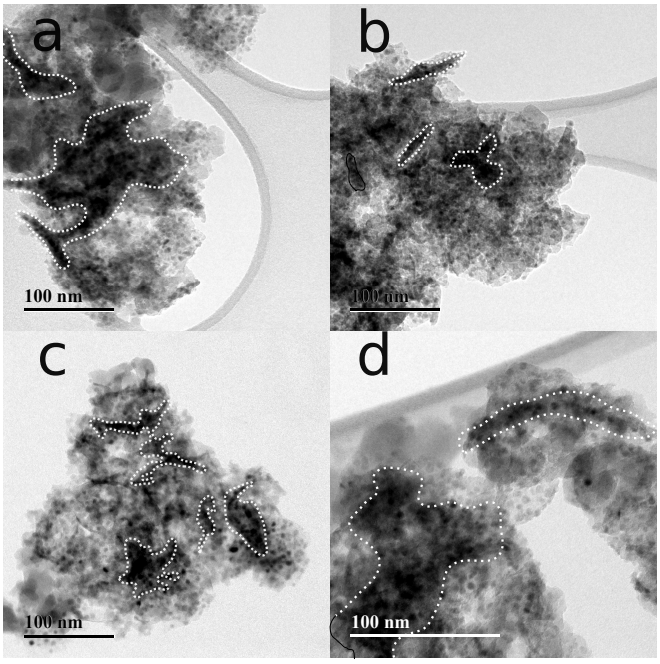

Figure 5.2.2 – BF images of the Ni50Fe50 catalysts on silica reduced at 500℃ (Sample 4). Features of formed phyllosilicates are isolated in the figures.

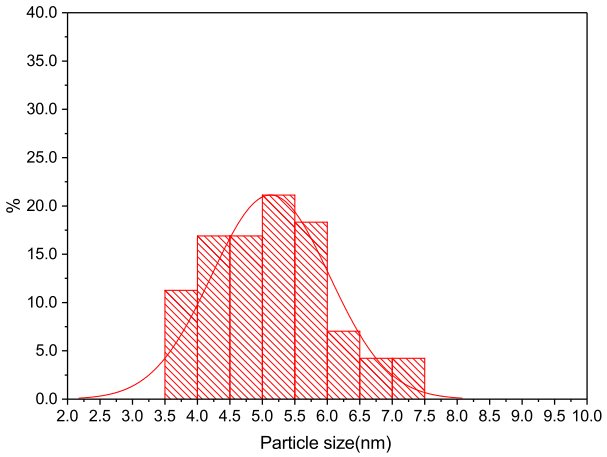

Figure 5.2.3 – Particle size distribution of the Ni50Fe50 particle reduced at 500 ℃ (Sample 4). The most abundant size is about around 5.25 nm and the size of the particle ranges from 3.5 nm to 7.5 nm.

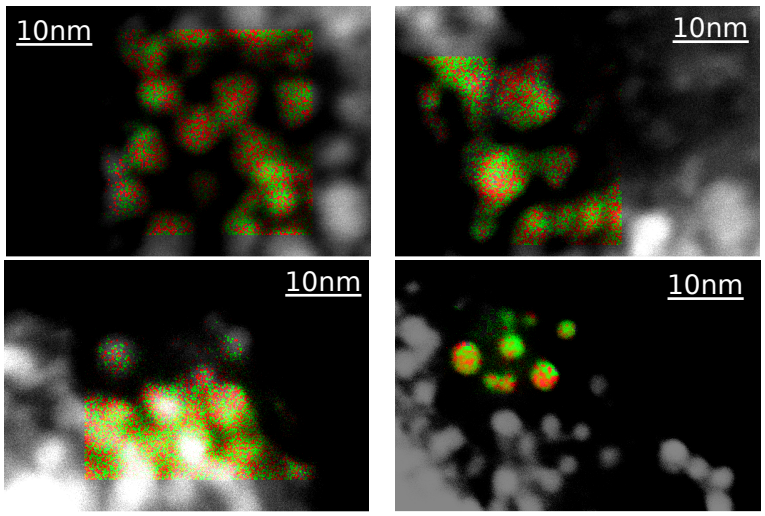

Figure 5.2.4 – EDX mappings of Ni50Fe50 particles reduced at 500℃ (Sample 4). The red colour represents Fe whilst the green colour represents Ni. Both Ni and Fe coexist in nanoparticles as small as 3nm.

5.3 Comparison of Ni50Fe50 and Ni50Co50 particles reduced at 700℃

An Fe deficiency compared to the nominal value has been observed in both samples reduced at 500°C and 700°C, respectively. As the intended route, it should be Fe(II) and Ni(II) ions present in the solution and these two ions should be precipitated simultaneously onto the substrates. However, it is shown that Ni(II) precipitation is preferential compared to Fe(II) during DPU. To further understand the details of the metal deposition process, Co was used to replace Fe, so as to check whether an Ni excess is also apparent in an alternative binary system. In Figure 5.3.1, BF images and HAADF images of the Ni50Co50 particles reduced at 700°C (Sample 5) are shown. The results show no significant difference in terms of the particle distribution and morphology after changing one of its constituent elements. HAADF images as shown in sub-figures e and f, reveal a clear round shape of the particles, and there is no agglomeration observed. The size distribution measurement, shown in Figure 5.3.2, further confirms the similarity of these particles with the Ni50Fe50 system. In the images, particles have an average diameter of 4.5 nm, with a distribution between 2 nm to 8 nm. EDX point scans on individual particles gives a reading of Co 34 at.% Ni 66 at.%, with a standard deviation of 7.9 at.%. Combining the composition data from the NiFe particles, it can be concluded Ni is preferentially deposited over both Fe and Co, respectively, in the DPU process.

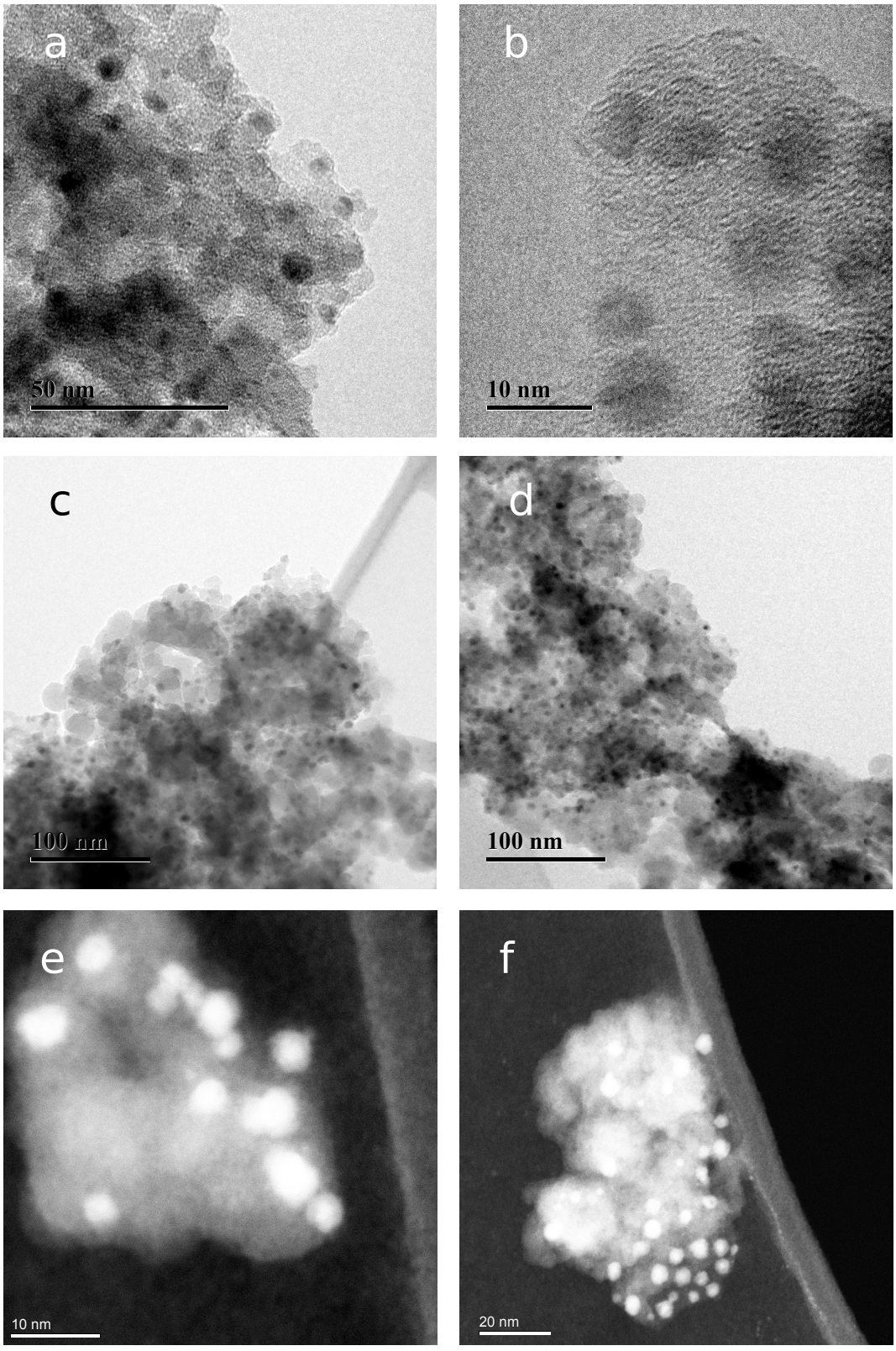

Figure 5.3.1 – BF images and HAADF images of the Ni50Co50 particles reduced at 700℃ (Sample 5). These images show particles evenly formed on a silica support.

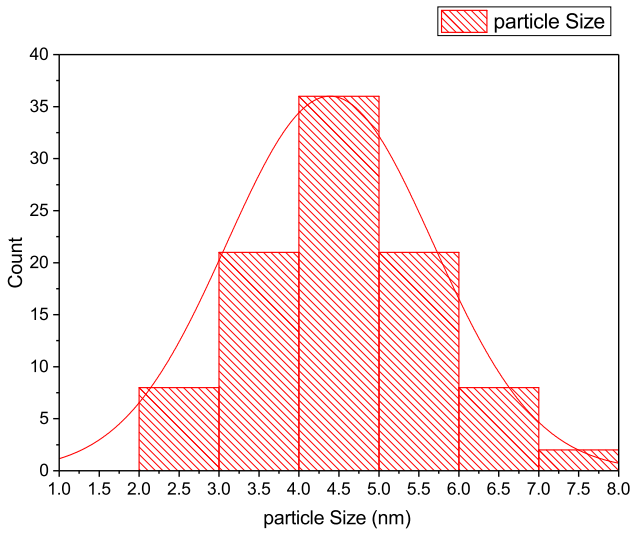

Figure 5.3.2 – Particle size distribution of the Ni50Co50 particles reduced at 700℃ (Sample 5). The most abundant size is around 4.5 nm and the size of the particles ranges from 2 nm to 8 nm.

5.4 Discussion

As this is the first step towards a shift from the analysis of model alloys to real catalysts, it is important to obtain particles which are consistent in terms of shape and composition. TEM is no doubt the easiest method to perform such examinations relatively routinely. BF images and HAADF images using TEM reveal the shape and particle distributions successfully. They confirm that particles fabricated by the DPU method present a narrow size distribution, centred on a small particle size with a high miscibility of constituent elements (Sample 1-5 except 3). Nevertheless, composition measurements, especially EDX point scans, show a consistent deficiency of Fe in the nominally Ni50Fe50 particle samples, regardless of reduction temperature variations, although there also appears to be a dependence on the selected size of the particles, as the larger Ni50Fe50 particles more closely match the nominal value. A corresponding deficiency of of Co is observed in the smaller nominally Ni50Co50 particle samples. These results showing that Ni is preferentially deposited over both Ni or Co, respectively, in these systems investigated.

Additional features observed on the Ni50Fe50 particles reduced at 500°C are associated to phyllosilicate, which is not fully reduced at that 500°C but is fully reduced at 700°C. This deduction comes from the fact that Fe silicate normally requires higher temperatures for full reduction as compared to Ni silicate [62]. EDX map scanning was also conducted on the flake-shaped feature but there was no direct evidence showing the presence of either Ni or Fe. As a conclusion, it can be understood that the particle composition is related to 1) particle size 2) DPU method but not related to the various oxidation states of participating ions at least for Fe ions. Additional characterisation and exploration of the synthesis conditions is therefore needed to further explain the cause of Fe content loss.

Overall, the initial attempt of shifting the focus of this research from model alloys to the nanoparticles has successfully demonstrated the advantage of using the DPU method for generating controlled bimetallic particles. However, it is difficult to develop a systematic advanced characterisation strategy on such systems given the artefacts of a chemical preparation, i.e. unexpected variation of compositions to what is intended, changes of composition

with particle sizes. Therefore, particles prepared with better control (via physical method) will be used for the APT analysis.

Chapter 6

Inspection of nanoparticles fabricated by physical method: IGC

Chapter 4 has examined surface segregations that occur in model catalytic alloys upon exposure to reactive atmospheres. Also, in Chapter 5, nanoparticles with similar compositions were synthesized to investigate complementary surface composition effects. The benefits of employing atom probe to the analysis of such catalytic materials is clear, and ultra-thin surface segregation layers were detected successfully as reported in the chapter 4. However, difficulties have been identified for the study of multimetallic nanoparticles, such as: complex sample preparations, limited field-of-view, sample contamination and reconstruction aberrations, all of which can impact the quality of the atom probe analysis. To address these difficulties (in this chapter), a unique method (IGC) was employed to fabricate particles. This route enabled the development of a new deposition-encapsulation method for atom probe sample preparation of particles. Furthermore, complementary analytical methods were employed to examine particles produced in the same batch, providing information at a larger length scale, which served to both confirm suitable reconstruction parameters in the atom probe data and address the issue of limited field-of-view.

6.1 Characterisation of Ag monometallic nanoparticles

Ag monometallic particles were selected as the candidate material for the first trial of this deposition-encapsulation approach. Monometallic Ag has several benefits. Ag has just two distinct masses at 106.91 Da and 108.91 Da enabling easy identification in mass spectra data. Ag also has a low evaporation field ($24 V nm^{-1}$calculated by Image Hump Model [242]) which reduces the chance of premature fracture of the specimen during the experiment, as it decreases the difference between the required evaporation fields of the capping layer and substrate, respectively. Monometallic particles were chosen to facilitate a relatively straightforward data interpretation for the initial atom probe analyses.

6.1.1 Mass filter (MesoQ)

Ag monometallic particles were produced by the IGC method, which has been described in the section 3.1.3 on page 71. As the IGC method can produce particles with accurate size control, the size distribution of the resulting fabricated nanoparticles was first examined. A quadrupole mass filter (MesoQ) was used to scan the particles and control their size. By applying AC and DC voltage with varying frequency and amplitude through the four rods, an electromagnetic field was created to only allow passage to particles with a specific mass-to-charge ratio [255]. At the exit of the mass filter, the sample ion flux was measured by a metal grid. DC frequency and ion flux were documented as the raw data. A schematic diagram of the apparatus together with the actual mass filter used in this research is shown in Figure 6.1.1.

To convert these data into information related to the particle sizes, there are several assumptions used to simplify the process. Particle sizes are calculated from the mass-to-charge ratios by assuming that 1) particles are in a single $(1+)$ charge state, 2) the samples are all spherical, and 3) density of the metal within the nanoparticles is known. The assumed values for the particle density are listed in Table 6.1.1. For multimetallic particles (these particles will be mentioned later in the chapter), the density is calculated assuming that

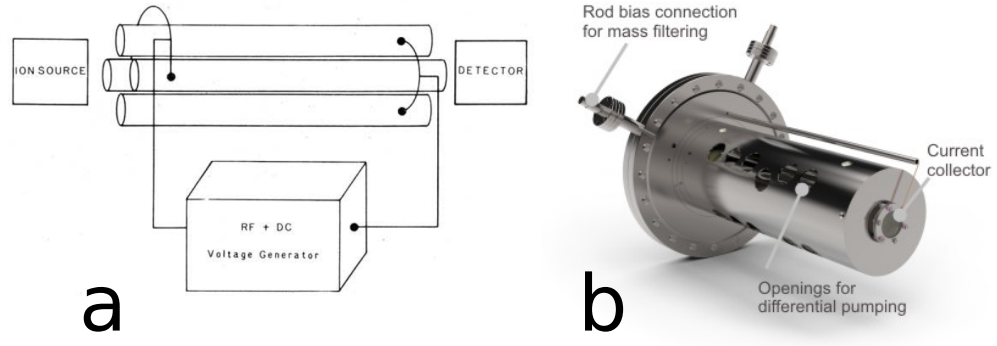

Figure 6.1.1 – a) a schematic diagram of a quadruple mass filter [255] b) the mass filter used in this research

the contribution from constituent elements are weighted by their atomic percentage. In addition, it is assumed that the crystal structure including the unit cell volume does not change upon alloying. It is well understood that these assumptions can deviate from the true density of particles formed but it is still the best estimation given little knowledge on the composition beforehand. Through such assumptions, the particle size can be calculated, from which a size distribution histogram can be generated, as shown in Figure 6.1.2. In this graph the frequency of given charged-particle size is represented by the resulting current, nA. Overall, a narrow distribution of Ag nanoparticle sizes is indeed observed, with the majority of particles deposited having a diameter ~6 nm and a satellite peak around 2nm. The size is consistent with the size expected on supported metal catalysts. For the accuracy of size measurement during the deposition, three independent scannings were carried out during one deposition. As shown in the figure, the three curves are closely overlapping with each other, reflecting the size stability throughout the particle making process.

6.1.2 SEM

The quality of the Ag nanoparticle deposition was also examined by SEM. Figure 6.1.4a shows SEM images of as-deposited Ag nanoparticles on the apex of a single Si post. The diameter of the exposed silicon post is about 2300nm. Bright and round spots can be ob-

Name	Density	Name	Density	Name	Density
Ag	$10.49 g/cm^3$	Au	$19.30 g/cm^3$	AuNi+He	$14.10 g/cm^3$
Cu	$8.92 g/cm^3$	AuCu	$14.11 g/cm^3$	AuNiMo	$12.83 g/cm^3$
Ni	$8.908 g/cm^3$	AuCuMo	$12.37 g/cm^3$		
Mo	$10.28 g/cm^3$	AuNi	$14.10 g/cm^3$		

Table 6.1.1 – Density assumptions for nanoparticles produced by IGC method. The density input listed here is used to drive particle size distribution. For multimetallic particles, the densities are calculated assuming the element abundances are equal (at.%).

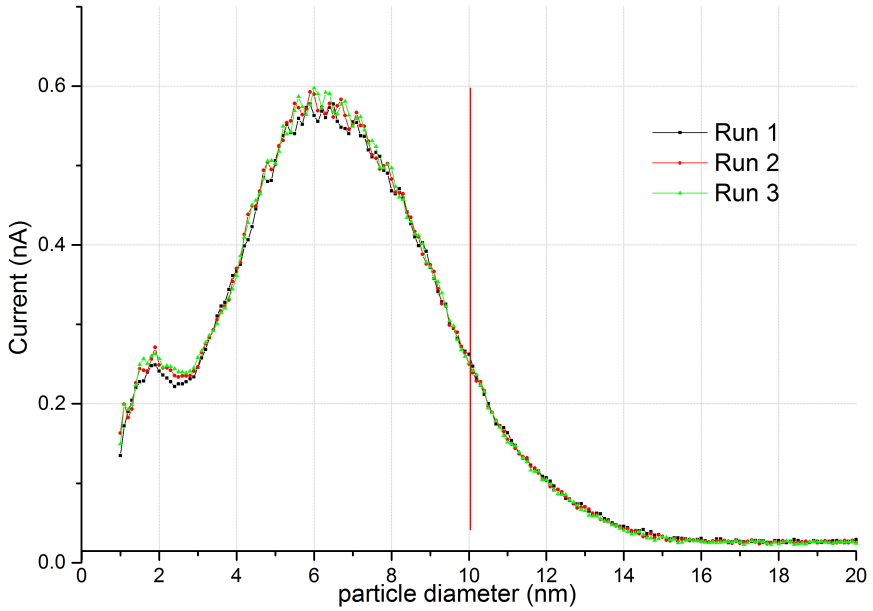

Figure 6.1.2 – Size distribution of the produced nanoparticles. The data is obtained from the mass-to-charge ratio detected from the quadrupole mass filter. The legends represent different runs during experiment, showing little change in the size distribution between different measurements. Particle size larger than 10 nm is filtered out, which is marked with the red line in the graph.

served on the post, indicating successful deposition. The abundance of the nanoparticles matches the designed parameters (less than one monolayer without particle coarsening), which at practice is approximately a monolayer deposition but not fully compacted as outlined in section 3.1.3 on page 71. Figure 6.1.4b provides more detail at higher magnification, from which it is possible to derive particle sizes. The measurement of the particle size is made using ImageJ software, and the average size is about 11nm, with a standard deviation

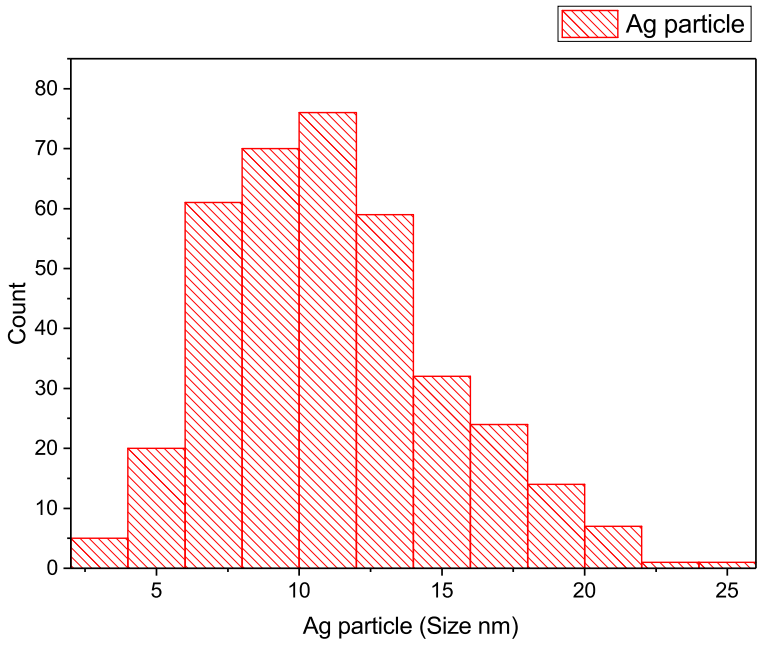

Figure 6.1.3 – Size distribution measurement of the Ag particles. Nanoparticles have a most abundant size at 10 nm. The size measurement is made manually.

3.9 nm, determined via 400 measurements (the histogram is shown in Figure 6.1.3). Considered the MesoQ data, there is coalescence or influence of multiply charged Ag particles.

Overall, the SEM images are in relatively close agreement with the results from the quadrupole mass filter (Figure 6.1.2), indicating a good control of particle size. To obtain further spatial information on the surface distribution of the nanoparticles, a nearest neighbour (NN) distribution was calculated using an image analysis algorithm based on MATLAB developed by Mr Aakash Varambhia and Dr Lewys Jones. The first stage in this analysis is to determine the centres of individual nanoparticles (green dots) and record the 2D coordinates, as shown in Figure 6.1.5a. The pixels of the image and the actual distance is calibrated, and therefore the nearest neighbour (NN) distance can be calculated by counting the pixels in between the green dots. Following this, a NN distribution can be determined (based on the 1-NN (first nearest neighbour)). The values obtained are plotted in Figure 6.1.5b, which shows that most nanoparticles lie within 10nm of each other. During the MATLAB process, a margin with a thickness of 20 pixels around the edge of the picture

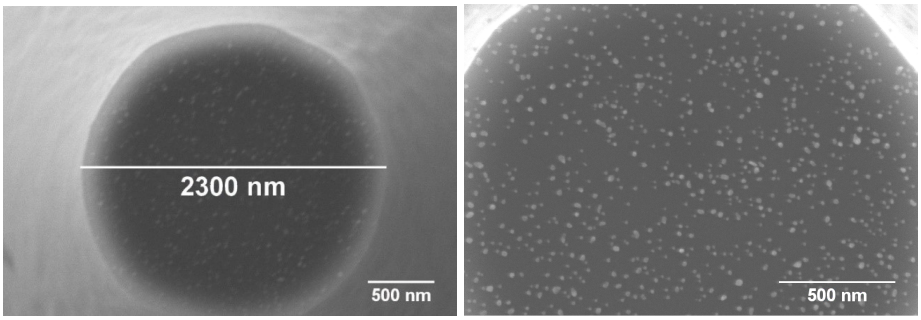

Figure 6.1.4 – SEM images of the deposited nanoparticles on the top of a silicon microtip post. a) A full picture of the flat end of a silicon post, the diameter of which is about 2300nm. b) A magnified picture of the silicon post, bright dots on which are individual Ag nanoparticles.

was left unprocessed to reduce the inaccurate reading around the picture edge.

6.1.3 APT

Since APT has the strict requirement for needle-shaped specimen, nanoparticles in the format (particle on flat surface) described above cannot be analysed directly. Previously, attempts have been made to produce an APT-ready sample by direct attachment of particle to a pre-made tip [214, 228]. The resulting reconstructions were however difficult to interpret. Therefore, a new approach is employed, the details of which have been described in sample preparation section 3.1.3. In this method, the first step consists of coating Ag particles by a protecting, encapsulating Pt layer.

Figure 6.1.6a shows an Ag nanoparticle-loaded post along with a series of tests aimed at burying the nanoparticles below a layer of Pt deposited using the FIB electron beam (which appear as the bright protrusion in the picture). One of these Pt-based deposition protrusion was then subject to annular milling using the Ga^+ beam to produce the final sample ready for APT analysis as shown in Figure 6.1.6b. In this image, the Pt capping layer and silicon post have good contrast which aids final sharpening; the Ag nanoparticles are supposed to lie at the interface between the bright and dark regions. The prepared needle samples were then analysed via APT, and the resulting atom map is shown in Figure 6.1.6c. In the reconstruction, the individual Ag nanoparticles, Pt coating layer and supporting Si post

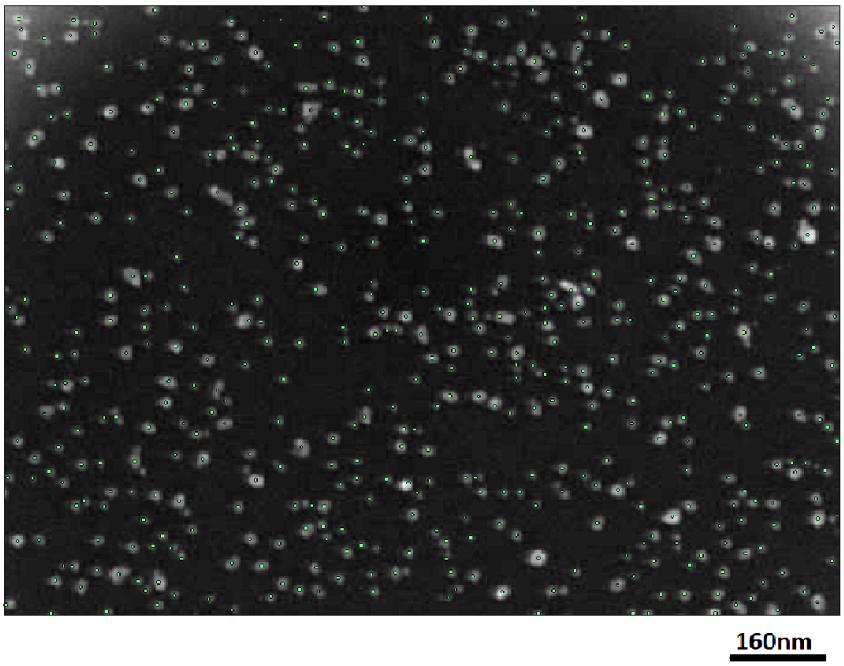

(a)

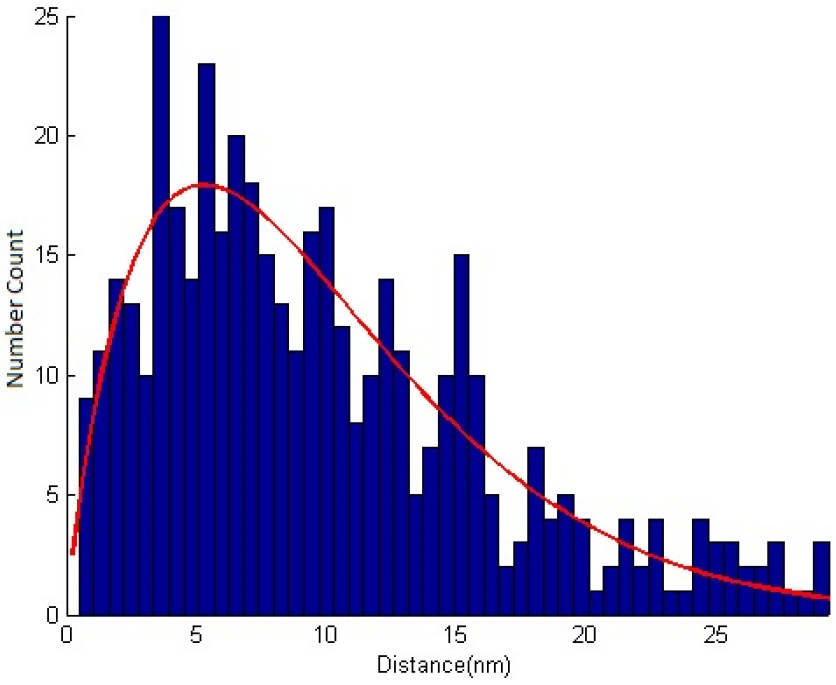

(b)

Figure 6.1.5 – a) SEM image with green dots shows the detected centres of deposited particles. Totally, 464 coordinates of those dots have been recorded. b) Resulting nearest neighbour distribution of all detected particles. The distribution indicates that 70% particles are within 10nm of each other.

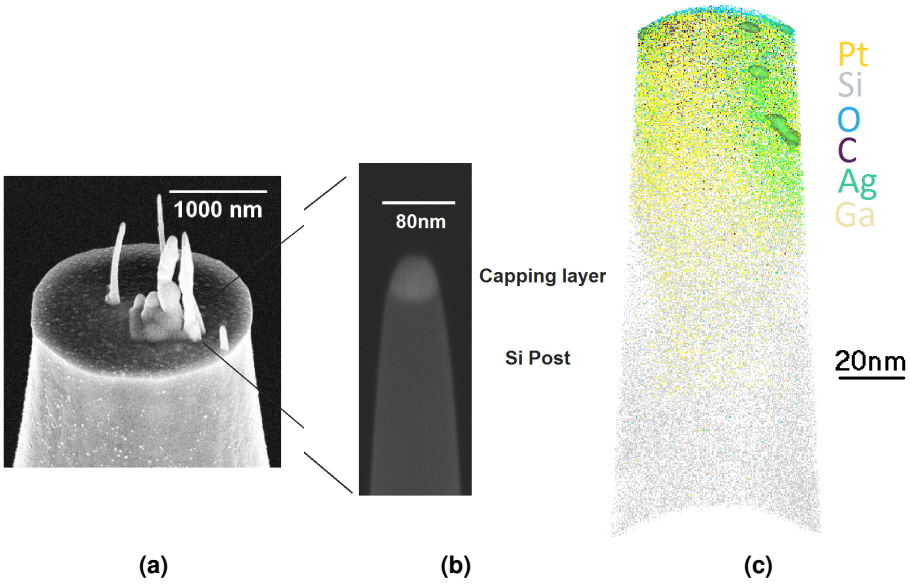

Figure 6.1.6 – Atom probe sample preparation under high resolution SEM. a) A single Si post following Ag nanoparticle deposition and subsequent in-situ capping in the FIB instrument by Pt using the electron beam. b) Final sample produced by annular milling. The radius of the tip is around 50nm. c) Atom map reconstruction of the tip shown in b). The data set shows distinct regions: an upper layer consisting of Pt and C species, then Ag nanoparticles before the Si atoms in the post are detected. (Ag particles are enclosed in green colour)

are clearly revealed upon application of the Ag iso-density surface ($2\ atoms/nm^3$). The data set thus closely correlates with the SEM image of Figure 6.1.6b. In the upper region, apart from Ag the major detected ions are O, Pt and Ga. Oxygen is abundant on the outer surface of the dataset, which is usual for samples exposed to the atmosphere. However, the oxygen layer is thin, indicating that the deposited Pt layer has preserved the embedded nanoparticles. The precursor species used to form the Pt layer contains substantial amounts of C, which is also detected, along with Ga^+ from ion implantation during the FIB milling process [314]. Efforts to refine the quality of the Pt coating, utilising higher purity dedicated coating instrumentation are investigated in the later sections. To examine the distribution of the Ag atoms, separate atom maps were generated, which are shown in Figure 6.1.7. The first of these, Figure 6.1.7a, shows that a significant quantity of the Ag atoms are distributed throughout the analysis volume, rather than being wholly within distinct nanoparticles. The origin of this Ag distribution may be due to a combination of effects. One cause may be trajectory aberrations in the evaporation of atoms during APT analysis,

due to the significant difference between the electric field strength required to evaporate Ag and Pt atoms respectively. Furthermore, the known high surface mobility of Ag under intense electric fields could further contribute to any trajectory aberration [315]. Another explanation is the possible presence of very small nanoparticles/individual Ag atoms on the microtip coupon following deposition. Evidence for the latter is shown in the particle distribution of Figure 6.1.4b, which indicates a substantial fraction of very small species (<1nm) present. Refining deposition conditions (including substrate bias which may also be causing nanoparticle breakup on impact) and the condition of the FIB-capping layer would help to identify the origin of the spatial-spread in Ag distribution. Nevertheless, the atom maps demonstrate a considerable improvement on previous attempts to analyse nanoparticles using electrophoresis-based methods, with distinct intact Ag nanoparticles clearly resolvable in the data by means of an Ag iso-density surface. This is shown in Figure 6.1.7a, highlighting five isolated Ag nanoparticles detected in the reconstruction. The volume and calculated equivalent diameters of the five isolated particles are listed in Figure 6.1.7b. The volume data is directly derived from isosurfaces, from which the equivalent diameters are then calculated with the approximation that all particles are spherical. The calculated equivalent diameters are all less than 10nm, in agreement with the mass filtering and SEM results in Figure 6.1.2 and Figure 6.1.3. The calculated nearest neighbour distances for the five nanoparticles are also listed in Figure 6.1.5b, and these, with the exception of Nanoparticle 5, all lie within the broad distribution based on the SEM observations in Figure 6.1.4b. Nanoparticle 5 resides just within the APT analysis field-of-view, and it may well be that further nearer nanoparticles are located just outside the analysis volume. A particle composition analysis shows there is a range of other elements enclosed within the isolated Ag particles. These are mostly Si, Pt and Ga, which are most likely introduced through trajectory aberrations and Ag surface mobility effects along with sample preparation issues in the FIB. Alternatively, the existence of Si within identified Ag nanoparticles could be the result of the particle deposition process, whereby a fraction of Ag particles impact on the surface and mix with Si atoms from the surface [232]. However, the accuracy of compositional analyses

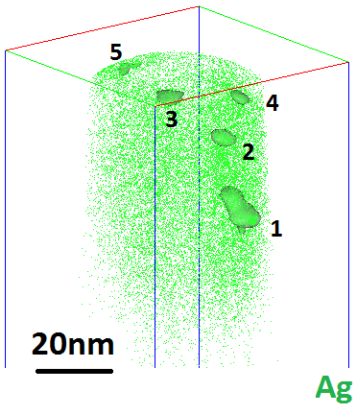

(a)

No.	Volume (nm^3)	Equivalent diameter (nm)	Nearest Neighbour distance (nm)
1	332	8.6	18.4
2	80.7	5.4	15.0
3	66.0	5.0	18.4
4	30.4	3.9	15.0
5	14.7	3.0	33.6

(b)

Figure 6.1.7 – a) Ag atoms detected during APT analysis, along with distinct Ag nanoparticles as identified using an iso-density surface (2atoms/nm3). Isolated nanoparticles labelled '1-5'. b) Dimensions of the isolated Ag nanoparticles. The volumes are derived from the isosurfaces and the equivalent diameters are based on a spherical volume. Nearest neighbour distances are calculated based on the central coordinates of those particles within the atom data reconstruction.

through this method could potentially be enhanced by improvements in deposition/sample preparation conditions.

6.2 Characterisation of AuCu and AuCuMo nanoparticles

Following the success of the Ag nanoparticle deposition methods, AuCu and AuCuMo particles were targeted for further investigation. AuCu and AuCuMo multimetallic nanoparticles were selected since they have the potential for catalytic applications as mentioned in section 2.2.2 on page 34. Furthermore, it is also important to verify the composition stability of any multimetallic particles produced by the IGC method. Finally, for this particular system, a development of the encapsulation method is also introduced to further improve the quality of the resulting APT reconstructions.

6.2.1 MesoQ (mass filter)

In a similar manner to the Ag nanoparticle work, in-line mass spectra were obtained through the application of the same quadrupole mass filter during particle fabrication. Figure 6.2.1 shows the recorded size distributions for the binary and ternary alloy particles, together with simple additions of each individual Au, Cu and Mo signals. By comparing the profiles for both the real and predicted summation scans, a clear difference is noted, again indicative of potential alloying effects. Upon examining in more detail, the figure shows that nearly all as-fabricated particles have a size distribution below 10 nm, with the most populated size around 3 nm. Fewer particles at the smallest size (<3 nm) are seen in the experimental curves comparing to the summations, which is consistent with the assumption that the elements are combining to form larger alloyed particles. For the AuCu line in Fig. 6.2.1a, there is a secondary broad peak around 8 nm in the experimental curve, which may be evidence of potential alloying. The addition of Mo changes the behaviour of particle fabrication, from the mass spectrum perspective, with no emergence of a side peak around 8 nm, but only instead a slight shift of the peak from 2.5 nm to 4 nm. Particle size filtering was applied to the AuCuMo particles with an upper-limit of 6 nm to monitor particle size control ability during the fabrication. The result of such filtering is presented in the following TEM subsection.

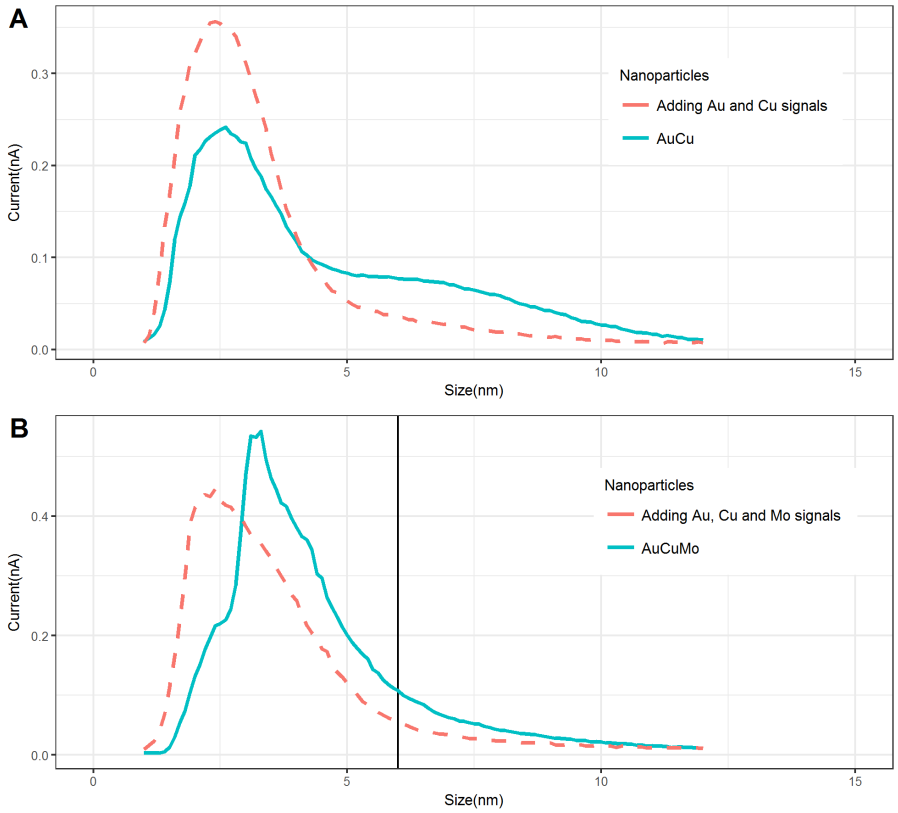

Figure 6.2.1 – Size distributions of deposited AuCu (A) and AuCuMo (B) nanoparticles. Dashed lines in the two figures represent the summation of individual Au, Cu (and Mo) singles. Solid lines represent the experimental curves from bimetallic and trimetallic nanoparticles. The vertical line in figure B indicates the size cut-off to 6nm in diameter implemented by the mass filter during depositions.

6.2.2 TEM

Apart from direct particle measurement by MesoQ data, TEM experiments were also used to investigate particle density, size, crystal structure and composition, all of which are crucial to assess the data accuracy from MesoQ and assist accuracy in the subsequent APT analysis.

In Figure 6.2.2, BF images of as-deposited AuCu and AuCuMo nanoparticles are shown at low and medium magnifications. Figures 6.2.2 a and c show a uniform and reproducible sub-monolayer coverage of nanoparticles on the carbon film (lacey carbon grid), which matches the intended deposition density (the number of particles per unit area). Furthermore, inspection of figures 6.2.2 b and d shows that the nearest neighbour distance of both nanoparticle batches is comparable, ranging from around 10 to 40 nm. This distance is also within the range of the field of view of APT analyses. Size measurements of both kinds of nanoparticles from the TEM images are shown in Figure 6.2.3 (based on 300 particle size counts). For both AuCu and AuCuMo, a bimodal distribution is seen with peaks centred at 3 nm and 8 nm. It is clear that the MesoQ and TEM measurements of AuCu particle distribution are in good agreement. However, the intensity of the peaks is different, specifically there is increased counting of larger particles measured by TEM. On the other hand, the AuCuMo analysis is quite not the same when comparing the two different kinds of measurements. The AuCuMo size distribution curve measured by TEM is very similar to the one of AuCu, showing little impact of the addition of Mo. As mentioned, a size filter was applied to limit the AuCuMo particles within a size of 6 nm and the resulting size distribution curve is slightly shifted towards the smaller end comparing to the AuCu. However, the measured particle sizes show a significant number of particles larger than 6 nm, which is beyond the nominal filtering limit. It is believed that both measurements are accountable, but they are measuring the particle size at different stages during their production and that particles do change in this interval.

Figures 6.2.4 and 6.2.5 show a closer look of both particle types. Minor particle agglomeration is evident in Figure 6.2.4 e, i and Figure 6.2.5 d and h, which may explain observation of larger particle sizes by TEM. In these images, some particles still retain a

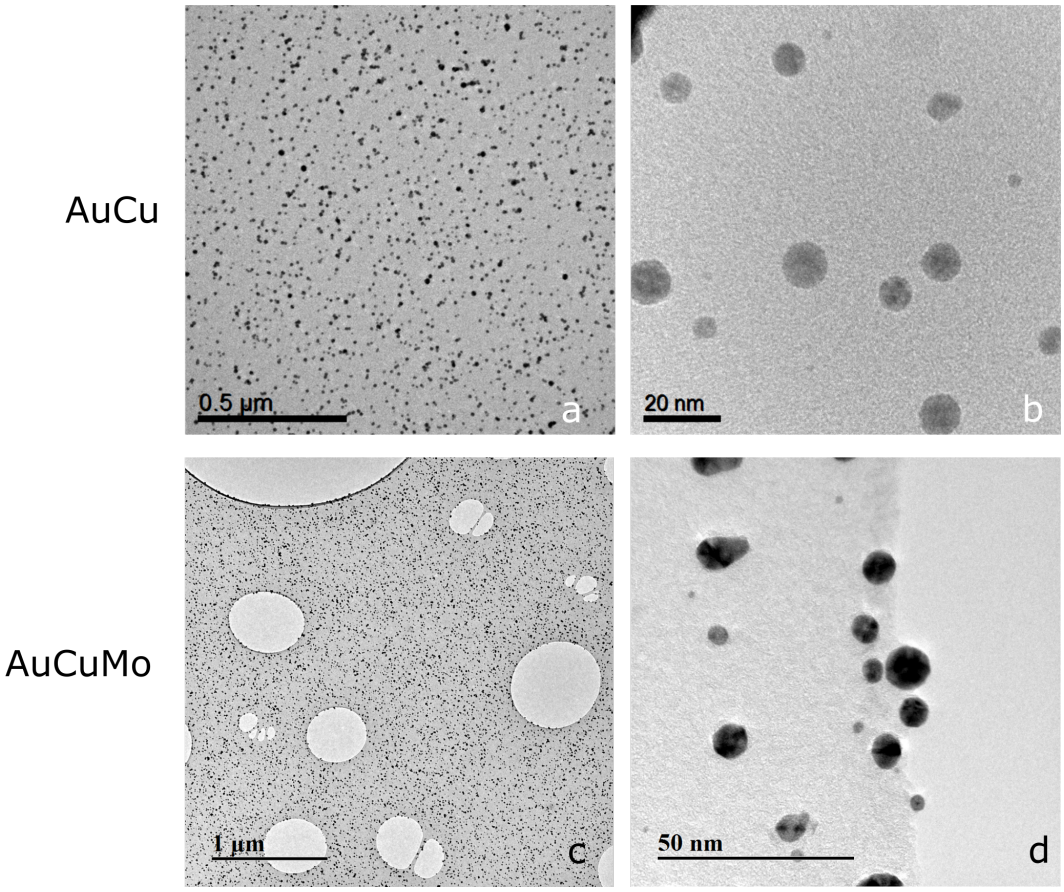

Figure 6.2.2 – TEM images of the as-deposited nanoparticles on lacey carbon TEM grid. Magnification of the images increase from left to right. The top row represents AuCu particles and the bottom shows AuCuMo particles. The images were taken on a JEOL 2100F.

round shape whereas others are merged together. In theory, particles carry negative charges, which prevent them from agglomerating. The agglomeration observed here could be the result of particle charge neutralised upon impact with the substrate. This coalescence phenomenon is also observed in Au particles as soon as they reach the substrate [316].

There are two dominant atomic structures observed in the BF image: an icosahedron and a decahedron, as apparent in Fig. 6.2.4 f-i, and Fig. 6.2.5 b-e. The icosahedron structure is dominant for both AuCu and AuCuMo particles, but some small particles as shown in Figure 6.2.5f present the decahedral structure. It confirms that multi crystal structures are presented in the resulting particles.

HAADF images and diffraction of these two particles are shown in Figure 6.2.6 and

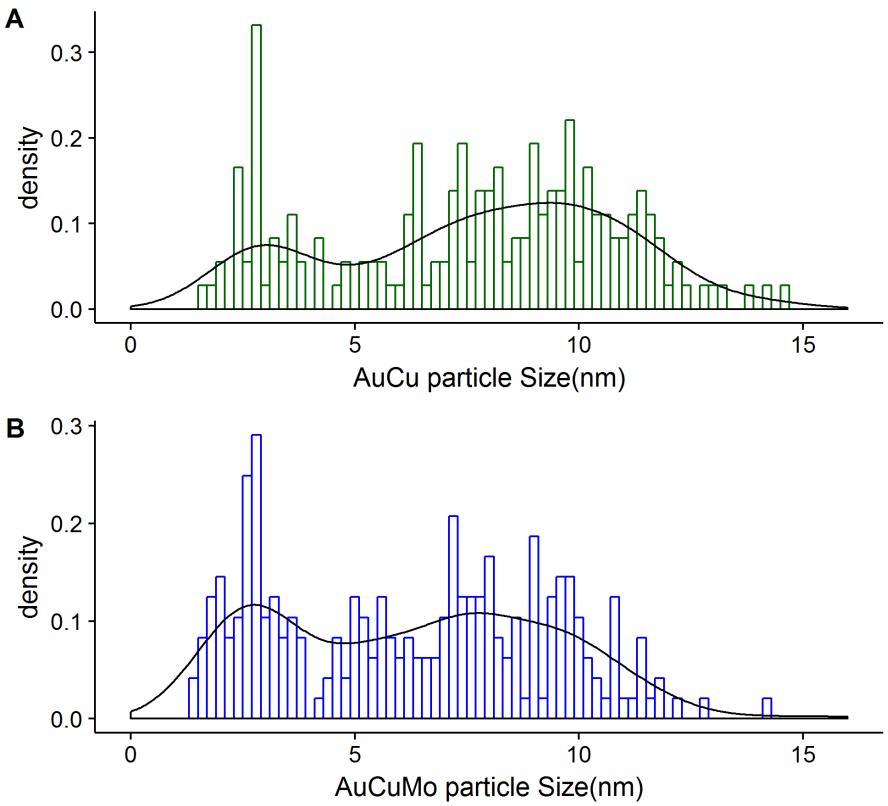

Figure 6.2.3 – Size distribution measured from bright field images of as-deposited (A)AuCu and (B)AuCuMo nanoparticles. Both sets of data show a trend of a bimodal size distribution, one of which peaks is around 3 nm and the other is around 10nm.

6.2.7. Apart from revealing the icosahedral structure more clearly, they also show no significant composition segregation occurring within the particles, given that this should be apparent due to the significant Z contrast between Au and Cu. Uniform structures are also proved via the diffraction image. A six-fold symmetry is evident in Figure 6.2.6a, which means the particle is relatively uniform in terms of structure, with no direct evidence for localised segregation. A similar uniform icosahedral structure is also observed in the AuCuMo particles, shown in Figure 6.2.7.

An icosahedral structure is also however an indication that the thermodynamic equilibrium was not achieved during the particle generation process. It has been claimed that a decahedral structure is instead a more stable structure after tempering [170]. Therefore, a mixture of particles with two distinct thermodynamic states coexists in the final products.

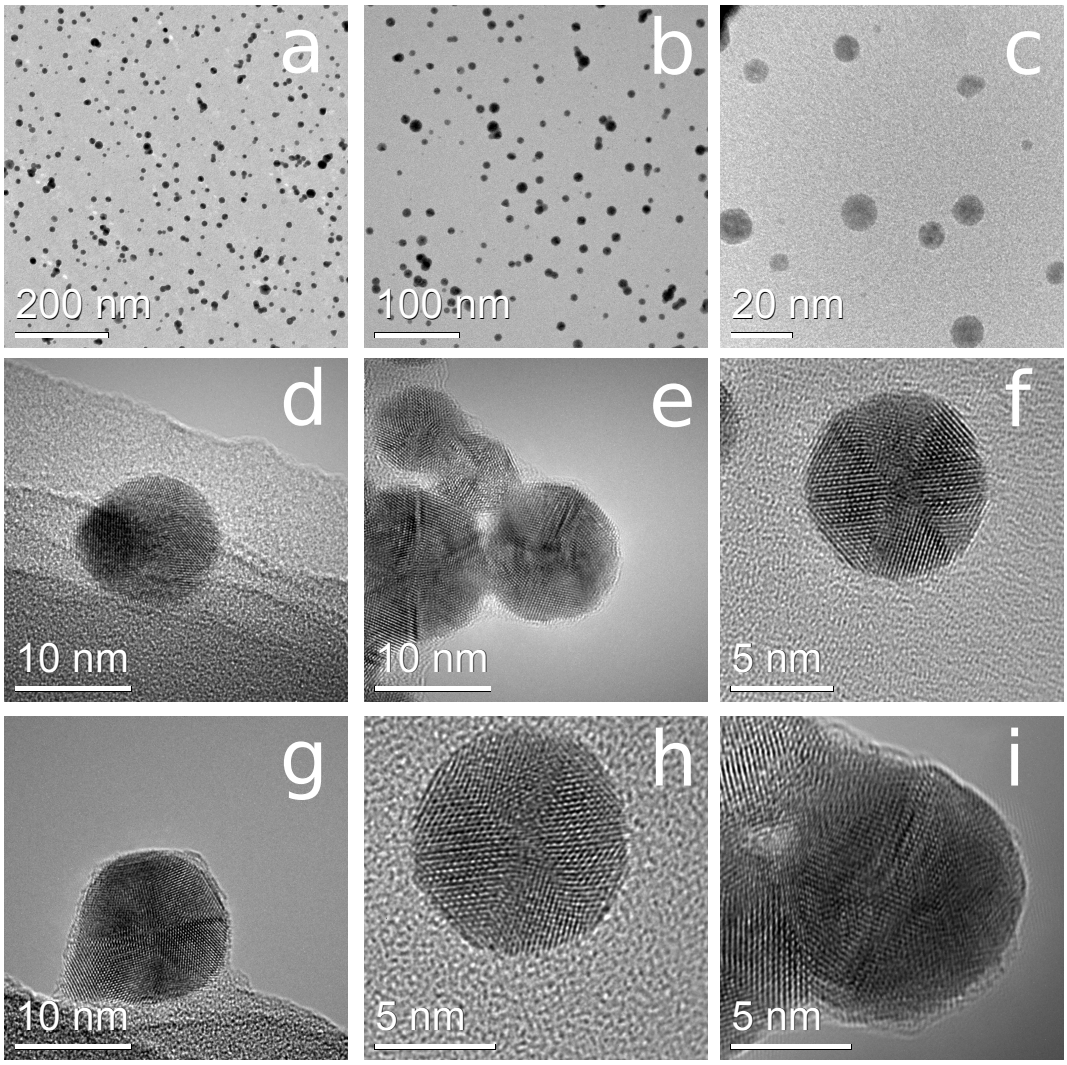

Figure 6.2.4 – Bright field images of AuCu nanoparticles imaged under 3000F field emission TEM. Beam voltage was 300kV.

This reflects that particles experienced various thermal conditions from the condensation zone to the landing substrates.

It is also of interest to observe new particle formation during the TEM analyses. In Figure 6.2.8, nucleation and growth of a satellite nanoparticle was observed directly via BF imaging under 300 keV. Atoms from a close-by particle of size ~5nm migrate to the small particle. This phenomenon demonstrates concerns about particle changes during TEM analysis, as the e-beam can alter the nature of the particle. Therefore, it is also the reason that a 200 keV TEM is used in subsequent analysis to check the observation.

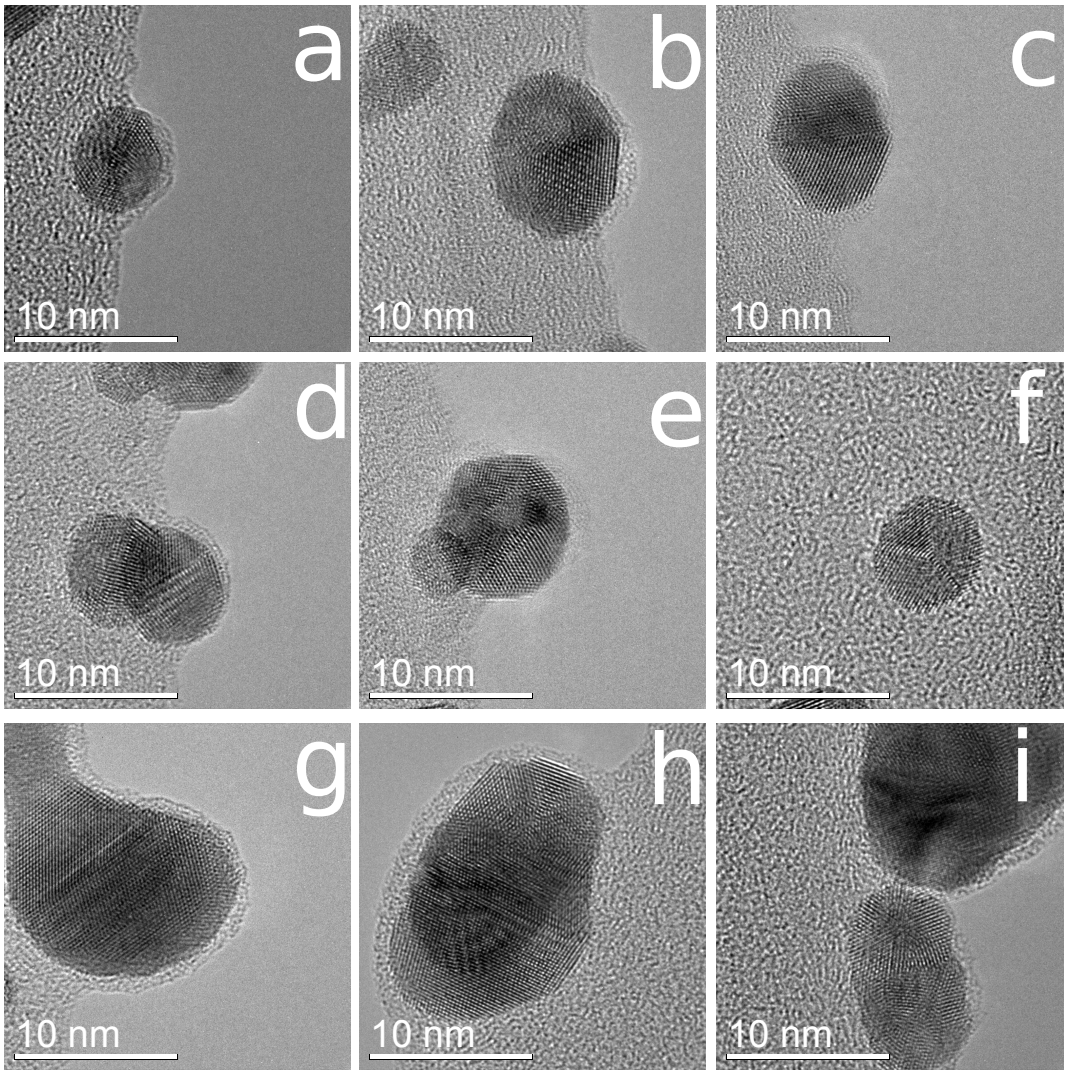

Figure 6.2.5 – Bright field images of AuCuMo nanoparticles imaged under 3000F field emission TEM. Beam voltage was 300kV. Sub-figure b and c show the two-fold symmetry of the decahedral structure. In sub-figure f, five-fold symmetry is shown. [170]

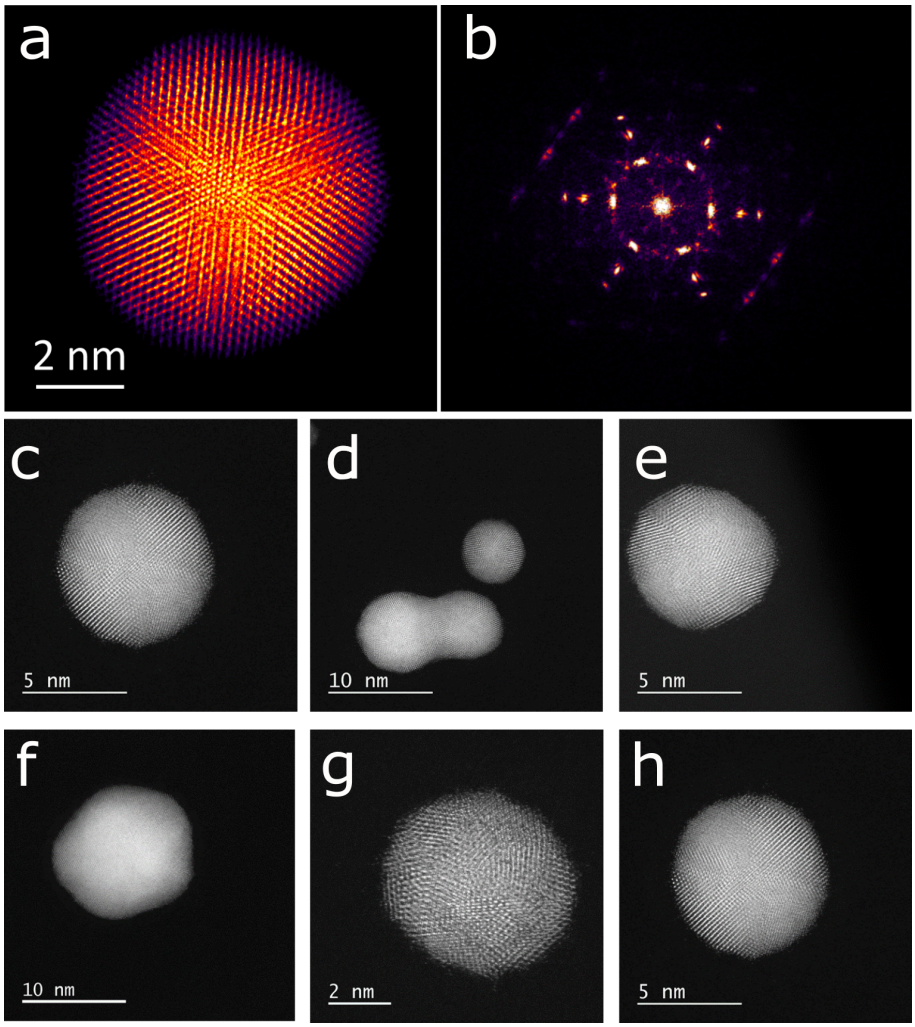

Figure 6.2.6 – AuCu nanoparticle analysed by 200kV ARM 300F C_s corrected TEM. Diffraction pattern resulting from analysis of particle is shown in fig. b. It is clear that the six-fold symmetry of a icosahedral particle is imaged (sub-figure 1 and b). From sub-figure c, e, h, more images of the two-fold projection of the icosahedral structure are shown [317]. In addition, the size of the particle is confirmed within 10 nm.

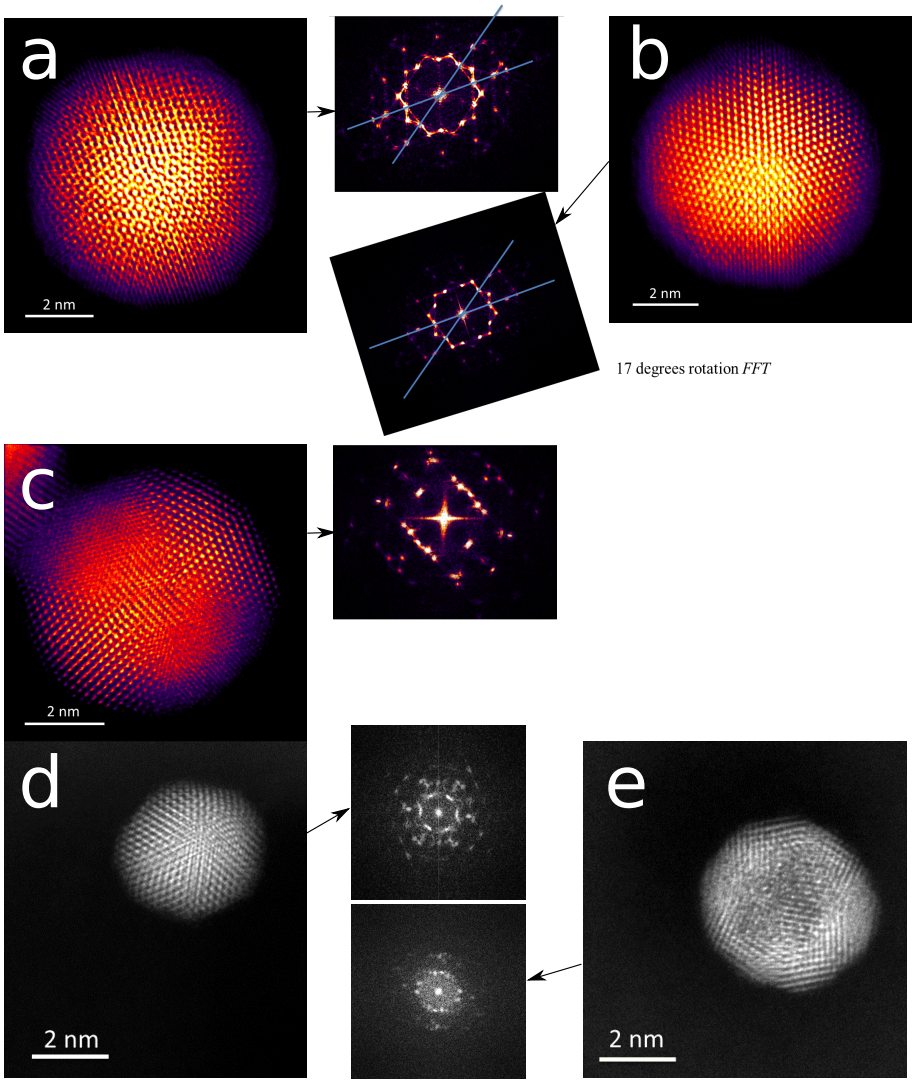

Figure 6.2.7 – AuCuMo nanoparticle analysed by 300kV ARM 300F C_s corrected TEM. HAADF images are corrected by rigid alignment. 10-fold diffraction of the decahedral structure is evident in the sub-figure a [318] and another similar decahedral structure is shown in the sub-figure b. Also, the sub-figures c-e show particles with icosahedral structure.

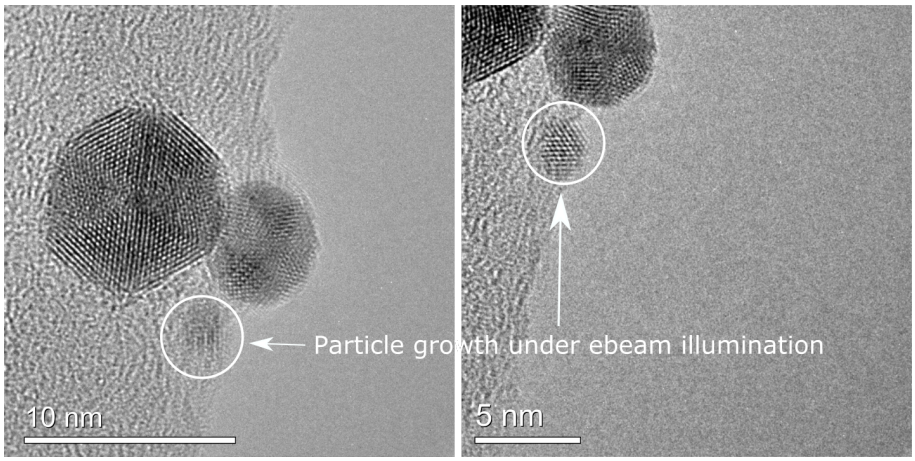

Figure 6.2.8 – AuCuMo nanoparticle atoms partitioning observed in TEM under the electron beam of 300 keV. The encircled area in the left figure grows gradually under the beam, forming a small particle as shown in the right side of the figure. It could be a evidence showing the TEM beam can affect the particle in terms of composition distribution.

6.2.3 EDX

EDX analysis capabilities within SEM and TEM instruments was used to probe particle chemical composition. There are two major questions that EDX was employed to address: a) what is the chemical distribution of Au and Cu in the particles? and b) Is Mo present, and if so, where is it located? The experiments were conducted using detectors attached to SEM and TEM, respectively, covering an analysis area from a few nanometres to a few micrometres. The Zeiss Merlin SEM EDX was used to examine the TEM grid (the same grid was subject to subsequent TEM analysis), conducting a large area scan in an attempt to locate the element Mo. In Figure 6.2.9, EDX data of a scan covering an area of $1.5\mu m \times 1.5\mu m$ is presented . Several elements were detected including Si, C, O, Au, Cu, Al, Fe and either Mo or S (similar energy peaks). Detection signals of Cu (and Al) originate from the Cu TEM grid loaded onto the Al stub. Si and Fe are however unexpected and could be a result of contamination from that particle transfer from the production to analysis. Au and Cu are two of the major alloying elements and are observed to be evenly distributed across those particles. Distinguishing between Mo and S is based on the peak intensity and Mo peak locations in the EDX spectra. No peaks of Mo are apparent at 17.51 keV and 19.61 keV (high energy region) and the expected peak location at 2.295 keV is slightly off the actual detected peak at 2.307 keV. On the other hand, S matches the distribution of these detected peaks well. Therefore, it reasonable to deduce that only S is detected, with no evidence of Mo.

Although this large EDX scan showed no definitive evidence of Mo, it could however be present in the form of segregated small particles or as a small fraction within single particles. Therefore, TEM-EDX analysis of the particles was conducted. In Figure 6.2.10 and 6.2.11, EDX analyses of AuCu and AuCuMo particles by the JEOL ARM 200F (200 keV) and JEOL 3000F (300 keV) are shown. In the analysis of AuCu, 2 nanoparticles on a silicon nitride grid, one about 5nm in diameter and the other 10nm, show clear composition variations at these length scales. For the larger particle, the Au level is greater than Cu, whilst Cu dominates in the smaller one. Cu is more abundant on the surface of the large

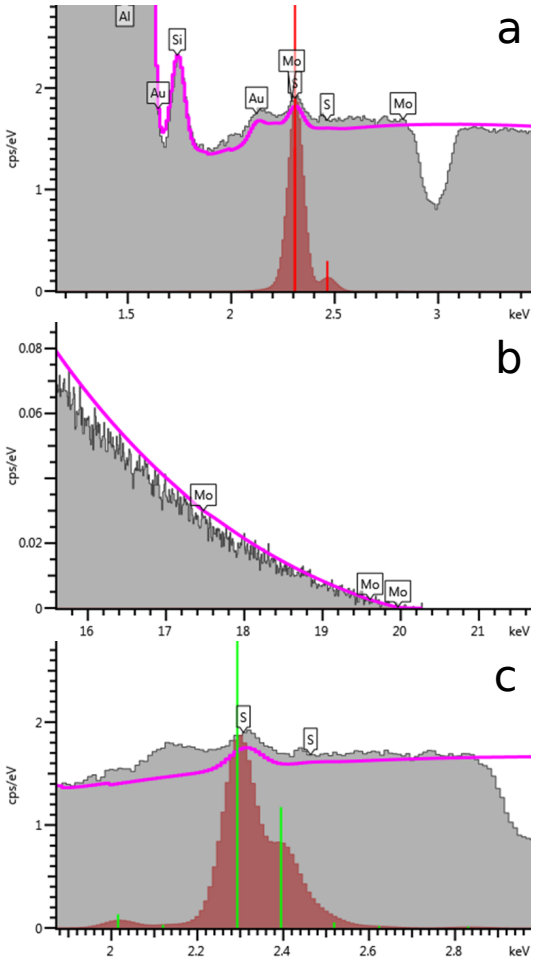

Figure 6.2.9 – SEM-EDX spectra of AuCuMo particles on a Cu TEM grid and peak fitting of potential elements. The red line represents theoretical fit of identified elements and the pink line is the average curve of the signal. a) shows the region where theoretical S peak should exist. b) shows the high energy region and Mo peak locations. c) a zoom on a) shows Mo peaks at low energy region that do not fit well to the detected peaks.

particle, particularly on the side of highest curvature. However, by referring to the BF image, the high intensity of Cu could originate from an overlap of two individual particles. A potential core-shell structure is found in the smaller particle, with an Au shell and Cu core.

Moving from AuCu to AuCuMo, three particles were analysed. For this analysis, there was however no strong composition variation observed across the particles; Au and Cu are quite uniformly distributed with no indication of local segregation. It is however possible that the strong energy input from the 300keV ebeam influenced any local composition differences, effect of which has been mentioned previously. Due to the limitation of instrumentation, the AuCuMo particle was not analysed on JEOL 200F, therefore no direct comparison could be made. In addition, the search for Mo via TEM-EDX was delivered

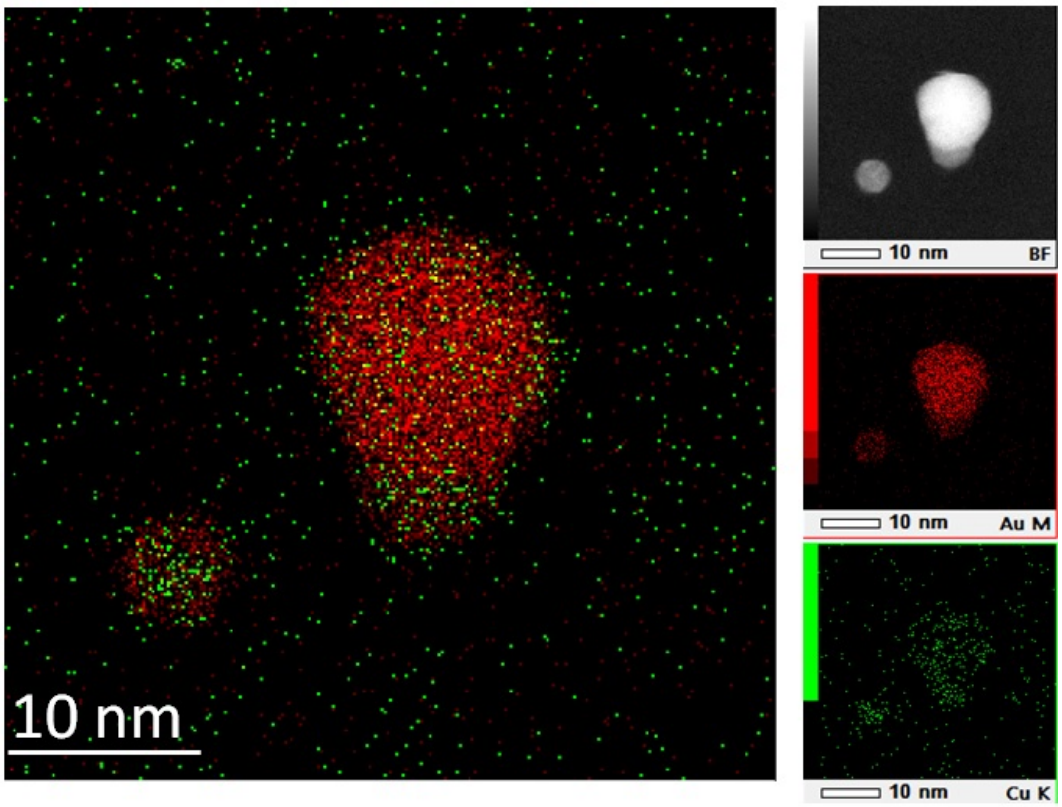

Figure 6.2.10 – EDX map of AuCu particles analysed by JEOL ARM 200F. The smaller particle (4nm in diameter) has a Cu enriched region in core region and Au enriched region in the shell region. The larger particle (12nm in diameter) has Au enriched core region. From the HAADF image, the bigger particle could be two particles overlapping together. In that case, the Cu enrichment on the high curvature side of the large particle could attributed to the overlapped small particle. It is however noted that the EDX signal is not significant and the core-shell structure is a possible speculation.

and also failed discover any Mo. Therefore, it is important to understand in the following chapter that "AuCuMo particles" are particles resulting from the set of preparation involving Mo, although it has been shown that no Mo has deposited along with Au and Cu.

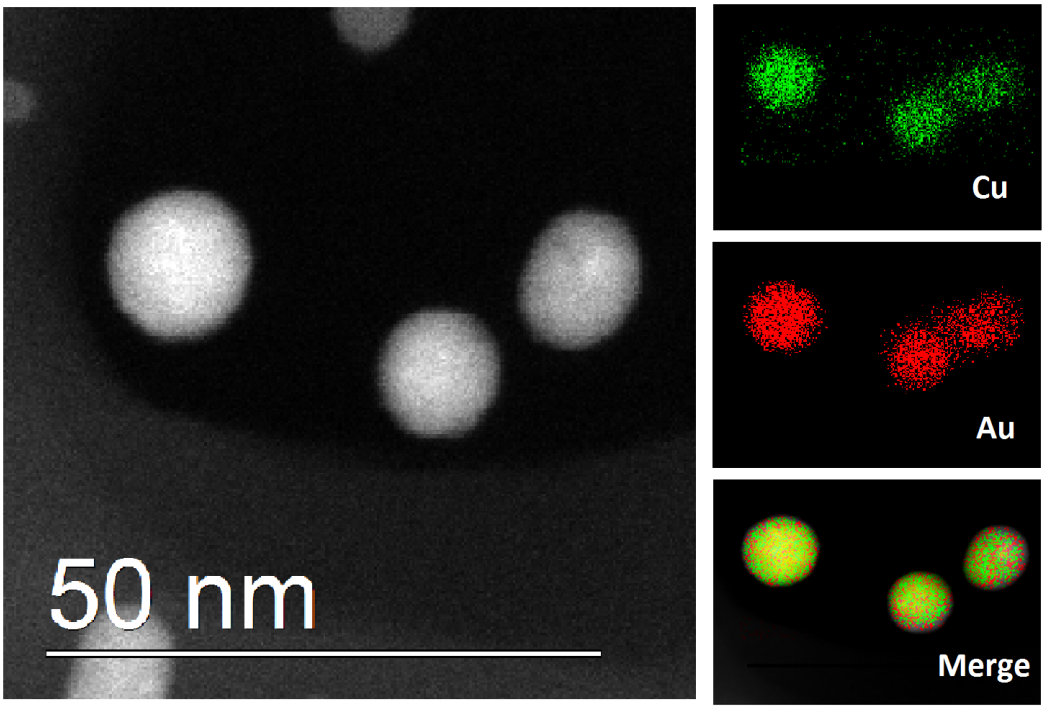

Figure 6.2.11 – HAADF image and EDX maps of Cu and Au atoms within the detected AuCuMo nanoparticles. Cu and Au are evenly distributed across the nanoparticles without showing any segregation. The experiment was done on JEOL 3000F (300 keV)

6.2.4 APT

APT analysis of Ag nanoparticles mentioned in section 6.1 is a pilot trial and uses the simplified FIB in-situ deposition methods, which involves Pt as capping layer. The deposition was conducted single Si post basis. In the following work (AuCu, AuCuMo, AuNi, AuNi with He and AuNiMo), Ag is used as the coating layer and the coating is applied to a silicon coupon (containing 36 posts) as a whole via either magnetron deposition or ebeam deposition. In total, five successful APT datasets were obtained in this study, 3 from the attempted synthesis of AuCu nanoparticles and 2 from the AuCuMo case. Similar to the APT analysis of the Ag particles, the initial analysis step is to identify the peaks occurring in the resulting mass spectrum. A typical mass spectrum of a AuCuMo particle is presented in Figure 6.2.12, together with the mass spectrum generated by isolating the analysis of a nanoparticle from its surrounding. Ions are labelled based on the initial knowledge of the particle, i.e. from the metal targets used for creating particles. Au and Cu are identified in a pure metallic state as well as forming oxides and hydrides. It is worth noting that the detection of AuO_x ions does not necessarily mean that such species are present in the sample, but rather are an artefact brought about by the high electric field applied during the analysis. Likewise, this also applies to the CuH signal. Ag originates from the capping layer, while Si comes from the substrate. Oxygen ions are mostly from SiO_2 since they are located in the region of silicon substrate. Ga ions originate from the FIB milling source. Mo is however not found in the mass spectrum at all. The detailed ion list is presented in Table 6.2.1.

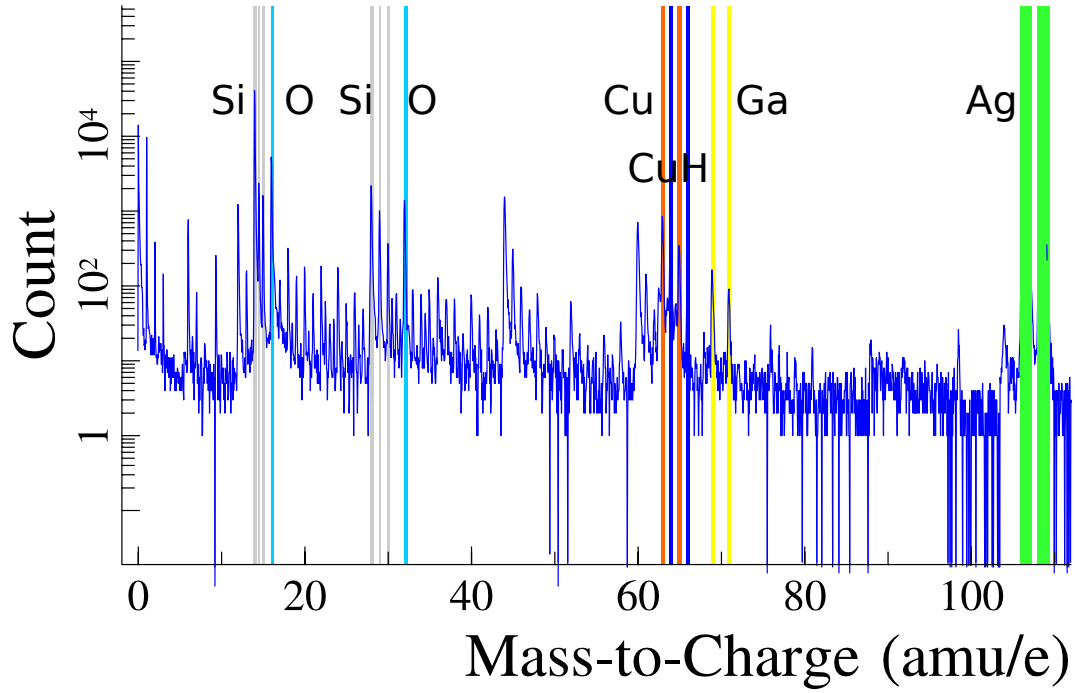

(a)

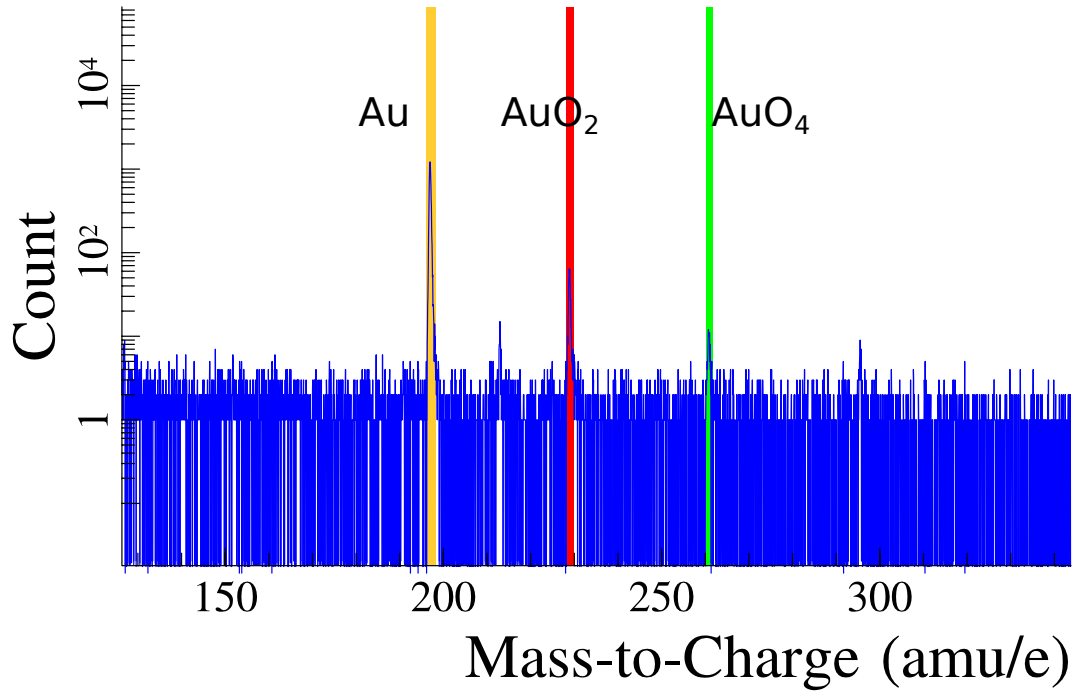

(b)

Figure 6.2.12 – a) Mass spectrum between 0 Da to 120 Da from the entire reconstruction of a AuCuMo nanoparticle. Major peaks identified are Si, O, Cu, Ga, Ag. However, there is no indication of the presence of Mo. b) Mass spectrum contributions between 120 Da to 360 Da shows the detection of Au related ions. It is possible that AuO_2^+ and AuO_4^+ are AuS^+ and AuS_2^+, but the labelling is of no significance for subsequent analysis.

Mass-to-charge-state ratio	Ions	Mass-to-charge-state ratio	Ions	Mass-to-charge-state ratio	Ions
14.0	$^{28}Si^{2+}$	64.0	$^{1}H^{63}Cu^{+}$	229.0	$^{16}O^{16}O^{197}Au^{+}$
14.5	$^{29}Si^{2+}$	65.0	$^{65}Cu^{+}$	261.0	$^{16}O^{16}O^{16}O^{197}Au^{+}$
15.0	$^{30}Si^{2+}$	66.0	$^{1}H^{65}Cu^{+}$		
16.0	$^{16}O^{+}$	69.0	$^{69}Ga^{+}$		
28.0	$^{28}Si^{+}$	71.0	$^{71}Ga^{+}$		
29.0	$^{29}Si^{+}$	107.0	$^{107}Ag^{+}$		
30.0	$^{30}Si^{+}$	109.0	$^{109}Ag^{+}$		
63.0	$^{63}Cu^{+}$	197.0	$^{197}Au^{+}$		

Table 6.2.1 – List of ions detected in APT experimental analysis of AuCuMo and AuCu nanoparticles. In this table, only the peaks (ions) labelled are shown.

A typical AuCuMo nanoparticle reconstruction element distribution map is shown in Figure 6.2.13. It is clear that the reconstruction has a sandwich structure with a Ag capping layer, embedded AuCuMo nanoparticle in the middle and Si substrate beneath. From the top-down view, the nanoparticle is in the middle of the post. Au, Cu and Ag distribution maps are also shown in the figure; Au and Cu ions are constrained within the particle whereas Ag is present in the capping layer as well as in the particle. This was identified in the Ag monometallic experiment as well, and is attributed to the high mobility/low evaporation field of Ag ions [190]. *O* ions are exclusively located in the *Si* post region, which indicates the surfaces of the posts are SiO_2; the *Ag* layer protects the particle itself from air oxidation during sample preparation. Another feature in this reconstruction is that there is an apparently smeared layer of atoms on the top surface of the particle, which is caused by a premature "microfracturing" of the APT specimen while the Ag layer was subject to field evaporation during analysis. This micro fracture is also the cause of the low-density region between the Ag capping layer and the Si post in the reconstruction. This phenomenon has also been identified in similar analyses, where various combinations of metallic capping layers and Si surfaces are examined [319].

To further analyse the particle, it should be isolated from the contributions from the rest

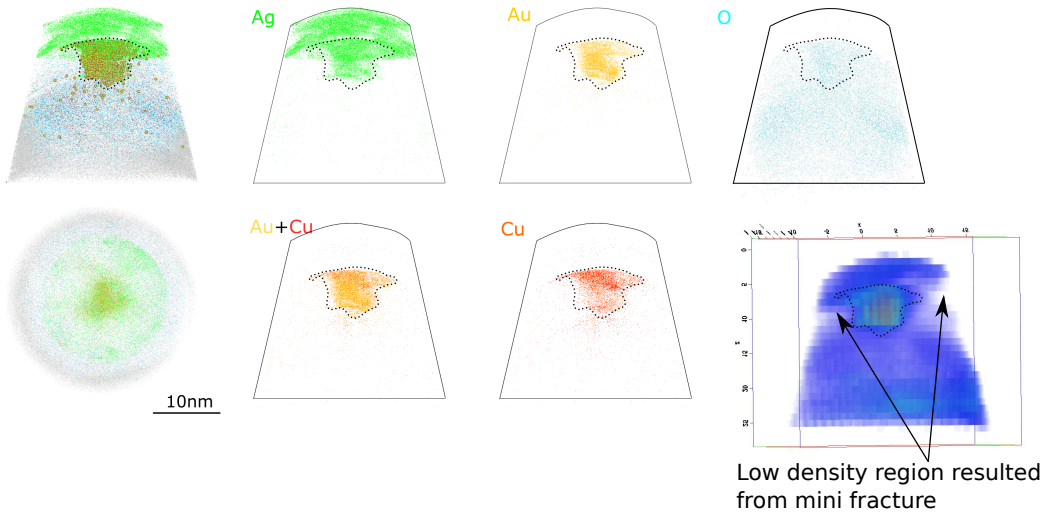

Figure 6.2.13 – Element distribution in an APT reconstruction of embedded AuCuMo nanoparticles. Side and overhead perspective of the maps together with element-specific distribution maps are shown. The existence of a nanoparticle in the reconstruction is obvious as the confined location of Au and Cu outlines the boundaries. Ion density map is also shown to illustrate the low-density region resulted from mini fracture.

of the dataset. However, the wide dispersion of Au ions (containing background signals) in the reconstruction increases the difficulty defining the edge of the particle. To account for this, the relative concentration of a localised region, with a cut-off value of 1 nm in radius (sampling volume), within the whole reconstruction is calculated was defined by Equation 6.2.1. Through this calculation, it is possible to obtain an isolated particle with less noise signal included.

$$Relative\ Concentration\,(at.\%) = \frac{\sum(Au, Cu, CuH, AuO_2, AuO_4)}{\sum(Ag, O, Ga, Si, Au, Cu, CuH, AuO_2, AuO_4)} \times 100\% \tag{6.2.1}$$

In Figure 6.2.14a, the calculations based on the Equation 6.2.1 are performed on the AuCuMo dataset (blue line) and the same dataset however with all ions now randomly rearranged (red line). The analysis from the spatially randomized data shows that there is no feature or region with a relative concentration higher than 35 % (the point where two spectra intercept). Therefore, the cut-off value for defining the particle in the actual dataset is chosen as 35 %, since it is believed that no aberration from the noise of the dataset

Composition	Au	Cu	Mo
AuCu (at.%)	69.4	30.6	No detection
AuCuMo (at.%)	65.2	34.8	No detection

Table 6.2.2 – Composition analyses of AuCu and AuCuMo nanoparticles. The data are from averaging all nanoparticles detected.

is included in the isolated particle. The defined nanoparticle as a result of this analysis is isolated and shown on the left of Figure 6.2.14b. The colour difference in the particle and in the whole reconstruction on the right , represents the difference of the relative concentration as calculated. The brighter the colour, the higher the content of Au, Cu and related species included. In Figure 6.2.14c, the ion species contained in the isolated AuCuMo particle are shown; the yellow colour represents Au related ions whilst the red colour represents the Cu species. The separation of Au and Cu ions are evident in this ion map. This is the protocol to isolate nanoparticles within the reconstructed datasets and all similar analysis follow the same procedure.

As a result, utilising the isolation method mentioned above, there is a total of 7 nanoparticles identified across the different APT datasets, and they are all shown in Figure 6.2.15. Following the isolation of the particle, concentration analyses are performed on the 2 AuCuMo and 5 AuCu nanoparticles. The composition is listed in Table 6.2.2. The AuCu particles reach the 7:3 ratio between Au and Cu. On the other hand, the Au fraction is 65.2 at.% in AuCuMo particles. Overall, the particle composition loosely matches with the initial design given relatively small number of particles analysed. Also, the naming of the particles still follows AuCu and AuCuMo regardless the absence of Mo for the sake of the consistency through the presentation of data.

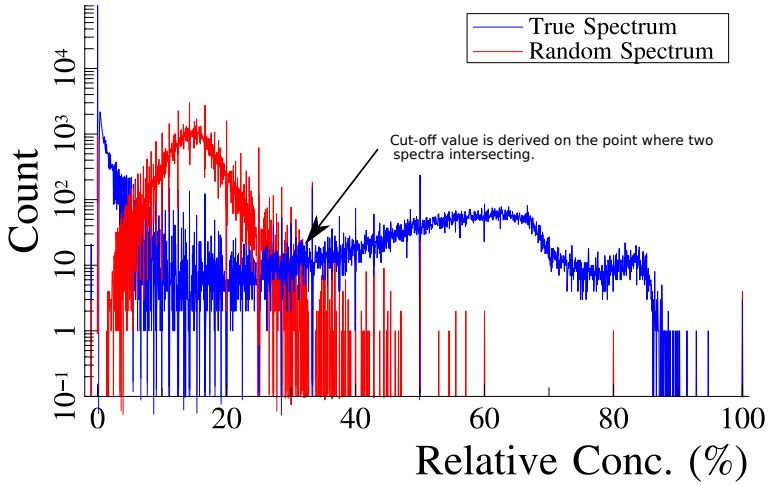

(a) Count plot of the data calculated from Equation 6.2.1. The blue line is the relative concentration in the real data and the red line is from the same dataset but with shuffled mass values. It is clear that 35% is a cut-off value for nanoparticle separation since it is the interception point of the random and true calculations.

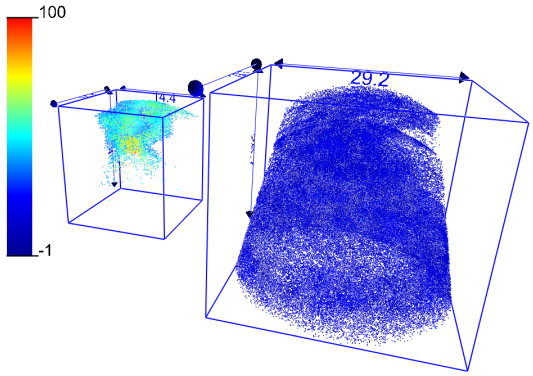

(b) Local chemistry calculation of embedded AuCuMo particles. Isolated nanoparticle is shown on the left and a reconstruction of the full tip is shown on the right. The colour bar shows the level of relative concentration calculated via Equation 6.2.1.

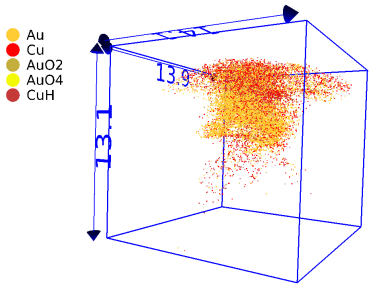

(c) Isolated AuCuMo nanoparticle with ion labels. Au related species are in yellow colours and Cu related species are in red colours.

Figure 6.2.14 – An isolation process of an AuCuMo nanoparticle from the whole data reconstruction.

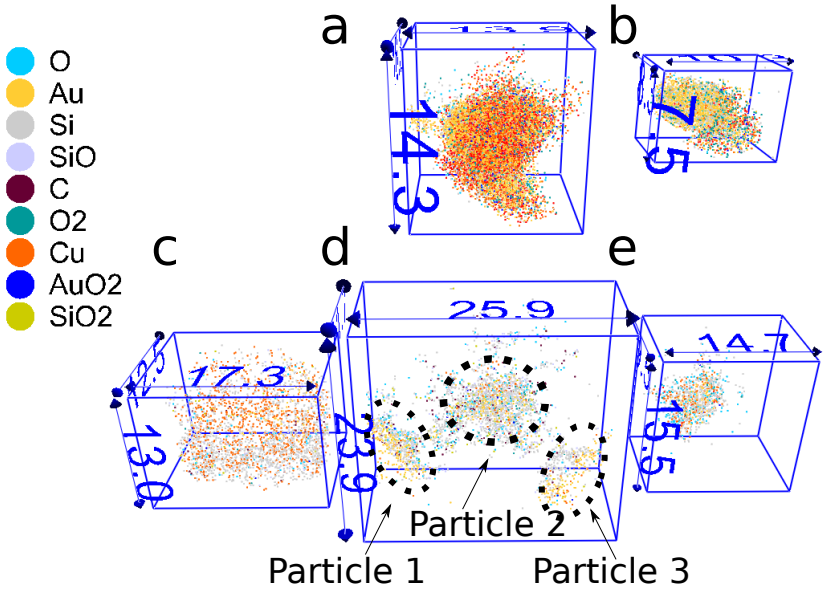

Figure 6.2.15 – All detected AuCuMo (a,b) and AuCu (c,d,e) nanoparticles. Note that the letters are used in the text to refer specific detected particles.

Particle	label a	label b	label c	label d particle 1	label d particle 2	label d particle 3	label e
	AuCuMo				AuCu		
Au(ions)	10977	1994	949	324	320	230	104
Cu(ions)	6339	558	78	44	300	52	231
C_{Au} (at.%)	63.4	78.1	92.4	88.0	51.7	81.6	31
C_{Cu}(at.%)	36.6	21.9	7.6	12.0	48.3	18.4	69.0
Counting error(at.%)	0.3	0.8	0.8	1.6	2.0	2.3	2.5

Table 6.2.3 – Composition analyses of individual AuCu and AuCuMo nanoparticles as shown in Figure 6.2.15.

6.2.4.1 AuCuMo

It is therefore of interest to characterise single particles to further investigate compositional variations. In Table 6.2.3, compositions of individual nanoparticles have been listed. Compared to the global composition, measurements from individual particles show more composition variation. It is consistent that Au is enriched in the AuCuMo particles whereas fluctuation exists on AuCu particles, the Au content of which is as high as 92.4 at.%.

To further investigate the heterogeneity compositions, iso-concentration surface (proximity histograms) proxigrams and 1D concentration analyses were used to examine composition segregation within individual particles. The proxigram for an AuCuMo particle is shown in Figure 6.2.16a. Regardless of the high counting error on the surface of the particle, Cu segregation is clearly observed on the surface with a thickness of ~1nm. The atomic ratio of Au:Cu on the surface is 1:2. Beneath the initial surface layer, the ratio of Au:Cu reaches 1:1. Inside the particle, there is a volume with an Au:Cu ratio of 2:1 with a thickness of ~2nm. Further inside the particle, the Au content increases. The Cu enrichment is further confirmed by 1D concentration analyses (the size of the analysis bar is 3*nm* in diameter). Figure 6.2.16b shows a 1D concentration profile from the z-direction (analysis depth direction) and side direction, respectively, of the same particle as shown in Figure 6.2.16a. It is clear that Cu segregates to the top and bottom surface of the particle from the z profile:

the Au:Cu ratio reaches 1:1 at the surface and bottom, while is ~5:1 in the centre. Results from the side direction show a similar trend; the Au:Cu ratio nears 1:1 towards the surface and climbs to 2:1 in the centre. From the reconstruction, the volume of the particle is about $1250 nm^3$. A nominal diameter could be derived as $13.4nm$ assuming the particle is a perfect sphere.

Analyses on the second AuCuMo particle (label b in Figure 6.2.15), similarly show the segregation of Au and Cu elements at the particle surface. Proxigram analysis defined by the 70 at.% of Au, Cu, AuO_x and CuH over total ions iso-concentration surface is shown in Figure 6.2.17a. For the result, the centre is enriched with Au, with a ratio of Au:Cu of 5:1. At the surface of the particle, the ratio declines to ~1:1. On the other hand, 1D concentration analyses (cylindrical region of interest with a diameter of 3nm) were conducted from x, y, z directions, respectively, through the same particle, and the results are shown in Figure 6.2.17b. Alone the z direction, Cu clearly enriches to the surface with a thickness about 1-2nm, reaching the Au:Cu atomic ratio of ~1:1. However, along the x and y directions, Cu enrichment is not as clear, but, overall, Cu is consistently seen to be enriched at the particle surface even it is not entirely uniform. Besides, the reading of the Au values are different in the two orthogonal 1D concentration profiles. It is supposed that a local variation of Au exists, however the variation region is smaller than the diameter of the 1D cylinder.

To further assess the localised surface segregation, 2D concentration contour plots of the 2 AuCuMo particles are shown in Figure 6.2.18. Nano-scale segregation of Cu at the particle surface is evident. The plots also confirm that there is not a uniform Cu layer at the particle surface, which explains the inconsistency between the proximity histogram (which averages the entire isolated surface) and 1D concentration profiles (which only assess limited ROIs). This result is important to understand the chemical nature of the deposited particles, indicating the deposition process could be refined further (i.e. making composition balanced particles, core-shell particles and etc.).

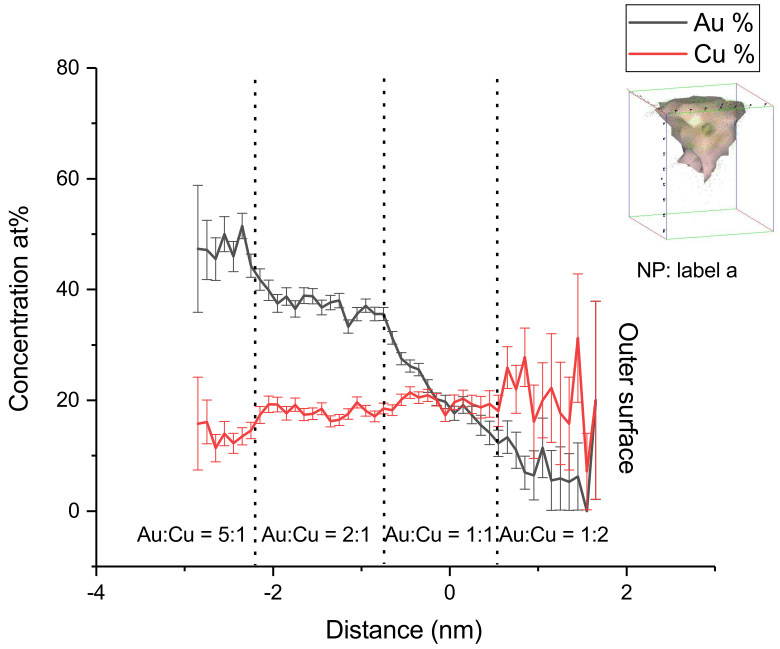

(a) Proximity histogram based on iso-concentration surface. The surface is calculated by the function 6.2.1 and the value is set as 70 at.% of Au, Cu, AuO_x and CuH over total ions. Histogram is calculated with a bin size of 0.1nm.

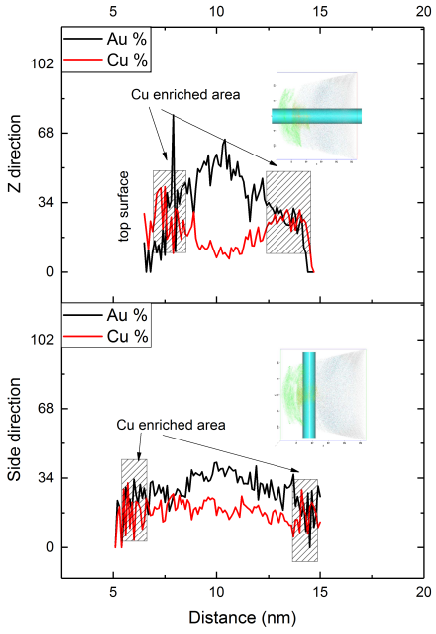

(b) 1D concentration profiles along orthogonal directions through the AuCuMo particle

Figure 6.2.16 – Proximity histogram and 1D concentration analyses on the particle labelled a in Figure 6.2.15. (a AuCuMo particle)

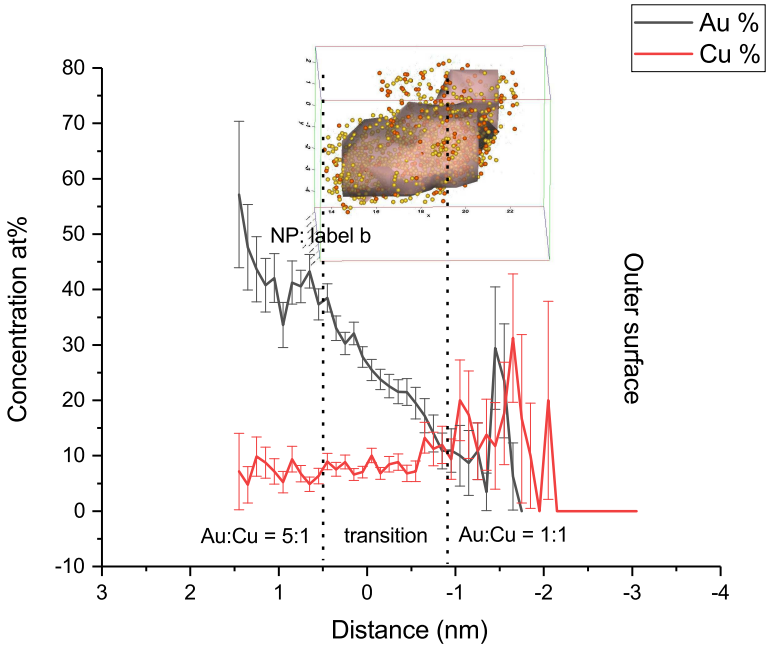

(a) Proximity histogram based on iso-concentration surface.The surface is calculated by the function 6.2.1 and the value is set as 32 at.% of Au, Cu, AuO_x and CuH over total ions. Histogram is calculated with a bin size of 0.1nm.

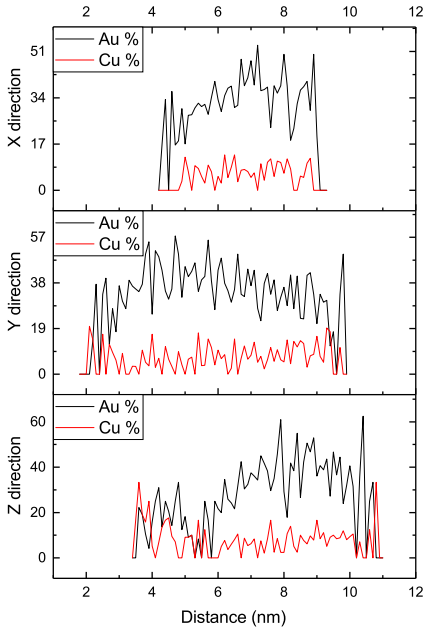

(b) 1D concentration profiles along orthogonal directions through the AuCuMo particle.

Figure 6.2.17 – Proximity histogram and 1D concentration analyses on the particle labelled b in Figure 6.2.15. (a AuCuMo particle)

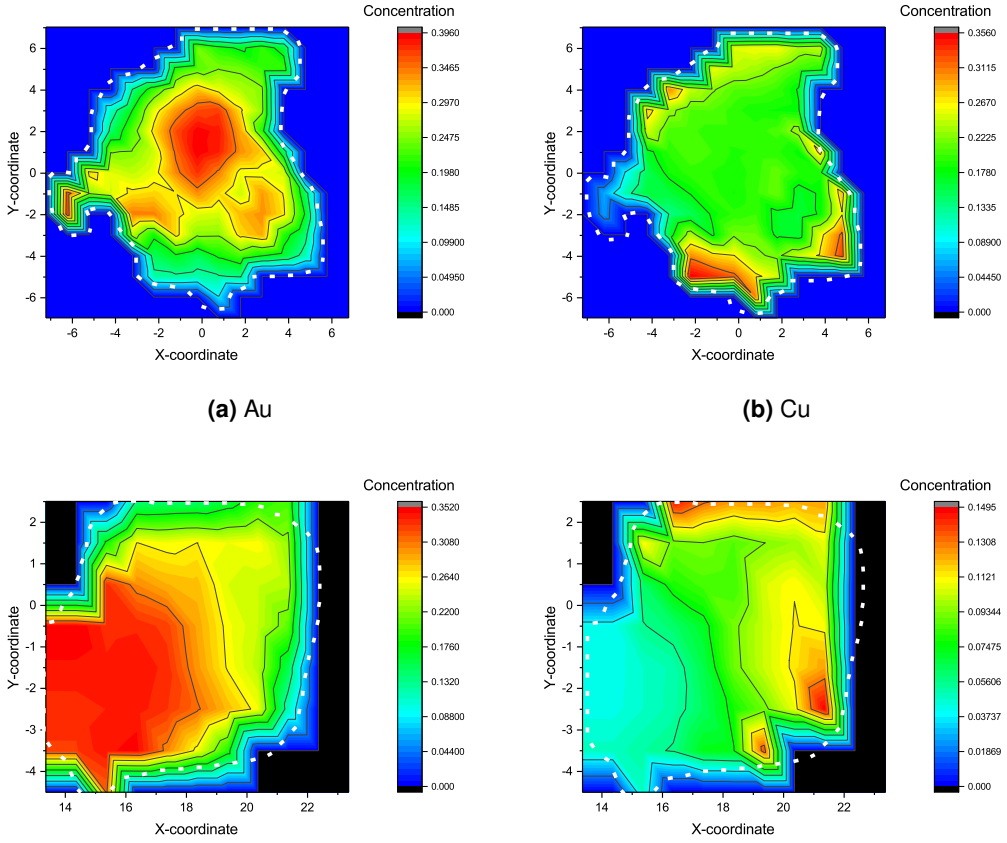

(a) Au **(b)** Cu

(c) Au **(d)** Cu

Figure 6.2.18 – 2D contour plot of Au and Cu elemental concentration within the AuCuMo particles (sub a, b for label a, sub c, d for label b). The scale is calculated by the selected ion over total ions and the white dot line indicates the outline of the analysed particle

6.2.4.2 AuCu

In the case of the AuCu particles, a key interest centres around the surface segregation, as without the effect of added Mo (although there was no detection of Mo in the nominally AuCuMo particles, there is still a difference shown in the MesoQ results in Figure 6.2.1 and 6.2.3), the formation of the resulting particles might have experienced changes. From the composition information listed in Table 6.2.3, the size of the detected AuCu is smaller in comparison to the AuCuMo counterparts. Attempts were made to produce proxigram analyses defined by an applied iso-concentration surface, but no significant information could be obtained due to the small size of the samples. The similar limitation is also encountered in the 1D concentration analysis. Due to the small region analysed, high counting error overlaps the underlying information. Composition measurements of particles obtained via averaging contributions from numerous particles together have been previously reported in literature [219, 320], however this approach cannot be applied to this case since the particles detected are not in the form of core-shell structure, therefore there is no robust method to overlay the information of segregation elements. 2D contour plot analyses have been applied to show the local concentration segregation and the results are shown in Figure 6.2.19. Au and Cu are segregated to distinct locations within individual particles. Comparing to the EDX results obtained from TEM, there is no consistent form of the observed surface enrichment of Au, even when the size of the particles is similar (the particles as shown in Figure 6.2.19 and Figure 6.2.10). It has previously been speculated that Au can be segregated towards the particle surface due to the lower surface energy [321], and longer exposure of the TEM sample in ambient atmosphere facilitates such segregation. Nevertheless, the APT data clearly show the localised separation of Au and Cu, which strongly indicates particles were deposited at a non-thermodynamic equilibrium state.

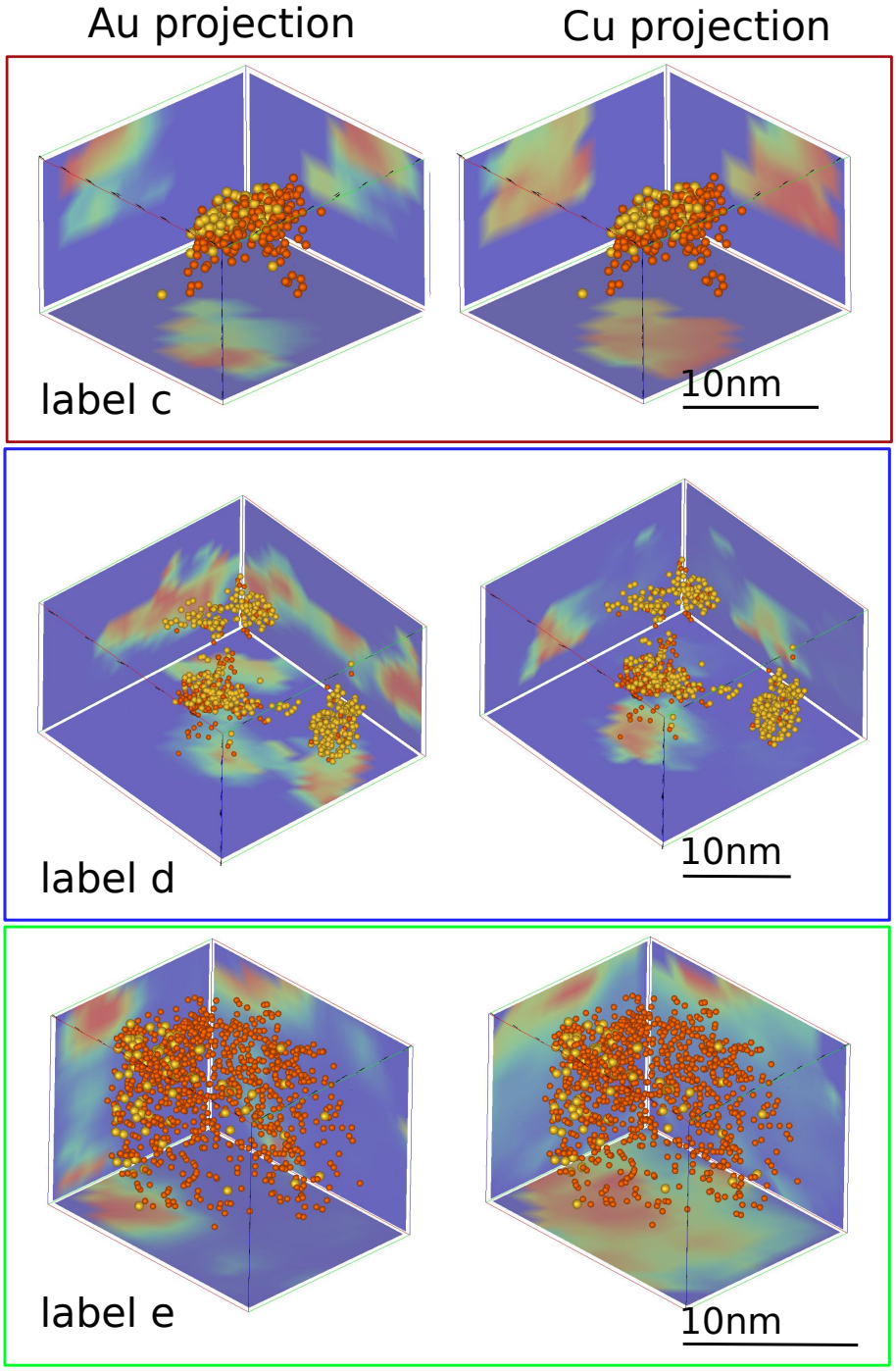

Figure 6.2.19 – 2D contour plots of Au and Cu within the AuCu particles as shown in Fig. 6.2.15 c, d, e. Yellow dots in the figure represent Au and orange dots represent Cu. Purple is the background colour representing represents the lowest relative concentration whilst red represents the highest relative concentration.

6.3 Characterisation of AuNi and AuNiMo nanoparticles

Following the successful deposition of Ag, AuCu and AuCuMo nanoparticles, a broader approach to nanoparticle characterisation involving additional techniques was undertaken for a better understanding the chemical nature of the deposited particles. Techniques including AFM, XPS and LEIS were therefore used to characterise a new series of AuNi and AuNiMo particles. In addition, the IGC particle generation conditions were modified, using He together with Ar as the plasma source, to further explore the relationship between the deposition conditions and resulting particles. Synthesis of a trimetallic AuNiMo particle was again attempted to assess the behaviour of Mo during the deposition.

6.3.1 MesoQ (mass filter)

Size distribution (Meso-Q) data from as-prepared AuNi, AuNi with He and AuNiMo particles are plotted in Figure 6.3.1. In this figure, comparisons are plotted in a similar manner to those in the AuCu and AuCuMo measurements, with both experimental curves and theoretical additions. For all three types, the data show the bimodal size distributions of the particles, peaking in at diameter in 3nm and 6nm. In all three cases, the summation curve is different as compared to the experimentally obtained curve. The summation curve only has a single peak ~3nm, whilst a satellite broad peak also exists at ~6nm in the experimental data, indicating larger particles are forming. AuNiMo particles have the highest abundance of particle of small size. The addition of He to Ar in the AuNi system increases the abundance of small particles as well, as shown in the green lines in Figure 6.3.1b. MesoQ data clearly shows the impact in terms of new particle formation during deposition. The emerging peaks (around 6-8nm) show high potential of alloying in resulting particles.

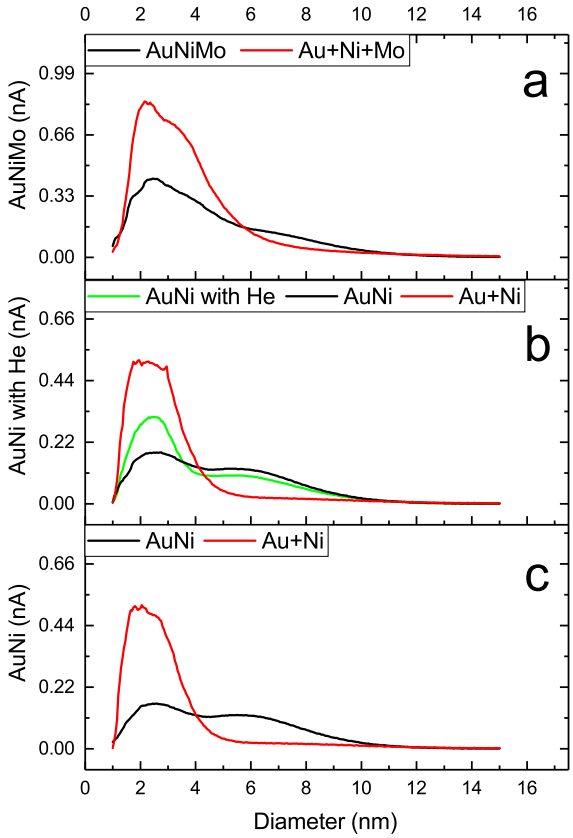

Figure 6.3.1 – Meso-Q data for AuNi, AuNi with He and AuNiMo nanoparticles. In the figure, '+' means that the data are derived from the addition of individual scans. For example, 'Au +Ni' means the signals of Au particles and Ni particles are mathematically added together whilst 'AuNi' means both Au and Ni targets are activated to produce bimetallic particles.

6.3.2 AFM

AFM is a conventional surface characterisation method to probe nano sized features and it has previously been used to probe the morphology of deposited particles on flat Si surface. In Figure 6.3.2, AFM images of AuNi, AuNi with He and AuNiMo particles are shown. These images were produced using adhesion signals (i.e. no direct contact between the tip and sample). A clear observation from the images is that there is a contrast between the outer layer and core of the particles (bright colour on the particle edges whilst a dark colour is shown in the centre). This trend persists in analyses from varying scanning directions, which were employed to minimize the effect of aberrations originating from the large shape tip size compared to the rather small particles. It is thus reasonable to conclude that there is a difference in terms of composition within the particles. This can be attributed to a number of possible mechanisms: a) interaction of the analysing tip and particle b) formation of a core-shell particle structure c) surface contamination or d) particle surface oxidation. Interaction of tip and particle is most possible reason but other reason could not be eliminated.Therefore, other surface sensitive techniques were employed to elucidate the cause and further investigation of these structures is presented in the following subsections.

In terms of morphology, round shaped particles are observed in the AuNi and AuNi with He systems. In comparison, the AuNiMo particles are more irregular. The addition of Mo (in the AuNiMo system) could be the factor to cause such change. The particle size distributions can also be directly observed in the AFM images. Very small particles can be seen to exist alongside larger particles. The small particles have a size as low as 1 nm whereas others are up to 15nm. Adding He into Ar for the plasma reduces the mean size from 6 nm to 4 nm. The addition of Mo also reduces the particle size, from 6 nm to 3 nm. The average size reduction is mainly due to an increase in population of smaller particles around 1nm.

The results of particle size measurement are shown in Figure 6.3.3. In the figure, the histogram is the manual size measurement of the particles shown in the Figure 6.3.2. The most abundant size is around 6~8 nm. It matches well with the MesoQ data showing the

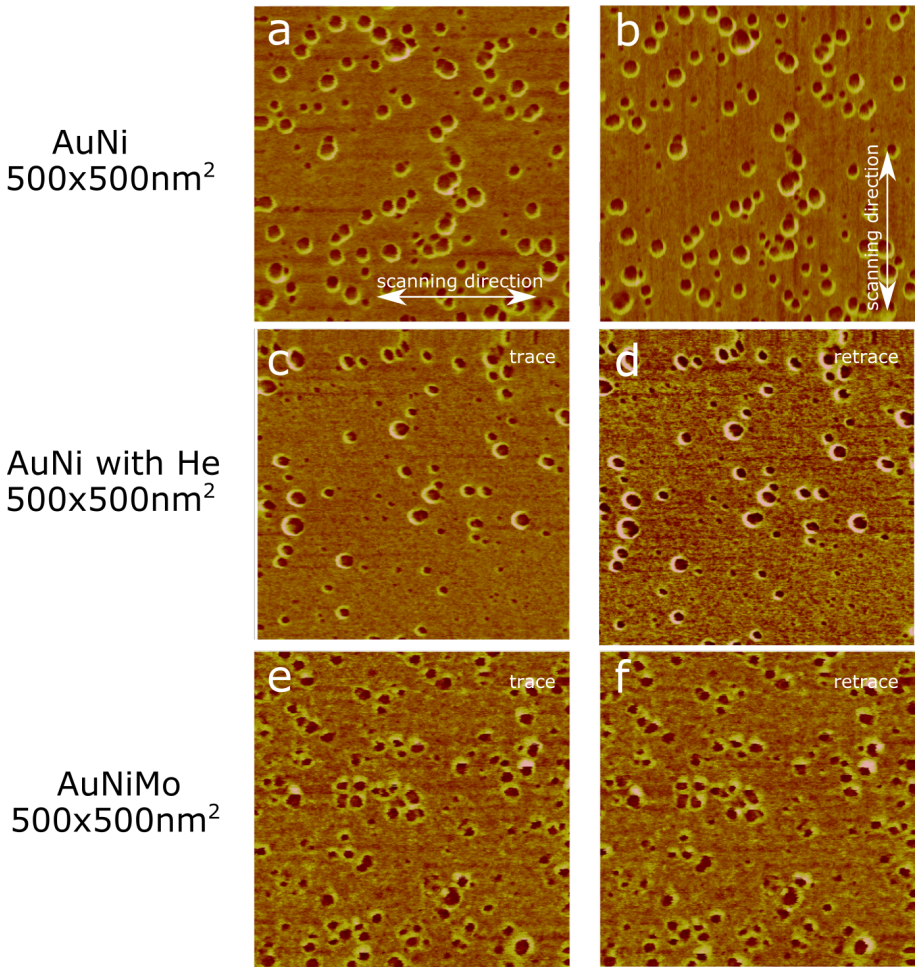

Figure 6.3.2 – AFM images of pre-prepared AuNi(a,b) AuNi with He (c,d) and AuNiMo (e,f) nanoparticles. Adhesion signals were collected to produce images as shown. For each sample, analyses from two directions were employed to reduce artefacts induced from the analysis direction.

good consistency. In addition, size measurement is also conducted via software (Nanoscope analysis) and the results are listed in the green box with the figure. The software reading identifies more small particles, which are difficult to identify manually. Overall, it confirms that particles have two apparent populations of size distribution; one centred approximately around 2-4 nm and the other around 6-8 nm.

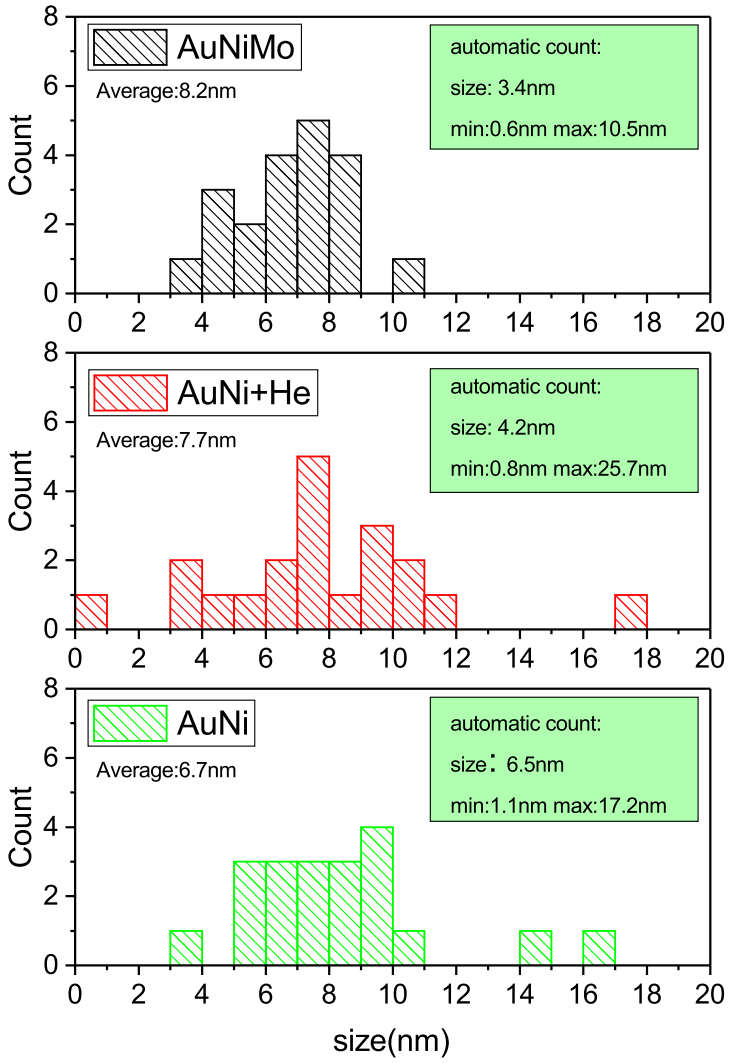

Figure 6.3.3 – Particle size distribution derived from AFM results. The height of particles was measured manually by visual inspection and by software (Nanoscope Analysis). The average size is derived from manual reading is listed under the legend, whereas the result from the software is listed on the right.

6.3.3 TEM

TEM was used to investigate the particle structures of AuNi, AuNi with He and AuNiMo particles. In Figure 6.3.4, all BF images are shown, in which the first row is AuNi, the second AuNi with He and the third AuNiMo. In the first column, the images show an even distribution of all particles deposited on the TEM grid. The Marks-decahedral structure of the particle is clearly evident in the sub-figure b, c, d for the AuNi particles. For the AuNi with He particles, decahedral structure is also observed in sub-figure f, g and sub-figure i indicates the AuNiMo particles also have a decahedral structure. In the meantime, an icosahedral structure also exists in sub-figure g, h, j, k. (The matching of the particle structure can be referred to Figure 2.2.12 and reference [166, 170, 171, 317, 318, 322]).

As discussed in the previous section (Section 6.2.2 on page 183), the diversity of the structures indicates thermodynamic variations even within the same batch of particles. The high fraction of particles with a decahedral structure in the AuNi systems (around 80% of particle imaged in all the three AuNi based particles) reflects the effect that Ni can have on the final structure formed, as comparing to the AuCu systems analysed in the previous section.

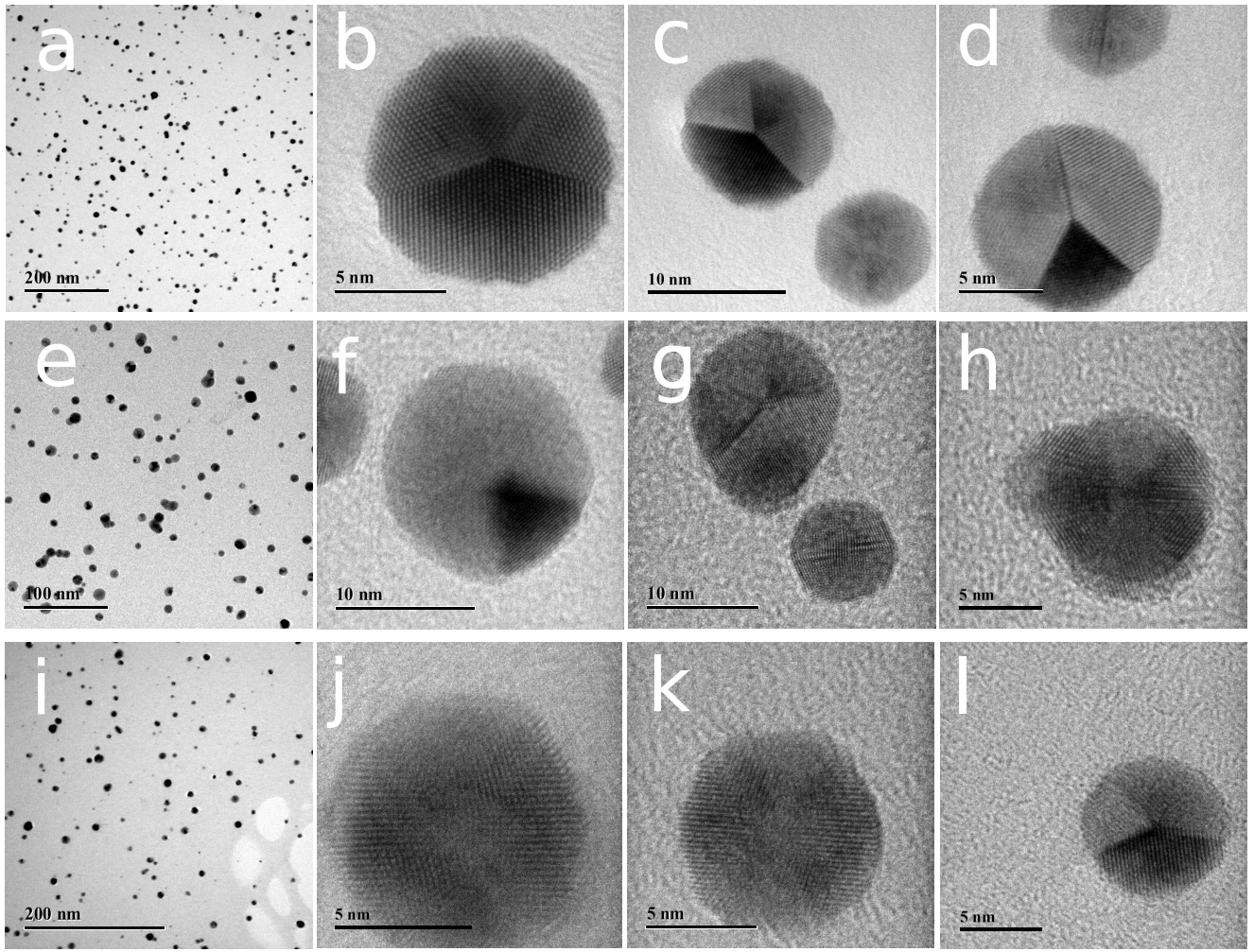

Figure 6.3.4 – BF images of AuNi, AuNi with He and AuNiMo nanoparticles. The first row represents AuNi particles, the second row represents AuNi with He and the third row represents AuNiMo particles. Decahedral structure is observed in Sub-figure b, c, d, f, g, l and icosahedral structure is observed in sub-figure g,j,k.

6.3.4 XPS

The XPS analyses of the AuNi, AuNi with He and AuNiMo nanoparticles are shown in Figure 6.3.5. In Figure 6.3.5a, the Ni 2p spectra are shown indicating the existence of $Ni^{2+}$from NiO, as seen in all three samples. Similarly, Mo in the AuNiMo particles is successful detected, which is shown in Figure 6.3.5b, is in an oxidised state of Mo^{6+}. On the other hand, Au spectra (shown in Figure 6.3.5c) show that Au is present in its metallic state in all three samples. The states of all three thus follow with their expected oxidation behaviour. The surface atomic composition of the particles is identified by measuring the peak height after normalisation by the photo-ionisation cross-section. In Table 6.3.1, the atomic percentage of each detected element is listed. The atomic composition ratios between Ni and Au in both AuNi and AuNi with He are quite consistent, in agreement with the initial assumption about equal Au and Ni levels. However, the addition of Mo is not as predicted, only making up a total 12.5 at.% of the total count (Au, Ni and Mo), and also altering the ratio between Ni and Au. Composition of those detected particles are (in at.%): $Au_{50}Ni_{50}$, $Au_{43}Ni_{57}$ *with He* and $Au_{50}Ni_{38}Mo_{12}$ (within the penetration depth of XPS, 4nm, which roughly corresponds to the particle size).

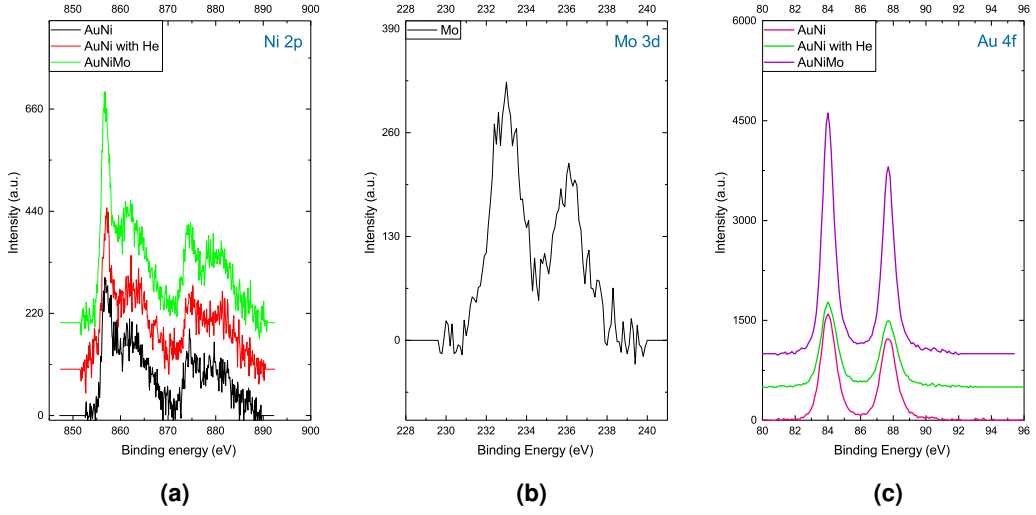

Figure 6.3.5 – XPS spectra of (a) Ni 2p (b) Mo 3d specifically in AuNiMo and (c) Au 4f peaks of AuNi, AuNi with He and AuNiMo, respectively.

Sample	Elemental atomic composition (%)					
	Si	O	Ni	Au	C	Mo
AuNi	25.6	61.5	0.3	0.3	12.3	-
AuNi with He	26.1	60.7	0.4	0.3	12.5	-
AuNiMo	34.9	42.1	0.6	0.8	21.4	0.2
	Binding energy (BE, eV)					
	Si 2p	O 1s	Ni $2p_{3/2}$	Au $4f_{7/2}$	C 1s	Mo $3d_{5/2}$
AuNi	103.8	533.2	856.7	84.0	284.8	-
AuNi with He	103.7	533.0	857.1	84.0	285.1	-
AuNiMo	99.7	532.8	856.8	84.0	285.1	233.0

Table 6.3.1 – Element composition detected from XPS results. The respective binding energies of these elements are based on the reference point of Au $4f_{7/2}$

6.3.5 LEIS

LEIS experiments were conducted to characterise the surface composition in complement to XPS results, as this is key for catalytic applications. As mentioned in the section 3.5, LEIS has the capability to probe the composition of the first atomic layer of the deposited nanoparticles. In Figures 6.3.6, 6.3.7, 6.3.8, LEIS scans of AuNi, AuNi with He and AuNiMo nanoparticles deposited on flat Si surface are shown. Similar behaviour is observed across the three samples, therefore the following description is based on the AuNi analysis. Figure 6.3.6a confirms that the initial surface is contaminated with carbon species, possibly from environmental exposure before analysis. Because of this significant surface covering of carbon, it is difficult to obtain any valuable information. Elimination of carbon was conducted by using an oxygen plasma (parameters used are described in Section 3.5 on page 98). During the cleaning procedure, oxygen reacts with carbon forming gaseous carbon dioxide, which is extracted from the system by pumping. As a result of the oxygen plasma cleaning subsequent analysis shows no carbon residue remaining on the sample surface, instead Si and O signals emerge, indicating that the substrates are being analysed. It is then of interest to evaluate the consistency of the particle compositions by scanning several random locations on the sample substrate. A single scan covers an area of up to $1mm \times 1mm$, however sampling random locations ensures a more comprehensive analysis. Figure 6.3.6b shows scanning data from five random locations on the deposited silicon substrate. Ni atoms are observed to be located on the surface, with Au located underneath, judging from the broad spectra close to the main Au peak. Apart from some minor variation, these datasets show good consistency among the samples, which proves the IGC produces nanoparticle samples with compositions at l micrometre level.

Due to the He ion bombardment, the top surface layer is removed during the analysis. Therefore, multi-scans on a fixed area can essentially act as a depth profiling tool. The result of the sustained bombardment on AuNi sample is shown in the Figure 6.3.6c. After several scans have been performed, a so-called waterfall diagram with depth profiling information is shown. The very first scan shows a strong Ni signal on the outermost surface of the

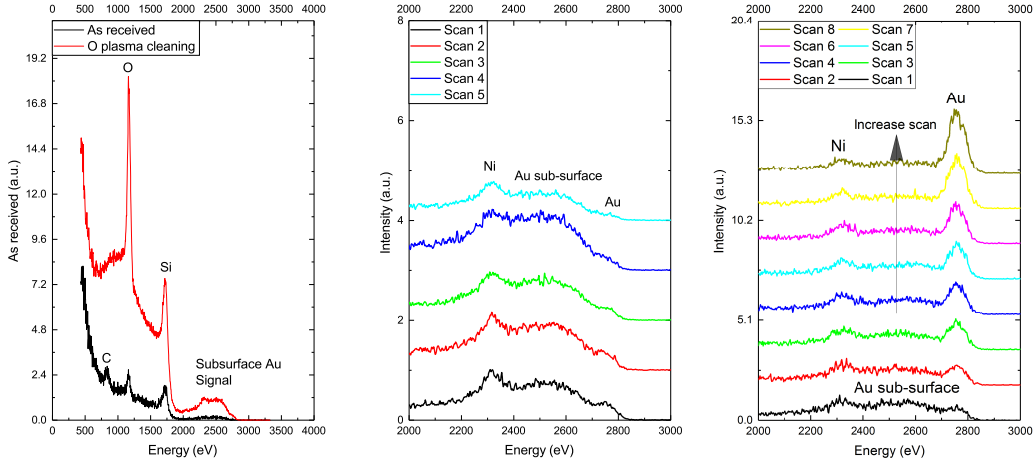

Figure 6.3.6 – (a) LEIS spectra of AuNi sample analysed before and after plasma cleaning. Before cleaning, there is a clear C signal present in the spectrum, whereas only O and Si peaks are observed after cleaning. (b) Five scans of randomly selected areas on the sample surface to check the stability of the composition across the entire sample. Each scan was conducted on a $1mm \times 1mm$ area. (c) Depth scan on one $1mm \times 1mm$ area. An increase of the Au signal and relative decrease of the Ni signal were observed.

particles, whereas the Au signals are mostly concentrated from the subsurface. In detail, the Au signals consistent of a broad peak spanning in energy from 2400 to 2650 eV, just less that the characteristic energy peak of 2750 eV, which represents Au atoms on the surface. Since the area of the LEIS analysis is about $1mm \times 1mm$, the signal is averaged over many particles. As illustrated in Figure 6.3.6c, LEIS suggests that the particles are in a core-shell configuration with Ni on the shell, as otherwise a surface Au peak should have been detected.

Comparison between AuNi and AuNi with He from the LEIS data shows little difference between these two samples. Ni is identified at the beginning of the scan with Au beneath the surface. During the period of the scanning, an Au enriched core is again revealed, as shown in Figure 6.3.7c. Therefore, there is no direct observation by LEIS of changing particle compositions when He is added to the plasma composition during the synthesis of the particles. For the AuNiMo sample, the existence of Mo is observed in Figure 6.3.8b. With the information from the z direction profiling, the Mo signal decreases together with

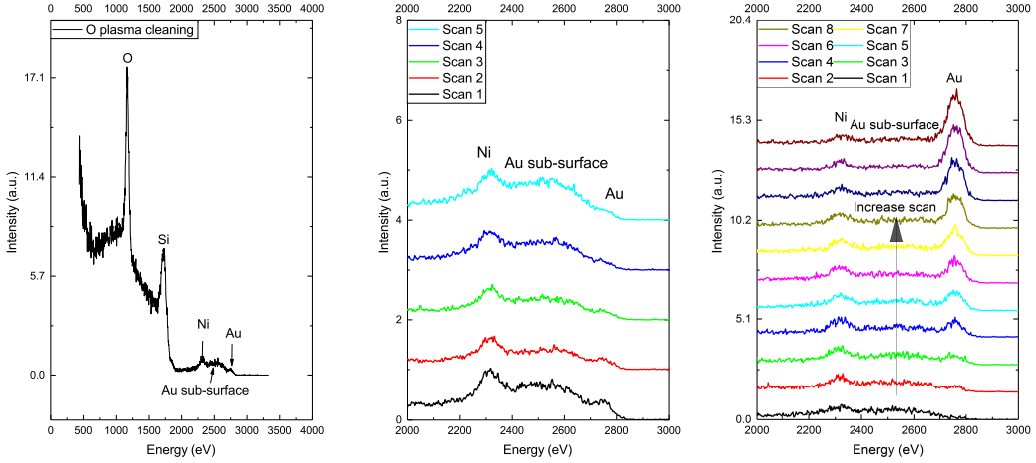

Figure 6.3.7 – (a) LEIS spectra of AuNi with He analysed before and after plasma cleaning. (b) Five random scans on the sample surface to check the stability of the composition across the entire sample. Each scan was conducted on a $1mm \times 1mm$ area. (c) Depth scan on one $1mm \times 1mm$ area. An increase of the Au signal and decrease of the Ni signal were observed.

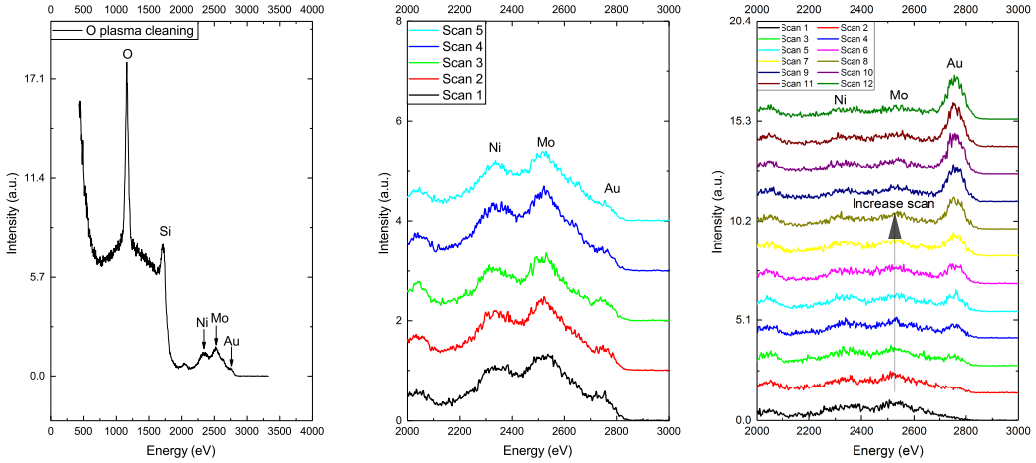

Figure 6.3.8 – (a) LEIS spectra of AuNiMo sample analysed before and after plasma cleaning. (b) Five random scans on the sample surface to check the stability of the composition across the entire sample. Each scan was conducted on a $1mm \times 1mm$ area. Mo signal is observed on the surface of the particles (c) Depth scan on one $1mm \times 1mm$ area. An increase of the Au signal and decrease of the Ni signal were observed. The Mo signal also decreases with increasing scanning number.

the Ni signal whilst the Au signal increases. This suggests that the AuNiMo particles have a Ni and Mo shell, and an Au core.

Overall, the LEIS results offer a basic understanding of the location of elements within the deposited particles. The structure of the particle shows a thin shell of Ni (or Ni with Mo in the AuNiMo particles) and Au core. However, the data are based on averaging over a large number of particles, which is invaluable for predicting overall catalytic properties, but cannot reveal variations between particles.

6.3.6 APT

Similar to the AuCu and AuCuMo characterisation, APT analyses were performed based on the deposition-encapsulation method. The same sample making procedures were followed to produce the atom probe tips. It is however particularly important to recognise peak overlaps in the mass spectra resulting from the APT analysis of this system. Si has three isotope masses: 28, 29 and 30 whilst Ni has five isotope masses: 58, 60, 61, 62 and 64. Therefore there is a potential significant overlap for the peak at 29 Da ($^{29}Si^{+}$and $^{58}Ni^{2+}$) and 30 Da ($^{30}Si^{+}$and $^{60}Ni^{2+}$). In Figure 6.3.9, 2D contour plots of potential clashing mass-to-charge-state ratios are listed. The projections in these figures are based on the APT reconstruction shown in Figure 6.3.10, in which a AuNi particle is embedded in the centre. Ion measured with mass-to-charge-state ratio of 28 Da is due to $^{28}Si^{+}$, which is not present in the centre where the particle locates. 29 Da peak, where $^{29}Si^{+}$ overlaps with $^{58}Ni^{2+}$, shows some similarity in distribution to those from the 28 Da peak. However, there is a spot in the centre of the reconstruction, which is the location of the particle, implying that $^{58}Ni^{2+}$ contributes to the 29 Da signal. To avoid any aberrant Si signal contribution to the nanoparticle analysis, ions associated to 29 Da are labelled as $^{29}\mathrm{Si}^{+}$ and thus regarded as primarily arising from the substrate. The 2D contour map of 30 Da ions in Figure 6.3.9 on page 224 shows homogeneous distribution. Therefore, it provides little information around the possible distribution of $^{60}Ni^{2+}$. On the other hand, the main Ni peak at 58 Da shows an abundance in the centre of reconstruction. The ions associated to 60, 61 and 62 Da signals appear randomly distributed. However, 64 Da contains a signal which is excessive for Ni given, comparison with the 58 Da ($^{58}Ni^{+}$), and the fact that the ^{64}Ni isotope has a natural abundance of 0.92 at.% of the total Ni content. However it is possible that these ions originate due to the detection of S_2^{+}. Therefore, 58 Da is used as the characteristic peak to describe Ni. The full set of identified peaks are listed in Table 6.3.2.

Based on the mass peak identification, a typical AuNi particle reconstruction is shown in Figure 6.3.10. Separation of the Ag and Si signals forms the distinct structure of a capping layer and substrate. Oxygen is mostly associated with Si, indicating no oxygen penetration

Mass to charge	Ions	Mass to charge	Ions	Mass to charge	Ions
14.0	$^{28}Si^{2+}$	29.0	$^{29}Si^{+}$	107.0	$^{107}Ag^{+}$
14.5	$^{29}Si^{2+}$	30.0	$^{30}Si^{+}$	109.0	$^{109}Ag^{+}$
15.0	$^{30}Si^{2+}$	58.0	$^{58}Ni^{+}$	197.0	$^{197}Au^{+}$
16.0	$^{16}O^{+}$	69.0	$^{69}Ga^{+}$	229.0	$^{16}O^{16}O^{197}Au^{+}$
28.0	$^{28}Si^{+}$	71.0	$^{71}Ga^{+}$		

Table 6.3.2 – Ion table for AuNi particle systems. Here are the peaks successfully identified in the APT analysis.

through the capping layer. A single AuNi nanoparticle is located beneath the capping layer. To further analyse the particle, it is isolated from the rest of the reconstruction using the same procedure as for the AuCu systems (in section 6.2.4 on page 195).

In summary, five particles in total were detected, including 2 AuNi, 2 AuNi with He and 1 AuNiMo particle. Composition information is listed in Table 6.3.3. Au is abundant in all detected particles, reaching as high as 90 at.% in one of the AuNi with He particles. Such a high abundance of Au could explain the high fraction of decahedral structure observed, which is the structure of pure Au particle under equilibrium status. There is also a detection of a pure Au particle in AuNi particle batch. This composition data from APT exhibit differences in comparison to the XPS results. Firstly, Au is more abundant in the APT result and no Mo is detected for the AuNiMo particles. Local composition variation of the particles is confirmed via the comparison. With the information obtained from LEIS, it is highly possible that Mo exists as monometallic particles or oxidic species, separated on the substrate from AuNi-rich ones.

Apart from the general composition information, the location of the Ni and Au within the particle is a key benefit from the APT data. In Figure 6.3.11, 2D contour plots of Au and Ni of AuNi systems are shown. Ni segregation is observed in all AuNi systems, whereby Ni is more likely segregated to the edge of the particles. Au is also more likely to be detected in the centre of the particle. Combined with the LEIS data, it is believed that APT detection shows the evidence of forming a Ni shell and Au core particles.

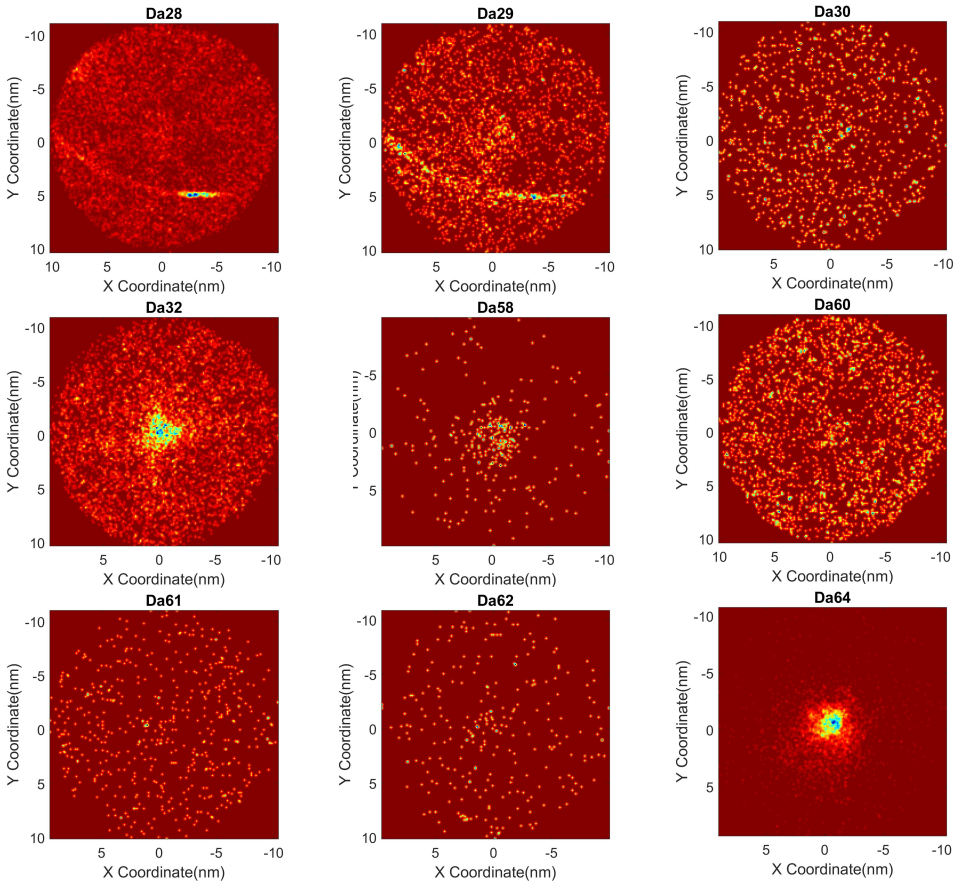

Figure 6.3.9 – 2D contour plots of mass-to-charge-state ratio (Da) for one AuNi particle. The 2D contour plot is based on 3D reconstructed atom map as shown in Figure 6.3.10.

Run ID.	00345	22451	22973	23796	22512
	AuNi	AuNi with He			AuNiMo
Au(number)	928	1540	598	668	854
Ni(number)	166	0	53	72	185
Mo(number)	-	-	-	-	-
Particle size (nm)	8	20	10	4	8
C_{Au} (at.%)	84.8	100	91.9	90.2	82.2
C_{Ni} (at.%)	15.2	0	8.1	9.8	17.8
Counting error	1.0	0	1.0	1.0	1.2

Table 6.3.3 – Atomic composition as measured by APT of detected AuNi, AuNi with He and AuNiMo particles.

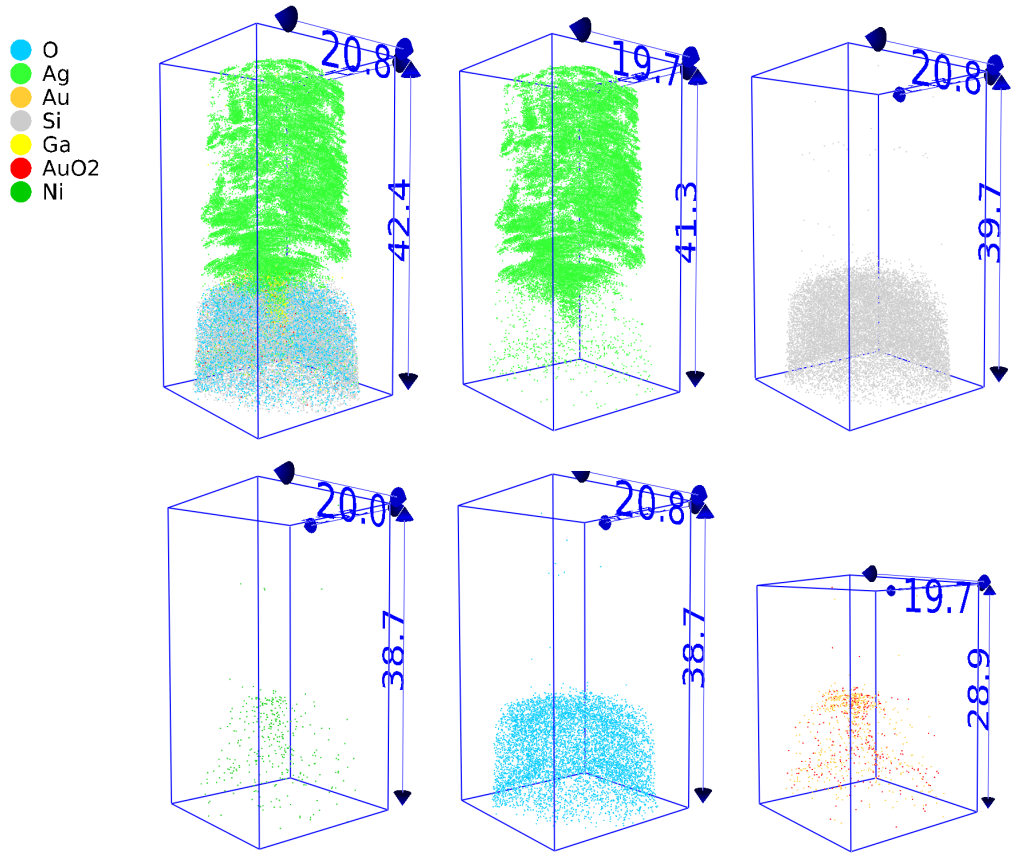

Figure 6.3.10 – 3D elemental APT maps of the AuNi particle analysis. Nanoparticle is located at the interface between Ag (green) capping layer and Si (grey) substrate. The detected nanoparticle is located in the centre of the reconstruction.

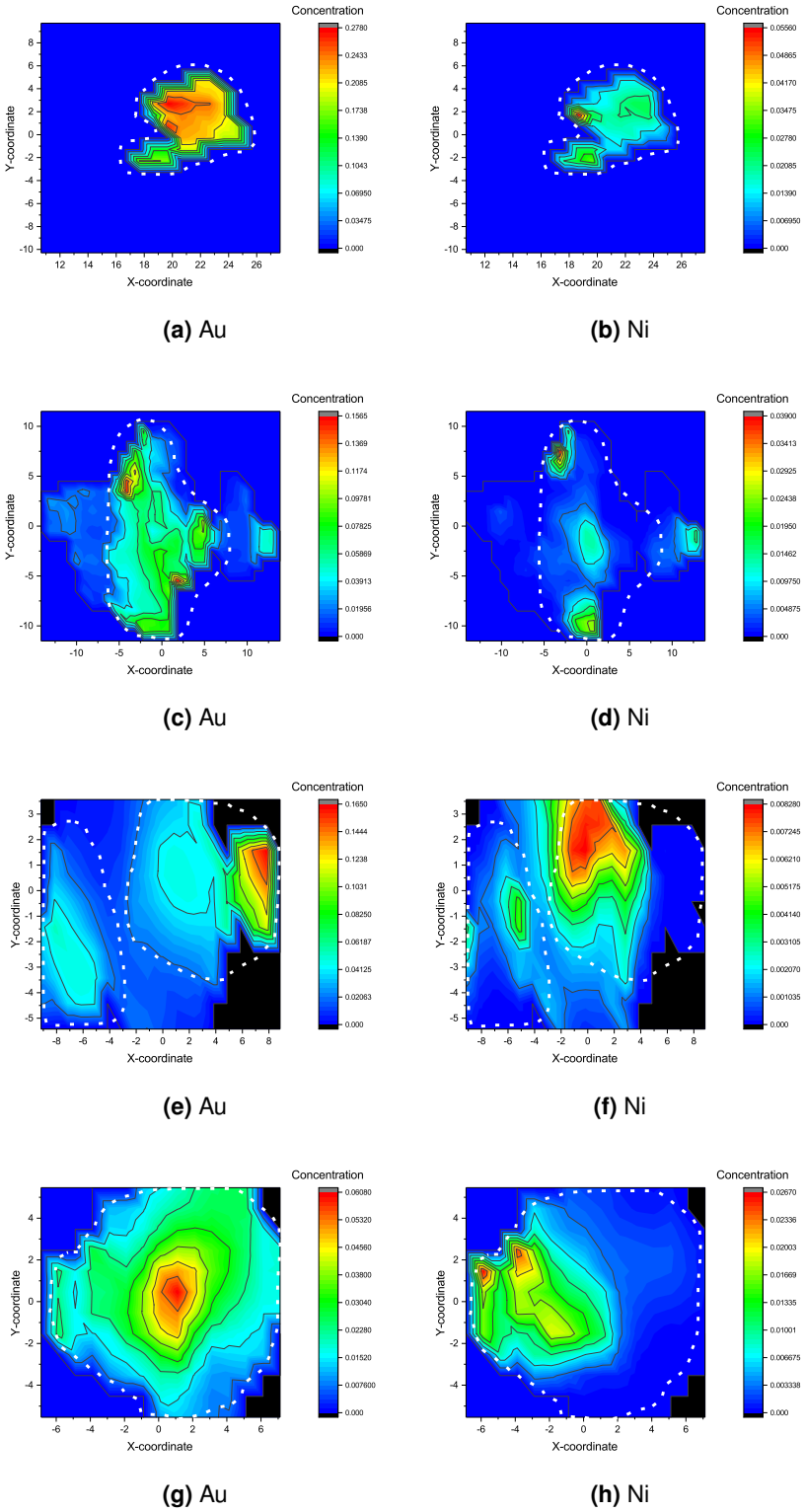

Figure 6.3.11 – Composition segregation of Au and Ni within detected particles. (a) and (b) are from AuNi. (c) and (d) are AuNi with He. (e) and (f) are AuNi with He. (g) and (h) are AuNiMo particle. Au signal is more likely found in the centre of particle whereas Ni is more likely on the edge.

6.4 Discussion

6.4.1 Assessment of the IGC method for particle production

Composition control ability XPS results have shown that this particle synthesis approach can generate nanoparticles with designed composition at micrometre-scale. In this research, the particles were made with a target of a final composition with equal atomic percent of the constituent elements by attempting to supply the same energy input for the magnetron plasma. However, producing alloyed particles is not as simple as introducing more plasma heads [323]. As observed in both AuCu systems and AuNi systems, Mo was either not detected or only can be detected at macro-scale (mm). It therefore suggests that more work is needed in terms of understanding the mixing behaviour of metal containing plasmas during particle formation. Nevertheless, the multi-scale analysis accurately identified this crucial problem at an early stage. Furthermore, APT results show that there is quite a composition variation on the level of the comparison of individual particles. Although the average of the 7 detected particles in AuCu system shows an Au:Cu ratio of 7:3, locally Au can be as much as 90 at.% in a specific particle. Similarly, Au is consistently abundant in particles of AuNi systems regardless of the equal power input during fabrication.

Advantages of the IGC method have been demonstrated in this research. As a relatively new way of making particulate materials, the method possesses a number of unique abilities compared to the chemical method for particle making. One of the most important factors is the control of the chemical composition of the particles. In the IGC methods, composition control is subject to various factors, such as plasma power supply, composition of plasma gas, the length of condensation zone, etc. [324]. Most importantly, the composition variation is also time dependent, meaning that the particle composition can be changed with time during the deposition. It is therefore very versatile to make texture deposition with very defined fine-scale composition along the deposition direction. Together with an in-line mass filter, particles can be further refined based on their sizes. Furthermore, the total deposition environment is under UHV, so little contamination is permitted into the system. In

terms of support/substrate, it opens a vast possibility of options with no obvious limitations.

MesoQ filtering ability The role of the in-line mass filter should be emphasised. In the particle size distribution plots, a systematic size reduction of AuCuMo particles was observed. The relationship between the diameter and density of the particle:

$$d = 2\sqrt[3]{\frac{3m}{4\rho\pi}} \tag{6.4.1}$$

where d is the diameter, m is the mass and ρ is the assumed density. The size measurement in MesoQ software is affected by the particle density. With the compositions of the AuCu and AuCuMo particles are detected (Table 6.2.2), the densities upon APT are $10.0 g/cm^3$ for AuCu and $9.9 g/cm^3$. The density difference is not the factor to affect the MesoQ measurement. It is then ascertained that in-line mass filter actively filters out particles outside of the targeted range, although it was also shown that the TEM measurement does not exactly match the MesoQ. It therefore must be taken into account that the size of the produced particles is significantly affected by other factors. One such factor is associated to the loss of charge of the particles once they are deposited on a grounded conducting substrate that could cause particle agglomeration, resulting in an over-estimated measurement of size via TEM. Nevertheless, the difference between the MesoQ and TEM is within few nanometres. Results from AFM measurements on AuNi systems indicate that the MesoQ reading is accurate in terms of particle size distribution. The bimodal shape of the particle size distributions is double confirmed via various investigation methods (MesoQ, TEM and APT).

6.4.2 APT sample preparation

Development of sample encapsulation method The development of the particle encapsulation is initiated by the in-situ deposition of Pt with SEM. In the case of the Ag particles, these were initially examined by SEM to obtain the information on the particle size and spatial distribution. Subsequently, particle encapsulation was performed directly

by use of the ebeam for deposition of Pt. It is a great convenience of having such a capability since the encapsulation is hence based on the successful identification of the particle location on the silicon posts. Therefore, this enabled precision in the subsequent FIB-milling procedure, and increased the likelihood that the particles shall be properly incorporated in the resulting tips for APT analysis. However, this method also has some disadvantages; the transition of deposited particles to the SEM for encapsulation introduces contamination from the atmosphere. In the case of the Ag particles this is not a problem since the Ag will not oxidise under the atmospheric conditions, but this poses a significant challenge for particles composed of other elements. Also, the quality of the capping layer deposited under SEM is not optimised for the APT analysis due to the residue of organic species from the original metal (Pt) carrier gas and potential low-density regions in the deposited layer, which could result in a premature fracture of the specimen under field evaporation conditions [325]. Thus, a direct deposition-encapsulation method was then developed to increase reliability. Magnetron deposition and ebeam deposition of Ag was used to encapsulated AuCu based particles and AuNi based particles in this thesis. An important additional benefit to APT is that entire Si micro-tip arrays can be coated, rather than just single tips as for previous studies [42, 228, 231]. This approach also avoids the conventionally used FIB lift-out approach for APT sample preparation, and thus significantly reduces preparation time and hence increases sample throughput [234]. The latter of these benefits is particularly important to ensure that representative data on catalyst particles can be obtained. Table 6.4.1 summarises the pros and cons of the currently developed methods for preparing viable nanoparticle-containing samples for APT. Note that in some cases, sample form (particle, nanowire etc.) will also play a significant factor; for example, the electrophoresis method requires nanoparticles to be suspended in a suitable solvent, while particle deposition methods require suitable target sources to be available. The fourth method in the table is the approach developed in this thesis.

Methods used for NP sample preparation	Electrophoresis method [42, 228, 326]	Liftout method[218, 231, 234]	In-situ growth method [235]	Particle deposition method [233, 327, 328]
Reconstruction accuracy	Low	High	High	High
Cost	Low	High	Medium	Medium
Time for preparation	Fast	Slow	Slow	Medium

Table 6.4.1 – Comparison of different sample preparation methods for nano-particle analysis. There are four methods listed. The first three have been previously reported in various publications. The fourth is the protocol proposed in this thesis.

Quality of the encapsulation layer The heart of the particle encapsulation method is the layer composition and the method of the layer deposition. Attempts have been made to produce the encapsulation layer using materials with an evaporation field as close as possible to the embedded particles [233]. To this, some success has been reported in the case using ZnO on Si-based materials [327, 328]. It is proposed that the oxygen of the SiO_2 forms a strong bond with Zn, resulting a strong binding between the coating layer and Si. Given the success of the ZnO in the Si case, it was crucially reported that a further layer, of material such as Ni, between the Si and ZnO resulted in 100% rate of premature fracture of the APT specimen. In this thesis, Ag is selected as the coating layer, in particular, for its low evaporation field comparing to Si substrate and embedded particles. The main driving force for that, as claimed before, is to minimise the rate of specimen failure during the APT analyses, i.e. it is harder to run a sample incorporating a capping layer requiring a high evaporation field with a low evaporation field material below. In addition, Ag surface atoms were observed to move under the high electric field [186], which could be the sign of force mitigation during field evaporation. As the direct result, successful APT analyses of nanoparticles were obtained without significant rate of fracture. It is also assumed that Ag ions were detected within the particle due to the aberration.

It has also been found there is an impact in terms of the method by which the encapsulation layer is deposited. The Ag layer deposited by magnetron is solid and packed with

minimal density variations as shown in Figure 6.2.13. As the result, there were no specimen mini-fracture events during field evaporation through this coating layer. On the other hand, the layer deposited by ebeam has strong variations within the Ag layer, which results in patchy regions of coverage within the detected Ag layer as shown in Figure 6.3.10. Also, this low quality of Ag coating further complicates the detection of the embedded particles making it hard to reconstruct a round shape. It is important to point out that the difference of the quality of the deposited layers is not visible under FIB-SEM and is only detectable under APT.

6.4.3 Technique capability and sample analysis protocol

A wide range of techniques were progressively involved in this part of particle characterisation research. For various practical reasons, SEM was involved in the Ag work to identify the particle density and performed subsequent deposition. Since this initial trial was on Ag monometallic particles, the particle distribution density information was enough to describe the system. However, more information was needed to understand the properties of bimetallic and trimetallic samples. Therefore, TEM with EDX capability was introduced for the AuCu based particle system. TEM has revealed the structure of the deposited particles and identified that the particles are in meta-stable states [170]. Also, the EDX information contributed the significant insight that particle composition is related to their sizes. There is however a question about the exact location of element Mo. Neither EDX via SEM and TEM, identified the location of the Mo on either the macro-scale or micro-scale. Due to the fact that AuCu based particles were only deposited on silicon coupon (which was encapsulated directly after the deposition) and TEM grid, implication of other characterisation techniques is limited for the quest of Mo.

MesoQ (mass filter), AFM, TEM, XPS, LEIS and APT were therefore combined for the analysis of the AuNi based particle systems. MesoQ, AFM, TEM investigated the nanoparticle confirming the consistency (shape, size distribution, crystal structure and composition) of the resulting particles across different characterisation platforms. Especially, both

AFM and TEM measurement show the bimodal features of the size distribution, which reflects the high accuracy of the measurement from the in-situ MesoQ mass filter. In order to solve the problem of the whereabouts of the location of Mo in the system, XPS and LEIS were both applied as they can probe much large analysis areas (on the millimetre scale).

Overall, this work has proven the combination of various techniques can provide important information on the understanding of nanoparticles. APT has a crucial position among these techniques for its extreme high 3D composition detecting ability. Therefore, APT should be the routing part for particle analysis provided that the particles are adaptable for the novel developed sample encapsulation method.

Chapter 7

Summary

To align with the structure of the thesis, this conclusion chapter is divided into three sections.

Model alloys

- NiFe and NiCo alloys were oxidised and analysed via APT. The initial oxidation of these alloys was analysed successfully and composition variations from the bulk alloy to the surface oxide were revealed to depend on alloy composition.

- Complex layered structures of oxides developed via in-situ oxidation were observed. In the case of NiFe alloys, transitional layers have been identified between the substrate and stable oxides (NiO, FeO and $FeNi_2O_4$). In contrast, there was no transitional layer observed in the oxidation of $Ni50Co50$.

- Preferential oxidation was observed along different crystallographic zone axes. In particular, in the case of $Ni10Fe90$ sample, fast Ni outwards diffusion along the (110) and {103} axes was observed. In addition, Ni diffusion along a grain boundary was also observed, which supports the explanation of excessive Ni in the oxide region.

- Hydrogen reduction on oxidised sample showed that the Ni surface enrichment formed during oxidation is stable.

- Identified surface enrichment of Ni in the NiFe systems means the Fe could be dwarfed during the chemical reactions, resulting persistent deviation of product constitution and catalytic performance from designed parameters.

Nanoparticles by synthesis

- A Deposition Precipitation by Urea method has been verified for producing NiFe and NiCo nanoparticles with a narrow size distribution and stable composition variation.
- The levels of Fe and Co detected in the particles were consistently below their target compositions. Further investigations of the sample preparation processes are required to further understand this deviation.
- Additional refinement of the particle producing process is needed to produce particles with a tighter composition deviation prior to the APT analysis.

Nanoparticles by condensation

- It has been shown that it is essential to have a wide combination of complementary techniques including SEM, TEM-EDX, AFM, XPS, LEIS and APT to thoroughly characterise alloy nanoparticle. The contribution of APT among these techniques is crucial due to the unique chemical and 3D spatial information that it provides. A thorough understanding of the composition, shape, crystal structure etc. of various particles is obtained in this work. The significance of APT characterisation among these techniques is demonstrated via the identification of nanometre-level segregation on individual particles.
- A relatively simple and cost-effective sample preparation method is introduced and refined for producing APT specimens with nanoparticles embedded. Using this IGC method, embedded particles can be routinely analysed by APT, yielding high quality data. Selection of the capping layer used in this method is based on the merits of low evaporation field, few isotopes and oxidation resistance. Ag meets all of these

requirements, and was shown to be an effective capping layer allowing good yield of successfully analysed samples with limited trajectory aberrations in the data. In addition, it is shown that the magnetron deposition method for producing such capping layers is overwhelmingly better compared to an ebeam deposition method.

- The Inert Gas Condensation method is a novel method to fabricate multi-metallic nanoparticles. Narrow size distributions of the particles are observed in both in-situ (in-line mass spectrometer) and ex-situ measurements (AFM, TEM). It is also confirmed that the resulting particles are a mixture of non-equilibrium and equilibrium status.

- These APT developments present a method to perform routine analysis and inspection on nanoparticles produced by Inert Gas Condensation method. This effectively builds the feedback loop between individual particles to catalytic performance and in turn improves bottom-up particle design.

Chapter 8

Conclusions

Work conducted in this thesis contributes to the field of atom probe tomography research on catalytic materials. Based on the previous atom probe research on noble metals, this thesis makes the progress by investigating into the non-noble materials. Due to the active nature of the surface of non-noble metals, it creates additional sophistication of surface treatment prior to APT analysis. In this thesis, it has been shown that a new route involving surface field evaporation, in-situ oxidation, and subsequent atom probe tomography analysis, can overcome routinely occurred hurdles, such as surface contamination (unwanted oxides) and pressure gap (pressure gap between real application and experimental condition). It therefore presents a good opportunity to further extend this atom probe analysis to similar catalytic metals, exploring their surface changes at better representative conditions.

The attempt to analyse an actual catalyst in the form of nanoparticle was also conducted. Extensive TEM analyses show that particles made by chemical synthesis have good control on size distribution. However, it is still challenging to have particles obtaining designed bi-metallic composition. It has been realised that it is a good progress to shift model alloy tip to real catalysts, but it is necessary to have a tight control of particle composition before the atom probe analysis given the complexity of the sample preparation. Alternatively, particles deposition by gas condensation method is successfully analysed by atom probe. A relative simplified sample encapsulation method was used, resulting good data quality

of nanoparticles. It shows that, rather than an intricate analysis, atom probe tomography can be used for particle analysis routinely by using the improved sample encapsulation method. Although this routinely analysis is still limited to the particles manufactured by certain method (IGC in this thesis), it is very promising to phase atom probe into the field of particle analysis due to the 3D composition information obtained.

Chapter 9

Bibliography

[1] Haruta, M., et al. *Novel Gold Catalysts for the Oxidation of Carbon Monoxide at a Temperature far Below 0Â°C*. Chemistry Letters, 16(2):405, 1987.

[2] Hutchings, G.J. *New directions in gold catalysis*. Gold Bulletin, 37(1-2):3, 2004.

[3] Ross, J.R.H. *Heterogeneous Catalysis: Fundamentals and Applications*. Elsevier, 2012.

[4] Dorling, D. *Population 10 Billion*. Constable & Robinson Limited, 2013.

[5] Ullmann. *Ullmann's Encyclopedia of Industrial Chemistry*. Wiley-VCH Verlag GmbH & Co., Weinheim, Germany, 2000.

[6] Wolfe, D.W. *Tales from the Underground: A Natural History of Subterranean Life*. Perseus Pub., 2002.

[7] Jennings, J. *Catalytic Ammonia Synthesis: Fundamentals and Practice*. Springer Science & Business Media, 1991.

[8] Bielawa, H., et al. *The Ammonia-Synthesis Catalyst of the Next Generation: Barium-Promoted Oxide-Supported Ruthenium.* Angewandte Chemie (International ed. in English), 40(6):1061, 2001.

[9] Nishida, R., et al. *Synthesis of nickel nanoparticles supported on hollow samaria-doped ceria particles via the solution-spray plasma technique: Anode catalysts for SOFCs*. Solid State Ionics, 180(14-16):968, 2009.

[10] Degnan, T.F., et al. *History of ZSM-5 fluid catalytic cracking additive development at Mobil*. Microporous and Mesoporous Materials, 35-36:245, 2000.

[11] Vogt, E.T.C., et al. *Fluid catalytic cracking: recent developments on the grand old lady of zeolite catalysis*. Chem. Soc. Rev., 44(20):7342, 2015.

[12] BP. *Oil production | About BP | BP Global*, 2013.

[13] Schrick, B., et al. *Hydrodechlorination of Trichloroethylene to Hydrocarbons Using Bimetallic Nickel-Iron Nanoparticles*. Chemistry of Materials, 14(12):5140, 2002.

[14] Samolada, M.C., et al. *Catalyst Evaluation for Catalytic Biomass Pyrolysis*. Energy & Fuels, 14:1161, 2000.

[15] Babich, I.V., et al. *Science and technology of novel processes for deep desulfurization of oil refinery streams: A review*. Fuel, 82(6):607, 2003.

[16] Wang, L., et al. *Catalytic performance and characterization of Ni-Fe catalysts for the steam reforming of tar from biomass pyrolysis to synthesis gas*. Applied Catalysis A: General, 392(1-2):248, 2011.

[17] Tijmensen, M. *Exploration of the possibilities for production of Fischer Tropsch liquids and power via biomass gasification*. Biomass and Bioenergy, 23(2):129, 2002.

[18] Nagy, A., et al. *High temperature partial oxidation reactions over silver catalysts*. Applied Catalysis A: General, 188(1):337, 1999.

[19] Kandemir, T., et al. *The Haber-Bosch Process Revisited: On the Real Structure and Stability of "Ammonia Iron" under Working Conditions*. Angewandte Chemie International Edition, 52(48):12723, 2013.

[20] Ertl, G., et al. *Formation and Decomposition of Nitrides on Iron Surfaces*. Zeitschrift für Naturforschung A, 34(1):30, 1979.

[21] Herzog, B., et al. *In situ X-ray powder diffraction analysis of the microstructure of activated iron catalysts for ammonia synthesis*. Applied Catalysis A: General, 141(1-2):71, 1996.

[22] Mittasch, A., et al. *Early Studies of Multicomponent Catalysts*. Advances in Catalysis, 2:81, 1950.

[23] Newsome, D.S. *The Water-Gas Shift Reaction*. Catalysis Reviews, 21(2):275, 1980.

[24] Iglesia, E. *Design, synthesis, and use of cobalt-based Fischer-Tropsch synthesis catalysts*. Applied Catalysis A: General, 161(1-2):59, 1997.

[25] Campbell, C.T., et al. *The Effect of Size-Dependent Nanoparticle Energetics on Catalyst Sintering*. Science, 298(5594), 2002.

[26] Valden, M., et al. *Onset of Catalytic Activity of Gold Clusters on Titania with the Appearance of Nonmetallic Properties*. Science, 281(5383), 1998.

[27] Haruta, M. *Size- and support-dependency in the catalysis of gold*. Catalysis Today, 36(1):153, 1997.

[28] Moulijn, J.A., et al. *Catalyst deactivation: Is it predictable? What to do?* Applied Catalysis A: General, 212(1-2):3, 2001.

[29] Golunski, S.E. *Why use platinum in catalytic converters?* Platinum Metals Review, 51(3):162, 2007.

[30] Primo, A., et al. *Synergy between the metal nanoparticles and the support for the hydrogenation of functionalized carboxylic acids to diols on Ru/TiO2*. Chemical communications (Cambridge, England), 47(12):3613, 2011.

[31] Bartholomew, C.H. *Carbon Deposition in Steam Reforming and Methanation*. Catalysis Reviews, 24(1):67, 1982.

[32] Oudar, J. *Sulfur Adsorption and Poisoning of Metallic Catalysts*. Catalysis Reviews, 22(2):171, 1980.

[33] Guinot, J., et al. *Formation and characterization of catalytic carbons obtained from CO disproportionation over an iron nickel catalyst*. Carbon, 19(2):95, 1981.

[34] Kustov, A., et al. *CO methanation over supported bimetallic Ni-Fe catalysts: From computational studies towards catalyst optimization*. Applied Catalysis A: General, 320:98, 2007.

[35] Liu, R.J., et al. *Metal sintering mechanisms and regeneration of palladium/alumina hydrogenation catalysts*. Applied Catalysis A: General, 282(1-2):111, 2005.

[36] Hagelüken, B.C. *Recycling the Platinum Group Metals: A European Perspective*. Platinum Metals Review, 56(1):29, 2012.

[37] Debe, M.K. *Electrocatalyst approaches and challenges for automotive fuel cells*. Nature, 486(7401):43, 2012.

[38] Sinfelt, J.H. *Catalysis by alloys and bimetallic clusters*. Accounts Of Chemical Research, 10(1):15, 1977.

[39] Schwab, G.M. *Alloy catalysts in dehydrogenation*. Discussions of the Faraday Society, 8(0):166, 1950.

[40] Sinfelt, J.H. *Catalytic hydrogenolysis and dehydrogenation over copper-nickel alloys*. Journal of Catalysis, 24(2):283, 1972.

[41] Sinfelt, J.H. *Nature of ruthenium-copper catalysts*. Journal of Catalysis, 42(2):227, 1976.

[42] Tedsree, K., et al. *Hydrogen production from formic acid decomposition at room temperature using a Ag-Pd core-shell nanocatalyst*. Nature Nanotechnology, 6(5):302, 2011.

[43] Sachtler, W., et al. *The role of individual surface atoms in chemisorption and catalysis by nickel-copper alloys*. Surface Science, 18(1):62, 1969.

[44] Williams, F. *Surface composition of nickel-gold alloys*. Journal of Catalysis, 30(3):438, 1973.

[45] Sinfelt, J. *Structure of metal catalysts*. Reviews of Modern Physics, 51(3):569, 1979.

[46] Ertl, G., et al. (eds.). *Handbook of Heterogeneous Catalysis*. Wiley-VCH Verlag GmbH & Co. KGaA, Weinheim, Germany, 2008.

[47] Burch, R. *Importance of electronic ligand effects in metal alloy catalysts*. Accounts of Chemical Research, 15(1):24, 1982.

[48] Muraza, O., et al. *Selectivity control in hydrogenation reactions by nanoconfinement of polymetallic nanoparticles in mesoporous thin films*. Applied Catalysis A: General, 368(1-2):87, 2009.

[49] Meitzner, G., et al. *Structure of bimetallic clusters. Extended x-ray absorption fine*

structure (EXAFS) studies of Ag-Cu and Au-Cu clusters. The Journal of Chemical Physics, 83(9):4793, 1985.

[50] Sinfelt, J.H., et al. *Structure of bimetallic clusters. Extended x-ray absorption fine structure (EXAFS) studies of Ru-Cu clusters*. The Journal of Chemical Physics, 72(9):4832, 1980.

[51] Meitzner, G., et al. *Structure of bimetallic clusters. Extended x-ray absorption fine structure (EXAFS) studies of Ir-Rh clusters*. The Journal of Chemical Physics, 78(5):2533, 1983.

[52] Meitzner, G., et al. *Structure of bimetallic clusters. Extended x-ray absorption fine structure (EXAFS) studies of Re-Cu, Ir-Cu, and Pt-Cu clusters*. The Journal of Chemical Physics, 83(1):353, 1985.

[53] Rodriguez, J.A., et al. *The Nature of the Metal-Metal Bond in Bimetallic Surfaces*. Science, 257(5072):897, 1992.

[54] Cameron, D., et al. *Carbons as supports for precious metal catalysts*. Catalysis Today, 7(2):113, 1990.

[55] Somorjai, G.A., et al. *Introduction to Surface Chemistry and Catalysis*. John Wiley & Sons, 2010.

[56] Yates, I.C., et al. *Intrinsic Kinetics of the Fischer-Tropsch Synthesis on a Cobalt Catalyst*. Energy & Fuels, 5(1):168, 1991.

[57] Trimm, D.L. *The Formation and Removal of Coke from Nickel Catalyst*. Catalysis Reviews, 16(1):155, 1977.

[58] D.B. Bukur, K. Okabe, M.P. Rosynek, C.P. Li, D.J. Wang, K.R.P.M. Rao, G.H. *Activation Studies with a Precipitated Iron Catalyst for Fischer-Tropsch Synthesis: I. Characterization Studies*, 1995.

[59] Greenwood, N.N., et al. *Spectroscopic Properties of Inorganic and Organometallic Compounds*, vol. 4 of *Spectroscopic Properties of Inorganic and Organometallic Compounds*. Royal Society of Chemistry, Cambridge, 1971.

[60] Amelse, J.A., et al. *Carburization of supported iron synthesis catalysts*. The Journal of Physical Chemistry, 82(5):558, 1978.

[61] Ishihara, T., et al. *Hydrogenation of carbon monoxide over SiO2-supported Fe-Co, Co-Ni and Ni-Fe bimetallic catalysts*. Applied Catalysis, 30(2):225, 1987.

[62] UNMUTH, E. *Iron alloy Fischer-Tropsch catalysts I. Oxidation-reduction studies of the Fe-Ni system*. Journal of Catalysis, 61(1):242, 1980.

[63] Brown, R., et al. *Temperature programmed reduction of alumina-supported iron, cobalt and nickel bimetallic catalysts*. Applied Catalysis, 3(2):177, 1982.

[64] Xu, J., et al. *Methane steam reforming, methanation and water-gas shift: I. Intrinsic kinetics*. AIChE Journal, 35(1):88, 1989.

[65] Sehested, J. *Four challenges for nickel steam-reforming catalysts*. Catalysis Today, 111(1-2):103, 2006.

[66] Mizushima, T. *Characterization of silica-supported bimetallic iron-nickel catalysts by EXAFS*. Journal of Catalysis, 112(1):282, 1988.

[67] Matsuyama, M. *Catalytic inactivities of Ni alloys expressed by surface and bulk compositions*. Journal of Catalysis, 102(2):309, 1986.

[68] Takanabe, K., et al. *Titania-supported cobalt and nickel bimetallic catalysts for carbon dioxide reforming of methane*. Journal of Catalysis, 232(2), 2005.

[69] Choudhary, V., et al. *Partial oxidation of methane to CO and H2 over nickel and/or cobalt containing ZrO2, ThO2, UO2, TiO2 and SiO2 catalysts*. Fuel, 77(15):1803, 1998.

[70] Wu, H., et al. *Synergetic effect of Ni and Co in Ni-Co/SBA-15-CD catalysts and their catalytic performance in carbon dioxide reforming of methane to syngas*. Catal. Sci. Technol., 6(14):5631, 2016.

[71] Raupp, G.B., et al. *Moessbauer investigation of supported Fe and FeNi catalysts. II. Carbides formed Fischer-Tropsch synthesis*. Journal of Catalysis, 58(3):348, 1979.

[72] Koike, M., et al. *A highly active and coke-resistant steam reforming catalyst comprising uniform nickel-iron alloy nanoparticles.* ChemSusChem, 5(12):2312, 2012.

[73] Fazle Kibria, A., et al. *Synthesis of narrow-diameter carbon nanotubes from acetylene decomposition over an iron-nickel catalyst supported on alumina*. Carbon, 40(8):1241, 2002.

[74] Münster, P. *Kinetics of the steam reforming of methane with iron, nickel, and iron-nickel alloys as catalysts*. Journal of Catalysis, 72(2):279, 1981.

[75] Pandey, D., et al. *Promotional effects in alumina and silica supported bimetallic Ni-Fe catalysts during CO2 hydrogenation*. Journal of Molecular Catalysis A: Chemical, 382:23, 2014.

[76] Sitthisa, S., et al. *Selective conversion of furfural to methylfuran over silica-supported NiFe bimetallic catalysts*. Journal of Catalysis, 284(1):90, 2011.

[77] Kumbhar, P.S., et al. *Geometric and electronic effects in silica supported bimetallic nickel-copper and nickel-iron catalysts for liquid-phase hydrogenation of acetophenone and benzonitrile*. Journal of the Chemical Society, Chemical Communications, (7):584, 1992.

[78] Chen, L., et al. *Development of a Co-Ni bimetallic aerogel catalyst for hydrogen production via methane oxidative CO2 reforming in a magnetic assisted fluidized bed*. International Journal of Hydrogen Energy, 35(16):8494, 2010.

[79] Xu, J., et al. *Biogas reforming for hydrogen production over a Ni-Co bimetallic catalyst: Effect of operating conditions*. International Journal of Hydrogen Energy, 35(23):13013, 2010.

[80] Son, I.H., et al. *Hydrogen production from carbon dioxide reforming of methane over highly active and stable MgO promoted Co-Ni/γ-Al2O3 catalyst*. International Journal of Hydrogen Energy, 39(8):3762, 2014.

[81] Barakat, N.A.M., et al. *CoxNiy-decorated graphene as novel, stable and super effective non-precious electro-catalyst for methanol oxidation*. Applied Catalysis B: Environmental, 154-155:221, 2014.

[82] Barakat, N.A.M., et al. *Carbon nanofibers doped by NixCo1-x alloy nanoparticles as*

effective and stable non precious electrocatalyst for methanol oxidation in alkaline media. Journal of Molecular Catalysis A: Chemical, 394:177, 2014.

[83] Homs, N., et al. *Low-temperature steam-reforming of ethanol over ZnO-supported Ni and Cu catalysts: The effect of nickel and copper addition to ZnO-supported cobalt-based catalysts*. Catalysis Today, 116(3):361, 2006.

[84] Feng, W., et al. *In situ facile synthesis of bimetallic CoNi catalyst supported on graphene for hydrolytic dehydrogenation of amine borane*. International Journal of Hydrogen Energy, 39(7):3371, 2014.

[85] Swartzendruber, L.J., et al. *The Fe-Ni (iron-nickel) system*. Journal of Phase Equilibria, 12(3):288, 1991.

[86] Massalski, T.B., et al. *Binary Alloy Phase Diagrams*. v. 1. ASM International, 1990.

[87] Zhang, H., et al. *Structural Study on Co-Ni Bimetallic Nanoparticles by X-ray Spectroscopy*. The Journal of Physical Chemistry C, 114(32):13596, 2010.

[88] Smithells, C.J.C.J., et al. *Smithells metals reference book.* Elsevier Butterworth-Heinemann, 2004.

[89] Chambridge Materials. *DoITPoMS*, 2017.

[90] Scully, J.C. *The fundamentals of corrosion*. International series of monographs on materials science and technology. Pergamon Press, 1975.

[91] Over, H., et al. *Oxidation of Metal Surfaces*. Science, 297(5589):2003 LP , 2002.

[92] Stuckless, J.T., et al. *A novel single-crystal adsorption calorimeter and additions for determining metal adsorption and adhesion energies*. Review of Scientific Instruments, 69(6):2427, 1998.

[93] Carlisle, C.I., et al. *Atomic imaging of the transition between oxygen chemisorption and oxide film growth on Ag{111}*. Surface Science, 470(1-2):15, 2000.

[94] Thürmer, K., et al. *Autocatalytic oxidation of lead crystallite surfaces*. Science, 297(5589):2033, 2002.

[95] Cox, M.G., et al. *A chemical diffusion model for partitioning of transition elements in oxide scales on alloys*. Philosophical Magazine, 26(4):839, 1972.

[96] Barnes, D.G., et al. *The role of oxygen transport in oxidation of Fe-Cr alloys*. Philosophical Magazine, 28(6):1303, 1973.

[97] Smentkowski, V., et al. *The adsorption of oxygen on Fe(110) in the temperature range of 90 to 920 K*. Surface Science, 232(1-2):113, 1990.

[98] Uhlig, H.H. *Corrosion and Corrosion Control: An Introduction to Corrosion Science and Engineering*. Wiley, 1963.

[99] Evans, U.R. *The Corrosion and Oxidation of Metals: Scientific Principles and Practical Applications, Volume 3*. Edward Arnold, 1977.

[100] West, J.M. *Basic Corrosion and Oxidation*. John Wiley & Sons, Incorporated, 1980.

[101] Ghatee, M.H., et al. *Structures, thermal stability, and melting behaviors of bimetallic Cs-Na clusters studied via molecular dynamics simulation*. Fluid Phase Equilibria, 355:114, 2013.

[102] Pignocco, A., et al. *Leed studies of oxygen adsorption and oxide formation on an (011) iron surface*. Surface Science, 7(3):261, 1967.

[103] Busch, M., et al. *FeO(111) formation by exposure of Fe(110) to atomic and molecular oxygen*. Surface Science, 600(13):2778, 2006.

[104] Cornell, R.M., et al. *The Iron Oxides: Structure, Properties, Reactions, Occurrences and Uses*. John Wiley & Sons, 2006.

[105] Chen, R.Y., et al. *Review of the high-temperature oxidation of iron and carbon steels in air or oxygen*. Oxidation of Metals, 59(5-6):433, 2003.

[106] Wood, G., et al. *The oxidation of Ni and Co and of Ni/Co alloys at high temperatures*. Corrosion Science, 5(9):645, 1965.

[107] Graham, M.J.M., et al. *On the Mechanism of Low-Temperature Oxidation (23Â°-450Â°C) of Polycrystalline Nickel*. Journal of The Electrochemical Society, 119(7):879, 1972.

[108] Wagner, C. *Dissociation of molecular O2 as the rate determining step during the initial stage of the oxidation of Ni at 250Â°C*. Corrosion Science, 10(9):641, 1970.

[109] Jeangros, Q., et al. *Oxidation mechanism of nickel particles studied in an environmental transmission electron microscope*. Acta Materialia, 67:362, 2014.

[110] Reed, R.C. *The Superalloys: Fundamentals and Applications*. Cambridge University Press, 2006.

[111] England, D.M. *Oxidation Kinetics of Some Nickel-Based Superalloy Foils and Electronic Resistance of the Oxide Scale Formed in Air Part I*. Journal of The Electrochemical Society, 146(9):3196, 1999.

[112] England, D.M., et al. *Oxidation Kinetics of Some Nickel-Based Superalloy Foils in Humidified Hydrogen and Electronic Resistance of the Oxide Scale Formed Part II*. Journal of The Electrochemical Society, 148(4):A330, 2001.

[113] Gulbransen, E.A., et al. *The Kinetics of the Oxidation of Cobalt*. Journal of The Electrochemical Society, 98(6):241, 1951.

[114] Nan, Z., et al. *Investigation of thermodynamic properties of Co2O3 powder*. Thermochimica Acta, 404(1):245, 2003.

[115] Metz, R., et al. *Direct oxidation route from metal to ceramic: Study on cobalt oxide*. Materials Research Bulletin, 44(10):1984, 2009.

[116] Przybylski, K. *High Temperature Oxidation Mechanism of CoO to Co[sub 3]O[sub 4]*. Journal of The Electrochemical Society, 128(4):897, 1981.

[117] Carter, R.E., et al. *Oxidation of Cobalt Metal*. JOM, 7(2):336, 1955.

[118] Reti, A.R., et al. *Short-time, High Temperature Oxidation of Cobaltous Oxide*. Industrial & Engineering Chemistry Process Design and Development, 5(2):171, 1966.

[119] Matsuyama, T., et al. *LEED-AES Study of the Temperature Dependent Oxidation of The Cobalt (0001) Surface*. Surface Science, 102(1):18, 1981.

[120] Guillaume, C.E. *The Anomaly of the Nickel-Steels*. Proceedings of the Physical Society of London, 32(1):374, 1919.

[121] Barnett, S.J., et al. *A New gyromagnetic effect in permalloy and iron*. Physical Review, 88:28, 1952.

[122] Menzies, I.A., et al. *Oxidation of an Fe-12% Ni alloy in oxygen at 700-1000Â°C*. Oxidation of Metals, 3(1):41, 1971.

[123] Wulf, G., et al. *The oxidation of FeNi alloys*. Corrosion Science, 9(9):689, 1969.

[124] Foley, R.T. *Oxidation of Iron-Nickel Alloys*. Journal of The Electrochemical Society, 109(12):1202, 1962.

[125] Carter, T., et al. *The oxidation of Fe-1%Ni alloys*. Corrosion Science, 9(7):471, 1969.

[126] Inaba, M., et al. *Effects of the annealing conditions on the oxidation behavior of Fe-36Ni alloys*. Applied Surface Science, 27(2):164, 1986.

[127] Wandelt, K., et al. *Electron spectroscopic studies of the oxidation of Fe/Ni alloys*. Surface Science, 55(2):403, 1976.

[128] Pollak, R.A., et al. *Surface composition and chemistry of evaporated Permalloy films observed by xâray photoemission spectroscopy and by Auger electron spectroscopy*. Journal of Applied Physics, 46(3):1382, 1975.

[129] Brundle, C.R., et al. *Oxygen interaction with Ni/Fe surfaces (1) LEED and XPS studies of Ni 76%/Fe 24% (100)*. Journal of Vacuum Science and Technology, 16(2):474, 1979.

[130] Olefjord, I., et al. *ESCA studies of Ni-25 At% Fe alloy. 1?surface preparation treatments and oxidation*. Surface and Interface Analysis, 4(1):23, 1982.

[131] Tanaka, H., et al. *Comparative study of Rh/MgO modified with Fe, Co or Ni for the catalytic partial oxidation of methane at short contact time. Part II: Catalytic performance and bed temperature profile*. Applied Catalysis A: General, 378(2):187, 2010.

[132] Fan, M.S., et al. *Utilization of greenhouse gases through carbon dioxide reforming of methane over Ni-Co/MgO-ZrO2: Preparation, characterization and activity studies*. Applied Catalysis B: Environmental, 100(1-2):365, 2010.

[133] Chattopadhyay, B., et al. *The transient oxidation of alloys*. Oxidation of Metals, 2(4):373, 1970.

[134] Law, Y., et al. *Surface oxidation of NiCo alloy: A comparative X-ray photoelectron*

spectroscopy study in a wide pressure range. Applied Surface Science, 258(4):1480, 2011.

[135] Law, Y.T., et al. *Bimetallic nickel-cobalt nanosized layers supported on polar ZnO surfaces: Metal-support interaction and alloy effects studied by synchrotron radiation X-ray photoelectron spectroscopy*. Journal of Physical Chemistry C, 116(18):10048, 2012.

[136] Hajcsar, E.E., et al. *Initial stages of oxidation on Co-Ni alloys: Island nucleation and growth*. Langmuir, 11(12):4862, 1995.

[137] Haruta, M. *Gold catalysts prepared by coprecipitation for low-temperature oxidation of hydrogen and of carbon monoxide*. Journal of Catalysis, 115(2):301, 1989.

[138] Hashmi, A.S.K., et al. *Gold Catalysis*. Angewandte Chemie International Edition, 45(47):7896, 2006.

[139] Hutchings, G.J. *Vapor Phase Hydrochlorination of Acetylene : Correlation of Catalytic Activity of Supported Metal Chloride Catalysts*. Journal of Catalysis, 96(1):292, 1985.

[140] Hvolbæk, B., et al. *Catalytic activity of Au nanoparticles*. Nano Today, 2(4):14, 2007.

[141] Janssens, T.V.W., et al. *Insights into the reactivity of supported Au nanoparticles: combining theory and experiments*. Topics in Catalysis, 44(1-2):15, 2007.

[142] Campbell, C.T. *Nanoparticle Gold Catalysis*. Science, 234(2004), 2011.

[143] Avgouropoulos, G., et al. *A comparative study of Pt/γ-Al2O3, Au/α-Fe2O3 and CuO-CeO2 catalysts for the selective oxidation of carbon monoxide in excess hydrogen*. Catalysis Today, 75(1-4):157, 2002.

[144] Trimm, D.L. *Minimisation of carbon monoxide in a hydrogen stream for fuel cell application*. Applied Catalysis A: General, 296(1):1, 2005.

[145] Conte, M., et al. *Hydrochlorination of acetylene using a supported gold catalyst: A study of the reaction mechanism*. Journal of Catalysis, 250(2):231, 2007.

[146] Bracey, C.L., et al. *Application of copper-gold alloys in catalysis: current status and future perspectives.* Chemical Society reviews, 38(8):2231, 2009.

[147] Zhu, H. *An empirical comparison of credit spreads between the bond market and the credit default swap market*. Journal of Financial Services Research, 29(3):211, 2006.

[148] Bracey, C.L., et al. *Understanding the effect of thermal treatments on the structure of CuAu/SiO2 catalysts and their performance in propene oxidation*. Catalysis Science & Technology, 1(1):76, 2011.

[149] Chimentão, R.J., et al. *Propene epoxidation by nitrous oxide over Au-Cu/TiO2 alloy catalysts*. Journal of Molecular Catalysis A: Chemical, 274(1-2):159, 2007.

[150] Della Pina, C., et al. *Highly selective oxidation of benzyl alcohol to benzaldehyde catalyzed by bimetallic gold-copper catalyst*. Journal of Catalysis, 260(2):384, 2008.

[151] He, P., et al. *Reverse micelle synthesis of AuNi alloy as electrocatalyst of borohydride oxidation*. International Journal of Hydrogen Energy, 37(2):1254, 2012.

[152] Besenbacher, F., et al. *Design of a Surface Alloy Catalyst for Steam Reforming*. Science, 279(5358):1913, 1998.

[153] Jiang, H.L., et al. *Bimetallic Au-Ni nanoparticles embedded in SiO2 nanospheres: Synergetic catalysis in hydrolytic dehydrogenation of ammonia borane*. Chemistry - A European Journal, 16(10):3132, 2010.

[154] Wang, J., et al. *Thermodynamic assessment of the Au-Ni system*. Calphad, 29(4):263, 2005.

[155] Fedorov, P.P., et al. *Au-Cu Phase Diagram*. Russian Journal of Inorganic Chemistry, 61(6):772, 2016.

[156] Peng, L., et al. *Segregation in bimetallic nanoparticles*. Physical Chemistry Chemical Physics, 17(17):27940, 2015.

[157] Xiang, X., et al. *Structural evolution of NiAu nanoparticles under ambient conditions directly revealed by atom-resolved imaging combined with DFT simulation*. Nanoscale, 6(21):12898, 2014.

[158] Molenbroek, A.M., et al. *Structure and Reactivity of Ni-Au Nanoparticle Catalysts*. The Journal of Physical Chemistry B, 105(23):5450, 2001.

[159] Pauwels, B., et al. *Transmission electron microscopy and Monte Carlo simulations of ordering in Au-Cu clusters produced in a laser vaporization source*. Physical Review B, 63(16):1, 2001.

[160] Greeley, J.P. *Active Site of an Industrial Catalyst*. Science, 336(6083), 2012.

[161] Marks, L.D. *Experimental studies of small particle structures*. Reports on Progress in Physics, 57(6):603, 1994.

[162] Conyers, H. *Some Theorems on the Free Energies of Crystal Surfaces*. Physical re, 82(1):87, 1951.

[163] Heyraud, J., et al. *Equilibrium shape and temperature: lead on graphite*. Surface Science, 128:334, 1983.

[164] Ajayan, P.M., et al. *Phase instabilities in small particles*. Phase Transitions, 24-26(1):229, 1990.

[165] Sarangi, S.S., et al. *Molecular dynamics simulation studies of gold nano-cluster on silicon (001) surface*. Indian Journal of Physics, (001), 2017.

[166] Barnard, A.S., et al. *Nanogold: A Quantitative Phase Map*. ACS Nano, 3(6):1431, 2009.

[167] Darby, S., et al. *Theoretical study of Cu-Au nanoalloy clusters using a genetic algorithm*. Journal of Chemical Physics, 116(4):1536, 2002.

[168] Lambers, E.S., et al. *Room-temerature oxidation of Ni(110) at low and atmospheric oxygen pressures*. Oxidation of Metals, 45(3-4):301, 1996.

[169] Li, Z.Y., et al. *Three-dimensional atomic-scale structure of size-selected gold nanoclusters.* Nature, 451(7174):46, 2008.

[170] Young, N.P., et al. *Transformations of gold nanoparticles investigated using variable temperature high-resolution transmission electron microscopy*. Ultramicroscopy, 110(5):506, 2010.

[171] MacArthur, K.E., et al. *'Ex-situ' annealing and structural transformations in gold*

nanoparticles. In *Journal of Physics: Conference Series*, vol. 371, 012068. IOP Publishing, 2012.

[172] Ascencio, J., et al. *Structure determination of small particles by HREM imaging: theory and experiment*. Surface Science, 396(1-3):349, 1998.

[173] Ascencio, J.A., et al. *Truncated icosahedral structure observed in gold nanoparticles*. Surface Science, 447(1):73, 2000.

[174] Sun, S. *Monodisperse FePt Nanoparticles and Ferromagnetic FePt Nanocrystal Superlattices*. Science, 287(5460):1989, 2000.

[175] Deepak, F.L., et al. *New Insights into the structure of Pd-Au nanoparticles as revealed by aberration-corrected STEM.* Journal of crystal growth, 325(1):60, 2011.

[176] Rosenauer, A., et al. *Composition mapping in InGaN by scanning transmission electron microscopy.* Ultramicroscopy, 111(8):1316, 2011.

[177] Chu, M.W., et al. *Emergent Chemical Mapping at Atomic-Column Resolution by Energy-Dispersive X-Ray Spectroscopy in an Aberration-Corrected Electron Microscope*. Physical Review Letters, 104(19):196101, 2010.

[178] LeBeau, J., et al. *Quantitative Atomic Resolution Scanning Transmission Electron Microscopy*. Physical Review Letters, 100(20):206101, 2008.

[179] Tran, D.T., et al. *Configuration of microbially synthesized Pd-Au nanoparticles studied by STEM-based techniques.* Nanotechnology, 23(5):055701, 2012.

[180] E, H., et al. *Towards quantitative analysis of core-shell catalyst nano-particles by aberration corrected high angle annular dark field STEM and EDX*. Journal of Physics: Conference Series, 241(1):012067, 2010.

[181] Batenburg, K.J., et al. *3D imaging of nanomaterials by discrete tomography*. Ultramicroscopy, 109(6):730, 2009.

[182] Miao, J., et al. *Atomic electron tomography: 3D structures without crystals*. Science, 353(6306), 2016.

[183] Behan, G., et al. *Three-dimensional imaging by optical sectioning in the aberration-*

corrected scanning transmission electron microscope. Philosophical Transactions of the Royal Society A, 367(1903):3825, 2009.

[184] Alania, M., et al. *Depth sectioning combined with atom-counting in HAADF STEM to retrieve the 3D atomic structure*. Ultramicroscopy, 177:36, 2017.

[185] Nicoletti, O., et al. *Three-dimensional imaging of localized surface plasmon resonances of metal nanoparticles*. Nature, 502(7469):80, 2013.

[186] Castro, T., et al. *Studies of individual nanometerâsized metallic clusters using scanning tunneling microscopy, field emission, and field ion microscopy*. Journal of Vacuum Science & Technology A: Vacuum, Surfaces, and Films, 7(4):2845, 1989.

[187] Bowles, R., et al. *Generation of molecular clusters of controlled size*. Surface Science, 106(1-3):117, 1981.

[188] Buffat, P., et al. *Size effect on the melting temperature of gold particles*. Physical Review A, 13(6):2287, 1976.

[189] Castro, T., et al. *A field emission technique to measure the melting temperature of individual nanometer-sized clusters*. Surface Science, 234(1-2):43, 1990.

[190] Castro, T., et al. *Size-dependent melting temperature of individual nanometer-sized metallic clusters*. Physical Review B, 42(13):8548, 1990.

[191] Lovall, D., et al. *Resolving the atomic structure of supported nanometer-size Au clusters*. Physical Review B, 58(23):15889, 1998.

[192] Lin, M., et al. *Electron emission from an individual, supported C60 molecule*. Physical Review B, 47(12):7546, 1993.

[193] Visart de Bocarmé, T., et al. *Surface segregation of Au-Pd alloys in UHV and reactive environments: Quantification by a catalytic atom probe*. Ultramicroscopy, 109(5):619, 2009.

[194] Barroo, C., et al. *Hydrogenation of NO and NO2 over palladium and platinum nanocrystallites: case studies using field emission techniques*. New Journal of Chemistry, 38(5):2090, 2014.

[195] Barroo, C., et al. *Complex Oscillation Patterns During the Catalytic Hydrogenation*

of NO 2 over Platinum Nanosized Crystals. The Journal of Physical Chemistry C, 118(13):6839, 2014.

[196] Bagot, P., et al. *3D atom probe study of gas adsorption and reaction on alloy catalyst surfaces II: Results on Pt and Pt-Rh*. Surface Science, 601(10):2245, 2007.

[197] Antczak, G., et al. *Jump processes in surface diffusion*. Surface Science Reports, 62(2):39, 2007.

[198] Gaussman, A., et al. *Field ion microscopy of the CO-induced structural changes of Pd and Pt single crystal planes*. Surface Science, 266(1-3):46, 1992.

[199] Bär, T., et al. *Structural changes of Ag crystals during reaction with nitric oxide*. Surface Science, 454-456(1):240, 2000.

[200] Visart de Bocarmé, T., et al. *Field ion microscopy study of the structural changes in Rh crystals during the reaction of oxygen-hydrogen gas mixtures*. Surface Science, 454-456(1):320, 2000.

[201] McEwen, J.S., et al. *Field-assisted oxidation of rhodium*. Chemical Physics Letters, 452(1-3):133, 2008.

[202] Bagot, P., et al. *3D atom probe study of gas adsorption and reaction on alloy catalyst surfaces I: Instrumentation*. Surface Science, 600(15):3028, 2006.

[203] Barroo, C., et al. *Fluctuating dynamics of nanoscale chemical oscillations: Theory and experiments*. Journal of Physical Chemistry Letters, 6(12):2189, 2015.

[204] Barroo, C., et al. *Nonlinear behavior during NO 2 hydrogenation on a nanosized Pt-Rh catalyst sample*. Applied Surface Science, 412:564, 2017.

[205] Mueller, E.W. *The Atom-Probe Field Ion Microscope*. Review of Scientific Instruments, 39(1):83, 1968.

[206] Cerezo, A., et al. *Application of a position-sensitive detector to atom probe microanalysis*. Review of Scientific Instruments, 59(6):862, 1988.

[207] Kelly, T.F., et al. *First data from a commercial local electrode atom probe (LEAP).* Microscopy and microanalysis : the official journal of Microscopy Society of Amer-

ica, Microbeam Analysis Society, Microscopical Society of Canada, 10(3):373, 2004.

[208] Ng, Y.S., et al. *ToF atom-probe fim investigation of surface segregation in dilute alloys*. Surface Science, 78(2):419, 1978.

[209] Cranstoun, G., et al. *The oxidation of clean ruthenium surfaces. II. Atom probe analyses of oxide films*. Applications of Surface Science, 2(3):375, 1979.

[210] Kellogg, G. *Oxide formation and reduction on rhodium surfaces*. Surface Science, 171(2):359, 1986.

[211] Bagot, P., et al. *3D atom probe study of gaseous adsorption on alloy catalyst surfaces III: Ternary alloys -NO on Pt-Rh-Ru and Pt-Rh-Ir*. Surface Science, 602(7):1381, 2008.

[212] Bagot, P., et al. *A model for oxidation-driven surface segregation and transport on Pt-alloys studied by atom probe tomography*. Surface Science, 605(15-16):1544, 2011.

[213] Dumpala, S., et al. *An integrated high temperature environmental cell for atom probe tomography studies of gas-surface reactions: instrumentation and results.* Ultramicroscopy, 141:16, 2014.

[214] Li, T., et al. *Characterization of oxidation and reduction of a platinum-rhodium alloy by atom-probe tomography*. Catalysis Today, 175(1):552, 2011.

[215] Li, T., et al. *Characterization of Oxidation and Reduction of Pt-Ru and Pt-Rh-Ru Alloys by Atom Probe Tomography and Comparison with Pt-Rh*. The Journal of Physical Chemistry C, 116(33):17633, 2012.

[216] Li, T., et al. *Characterization of Oxidation and Reduction of a Palladium-Rhodium Alloy by Atom-Probe Tomography*. The Journal of Physical Chemistry C, 116(7):4760, 2012.

[217] Li, T., et al. *Atomic engineering of platinum alloy surfaces*. Ultramicroscopy, 132:205, 2013.

[218] Miller, M.K., et al. *Performance of a local electrode atom probe*. Surface and Interface Analysis, 39(2-3):262, 2007.

[219] London, A.J., et al. *Quantification of oxide particle composition in model oxide dispersion strengthened steel alloys.* Ultramicroscopy, 2015.

[220] London, A.J., et al. *Effect of Ti and Cr on dispersion, structure and composition of oxide nano-particles in model ODS alloys*. Acta Materialia, 97:223, 2015.

[221] Marquis, E.A. *Core/shell structures of oxygen-rich nanofeatures in oxide-dispersion strengthened Fe-Cr alloys*. Applied Physics Letters, 93(18):1, 2008.

[222] Vurpillot, F., et al. *A new approach to the interpretation of atom probe field-ion microscopy images*. Ultramicroscopy, 89(1-3):137, 2001.

[223] Williams, C.A., et al. *Nanoscale characterisation of ODS-Eurofer 97 steel: An atom-probe tomography study*. Journal of Nuclear Materials, 400(1):37, 2010.

[224] Williams, C.A., et al. *Defining clusters in APT reconstructions of ODS steels*. Ultramicroscopy, 132:271, 2013.

[225] Williams, C.A., et al. *Quantifying the composition of yttrium and oxygen rich nanoparticles in oxide dispersion strengthened steels*. Ultramicroscopy, 125:10, 2013.

[226] Li, T. *Atomic Scale Chararcterisation of Platinum Group Alloy Catalyst Materials*. Ph.D. thesis, University of Oxford, 2011.

[227] Yu, K.M.K., et al. *Non-syngas direct steam reforming of methanol to hydrogen and carbon dioxide at low temperature.* Nature communications, 3:1230, 2012.

[228] Li, T., et al. *Atomic Imaging of Carbon-Supported Pt, Pt/Co, and Ir@Pt Nanocatalysts by Atom-Probe Tomography*. ACS Catalysis, 4(2):695, 2014.

[229] Larson, D., et al. *Focused ion-beam milling for field-ion specimen preparation:*. Ultramicroscopy, 75(3):147, 1998.

[230] Xiang, Y., et al. *Long-Chain Terminal Alcohols through Catalytic CO Hydrogenation*. Journal of the American Chemical Society, 135(19):7114, 2013.

[231] Felfer, P., et al. *Revealing the Distribution of the Atoms within Individual Bimetallic*

Catalyst Nanoparticles. Angewandte Chemie International Edition, 53(42):11190, 2014.

[232] Folcke, E., et al. *Laser-assisted atom probe tomography investigation of magnetic FePt nanoclusters: First experiments*. Journal of Alloys and Compounds, 517:40, 2012.

[233] Larson, D.J., et al. *Encapsulation method for atom probe tomography analysis of nanoparticles.* Ultramicroscopy, 159:420, 2015.

[234] Felfer, P., et al. *New approaches to nanoparticle sample fabrication for atom probe tomography*. Ultramicroscopy, 2015.

[235] Moutanabbir, O., et al. *Colossal injection of catalyst atoms into silicon nanowires*. Nature, 496(7443):78, 2013.

[236] Devaraj, A., et al. *Understanding Atom Probe Tomography of Oxide-Supported Metal Nanoparticles by Correlation with Atomic-Resolution Electron Microscopy and Field Evaporation Simulation*. The Journal of Physical Chemistry Letters, 5(8):1361, 2014.

[237] Marquis, E.A., et al. *Chromatic Aberrations in the Field Evaporation Behavior of Small Precipitates*. Microscopy and Microanalysis, 14(6):561, 2008.

[238] Oberdorfer, C., et al. *On the field evaporation behavior of dielectric materials in three-dimensional atom probe: a numeric simulation.* Microscopy and microanalysis : the official journal of Microscopy Society of America, Microbeam Analysis Society, Microscopical Society of Canada, 17(1):15, 2011.

[239] Vurpillot, F., et al. *Modeling image distortions in 3DAP.* Microscopy and microanalysis : the official journal of Microscopy Society of America, Microbeam Analysis Society, Microscopical Society of Canada, 10(3):384, 2004.

[240] Baik, S.I., et al. *Correlative atom-probe tomography and transmission electron microscope study of a chemical transition in a spinel on an oxidized nickel-based superalloy*. Scripta Materialia, 68(11):909, 2013.

[241] Rigutti, L., et al. *Correlation of Microphotoluminescence Spectroscopy, Scanning Transmission Electron Microscopy, and Atom Probe Tomography on a Single*

Nano-object Containing an InGaN/GaN Multiquantum Well System. Nano Letters, 14(1):107, 2014.

[242] Gault, B., et al. *Atom Probe Microscopy*. Springer Science & Business Media, 2012.

[243] Miller, M.K., et al. *Atom probe microanalysis: principles and applications to materials problems*. Materials Research Society, 1989.

[244] Zanella, R., et al. *Characterization and reactivity in CO oxidation of gold nanoparticles supported on TiO2 prepared by deposition-precipitation with NaOH and urea*. Journal of Catalysis, 222(2):357, 2004.

[245] Zanella, R., et al. *Mechanism of deposition of gold precursors onto TiO2 during the preparation by cation adsorption and deposition-precipitation with NaOH and urea*. Applied Catalysis A: General, 291(1-2):62, 2005.

[246] Ostgard, D.J., et al. *Comparison of Pt / KL Catalysts Prepared by Ion Exchange or Incipient Wetness Impregnation*. Journal of Catalysis, 357:342, 1992.

[247] Carrero, A., et al. *Hydrogen production by ethanol steam reforming over Cu-Ni/SBA-15 supported catalysts prepared by direct synthesis and impregnation*. Applied Catalysis A: General, 327(1):82, 2007.

[248] Haberland, H., et al. *Atoms, Molecules and Clusters*. Molecules, 415(1):413, 1991.

[249] Haberland, H. *Filling of micron-sized contact holes with copper by energetic cluster impact*. Journal of Vacuum Science & Technology A: Vacuum, Surfaces, and Films, 12(5):2925, 1994.

[250] Ellis, P.R., et al. *The cluster beam route to model catalysts and beyond*. Faraday Discuss., 188:39, 2016.

[251] Wegner, K., et al. *Cluster beam deposition: a tool for nanoscale science and technology*. Journal of Physics D: Applied Physics, 39(22):R439, 2006.

[252] Cassidy, C., et al. *Inoculation of silicon nanoparticles with silver atoms*. Sci. Rep., 3:3083, 2013.

[253] Singh, V., et al. *Assembly of tantalum porous films with graded oxidation profile from size-selected nanoparticles*. Journal of Nanoparticle Research, 16(5):2373, 2014.

[254] Srivastava, S., et al. *Efficient photoelectrochemical water splitting on ultrasmall defect-rich TaO _x nanoclusters enhanced by size-selected Pt nanocluster promoters*. Nanoscale, 9(38):14395, 2017.

[255] Miller, P.E., et al. *The quadrupole mass filter: Basic operating concepts*. Journal of Chemical Education, 63(7):617, 1986.

[256] Elam, J.W., et al. *Viscous flow reactor with quartz crystal microbalance for thin film growth by atomic layer deposition*. Review of Scientific Instruments, 73(8):2981, 2002.

[257] Thompson, K., et al. *In situ site-specific specimen preparation for atom probe tomography*. Ultramicroscopy, 107(2-3):131, 2007.

[258] Muller, E.W. *The imaging process in field ion microscopy from the fem to the atom probe*. C R C Critical Reviews in Solid State Sciences, 6(2):85, 1976.

[259] Fowler, R.H., et al. *Electron Emission in Intense Electric Fields*. Proceedings of the Royal Society of London. Series A, Containing Papers of a Mathematical and Physical Character, 119(781):173, 1928.

[260] Drechsler, M. *Erwin Müller and the early development of field emission microscopy*. Surface Science, 70(1):1, 1978.

[261] Chen, Y.C., et al. *On the atomic resolution of a field ion microscope*. Surface Science, 26(1):61, 1971.

[262] Müller, E.W., et al. *Field ion microscopy: principles and applications*. American Elsevier Pub. Co., 1969.

[263] Vurpillot, F., et al. *Reconstructing atom probe data: A review*. Ultramicroscopy, 132:19, 2013.

[264] Bas, P., et al. *A general protocol for the reconstruction of 3D atom probe data*. Applied Surface Science, 88:298, 1995.

[265] Gipson, G.S. *An improved empirical formula for the electric field near the surface of field emitters*. Journal of Applied Physics, 51(7):3884, 1980.

[266] Geiser, B., et al. *Wide-Field-of-View Atom Probe Reconstruction*. Microscopy and Microanalysis, 15(2):292, 2009.

[267] Gault, B., et al. *Advances in the reconstruction of atom probe tomography data*. Ultramicroscopy, 111(6):448, 2011.

[268] Kelly, T.F., et al. *Local electrode atom probes*. Materials Characterization, 44(1-2):59, 2000.

[269] Nishikawa, O., et al. *Development of a scanning atom probe*. Journal of Vacuum Science & Technology B, 13(2):599, 1995.

[270] Cerezo, A., et al. *Performance of an energy-compensated three-dimensional atom probe*. Review of Scientific Instruments, 69(1):49, 1998.

[271] Tsong, T.T. *Photon stimulated field ionization*. The Journal of Chemical Physics, 65(6):2469, 1976.

[272] Gault, B., et al. *Design of a femtosecond laser assisted tomographic atom probe*. Review of Scientific Instruments, 77(4):043705, 2006.

[273] Kelly, T.F., et al. *On the many advantages of local-electrode atom probes*. Ultramicroscopy, 62(1-2):29, 1996.

[274] Kelly, T.F., et al. *Invited review article: Atom probe tomography.* The Review of scientific instruments, 78(3):031101, 2007.

[275] Oberdorfer, C., et al. *Laser-Assisted Atom Probe Tomography of Oxide Materials*. Microscopy and Microanalysis, 13:342, 2007.

[276] Geiser, B.P., et al. *Spatial Distribution Maps for Atom Probe Tomography*. Microscopy and Microanalysis, 13(06):437, 2007.

[277] Moody, M.P., et al. *Qualification of the tomographic reconstruction in atom probe by advanced spatial distribution map techniques*. Ultramicroscopy, 109(7):815, 2009.

[278] London, A.J., et al. *Single-Ion Deconvolution of Mass Peak Overlaps for Atom Probe Microscopy*. Microscopy and Microanalysis, 23(2):300, 2017.

[279] Carter, C.B., et al. *Transmission Electron Microscopy: Diffraction, Imaging, and Spectrometry*. Springer International Publishing, 2016.

[280] Williams, D.B., et al. *Transmission Electron Microscopy: A Textbook for Materials Science*. No. v. 2 in Cambridge library collection. Springer, 2009.

[281] Varela, M., et al. *MATERIALS CHARACTERIZATION IN THE ABERRATION-CORRECTED SCANNING TRANSMISSION ELECTRON MICROSCOPE*. Annual Review of Materials Research, 35(1):539, 2005.

[282] Cliff, G., et al. *The quantitative analysis of thin specimens*. Journal of Microscopy, 103(2):203, 1975.

[283] MacArthur, K.E., et al. *Quantitative Energy-Dispersive X-Ray Analysis of Catalyst Nanoparticles Using a Partial Cross Section Approach*. Microscopy and Microanalysis, 22(1):71, 2016.

[284] Watanabe, M., et al. *Comparison of detectability limits for elemental mapping by EF-TEM and STEM-XEDS*. Micron, 34(3-5):173, 2003.

[285] Niehus, H., et al. *Low-energy ion scattering at surfaces*. Surface Science Reports, 17(4-5):213, 1993.

[286] Castner, D.G., et al. *X-ray Photoelectron Spectroscopy Sulfur 2p Study of Organic Thiol and Disulfide Binding Interactions with Gold Surfaces*. Langmuir, 12(21):5083, 1996.

[287] Morita, S., et al. *Noncontact Atomic Force Microscopy*. No. v. 3 in NanoScience and Technology. Springer International Publishing, 2015.

[288] Johnson, D., et al. *Characterisation and quantification of membrane surface properties using atomic force microscopy: A comprehensive review*. Desalination, 356:149, 2015.

[289] Bragg, P.W.H., et al. *The reflection of X-rays by crystals*. Proceedings of the Royal Society A, 88(605):428, 1913.

[290] Feng, Y., et al. *Preparation, characterization and microwave absorbing properties of FeNi alloy prepared by gas atomization method*. Journal of Alloys and Compounds, 513:455, 2012.

[291] Li, X.G., et al. *Preparation and magnetic properties of ultrafine particles of Fe-Ni alloys*. Journal of Magnetism and Magnetic Materials, 170:339, 1997.

[292] Hellman, O., et al. *Analysis of Three-dimensional Atom-probe Data by the Proximity Histogram*. Microscopy and Microanalysis, 6:437, 2000.

[293] Torres, K.L., et al. *Field evaporation behavior in [001] FePt thin films*. Ultramicroscopy, 111(6):512, 2011.

[294] Horvath, J., et al. *Diffusion in Nanocrystalline Materials*. Soild State Communications, 62(5):319, 1987.

[295] Maier, K. *Self -Diffusion in Copper at Low Temperatures*. Physica Status Solidi (a), 44:567, 1977.

[296] Stott, F.H., et al. *A Comparison of the Oxidation Behavior of Fe-Cr-AI, Ni-Cr-AI, and Co-Cr-Al Alloys*. Oxidation of Metals, 3(2):103, 1971.

[297] Kim, J.H., et al. *The role of grain boundaries in the initial oxidation behavior of austenitic stainless steel containing alloyed Cu at 700Â°C for advanced thermal power plant applications*. Corrosion Science, 96:52, 2015.

[298] Haugsrud, R. *On the high-temperature oxidation of nickel*. Corrosion Science, 45(1):211, 2003.

[299] Smeltzer, W.W., et al. *Oxidation of Metals by Short Circuit And lattice Diffusion of Oxygen*. Acta Metallurgica, 9:880, 1961.

[300] Herchl, R., et al. *Short-circuit diffusion in the growth of nickel oxide scales on nickel crystal faces*. Oxidation of Metals, 4(1):35, 1972.

[301] Bonfrisco, L.P., et al. *Effects of crystallographic orientation on the early stages of oxidation in nickel and chromium*. Journal of Materials Science, 45(6):1663, 2010.

[302] Cathcart, J., et al. *The Structure of Thin Oxide Films Formed on Nickel Crystals*. Journal of the Electrochemical Society, 116(5):664, 1969.

[303] Graham, M., et al. *Influence of oxide structure on the oxidation rate of nickel single crystals*. Journal of the Electrochemical Society, 120(11):1523, 1973.

[304] Hirano, K.I., et al. *Diffusion in cobalt-nickel alloys*. Journal of Applied Physics, 33(10):3049, 1962.

[305] Million, B., et al. *Concentration dependence of diffusion in nickel-cobalt alloys*. Acta Metallurgica, 17(3):339, 1969.

[306] Florencio, J., et al. *Absolute composition depth-profiles in surface segregation of Pt-Rh alloys*. Surface Science, 345(3):L29, 1996.

[307] Kruse, N., et al. *Formation of Rh-subcarbonyls during the reaction of CO, CO2and CH3OH with stepped Rh single crystal surfaces*. Surface Science, 211-212(C):1038, 1989.

[308] Kruse, N. *Surface reaction kinetics on the atomic scale: Studies by means of pulsed field desorption mass spectrometry*. Materials Science and Engineering A, 270(1):75, 1999.

[309] Kruse, N. *Nitric oxide interaction with Rh metal: Kinetics of elemental steps and reaction with carbon monoxide*. Journal of Molecular Catalysis A: Chemical, 163(1-2):79, 2000.

[310] Barroo, C., et al. *Catalysis and Atom Probe Tomography: Recent Progresses and Future Developments towards the Analysis of Nanoporous Samples*. Microscopy and Microanalysis, 21(S3):855, 2015.

[311] Barroo, C., et al. *Field Ion Microscopy and Pulsed Field Desorption Mass Spectrometry: Unique Tools for Surface and Subsurface Analysis*. Microscopy and Microanalysis, 22(S3):378, 2016.

[312] Perea, D.E., et al. *An environmental transfer hub for multimodal atom probe tomography*. Advanced Structural and Chemical Imaging, 3(1):12, 2017.

[313] Pyrz, W.D., et al. *Particle Size Determination Using TEM : A Discussion of Image Acquisition and Analysis for the Novice Microscopist*. Langmuir, (35):11350, 2008.

[314] Miller, M.K., et al. *Review of atom probe FIB-based specimen preparation methods.* Microscopy and microanalysis : the official journal of Microscopy Society of

America, Microbeam Analysis Society, Microscopical Society of Canada, 13(6):428, 2007.

[315] Moazed, K. *Field Emission Microscopy of Metal Crystal Nuclearion*. AIME, 230:234, 1964.

[316] Verrelli, E., et al. *Coalescence of Cluster Beam Generated Sub-2 nm Bare Au Nanoparticles and Analysis of Au Film Growth Parameters*. Annalen der Physik, 1700256:1700256, 2017.

[317] Ling, T., et al. *Icosahedral Face-Centered Cubic Fe Nanoparticles: Facile Synthesis and Characterization with Aberration-Corrected TEM*. Nano Letters, 9(4):1572, 2009.

[318] Reyes-Gasga, J., et al. *Analysis of the contrast in icosahedral gold nanoparticles*. Topics in Catalysis, 46(1-2):23, 2007.

[319] Douglas, J.O., et al. *Optimisation of sample preparation and analysis conditions for atom probe tomography characterisation of low concentration surface species*. Semiconductor Science and Technology, 31(8):084004, 2016.

[320] Chen, Y.S., et al. *Direct observation of individual hydrogen atoms at trapping sites in a ferritic steel*. Science, 355(6330):1196, 2017.

[321] Sundquist, B. *A direct determination of the anisotropy of the surface free energy of solid gold, silver, copper, nickel, and alpha and gamma iron*. Acta Metallurgica, 12(1):67, 1964.

[322] Johnson, C.L., et al. *Effects of elastic anisotropy on strain distributions in decahedral gold nanoparticles*. Nature Materials, 7(2):120, 2008.

[323] Kelly, P.J., et al. *Magnetron sputtering: a review of recent developments and applications*. Vacuum, 56(3):159, 2000.

[324] Khojasteh, M., et al. *Influence of source parameters on the growth of metal nanoparticles by sputter-gas-aggregation*. Applied Nanoscience, 2017.

[325] Yang, Q., et al. *A combined approach for deposition and characterization of atomic-*

ally engineered catalyst nanoparticles. Catalysis, Structure & Reactivity, 1(3):125, 2015.

[326] Eley, C., et al. *Nanojunction-Mediated Photocatalytic Enhancement in Heterostructured CdS/ZnO, CdSe/ZnO, and CdTe/ZnO Nanocrystals.* Angewandte Chemie (International ed. in English), 53(30):7838, 2014.

[327] Sun, Z., et al. *1-D Metal Nanobead Arrays within Encapsulated Nanowires via a Red-Ox-Induced Dewetting: Mechanism Study by Atom-Probe Tomography*. Nano Letters, acs.nanolett.7b03391, 2017.

[328] Sun, Z., et al. *Criteria and considerations for preparing atom-probe tomography specimens of nanomaterials utilizing an encapsulation methodology*. Ultramicroscopy, 184:225, 2018.

Appendix A

Appendix-peak labelling

A.1 Fe52Ni48

Peak identification of oxidised Ni48Fe52 sample is one of the most challenging case due to the over crowded peaks of oxides. Sample with this composition has the most significant oxidation development, which will be discussed later, brings multi overlaps in the oxide region. Also, an inclusion of Ti, Mo and Co as contamination, increases the difficulty further. A typical mass spectra of a oxidised Fe52Ni48 sample is shown in Figure A.1.1. Over crowded peaks are evident beyond Da 63 in three major regions: Da 63 to Da 80, Da 87 to Da 125 and Da 135 to Da 141. All these peaks in this region are located on the top surface of the data, therefore mislabelling could result a ex peculation of vastly different oxidation mechanism. These is a periodic nature of peak development which is the direct reflection of oxide since they are normal apart of half or one oxygen atomic weight due to different charge states. To correct label those oxide peaks, ion overlap relationship is calculated and illustrated in Figure A.1.2. There are 7 overlap relation groups with a strong complexity in the Fe oxide and Ni oxide region. As shown in Figure A.1.3a, identified species are FeO^{++} , NiO^{++} and O_5^{++}. The fitting results shows that there is a good fitting of O_5^{++} and it is certain FeO^{++} and NiO^{++} exists. However, the calculated intensity diverts to the true intensities. In figure A.1.3b, similar calculation is performed again and it identifies Da 44 as

FeO_2^{++}. However, it is more likely that CO_2 is the actual ions judging from the shape of the peaks (with significant tail) and various APT analyses. Also, mismatching in the intensity of the peaks indicate that there are species unknown. However, it is not possible to conduct further analysis due to the limit information given from surrounding peaks. In the region of larger mass-to-chagre number (as shown in Figure A.1.3c, A.1.3d and A.1.3e), fittings are more close to the measured intensity. It is mostly due to the increasing mass peaks coming with more information of species. As the direct result, there are quite a few ion species identified. For example, some oxides containing Mn have been identified. But their share in the overall oxide composition is minimum.

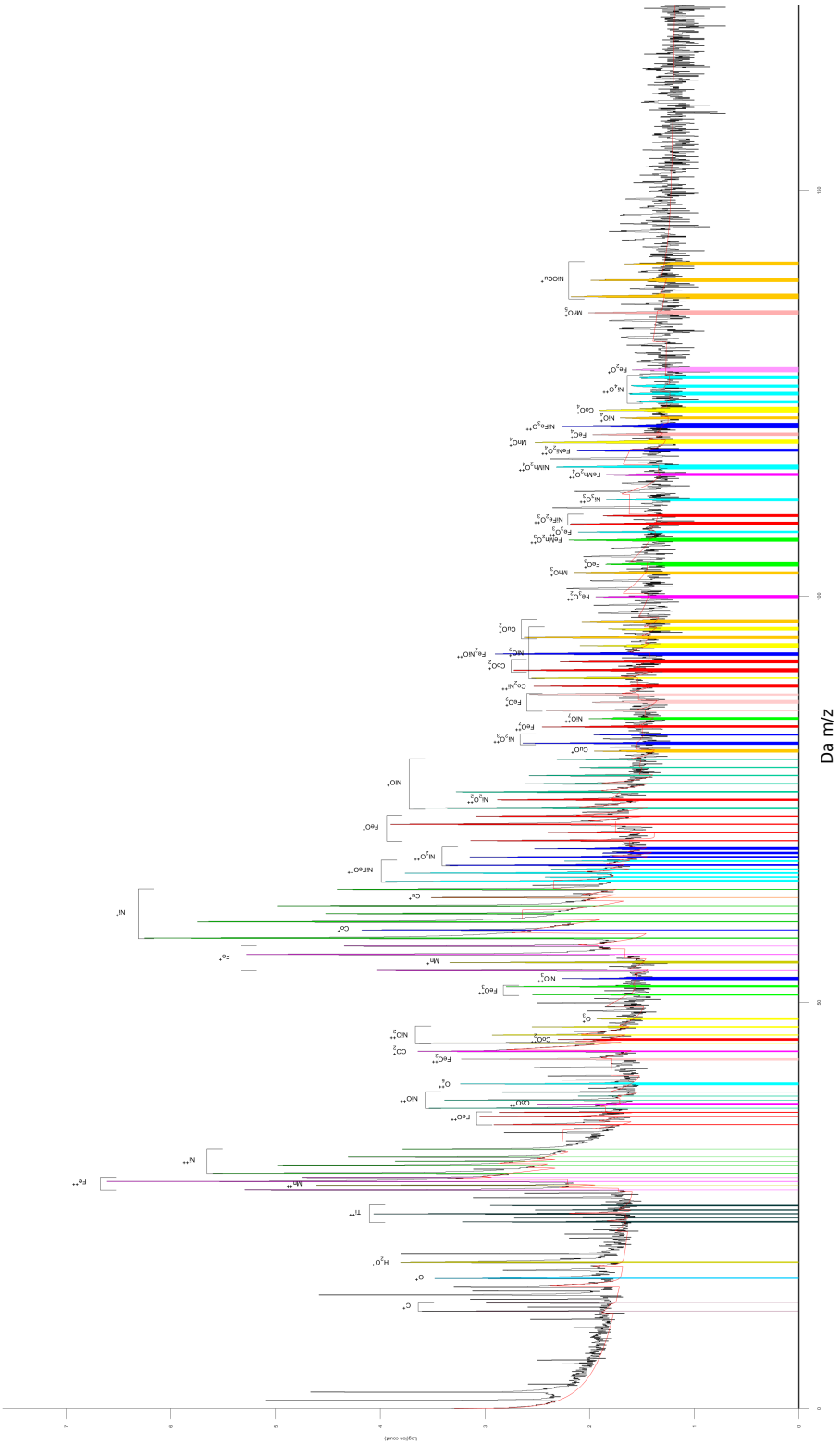

Figure A.1.1 – Peak labelling for a 360 mins oxidised Ni48Fe52 wire. There are multi peaks representing oxide species. Overlapping is severe in this region. Deconvolution has to be performed to solidify the decision of peak identification.

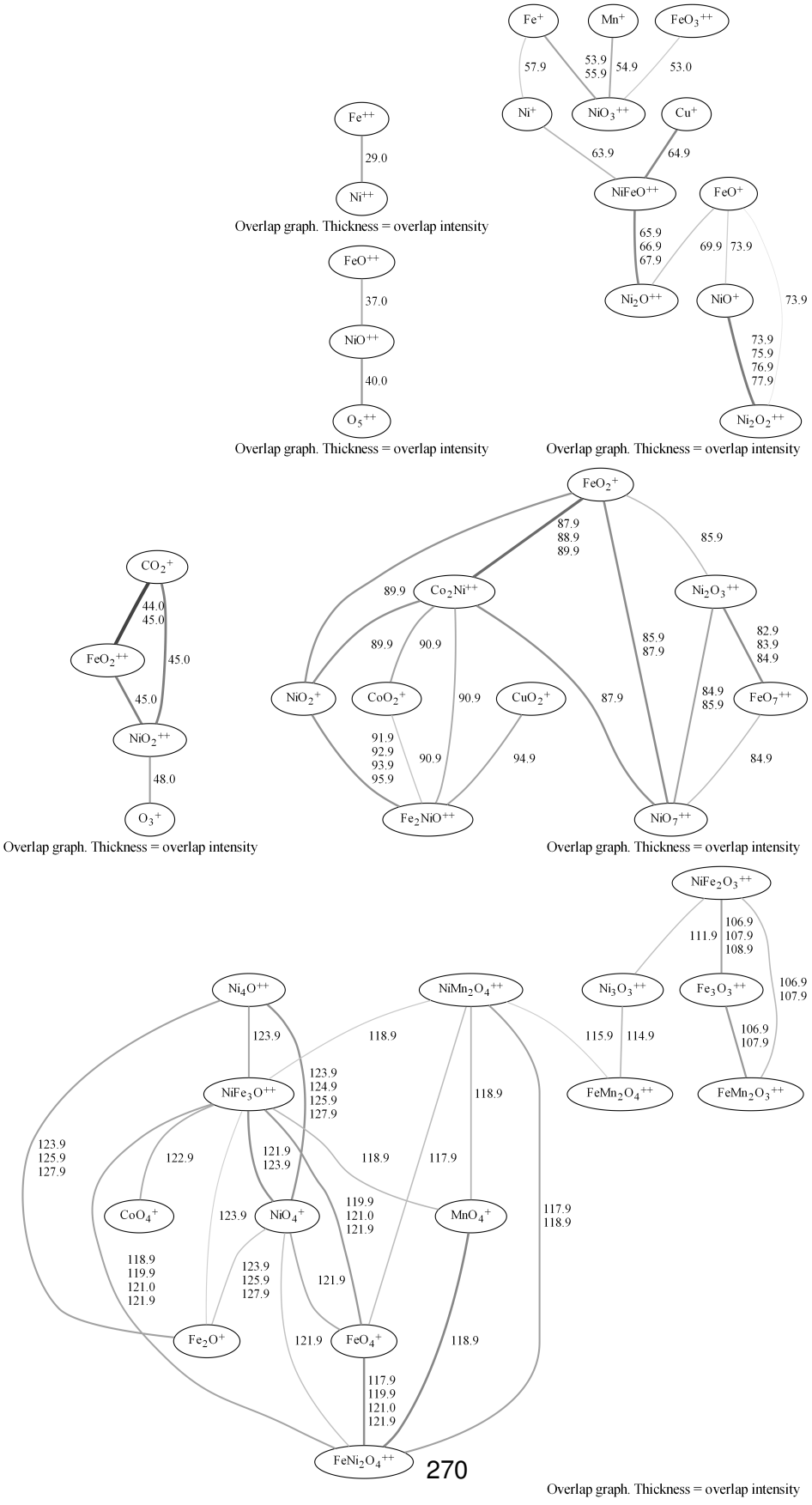

Figure A.1.2 – Overlap relationship of peaks in Ni48Fe52 wires.

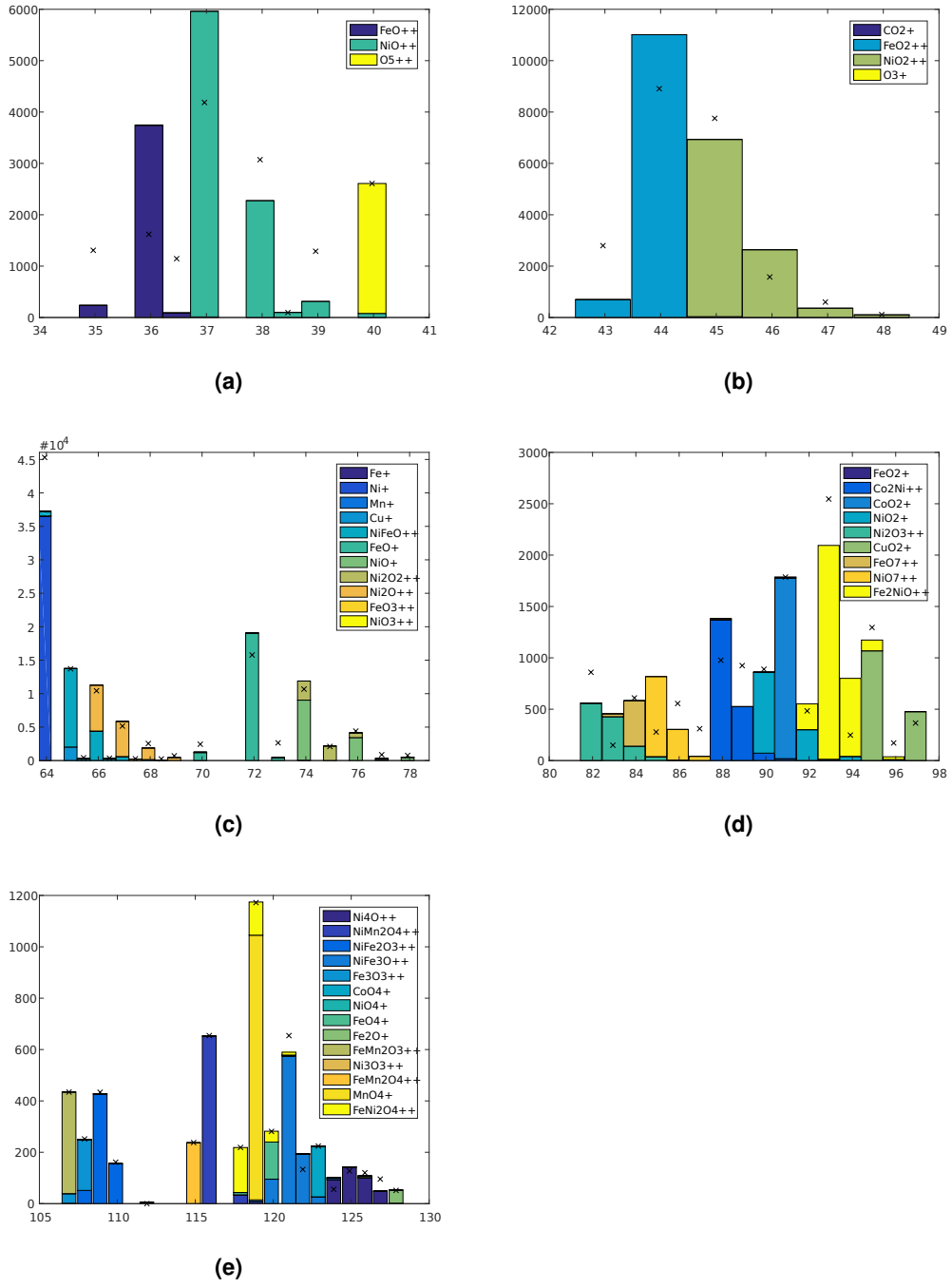

Figure A.1.3 – Peak deconvolution and fitting of oxidised Ni48Fe52 samples.

Da	Ions	Da	Ions	Da	Ions
12.0	$^{12}C^{+}$	54.0	$^{54}Fe^{+}$	88.5	$^{58}Ni^{60}Ni^{59}Co^{2+}$
13.0	$^{13}C^{+}$	55.0	$^{55}Mn^{+}$	89.0	$^{60}Ni^{59}Co^{59}Co^{2+}$
16.0	$^{16}O^{+}$	56.0	$^{56}Fe^{+}$	90.0	$^{58}Ni^{16}O^{16}O^{+}$
18.0	$^{16}O^{1}H^{1}H^{+}$	57.0	$^{57}Fe^{+}$	91.0	$^{59}Co^{16}O^{16}O^{+}$
23.0	$^{46}Ti^{2+}$	58.0	$^{58}Ni^{+}$	93.0	$^{54}Fe^{56}Fe^{60}Ni^{16}O^{2+}$
23.5	$^{47}Ti^{2+}$	59.0	$^{59}Co^{+}$	93.0	$^{61}Ni^{16}O^{16}O^{+}$
24.0	$^{48}Ti^{2+}$	60.0	$^{60}Ni^{+}$	94.0	$^{62}Ni^{16}O^{16}O^{+}$
24.5	$^{49}Ti^{2+}$	61.0	$^{61}Ni^{+}$	95.0	$^{16}O^{16}O^{63}Cu^{+}$
25.0	$^{50}Ti^{2+}$	62.0	$^{62}Ni^{+}$	96.0	$^{56}Fe^{58}Ni^{62}Ni^{16}O^{2+}$
27.0	$^{54}Fe^{2+}$	63.0	$^{63}Cu^{+}$	97.0	$^{16}O^{16}O^{65}Cu^{+}$
27.5	$^{55}Mn^{2+}$	64.0	$^{64}Ni^{+}$	100.0	$^{56}Fe^{56}Fe^{56}Fe^{16}O^{16}O^{2+}$
28.0	$^{56}Fe^{2+}$	65.0	$^{54}Fe^{60}Ni^{16}O^{2+}$	103.0	$^{16}O^{16}O^{16}O^{55}Mn^{+}$
28.5	$^{57}Fe^{2+}$	65.5	$^{54}Fe^{61}Ni^{16}O^{2+}$	104.0	$^{56}Fe^{16}O^{16}O^{16}O^{+}$
29.0	$^{58}Ni^{2+}$	66.0	$^{56}Fe^{60}Ni^{16}O^{2+}$	105.0	$^{57}Fe^{16}O^{16}O^{16}O^{+}$
30.0	$^{60}Ni^{2+}$	66.5	$^{56}Fe^{61}Ni^{16}O^{2+}$	107.0	$^{56}Fe^{16}O^{16}O^{16}O^{55}Mn^{55}Mn^{2+}$
30.5	$^{61}Ni^{2+}$	67.0	$^{58}Ni^{60}Ni^{16}O^{2+}$	108.0	$^{54}Fe^{56}Fe^{58}Ni^{16}O^{16}O^{16}O^{2+}$
31.0	$^{62}Ni^{2+}$	67.5	$^{57}Fe^{60}Ni^{16}O^{2+}$	109.0	$^{54}Fe^{56}Fe^{60}Ni^{16}O^{16}O^{16}O^{2+}$
35.0	$^{54}Fe^{16}O^{2+}$	68.0	$^{58}Ni^{62}Ni^{16}O^{2+}$	110.0	$^{56}Fe^{56}Fe^{60}Ni^{16}O^{16}O^{16}O^{2+}$
36.0	$^{56}Fe^{16}O^{2+}$	68.5	$^{60}Ni^{61}Ni^{16}O^{2+}$	112.0	$^{56}Fe^{58}Ni^{62}Ni^{16}O^{16}O^{16}O^{2+}$
36.5	$^{57}Fe^{16}O^{2+}$	69	$^{60}Ni^{62}Ni^{16}O^{2+}$	115.0	$^{56}Fe^{16}O^{16}O^{16}O^{16}O^{55}Mn^{55}Mn^{2+}$
37.0	$^{58}Ni^{16}O^{2+}$	70.0	$^{54}Fe^{16}O^{+}$	116.0	$^{58}Ni^{16}O^{16}O^{16}O^{16}O^{55}Mn^{55}Mn^{2+}$
37.5	$^{59}Co^{16}O^{2+}$	71.0	$^{55}Fe^{16}O^{+}$	118.0	$^{54}Fe^{58}Ni^{60}Ni^{16}O^{16}O^{16}O^{16}O^{2+}$
38.0	$^{60}Ni^{16}O^{2+}$	72.0	$^{56}Fe^{16}O^{+}$	119.0	$^{16}O^{16}O^{16}O^{16}O^{55}Mn^{+}$
38.5	$^{61}Ni^{16}O^{2+}$	73.0	$^{57}Fe^{16}O^{+}$	120.0	$^{56}Fe^{16}O^{16}O^{16}O^{16}O^{+}$
39.0	$^{62}Ni^{16}O^{2+}$	74.0	$^{58}Ni^{16}O^{+}$	120.5	$^{56}Fe^{57}Fe^{56}Fe^{56}Fe^{16}O^{2+}$
40.0	$^{16}O^{16}O^{16}O^{16}O^{16}O^{2+}$	75.0	$^{58}Ni^{60}Ni^{16}O^{16}O^{2+}$	121.0	$^{54}Fe^{56}Fe^{56}Fe^{60}Ni^{16}O^{2+}$
43.0	$^{54}Fe^{16}O^{16}O^{2+}$	76.0	$^{60}Ni^{16}O^{+}$	122.0	$^{58}Ni^{16}O^{16}O^{16}O^{16}O^{+}$
44.0	$^{56}Fe^{16}O^{16}O^{2+}$	77.0	$^{61}Ni^{16}O^{+}$	123.0	$^{59}Co^{16}O^{16}O^{16}O^{16}O^{+}$
44.0	$^{16}O^{16}O^{12}C^{+}$	78.0	$^{62}Ni^{16}O^{+}$	124.0	$^{58}Ni^{58}Ni^{58}Ni^{58}Ni^{16}O^{2+}$
44.5	$^{57}Fe^{16}O^{16}O^{2+}$	79.0	$^{63}Ni^{16}O^{+}$	125.0	$^{58}Ni^{60}Ni^{58}Ni^{58}Ni^{16}O^{2+}$
45.0	$^{58}Ni^{16}O^{16}O^{2+}$	80.0	$^{64}Ni^{16}O^{+}$	126.0	$^{54}Fe^{56}Fe^{16}O^{+}$
45.0	$^{16}O^{16}O^{13}C^{+}$	81.0	$^{16}O^{65}Cu^{+}$	126.0	$^{58}Ni^{60}Ni^{58}Ni^{60}Ni^{16}O^{2+}$
45.5	$^{59}Co^{16}O^{16}O^{2+}$	82.0	$^{58}Ni^{58}Ni^{16}O^{16}O^{16}O^{2+}$	126.0	$^{62}Ni^{16}O^{16}O^{16}O^{16}O^{+}$
46.0	$^{60}Ni^{16}O^{16}O^{2+}$	83.0	$^{58}Ni^{60}Ni^{16}O^{16}O^{16}O^{2+}$	127.0	$^{58}Ni^{60}Ni^{60}Ni^{60}Ni^{16}O^{2+}$
46.5	$^{61}Ni^{16}O^{16}O^{2+}$	84.0	$^{56}Fe^{16}O^{16}O^{16}O^{16}O^{16}O^{16}O^{16}O^{2+}$	128.0	$^{56}Fe^{56}Fe^{16}O^{+}$
47.0	$^{62}Ni^{16}O^{16}O^{2+}$	84.5	$^{57}Fe^{16}O^{16}O^{16}O^{16}O^{16}O^{16}O^{16}O^{2+}$	135.0	$^{16}O^{16}O^{16}O^{16}O^{16}O^{55}Mn^{+}$
48.0	$^{16}O^{16}O^{16}O^{+}$	85.0	$^{58}Ni^{16}O^{16}O^{16}O^{16}O^{16}O^{16}O^{16}O^{2+}$	137.0	$^{58}Ni^{16}O^{63}Cu^{+}$
51.0	$^{54}Fe^{16}O^{16}O^{16}O^{2+}$	86.0	$^{54}Fe^{16}O^{16}O^{+}$	139.0	$^{58}Ni^{16}O^{65}Cu^{+}$
52.0	$^{56}Fe^{16}O^{16}O^{16}O^{2+}$	88.0	$^{56}Fe^{16}O^{16}O^{+}$	141.0	$^{60}Ni^{16}O^{65}Cu^{+}$
53.0	$^{58}Ni^{16}O^{16}O^{16}O^{2+}$	88.5	$^{58}Ni^{60}Ni^{59}Co^{2+}$	143.0	$^{62}Ni^{16}O^{65}Cu^{+}$

Table A.1.1 – Ion species identification of the oxidised Ni48Fe52 wire sample.

A.2 Ni90Fe10

Similar peak identifications are conducted on Ni90Fe10 samples. Due to the limited development of oxide and relative contamination-free composition, there are significant less peaks associated to formed oxides comparing to the Ni48Fe52 samples. Mass spectrum of a oxidised Ni90Fe10 sample is shown in Figure A.2.1. Still, there are double charged region (around Da 33 to Da 44) and single charged region (beyond Da 63). Overlap relationship is shown in Figure A.2.2 and peak fittings are shown in Figure A.2.3. The relationship is quite similar to the Ni10Fe90 sample mentioned above and the peak fitting results matches quite well the actual mass spectrum detection. Especially in the single charged oxide region, the separation of Ni oxide and Fe oxide is distinct. Therefore, little composition dispute will occur when analysing oxide composition. Similar to the other oxide analysed above, the existence of Cu is observed which could be the contamination transferring from the Cu tube for sample handling during the whole sequence of high field surface cleaning and subsequent oxidation. A complete list of identified ions used to label this Ni90Fe10 sample is shown in Table A.2.1.

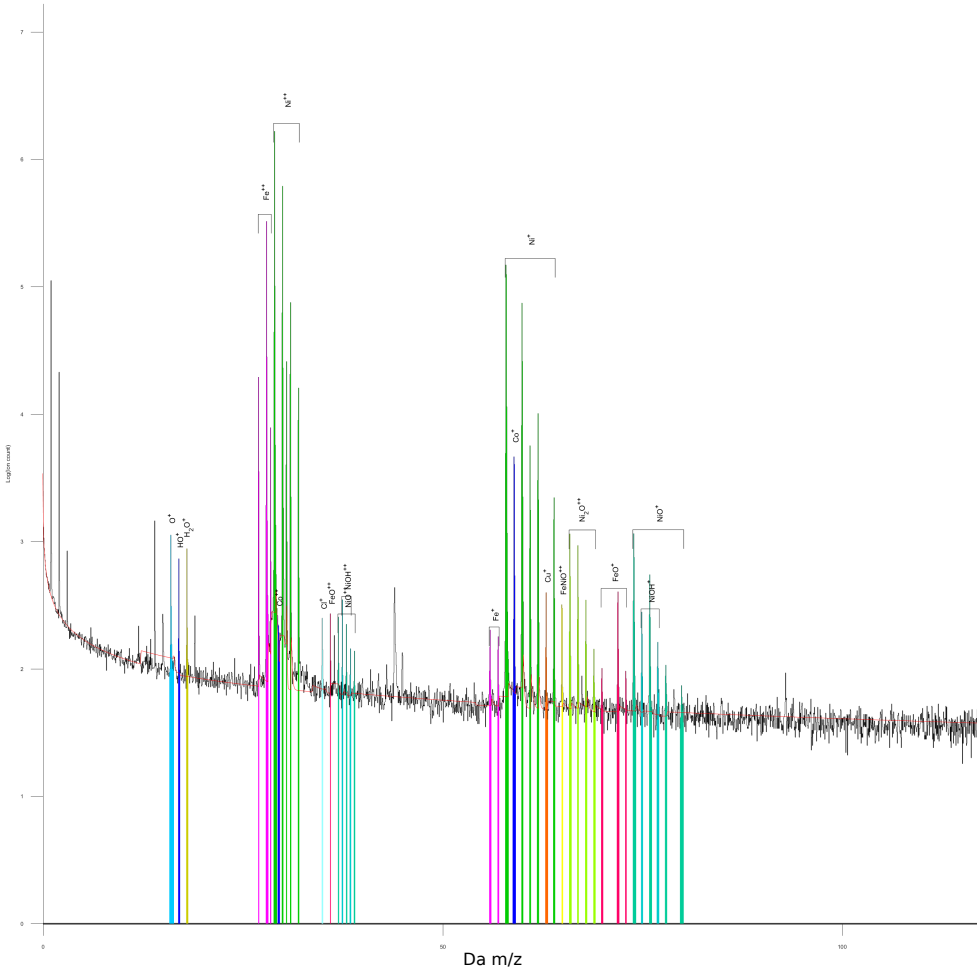

Figure A.2.1 – Peak labelling of a oxidised Ni90Fe10 sample. It shows a relative simple peak relationship comparing to Ni48Fe52 sample.

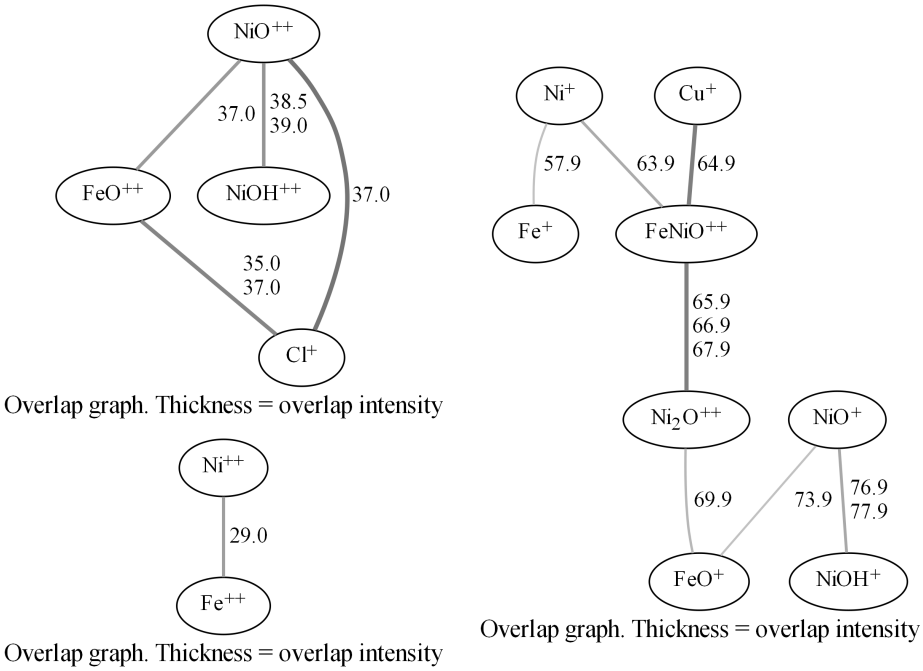

Figure A.2.2 – Peak relationship of oxidised Ni90Fe10 wires. There are three main associated overlap groups. Overlap between $FeNiO^{++}$ and Ni_2O^{++} is the most important overlap identified.

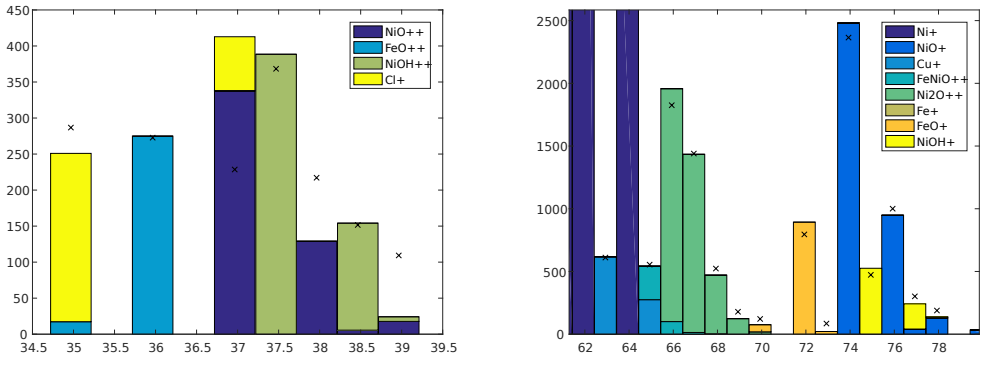

(a) **(b)**

Figure A.2.3 – Convolution of peaks from the oxidised Ni90Fe10 samples. (a) No significant overlap in the double charged oxide species. (b) Overlapped region of single and double charged oxide species. The most significant overlap is at Da 65, where Cu^{+} overlaps with $FeNiO^{++}$

Da	Ions	Da	Ions	Da	Ions
16.0	$^{16}O^{+}$	39.0	$^{62}Ni^{16}O^{2+}$	67.0	$^{58}Ni^{60}Ni^{16}O^{2+}$
17.0	$^{16}O^{1}H^{+}$	39.5	$^{62}Ni^{16}O^{1}H^{2+}$	67.0	$^{60}Ni^{58}Ni^{16}O^{2+}$
18.0	$^{16}O^{1}H^{1}H^{+}$	54.0	$^{54}Fe^{+}$	67.0	$^{58}Ni^{60}Ni^{16}O^{2+}$
27.0	$^{54}Fe^{2+}$	56.0	$^{56}Fe^{+}$	68.0	$^{58}Ni^{62}Ni^{16}O^{2+}$
28.0	$^{56}Fe^{2+}$	57.0	$^{57}Fe^{+}$	68.0	$^{58}Ni^{62}Ni^{16}O^{2+}$
28.5	$^{57}Fe^{2+}$	58.0	$^{58}Ni^{+}$	68.0	$^{58}Ni^{62}Ni^{16}O^{2+}$
29.0	$^{58}Ni^{2+}$	59.0	$^{59}Co^{+}$	68.0	$^{60}Ni^{60}Ni^{16}O^{2+}$
29.5	$^{59}Co^{2+}$	60.0	$^{60}Ni^{+}$	68.0	$^{62}Ni^{58}Ni^{16}O^{2+}$
30.0	$^{60}Ni^{2+}$	62.0	$^{62}Ni^{+}$	68.0	$^{58}Ni^{62}Ni^{16}O^{2+}$
31.0	$^{62}Ni^{2+}$	63.0	$^{63}Cu^{+}$	70.0	$^{54}Fe^{16}O^{+}$
35.0	$^{35}Cl^{+}$	64.0	$^{54}Fe^{58}Ni^{16}O^{2+}$	72.0	$^{56}Fe^{16}O^{+}$
35.0	$^{54}Fe^{16}O^{2+}$	64.5	$^{56}Fe^{57}Fe^{16}O^{2+}$	73.0	$^{57}Fe^{16}O^{+}$
36.0	$^{56}Fe^{16}O^{2+}$	65.0	$^{65}Cu^{+}$	74.0	$^{58}Ni^{16}O^{+}$
36.5	$^{57}Fe^{16}O^{2+}$	65.0	$^{56}Fe^{58}Ni^{16}O^{2+}$	75.0	$^{58}Ni^{16}O^{1}H^{+}$
37.0	$^{37}Cl^{+}$	66.0	$^{56}Fe^{60}Ni^{16}O^{2+}$	76.0	$^{60}Ni^{16}O^{+}$
37.0	$^{58}Ni^{16}O^{2+}$	66.0	$^{58}Ni^{58}Ni^{16}O^{2+}$	77.0	$^{60}Ni^{16}O^{1}H^{+}$
37.5	$^{58}Ni^{16}O^{1}H^{2+}$	67.0	$^{56}Fe^{62}Ni^{16}O^{2+}$	78.0	$^{62}Ni^{16}O^{+}$
38.0	$^{60}Ni^{16}O^{2+}$	67.0	$^{58}Ni^{60}Ni^{16}O^{2+}$	79.0	$^{62}Ni^{16}O^{1}H^{+}$
38.5	$^{60}Ni^{16}O^{1}H^{2+}$	67.0	$^{58}Ni^{60}Ni^{16}O^{2+}$		

Table A.2.1 – Ion species identification of the oxidised Ni90Fe10 wire sample.

A.3 Ni50Co50

Peak identification for the Ni50Co50 sample is relatively simple since there is no direct overlap between Ni an Co. Also, Co only has on isotope at Da 59, which leads to limited number of ion peaks associated to oxides (as shown in Figure A.3.2). There are two block of overlap peaks as shown in Fig. A.3.1a. The overlap at Da 29 between Ni and N has a relative small impact. Mostly, ions contained in the peak Da 29 is mostly made up with Ni. On the other hand, overlap in the region of oxides are more complicated. $Ni_2O^{++}$and Co_2O^{++} have a overlap at Da 66.9, which is hard to perform deconvolution. This overlap also exists between Ni_2O^{++} and $NiCoO^{+}$at Da 67.4, 67.9 and 68.4. The local deconvolution map around the oxide region is shown in Fig. A.3.1b. There are three species: Ni_2O^{++}, Co_2O^{++} and $NiCoO^{++}$ entangled in this region. In the peak of Da 66.9, the fraction of Ni_2O^{++} and $Co_2O^{++}$is half and half. Due to the lack of the number of Co_2O^{++} peak, the uncertainty of determining the Da 66.9 is high. In this research, Da 66.9 is labelled as Co_2O^{++}. It is therefore clear that the estimation of $NiCoO^{++}$ is overwhelmed at Da 66.5 whereas $NiCoO^{++}$is underestimated at Da 67.5 and 68.5. It can be ex peculated that some other components are contained in the peak of Da 66.5. However, it is not reasonable to label Da 66.5 into other specie since $NiCoO^{++}$ has a dominance. The overestimation of peak at Da 66 is also related to the missing composition at Da 66.5. However, the deviation is not strong enough to label those peaks into other species. Overall, the identified peaks are listed in Table A.3.1.

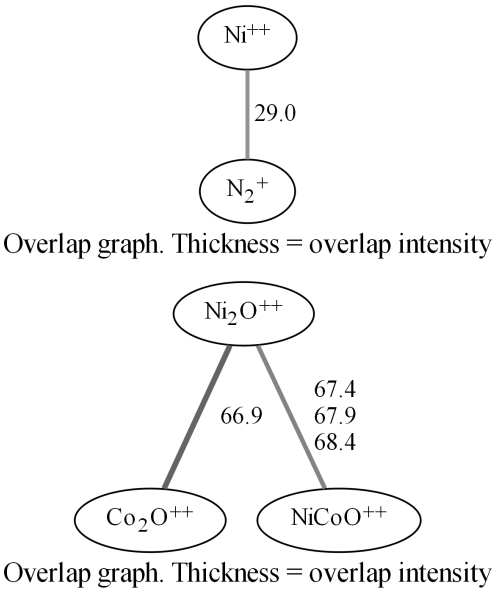

(a) Overlapped peak analysis

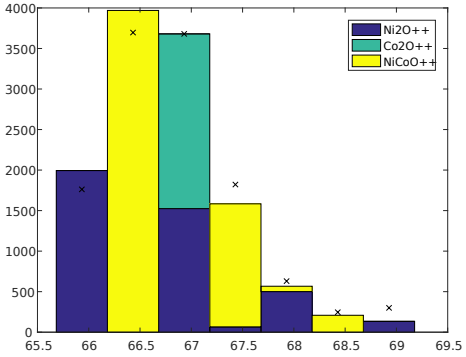

(b) overlap analysis of Ni and Co oxides

Figure A.3.1 – Peak overlap analysis of Ni50Co50 oxidised sample. (a) The overlap of Ni and N is minimum but the overlap between Ni_2O and Co_2O. The dark-line between the two bubble indicates the overlap is hard to solve. (b) Local deconvolution of peaks around the region of Ni and Co oxides.

Da	Ions	Da	Ions	Da	Ions
16.0	$^{16}O^{+}$	63.0	$^{63}Cu^{+}$	68.0	$^{58}Ni^{62}Ni^{16}O^{2+}$
27.0	$^{27}Al^{+}$	65.0	$^{65}Cu^{+}$	68.0	$^{58}Ni^{62}Ni^{16}O^{2+}$
28.0	$^{14}N^{14}N^{+}$	66.0	$^{58}Ni^{58}Ni^{16}O^{2+}$	68.0	$^{60}Ni^{60}Ni^{16}O^{2+}$
29.0	$^{58}Ni^{2+}$	66.5	$^{58}Ni^{59}Co^{16}O^{2+}$	68.0	$^{62}Ni^{58}Ni^{16}O^{2+}$
29.5	$^{59}Co^{2+}$	67.0	$^{59}Co^{59}Co^{16}O^{2+}$	68.0	$^{58}Ni^{62}Ni^{16}O^{2+}$
30.0	$^{60}Ni^{2+}$	67.0	$^{58}Ni^{60}Ni^{16}O^{2+}$	68.0	$^{58}Ni^{62}Ni^{16}O^{2+}$
31.0	$^{62}Ni^{2+}$	67.0	$^{58}Ni^{60}Ni^{16}O^{2+}$	68.5	$^{62}Ni^{59}Co^{16}O^{2+}$
58.0	$^{58}Ni^{+}$	67.0	$^{60}Ni^{58}Ni^{16}O^{2+}$	74.0	$^{58}Ni^{16}O^{+}$
59.0	$^{59}Co^{+}$	67.0	$^{58}Ni^{60}Ni^{16}O^{2+}$	75.0	$^{59}Co^{16}O^{+}$
60.0	$^{60}Ni^{+}$	67.0	$^{58}Ni^{60}Ni^{16}O^{2+}$	76.0	$^{60}Ni^{16}O^{+}$
62.0	$^{62}Ni^{+}$	67.5	$^{60}Ni^{59}Co^{16}O^{2+}$	78.0	$^{62}Ni^{16}O^{+}$

Table A.3.1 – Ion species identification of the oxidised Ni50Co50 wire sample.

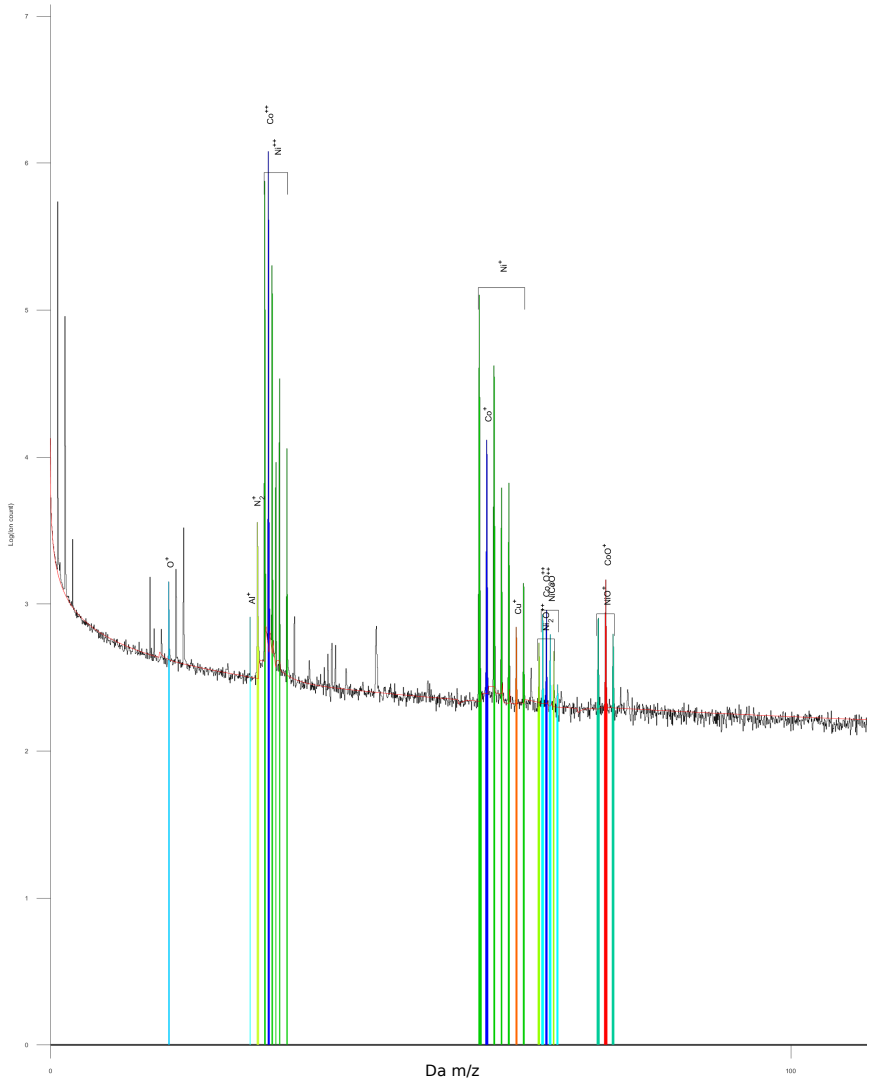

Figure A.3.2 – Identification of peaks from a typical oxidised Ni50Co50 sample.

Appendix B

Appendix-experiment table

Running ID	Running conditions	oxidation time/min	oxidation temperature/K	Data size/M	Purpose used in the thesis
02303	UV laser,50pJ,50K	-	-	4	reference running, initial 1M contains oxides
02564	UV laser,50pJ,50K	-	-	5.1	reference
02566	UV laser,50pJ,50K	-	-	1	data sheet, as-received
02568	UV laser,50pJ,50K	-	-	17	Reference running, mass spectrum checking
02572	UV laser,40pJ,50K	-	-	5	surface cleaning
02738	UV laser,50pJ,50K	-	-	32	polished to metal
02753	UV laser,50pJ,50K	-	-	5	polished to metal
02754	UV laser,40pJ,50K	-	-	3	laser changing
02755	UV laser,30pJ,50K	-	-	58	laser changing
02756	UV laser,20pJ,50K	-	-	7	laser changing
02706	UV laser,50pJ,50K	120	353	5.9	oxides
02636	UV laser,50pJ,50K	240	353	5.3	oxidation
02565	UV laser,50pJ,50K	280	353	6	oxidation
02604	UV laser,50pJ,50K	2100	353	4	oxidation
02759	UV laser,50pJ,50K	60	473	5	oxide

Table B.0.1 – Ni50Co50 sample sheet

Running ID	Running conditions	oxidation time/min	oxidation tempera-ture/K	Data size/M	Purpose used in the thesis
19376	Green laser, 0.5nJ,50K	30	353	1	No use, contamination
18747	Green laser, 0.5nJ,50K	30	353	4	small oxides
20718	Green laser, 0.5nJ,50K	30	353	10	thick oxide
19038	Green laser, 0.5nJ,50K	60	353	17	think Ni big block on the surface
19254	Green laser, 0.5nJ,50K	120	353	5	entire oxides
19699	Green laser, 0.5nJ,50K	180	353	1.2	just heating without Oxygen
02728	UV laser,50pJ,50K	360	353	3	oxides
02574	UV laser,50pJ,50K	1000	353	4.3	with FIM image called sample Up date 5/2/17
03310	UV laser,100pJ,65K	60	393	7	oxide, ran in Harvard
03279	UV laser,50pJ,50K	60	433	1.6	oxide, ran in Harvard
02677	UV laser,50pJ,50K	60	473	4.7	oxidation
02758	UV laser,50pJ,50K	60	473	5	oxide
02771	UV laser,50pJ,50K	60	673	1.6	oxide, with Cu
02839	UV laser,50pJ,50K	60	673	2.1	oxide, with Cu
18552	Green laser, 0.5nJ,50K	-	-	9	reference
02571	UV laser,50pJ,50K	-	-	5	reference running
02722	UV laser,50pJ,50K	-	-	13	from electrical polishing to flesh surface
23369	Voltage, 20%	-	-	2.1	reference
00563	Voltage, 20%	-	-	4	voltage reference running
00606	Voltage, 20%	-	-	2.2	voltage reference running
00634	Voltage, 20%	-	-	5.3	voltage reference running
01461	UV laser,50pJ,50K	-	-	3.8	laser and temperature calibration
01462	UV laser,40pJ,50K	-	-	3.3	laser and temperature calibration
01478	UV laser,30pJ,50K	-	-	2	laser and temperature calibration
01495	UV laser,20pJ,50K	-	-	5	laser and temperature calibration
01496	UV laser,10pJ,50K	-	-	2.3	laser and temperature calibration
01497	UV laser,60pJ,50K	-	-	8	laser and temperature calibration
01498	UV laser,70pJ,50K	-	-	8	laser and temperature calibration
01499	UV laser,80pJ,50K	-	-	8	laser and temperature calibration
01501	UV laser,40pJ,55K	-	-	8	laser and temperature calibration
01503	UV laser,40pJ,60K	-	-	8.6	laser and temperature calibration

Table B.0.2 – Ni90Fe10 sample sheet

Running ID	Running conditions	oxidation time/min	oxidation temperature/K	Data size/M	Purpose used in the thesis
18431	Green laser, 0.4nJ,50K	30	353	10	have oxide, a mini fracture during the middle of running
18506	Green laser, 0.4nJ,50K	60	353	9	no oxide
18657	Green laser, 0.4nJ,50K	60	353	17	no oxides
18673	Green laser, 0.5nJ,50K	240	493	1	have oxide
18591	Green laser, 0.73nJ,50K	360	353	12	have oxide
18764	Green laser, 0.5nJ,50K	360	353	19	no oxides
18471	Green laser, 0.4nJ,50K	1200	353	13	oxides forming on the side
18775	Green laser, 0.5nJ,50K	1440	353	3.7	Hydrogen reduction*
18783	Green laser, 0.5nJ,50K	1440	353	2	following the 18775 running
18162	Green laser, 0.4nJ,50K	-	-		0.42nJ and 0.52nJ reference
18166	Green laser, 0.4nJ,50K				reference
18167	Green laser, 0.42nJ,50K	-	-	18	laser, composition reference

Table B.0.3 – Fe52Ni48 sample running sheet

Running ID	Running conditions	oxidation time/min	oxidation temperature/K	Data size/M	Purpose used in the thesis
18926	Green laser, 0.5nJ,50K	30	353	6.6	good oxidation
18538	Green laser, 0.4nJ,50K	60	353	1	oxidation, data too small not use
18950	Green laser, 0.5nJ,50K	60	353	18	good oxides
18802	Green laser, 0.4nJ,50K	600	353	0.3	Hydrogen reduction† find Ni on the top
18951	Green laser, 0.5nJ,50K	720	353	31	good oxides
02230	UV laser,50pJ,45K	60	473	6	good oxides, ran in Harvard
18829	Green laser, 0.5nJ,50K	-	-	17	reference
21629	Voltage, 20%	-	-	8	reference

Table B.0.4 – Fe90Ni10 sample running sheet

Running ID	Running conditions	oxidation time/mins	oxidation temperature/K	Data size/M	Purpose used in the thesis
22352	Voltage, 20%	-	-	1.4	reference

Table B.0.5 – Fe sample sheet

Running ID	Running conditions	Sample	Data size/M	Purpose used in the thesis
16715	Green laser,0.55nJ,50K	Ag	10	Mantis pilot trial
20799	Green laser, 0.3nJ,55K	AuCuMo	0.27	One particle embedded in the center
20806		AuCuMo		1 NP, no Ag coating
20955		AuCu		one small NP
20956		AuCu		3 particles detected
20960		AuCu		one particle
22451	Green laser, 0.2nJ,55K	AuNi+He		definitely 2 NPs, Pure gold
22973	Green laser, 0.2nJ,55K,160kHz	AuNi+He		good runnings
23796	Green laser, 0.2nJ,55K,100kHz	AuNi+He		2 NPs large dataset
22512		AuNiMo		good
23888	Green laser, 0.2nJ,55K,100kHz	AuNiMo		1 NP. break in the middle
23971	Green laser, 0.2nJ,55K,100kHz	AuNiMo		good 1 NP
00345	UV laser, 44pJ,50K,100kHz	AuNi		One NP small

Table B.0.6 – Data sheet of APT analyses of nanoparticles made by IGC method including Ag, AuCu, AuCuMo, AuNi, AuNi with He and AuNiMo.